TECHNISCHE
UNIVERSITÄT
WIEN
Vienna | Austria

HABILITATIONSSCHRIFT

Electronic processes measured and controlled with strong laser fields

Zur Erlangung der Lehrbefugnis für das Fachgebiet

Ultrafast Photonics

eingereicht an der

Technischen Universität Wien
Fakultät für Elektrotechnik und Informationstechnik

von

Markus Kitzler-Zeiler
geboren am 14.11.1974 in Waidhofen/Thaya, Österreich

Wien, im Mai 2018

WEGE ENTSTEHEN DADURCH, DASS MAN SIE GEHT.
Franz Kafka

Contents

1

Introduction

Photonics — the science of generation, detection, transmission, modulation, switching, and amplification of light, and the interaction of light with matter[1] — has grown from its infancy in the 1960's to one of the key technologies for the 21st century. The term 'photonics' has been coined in reminiscence of the term 'electronics' to indicate that in photonics one studies and exploits the properties of photons (instead of electrons). Photonics, thus, deals with the properties and applications of light and light-particles (photons), and their interaction with matter. In terms of the considered portion of the electromagnetic spectrum it is nowadays usual to understand photonics in a broad sense and to define that the realm of photonics ranges from the THz and far-infrared region (frequency about 10^{12} Hz) throughout the visible spectral region (frequency about 10^{15} Hz) to the hard X-ray regime, corresponding to photon energies that range from about 10 meV to 10 keV and even beyond. During the last decades, the field of photonics has not only developed into one of the most important areas of technology and a huge business, but also into a very diverse and vivid research field consisting of numerous sub-fields that each specialize on certain aspects of photonics. The different sub-fields may be characterized by the properties of the light that is used, the considered application, the type of interaction, or through the type of matter that the light interacts with. Naturally, the boundaries between these different sub-fields are not sharply defined. Well-known examples of sub-fields are biophotonics[2], nanophotonics[3], quantum optics[4], optical telecommunication, etc.

Since its advent, many sub-fields of photonics have grown into large independent fields of science and technology such that it is no longer possible to be an expert in all fields of photonics and specialization has become inevitable. A common key aspect of most areas of photonics is, however, the interaction of light with matter. Of particular importance for the study of processes that take place during the interaction of light waves with different types of matter on a fundamental level is to obtain a thorough understanding of the underlying dynamics. Depending on the considered material, the size of the object, the type of the interaction, and the considered process, these dynamics may take place on time-scales ranging from nano- (10^{-9} s) and possibly even microseconds (10^{-6} s) down to attoseconds (10^{-18} s), see Fig. 1.1(a). Examples of dynamical processes that are of scientific interest are chemical processes such as the breakage of a molecular bond, the transfer of energy between two biological entities, the transport and recombination dynamics of electrons in different solids, the formation and propagation of plasmonic waves in metals, etc. Of particular relevance for many important processes in nature and technology is the time domain from pico- (10^{-12} s) to attoseconds. The study of processes on these time scales and the invention and construction of suitable methods and devices for this research, is the content of Ultrafast Photonics[5]. The scientific journal NATURE defines Ultrafast Photonics as follows:[6]

ULTRAFAST PHOTONICS IS THE STUDY OF LIGHT AND ITS INTERACTION WITH MATTER ON SHORT TIMESCALES, TYPICALLY LESS THAN A PICOSECOND. THIS INCLUDES INVESTIGATING PROCESSES THAT OCCUR IN ATOMS AND MOLECULES, SUCH AS THE DYNAMICS AND CORRELATIONS BETWEEN ELECTRONS DURING IONIZATION, AND OFTEN EMPLOYS ULTRAFAST LASERS OR MODE-LOCKED LASERS.

This thesis will provide an overview over the such defined field of *Ultrafast Photonics*. The main topic is the interaction of laser fields with atoms and molecules on femto- (10^{-15} s) to attosecond time scales with a focus on methods that allow experimentally studying the dynamical processes underlying this interaction.

Studying processes on short time scales requires, in general, clocking them with a suitable reference process that is shorter or at least equally short as the process under study itself. As sketched in Fig. 1.1(a), the oscillations of an electronic oscillator can serve as such a reference process for dynamics slower than roughly 10 ps, which is about the intrinsic speed-limit of electronic devices. To resolve faster dynamics taking place in the pico- and femtosecond range, a different reference process must be used. An ideal reference process for these time-scales are bursts of light with femtosecond duration produced using lasers. Such laser pulses can be applied for the implementation of pump-probe spectroscopy with femtosecond resolution that has been pioneered by Ahmed Zewail in the field of Femtochemistry, i.e., the study of the dynamics of atoms in molecules[7]. The temporal resolution achieved by pump-probe spectroscopy is roughly given by the cross-correlation of the laser pulses used for starting (pump) and stopping (probe) the dynamics of interest, see Fig. 1.1(b). Because the fundamental limit for the duration of a laser pulse is given by the oscillation period of the light used for the pulses (which is roughly 1 fs in the near UV), processes taking place on time-scales faster than about 1 fs cannot be studied by pump-probe spectroscopy with conventional laser pulses carried at near-UV or longer wavelengths. Thus, to study processes taking place on attosecond time-scales fundamentally different approaches are needed[8]. As will be shown in this thesis, strong electric fields provided by state-of-the-art laser sources constitute both a unique temporal reference and driving force that allows measuring and also controlling dynamical (and, as will be described, also structural) properties of matter in the attosecond time-domain.

The physical reason for this opportunity is the fact that the properties of matter are ultimately determined by its electronic structure. A suitable perturbation of the electrons' distribution from its equilibrium configuration in a system such as an atom, a molecule, or a solid, can therefore initiate certain dynamical processes. Intense and ultrashort light pulses are ideal tools for that purpose as their electric fields couple directly to the electrons. Therefore they are not only able to distort the equilibrium electron distribution but, moreover, even allow driving a system on sub-femtosecond time-scales with the light's Petahertz field-oscillations[**9**], see the sketch in Fig. 1.1(c).

This has been realized first in experiments that studied atoms in strong laser fields some 25 years ago. These experiments revealed a wealth of fundamentally important phenomena that are strictly timed to the laser-field oscillations such as the release of electrons by tunneling through the field-distorted Coulomb binding potential[10–13], or field-driven (re-)collisions of the released electrons with the atomic ion[14–17]. The latter, in turn, led to the discovery of a range of essential secondary processes such as the generation of very high orders of harmonics of the driving light[18,19] with photon energies that can extend into the X-ray range[20].

Since then, thanks to a true revolution in laser technology, tremendous progress has been made in this research field also known as *Attosecond and Strong-Field Science*[21,22]. Laser technology has now reached a level of perfection where it is possible to produce intense light pulses with durations down to a single oscillation cycle and with virtually arbitrary evolution of the electric field in a wide range of frequencies[23–29]. The availability of such field transients enabled a number of

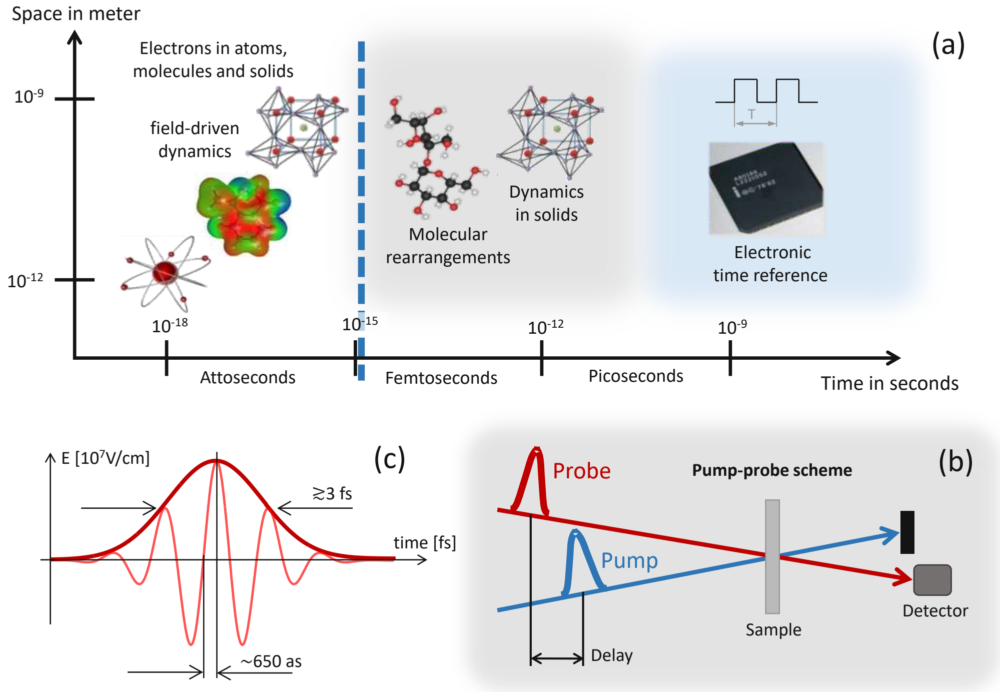

Figure 1.1: (a) Examples of dynamical processes. Depending on the considered material, the size of the object, the type of the interaction, and the considered process, dynamics may take place on time-scales ranging from nano- (10^{-9} s) to attoseconds (10^{-18} s). (b) Dynamics in the pico- and femtosecond range can be studied using the pump-probe scheme with ultrashort laser pulses. (c) In the attosecond regime the light oscillations of strong laser fields can be used as a temporal reference and a driving force.

exciting possibilities, such as control over the breakage of certain chemical bonds in molecules by directly driving the molecular valence electrons that actually form the bond, or the production of coherent attosecond pulses in the soft X-ray wavelength range that can be used for probing or initiating dynamics on time-intervals during which the electronic distribution in the system under study stays essentially frozen.

The recent years have seen a particularly vivid progress in the research of using ultrashort intense light pulses for controlling and probing ultrafast dynamics. On the one hand a number of groups have extended the research field to systems with a much increased complexity and have studied and controlled field-induced dynamics in large polyatomic molecules, cluster complexes, bio-matter, nanoparticles and crystals, and also in condensed phase systems such as solid surfaces, nanostructures and bulk solids. On the other hand the availability of new, coherent light sources in both the very short (X-rays) and very long (mid-infrared) wavelength ranges have allowed for the production and application of short and intense pulses in previously unexplored regimes.

Although the interaction of an intense laser pulse with a molecule or solid entails dynamics on very different timescales that may extend into the pico- or even nanosecond regimes, such as rotational and vibrational motion or phonon dynamics, these dynamics originate from electronic dynamics and processes that result from an essentially instantaneous distortion of the system's equilibrium electronic structure by an intense light pulse. And it is this electronic dynamics that can be initiated and driven with enormous precision and flexibility by gaining control over the electric field evolution of the light pulse.

Measurements of the light-induced structural dynamical evolution on the time-scale of attoseconds with strong laser fields can be performed by recording the systems' response with suitable detection schemes. Control over the structural dynamics is achieved by the use of tailored field evolutions for driving the electronic sub-system in a reproducible way. This opens up fascinating possibilities for field-control over a range of entailing processes such as the generation of secondary radiation in both the very high (XUV/X-ray) and low (THz) frequency regime, the creation and localization of Rydberg states, the dynamical correlation within the electronic cloud or of the electronic sub-system with the nuclei, or even bond-breaking events in molecules, which are a key process in any chemical reaction. This thesis provides a broad overview over existing methods and most important results obtained in the fields of Ultrafast Photonics and Attosecond and Strong-Field Science. Further information can be found in various review articles[21,30–34] and the recently published book Ref. [22].

Outline of thesis The structure of the thesis is as follows. It starts with an overview over Ultrafast Photonics by listing the most important quantum systems that are studied in this field and describing the key research questions that motivate the research for each system, thereby putting the research on atoms and molecules into a greater perspective (Section 2.1). After that, the basic processes that take place during the interaction of laser fields with matter are described (Section 2.2). Subsequently, different types of tailored laser waveforms and their specific properties (Chapter 3) as well as their application for the generation of secondary sources of radiation (Chapter 4) are reviewed. This is followed by a short description of detection techniques (Chapter 5). Chapters 6, 7 and 8 will then discuss in detail the most important methods and results in the measurement and control of atomic and molecular processes using strong laser fields. Papers that constitute the scientific basis of this thesis are listed in the Appendix and will be highlighted in the text as **Paper 1** to **Paper 18**. References to these and all other papers of the author are marked in **red color**. This also applies to the corresponding citations in the Bibliography.

2

Fundamental processes and research scope

Although electric fields couple only to the electrons in a physical system such as an atom, molecule or solid, the opportunity to drive the electronic sub-system at the pace of the field-evolutions opens up fascinating possibilities for controlling the dynamical and structural properties of matter on attosecond timescales. In principle, laser fields can drive electronic dynamics in any physical system of arbitrary complexity. Most studies so far, however, were performed, following a bottom-up approach, on isolated gas-phase atoms and molecules. This is, on the one hand, because of the natural desire to study fundamental processes as much as possible isolated from each other[35]. On the other hand, this approach is motivated by the high practical importance of molecular processes in the chemical, environmental and biological sciences. Still, the interaction of intense laser pulses with more complex physical systems such as clusters[36], dense gases (e.g. air at ambient pressure)[37], nanoobjects of various geometry[38], surfaces[39] and bulk solids[40–48] has been increasingly considered over the recent years.

2.1 Studied systems and key research questions

The absolute majority of works in the field of Attosecond and Strong-Field Science deals with the interaction of strong laser fields with atoms or molecules, which also constitutes the topic of this thesis. We will discuss in detail key concepts and insights that have emerged from this research below. The recent years have seen a considerable increase in the number of works that have tried to push the research towards systems of higher complexity, such as nanoobjects, surfaces or bulk solids. This research was largely driven by the availability of new light sources and detection and target preparation technologies. Here we want to briefly discuss a few of these new and exciting research directions and the questions that are tried to be answered by them.

If we proceed along the direction of increasing characteristic system size and complexity, then the next more complicated system after atoms and small molecules would be isolated **clusters** in the gas phase. A good review of processes observed in the interaction of strong laser fields with different clusters is provided by Fennel et al.[36]. The interesting property of clusters is that they can be produced of almost arbitrary size – from dimers and few-monomer clusters[49–55] up to very large clusters consisting of many thousands of monomers – and with a large variety of composition – from noble gas atoms over metal atoms to molecules and mixtures of atoms and molecules[56–66]. The basic idea of using clusters is that by increasing the size of the clusters and their composition, model systems with different response, from the one dominantly resembling that of isolated atoms to that of condensed phase systems and anything in between, can be imitated and gradually adjusted. Important processes investigated in the work on clusters are for example how the ionization dynamics is altered when the system size increases, what influence the surrounding monomers have on the ionization and electron acceleration dynamics, how the energy from the laser light is absorbed, how the cluster disintegrates during and after the laser interaction, and whether a possibly enhanced energy absorption mechanism can lead to energetic ions and/or electrons or even to the production of energetic particles such as neutrons[67], and whether clusters can be advantageously used for production of XUV or X-ray radiation[68–72].

So far, when talking about atoms, molecules and clusters, we have implicitly assumed that they are situated *isolated* from each other in a vacuum chamber and that they interact with the laser field each of them separately. That is, we explicitly excluded collective effects that can take place when a laser pulse propagates through **dense and extended gas media**. However, the study of the interaction of moderately intense light pulses with such media is in fact a very interesting research route by itself. A key process in this research is **filamentation**[73], i.e., the propagation of a beam of light through a medium without diffraction within a channel of small diameter over extended distances. The underlying mechanism for this type of propagation of a laser beam in a filament is a dynamic equilibrium between diffraction and self-focusing due to Kerr-type nonlinearity. Because the diameter of the filament is small, the intensity of the light pulse stays high during propagation. Therefore, during propagation, the pulse can experience a range of nonlinear transformations such as self- and cross-phase modulation, frequency conversion, pulse-splitting, etc. The important point is that during its propagation and interaction with the atoms and molecules inside the dense gas medium many of the processes observed with isolated atoms and molecules, as for example ionization, electron recollision, impact ionization, etc., still take place[37]. This makes filamentation a very attractive research platform of strong-field science at a distance. Consequently, currently major research efforts are undertaken to harness filamentation for molecule-specific atmospheric stand-off sensing[74–77], or to measure (and possibly control) atmospheric properties such as humidity[78] or aerosol concentration[79].

For higher laser intensity and increasing gas density the number of generated electrons and ions becomes so high that the laser pulse may likely generate a **plasma**. Plasma generation with intense laser pulses, propagation of the pulses through a plasma and the study of relativistic effects are a highly interesting and vast research field by itself[80,81], with a plethora of applications such as particle acceleration and X-ray generation[82,83]. However, the laser intensities necessary for this kind of research are beyond the laser parameters considered in this thesis.

Moving further in the direction of increasing system complexity we arrive at a highly fascinating field that has emerged only within the last decade: the interaction of ultrashort, intense and also tailored laser fields with **nanoparticles and nanostructures**, see, e.g., Refs. [38, 84–86] for reviews of this research field. We note that a cluster, isolated in vacuum, as considered above, may consist of several tens of thousands of monomers[87,88] and as such is also a nanoparticle. It is common in the literature, however, to distinguish between nanoscale clusters consisting of separate atoms and molecules, and nanoparticles consisting of solid material, e.g. of SiO_2 as used for example in Refs. [89, 90]. The main research thrust in this field is anyway devoted to the study of nanostructured solids. While on the one hand this type of research is interesting from a fundamental point of view as it investigates the interaction of light and matter in completely new regimes of parameters where collective effects, material parameters, and system geometries start to play a role, this research also comprises considerable potential for applications in that it could be used for, e.g., fabrication of devices for information transmission or fast switching[84,91]. Key points that render the interaction of strong light fields with nanoscale systems very interesting is their capability of locally enhancing the laser fields, and to confine optical fields to sub-wavelength structures. The former property can be tuned by the geometry of the nanoscale objects and can be exploited for driving strong-field dynamical processes such as electron emission[89,90,92–98] or high-harmonic generation[99–103] at a certain location defined with nanometer precision. The latter property is due to collective surface electron oscillations, called a surface plasmon polariton, whose propagation along a nanostructure can be influenced by geometry and material properties, and which can electronically transport energy (and information) across nanoscale distances[86,104]. This is fundamentally different from the case of isolated gas-phase atoms and molecules where the spatial extension of the system under study can be completely neglected. Currently, major research effort is put into transferring attosecond technology to nanoscale systems for generating, manipulating and measuring electron pulses to enable, e.g., exploitation of their special properties for imaging dynamics on nanoscale spatial and attosecond temporal scales[105,106].

Finally, we discuss the current status of the research on the interaction of strong laser fields with **bulk solids and solid surfaces**. Although, owing to the complexity of solid state materials, a wealth of processes can take place during such interaction, it has been found for bulk dielectrics that one of the dominant processes is field-ionization during laser-sub-cycle intervals from the valence to the conduction band[40,42,43,48,84,107–112] (dynamical Franz-Keldysh effect). The observed sub-cycle dynamics hold promise for applications in future signal processing in that it could be used for, e.g., Peta-Hertz (PHz) switching based on laser-sub-cycle currents or transient metallization[84]. These dynamics are reminiscent of the case of gas-phase systems (atoms, molecules and clusters), with the difference that in gas-phase systems tunneling occurs dominantly from valence states directly into the continuum. Very recent experiments have shown that such sub-cycle electron transitions from valence to conduction band also take place in semi-conductors that exhibit a much smaller bandgap than dielectrics[47,113]. Surprisingly, not only the ionization step in solids shows strong parallels to that in atoms and molecules, but a number of experiments and simulations on thin samples of bulk solids have shown that also the subsequent field-driven dynamics of the emitted electrons bears a notable resemblance to the dynamics in gas-phase systems which manifests itself in the emission of high-harmonic radiation in the XUV photon energy range[41,45,46,114–121]. Initially, it was debated whether the emitted high-frequency radiation originates from intra- or inter-band electron dynamics[45,109,116,117]. Experiments indicate, however, that both dynamics play a role in the XUV emission and that their relative importance depends on the material and laser parameters[45]. Given the possible applications that might emerge from the research on the interaction of strong laser-fields with bulk solids it is likely that this type of research will become still more important in the future.

Similarly, given the high practical importance of processes taking place on surfaces, such as catalysis, also the research on dynamics taking place on solid-gas interfaces is expected to become increasingly important in the future. Currently, several groups are in the position to perform the technically challenging experiments that investigate very fast electron dynamics happening close to such an interface. For example, one class of experiments investigates the very fast emission dynamics of electrons originating from different bands and energy levels triggered by the impingement of attosecond XUV pulses, with the aim of obtaining knowledge on electron dynamics and scattering mechanisms within solids and also on the solids' structure and its reaction to distortions on extreme time-scales[122–130]. It is foreseeable that in the future also dynamical processes involved in the interaction of atoms and molecules with surfaces[131,132], as they might be of relevance for catalysis, such as charge-transfer processes, will increasingly be investigated. For completeness, we would also like to mention that the interaction of laser light with surfaces is also studied with pulses of substantially higher intensity[39,133–141]. A key goal of this research is to generate intense XUV and X-ray radiation by controllably driving plasma dynamics on the surface using the intense laser field.

2.2 Basic processes of strong field-matter interaction

Early experiments on gas-phase atoms have shown that a fruitful way of describing the complex, nonlinear problem of the interaction of a strong light field with matter is to separate the different

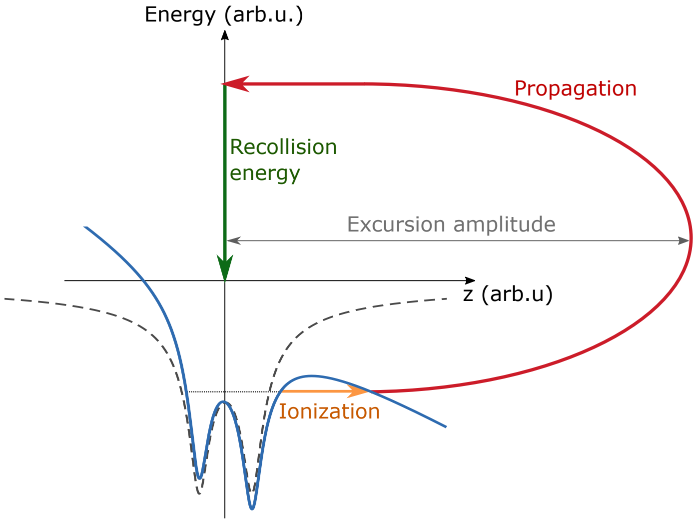

Figure 2.1: Graphical representation of the three-step model. See text for details.

phases of the interaction into steps. This approach has led to a simple model that unites the key processes that take place during the interaction of an intense laser pulse with matter[14–17]. In this picture the different phases of the laser-matter interaction are broken down into three consecutive steps, which is why this picture is commonly referred to as the *three-step model of strong-field physics*. Although the three-step model may not be applicable to all systems equally strictly, the key processes taking place during the three steps can be identified in the one or other form for almost all systems. Thus, it is a very convenient approach for providing an introduction to the most important processes in the interaction of strong fields with matter to proceed along the steps of the three-step model, and we will adopt this approach during Sections 2.2.1–2.2.5. Here, we start with a brief description of the three steps. A graphical representation of the three-step model is given in Fig. 2.1.

(i) **Ionization** The first and foremost process taking place during the interaction of strong fields with matter is the removal of electrons. Although this process is in detail very complex, one can loosely identify two different main regimes of ionization. One is a photon-dominated regime, where electrons are removed by absorption of different numbers of photons (*multi-photon ionization*). The other is a field-mediated regime of ionization (*field-ionization*) where removal of electrons takes place via tunneling of bound electrons through the combined potential well of the binding potential and the laser electric field. Field-ionization is exponentially sensitive to the electric field and therefore strictly linked to its evolutions with pronounced maxima at the maxima of the electric field. It is the dominant process in atoms and molecules when the so-called Keldysh parameter (discussed below) fulfils $\gamma \ll 1$[142–144]. In solids an equivalent process is observed[40,42,43,107,108,110,111] and electrons can tunnel from the valence to the conduction band (dynamical Franz-Keldysh effect[145]).

(ii) **Propagation in the laser field** After removal of an electron by ionization the electron is driven by the strong laser field[146–148] and instantaneously follows its evolutions on trajectories that can be determined almost at free will by shaping the laser field. The fact that both field-ionization and propagation of the emitted electron can be strictly linked to the evolution of the laser electric field constitutes a crucial opportunity that is at the heart of many common techniques in Attosecond Physics[149]. Deviations from a purely field-driven dynamics arise due to the presence of the parent ion's Coulomb field[150,151,152] and – in solids, near surfaces, as well as in dense gases and clusters – also due to the presence of the surrounding matter. Remarkably, however, a strong resemblance to the purely field-driven dynamics is identified also in the more complex matter, even in solids in the generation of extreme ultraviolet (XUV) radiation from dielectrics[45,119]. Therefore, in many cases, in particular for gas-phase systems driven by intense enough laser pulses, the force of the laser field is dominating. Depending on the electron's field-driven trajectory it may return to the parent ion with considerable energy (*recolliding electrons*), or it may leave the laser focus without further interaction (*direct electrons*).

(iii) **Recollision** Upon re-encounter with its parent ion four basic processes are possible: The electron may scatter elastically, thereby obtaining further momentum from the laser field[153–156]; it may scatter inelastically and knock out additional electrons from the parent ion[157]; it may excite the parent ion to an energetically higher state[158,159]; it can interfere with the bound state wavefunction and induce a fast oscillating dipole that gives rise to the emission of high-energy photons[18,19,160]; it may be trapped in the ion's Coulomb potential in a Rydberg state[50,54,161,162,**163–165**]. In solids[121], near surfaces[39,166] and also in clusters these process may take place in more complicated ways and also additional processes may arise.

Summarizing, the key message of the three-step model is that the interaction of strong laser light with matter can in many cases be decomposed into separate steps and, even more importantly, that each of the three steps may proceed strictly linked to the instantaneous laser electric field oscillations. Since any process that can be timed against the evolution of the laser electric field oscillations varying on the few- and sub-femtosecond timescale (which is the case even for long wavelenghts in the mid-infrared range), this finding constitues the foundation of Attosecond Science[21,30,31,146,149,167]. The fact that the trajectories of electrons emitted from a system (atom, molecule, solid,...) during laser-sub-cycle times can be controlled by a tailored strong laser field on sub-femtosecond and Ångström scales has a range of important consequences and can be applied, e.g., to the generation of isolated attosecond pulses in the XUV or X-ray photon energy range[8,168,169], for self-probing of atoms and molecules during the electron recollision step[170] and for many more important processes, a selection of which we will discuss below. Let us now discuss the three steps of the interaction of a strong laser field with matter in greater detail. For this discussion, for simplicity, we will restrict ourselves to the case of isolated gas-phase atoms or molecules.

2.2.1 Ionization

The way a strong laser field removes one or several electrons from an atom or molecules strongly depends, on the one hand, on the peak intensity and wavelength of the laser pulse and, on the other hand, on the ionization potential, electronic structure and geometry of the atom or molecule. While laser-ionization of atoms is now reasonably well understood[144,171–178], for molecules this process is much more complex and still under intense investigation. Because of this complexity caused by the structure, multi-electron character and dynamical electron-nuclear coupling of molecules, it takes large efforts to develop analytical theoretical descriptions of the ionization process, see for example Refs. [173, 177, 179], and mostly sophisticated numerical methods are applied. Popular numerical methods are multi-configuration time-dependent Hartree-Fock (MCTDHF)[**180–183**] or time-dependent density functional theory (TDDFT)[**184–188**]. In some cases multi-electron ionization can even be described by classical trajectory methods such as classical trajectory Monte Carlo (CTMC), where the different, randomly selected trajectories sample the initial state phase-space[**189–191**,192,193]. We will discuss ionization and other processes taking place during the interaction of strong laser fields with molecules in detail in Chapter 8. Here and in the following Sections we shall provide an overview over basic concepts in the understanding of the interaction of strong laser-fields with atoms and molecules.

To obtain a basic understanding of strong-field ionization, let us consider a very simple system: an atom or molecule with one electron bound by an energy $-I_p$ in a potential $V_0(\boldsymbol{r})$. To describe the

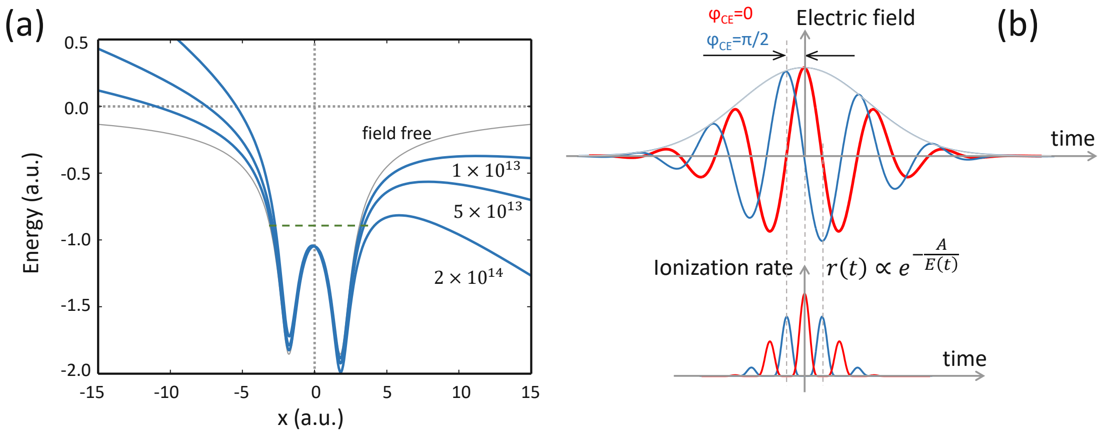

Figure 2.2: Ionization by a strong laser field. (a) A strong laser fields distorts the binding potential of atoms and molecules and enables an electron from a binding state (depicted by the green dashed line) to tunnel through the bent Coulomb potential into the continuum (tunnel or field ionization). Shown is a cut along the x-coordinate through the model-potential $V(x) = -1/\sqrt{(x-d/2)^2+a} - 1/\sqrt{(x+d/2)^2+a}$ of a diatomic molecule with internuclear distance $d = 3.6\,\text{a.u.}$ with a shielding parameter $a = 0.4$ for the field-free case (gray line) and at different laser intensities given in the figure (in units of W/cm^2). (b) The probability for tunneling is exponentially sensitive to the laser field strength, cf. (2.2). Thus, the tunneling rate depends on the instantaneous value of the laser field. Different laser waveforms (depicted in blue and red, characterized by their CE-phase) therefore lead to different ionization timing (lower sketch).

interaction of this system with an ultrashort laser pulse that exhibits an intensity in a usual range – which is to be defined below – and to write the corresponding Hamiltonian, some approximations are often justified. The first is that the laser field is weak enough such that relativistic effects can be excluded. Then, the interaction can be described using the time-dependent Schrödinger equation (TDSE) by neglecting the magnetic field of the laser light. The second one is the dipole approximation, justified when the interaction takes place in a volume small enough such that the dependence of the electric field of the laser pulse on the spatial coordinate $\boldsymbol{r}$ can be neglected and the field only depends on time, i.e. $\boldsymbol{E}(\boldsymbol{r},t) \approx \boldsymbol{E}(t)$. Here, we will only consider processes where both approximations stay valid throughout. Note, however, that in specific cases at least one of these approximations needs to be given up. Such cases are discussed in Section 2.1 and would, for example, be the study of the interaction of ultrashort laser pulses with extended objects such as nanoparticles, nanostructures or large clusters, or the study of the effects of very intense pulses impinging on surfaces, or also the application of pulses with a very long wavelength for which the electron is driven far away from the parent ion such that the magnetic component of the laser light has noticeable influence on the electron's trajectory. If both approximations can be made, the combined potential of the laser light and the atom/molecule in the length gauge reads[‡]

$$V(\boldsymbol{r},t) = V_0(\boldsymbol{r}) - \boldsymbol{E}(t)\cdot\boldsymbol{r}, \tag{2.1}$$

where $\boldsymbol{r}$ is the position of the electron.

For linearly polarized light, (2.1) describes a binding potential that is periodically distorted by the oscillating laser electric field. For strong laser fields the potential is bent down around the

---

[‡] The Atomic System of Units[194] is used throughout, unless otherwise noted. Conversion factors between Atomic Units and the SI System of Units are provided in the Appendix, see Chapter Atomic Units. Atomic units are indicated by a.u.; arbitrary units are abbreviated with arb.u.

maxima of the electric field oscillations such that the electron can escape by tunneling through the created potential barrier. This is visualized in Fig. 2.2(a) for different peak field strengths. For very high field strength the potential is bent down so strongly that the binding energy $-I_p$ is above the crest of the distorted potential. This regime is called *above barrier ionization* or also *barrier-suppression*[195]. For a purely Coulombic potential shape, $V_0(\boldsymbol{r}) = -1/|\boldsymbol{r}|$, the field strength above which barrier-suppression starts, can be derived as $E_{bs} = I_p^2/4$. For too weak fields no pronounced barrier is formed. In the intermediate regime the tunnel ionization probability takes the form[196,197]

$$\Gamma = \Gamma_0 \exp(-2(2I_p)^{3/2}/(3|E_0|)), \tag{2.2}$$

where E_0 is the laser field strength and the pre-factor Γ_0 depends on the structure of the bound state. For atoms the pre-factor has been calculated by Ammosov, Delone and Krainov[198] and the resulting rate is commonly called the *ADK*-rate. In the above-barrier (or barrier-suppression) regime an empirical correction factor can be introduced[199].

For molecules Γ_0 depends on their atomic and electronic structure, and on the orientation of the molecule with respect to the laser polarization direction. Obtaining analytical expressions for Γ_0 is difficult but possible within certain limits, see for example Refs. [200–203]. In general, strong-field ionization of molecules will be strongly affected by molecular dynamics and in most cases complex numerical modelling is required[184,186,187]. For obtaining a qualitative understanding of strong-field ionization of atoms, molecules and even of some more complicated systems (clusters, nanotips, etc.) it is in many cases sufficient to consider that the ionization rate depends exponentially on the field-strength E_0 and on the binding energy I_p, see (2.2) and Fig. 2.2(b).

The tunneling rate given by (2.2) is valid strictly only in the quasi-static limit, i.e., for sufficiently slowly varying fields. A parameter that is frequently used to determine whether a field is sufficiently slowly varying is the so-called Keldysh parameter, introduced by Leonid Keldysh in 1964[196],

$$\gamma = \frac{\omega_o \sqrt{2I_p}}{E_0}. \tag{2.3}$$

The Keldysh parameter compares half of the laser oscillation period, $\propto 1/\omega_o$, where ω_o is the laser oscillation frequency, to the time τ_T that the electron needed to transit the potential barrier if this motion would be classically allowed. If this hypothetical transit time

$$\tau_T = \sqrt{I_p/2}/E_0 \tag{2.4}$$

is much shorter than the laser half-cycle, i.e., for $\gamma \ll 1$, then the electric field does not change significantly during the tunneling process and it can be considered quasi-static; E_0 in (2.2) can then be replaced by $E(t)$. As the tunnel ionization rate (2.2), due to its exponential dependence on $E(t)$, peaks only within short intervals around the maxima of the laser oscillations, ionization takes place in very short bursts and results in the production of a sub-cycle electron wavepacket (EWP) every laser half-cycle. In the opposite case, $\gamma \gg 1$, which is reached for high laser frequency ω_o or weak laser fields (small E_0), ionization can no longer be considered quasi-static and should be understood as a multi-photon process that proceeds via the absorption of several photons. In this case the strict sub-cycle timing of the electron emission dynamics is lost.

Although the Keldysh parameter can be a useful quantity to obtain a rough idea about the dominant ionization mechanism, it should not be used too strictly. Ionization of atoms, molecules or even more complex types of matter in an oscillating strong laser field is in detail a complicated process and can in many cases not be characterized by a single parameter only. Its usefulness is also questioned[204,205]. Certainly the Keldysh parameter becomes meaningless when the photon energy $\omega_o \geq I_p$ or in the barrier-suppression regime (even though γ might be small in this case). In practice, many experiments that rely on the emission of sub-cycle EWPs are performed in a regime where $\gamma \approx 1$ or even slightly larger. Let's consider a system with an I_p of 16 eV (comparable to that of, e.g., an argon atom or a nitrogen molecule). For this system interacting with fields generated by the widely used Titanium-Sapphire laser (wavelength 800 nm), $\gamma \leq 1$ is reached for intensities above roughly $1.3 \times 10^{14}\,\mathrm{W/cm^2}$. However, barrier-suppression starts already at $2.6 \times 10^{14}\,\mathrm{W/cm^2}$. Thus, to avoid this regime, γ is indeed limited to values around 1 or only slightly below. The situation is still more severe for polyatomic molecules which usually exhibit still smaller I_p. For a typical value of $I_p = 10\,\mathrm{eV}$ and a laser wavelength of 800 nm, $\gamma = 1$ is reached for an intensity of $8.4 \times 10^{13}\,\mathrm{W/cm^2}$; well above the barrier-suppression intensity of $4 \times 10^{13}\,\mathrm{W/cm^2}$. Therefore, many experiments are performed in the regime $1 \lesssim \gamma \lesssim 2-3$. However, it has been shown that even for $\gamma \approx 1$ the ionization rate peaks strongly around the maxima of the electric field oscillations, although the dependence is somewhat less nonlinear than the ADK-rate[142,144].

A small Keldysh parameter, indicating that ionization takes place deeply in the tunneling regime, can therefore in general not be obtained by simply increasing E_0 in (2.3). In contrast, decreasing ω_o, or equivalent increasing the wavelength $\lambda_o = 2\pi c/\omega_o$ of the laser field (c is the speed of light), is a viable possibility. It has been shown that longer wavelengths in the mid-infrared regime with $2\,\mu\mathrm{m} \lesssim \lambda_o \lesssim 10\,\mu\mathrm{m}$ not only lead to better applicability of tunneling theories but also lead to better agreement with quasi-classical models for describing the laser-driven electron motion[156]. In addition to this, long-wavelength laser fields have a number of crucial advantages, for example for schemes that exploit electron recollision, see Sections 2.2.2 and 2.2.3. Consequently, currently in most labs large efforts are undertaken to generate ultrashort intense laser pulses in the mid-infrared wavelength range[206,207].

So far we have only considered the most simplest case of one electron ionizing from an atom or molecule. Thus, we have tacitly assumed that only one electron interacts with the laser field and the rest of the electron cloud stays frozen and does not influence the ionization (and the subsequent electron motion). This is the so-called *single active electron-approximation* (SAE) that is one of the corner-stones in most theories describing the interaction of strong laser fields with matter. However, in reality, atoms (with the exception of the hydrogen atom) and molecules, matter in general, are multi-electron systems. Therefore this approximation seems quite unrealistic. Interestingly, though, the SAE often leads to satisfying agreement between theory and experiment, in particular for atoms[13,208,209]. Still, even for atoms its applicability should be critically checked[210]. However, it is very difficult to incorporate multi-electron effects into analytical theories[173,177,179,211,212] such that in many cases, in particular for polyatomic molecules, only extensive numerical modelling is available**[184,186]**. Due to the interaction of the electrons with each other and their higher mobility as compared to that of atoms, the complicated energy level structure, the motion of the nuclei that might occur concomitantly with the ionization process, etc., ionization of molecules, even of small ones, can be a very complex process such that providing even a crude overview is well beyond the scope of this introductory account. We will discuss molecular ionization in more detail in Section 8.1.

As a consequence of the multi-electron character of matter, not only one but also several electrons can in principle be removed during a laser pulse. One possibility how this could happen is by sequential ionization. This means that the electrons are removed successively, one electron after another, without interaction between them. Within the SAE, this can be described by (2.2) when during each ionization step of some species A^{n+} to $A^{(n+1)+}$ the parameters of the pre-factor Γ_0 and I_p are adapted to those of A^{n+}, and at the same time depletion of the ionic state A^{n+} is properly accounted for. The latter condition takes into account that during ionization the number of A^{n+} within the laser focus volume decreases as they are further ionized to $A^{(n+1)+}$, whose number increases accordingly. The specimen $A^{(n+1)+}$ may themselves be further ionized to $A^{(n+2)+}$ and so on. As the I_p increases with every charge state, the ionization rate (2.2) decreases accordingly and the ionization process terminates. For very intense and very short pulses, for which the electric field strength rises quickly, a certain species, e.g., A^0, can become depleted within a single laser-cycle. This can for example be exploited for the production of isolated attosecond pulses[213] or for obtaining insight into the sub-cycle dynamics of electron emission[190]. In addition to sequential ionization, multiple electrons can also be removed *non*-sequentially. This vague term is used for historic reasons and originally indicated an initially unknown ionization dynamics underlying measured double-ionization yields[157,209,214] that were significantly higher than predicted by (2.2) for sequential removal of two electrons. Because the ionization dynamics was not in accord with a sequential scenario, it was called non-sequential double ionization (NSDI). Later it was confirmed that electron-recollision is behind the observed enhancement of the double-ionization yield[215]. This type of ionization is now mostly called recollision-ionization. The term NSDI was, however, kept and today is usually used to summarize all double-ionization phenomena that do not happen sequentially, e.g., recollision-ionization and recollision-induced excitation and subsequent field ionization (RESI)[158,159]. Double and multiple ionization phenomena in atoms and molecules will be discussed in detail in Chapters 6 and 8.

2.2.2 Electron dynamics in the laser field

When electron wavepackets (EWPs) are set free by tunneling through the bent-down potential barrier, as discussed in Section 2.2.1, their motion is governed by the combined forces of the strong laser electric field and the ionic Coulomb field. During their motion a number of processes can take place, such as scattering off the parent ion which in turn might spawn further processes. After the laser pulse has passed, the field-driven EWPs might interfere at the detector giving rise to complicated interference structures—depending on their relative phases. The different processes induced by the scattering of EWPs off the parent ion and interferences of EWPs will be discussed in detail in Chapters 4 to 8. Here we would like to provide an overview over the dynamics of EWPs in the laser-field and ion's Coulomb potential.

It is not straightforward at all, though, to incorporate the influence of the Coulomb field on, e.g., electron momentum spectra[179,216–219]. Therefore, a key ingredient in many theoretical descriptions is the so-called *strong-field approximation* (SFA)[196,220,221]. Within the SFA the influence of the Coulomb potential on the trajectory of an ionizing electron is considered only a weak distortion as compared to the force exerted by the strong laser field. As a consequence, the influence of the Coulomb field on the receding or recolliding wavepacket is completely neglected and it is possible to obtain instructive analytical solutions. In many cases SFA-based theoretical descriptions lead to an at least qualitatively acceptable agreement with experiments, although the influence of the Coulomb potential on, for example, electron momentum spectra has been demonstrated in numerous experiments, e.g. in Refs. **[150, 151]**. We will review the SFA and SFA-based descriptions for measurable observables resulting from the field-driven motion of EWPs and their interaction with the parent ion in Section 2.2.5.

A simple but instructive description of the field-driven dynamics of a tunneling electron can be obtained with the semi-classical variant of the SFA, the so-called *simple man's model* (SMM)[15–17,222]. In the SMM the trajectory of an ionizing electron is calculated purely classically. It is assumed that an electron after tunneling at some ionization time t_i is "born" at the position of the parent ion, which we can choose without loss of generality at $\boldsymbol{r}(t_i) = 0$. We furthermore assume that the electron appears with zero velocity, $\dot{\boldsymbol{r}}(t_i) = 0$. In reality, the EWP after tunneling exhibits some initial velocity distribution, but the center value is zero[223], justifying the assumption of zero initial velocity. As the influence of the Coulomb potential is neglected, the electron's trajectory is only determined by the force due to the strong laser field.

In this case the trajectory of a field-driven electron can be calculated purely classically simply by solving Newton's equation,

$$\ddot{\boldsymbol{r}} = -\boldsymbol{E}(t). \tag{2.5}$$

The momentum of the electron at some time $t > t_i$ is obtained by integration of (2.5) with $\dot{\boldsymbol{r}}(t_i) = 0$ as

$$\boldsymbol{p}(t, t_i) = \dot{\boldsymbol{r}}(t, t_i) = -\int_{t_i}^{t} \boldsymbol{E}(t')\mathrm{d}t', \tag{2.6}$$

where we explicitly denoted the ionization time t_i of the electron. Introducing the laser vector potential, $\boldsymbol{A}(t) = \int_{-\infty}^{t} \boldsymbol{E}(t')\mathrm{d}t'$, or equivalently, $\boldsymbol{E}(t) = -\mathrm{d}\boldsymbol{A}(t)/\mathrm{d}t$, we can write (2.6) as

$$\boldsymbol{p}(t, t_i) = -\int_{t_i}^{t} \boldsymbol{E}(t')\mathrm{d}t' = \int_{t_i}^{t} \frac{\mathrm{d}\boldsymbol{A}(t')}{\mathrm{d}t'}\mathrm{d}t' = \boldsymbol{A}(t) - \boldsymbol{A}(t_i). \tag{2.7}$$

Considering that the laser pulse exhibits some envelope such that the laser field vanishes for $t \to \pm\infty$, i.e., $\boldsymbol{A}(t \to \pm\infty) \to 0$, we arrive at the important result

$$\boldsymbol{p}(t \to \infty, t_i) = \boldsymbol{A}(t \to \infty) - \boldsymbol{A}(t_i) = -\boldsymbol{A}(t_i), \tag{2.8}$$

which states that the electron's momentum long after the laser pulse is given by the negative value of the vector potential at its release time. Fig. 2.3(a) visualizes the relation between the release time t_i and the momentum of the electron after the laser pulse. From the momentum (2.7) we can calculate the electron's position as

$$\boldsymbol{r}(t, t_i) = \int_{t_i}^{t} \boldsymbol{A}(t')\mathrm{d}t' - \boldsymbol{A}(t_i)(t - t_i), \tag{2.9}$$

where we have made use of $\boldsymbol{r}(t_i) = 0$. So far the results are independent of the polarization state of the laser field and the relations for the electron's momentum and position can be exploited in experiments by any convenient evolution of the laser field, which builds the basis for a number of mapping techniques discussed below.

The most common polarization state is linear and a range of important facts crucial for applications can be obtained by considering **linearly polarized laser fields**. We therefore now consider a field of the form $\boldsymbol{E}(t) = E_0 \cos(\omega_o t)\boldsymbol{e}_z$ which we, without the loss of generality, assume to be polarized along z. For simplicity we here assume a monochromatic laser field. This is a good description for not too short pulses. For very short pulses exhibiting only a few laser oscillation cycles (*few-cycle* laser pulses), additional terms from the derivative of the pulse's envelope function will appear. With the vector potential $\boldsymbol{A}(t) = -E_0/\omega_o \sin(\omega_o t)\boldsymbol{e}_z$, (2.9) can be written as

$$\begin{aligned} z(t, t_i) &= a_o\left[\cos(\omega_o t) - \cos(\omega_o t_i)\right] + a_o\omega_o \sin(\omega_o t_i)(t - t_i) \\ x(t, t_i) &= y(t, t_i) = 0, \end{aligned} \tag{2.10}$$

where we have defined the oscillation amplitude $a_o = E_0/\omega_o^2$ of the electron. We can see from (2.10) that the trajectory of the electron along the laser polarization direction consists of an oscillatory term that instantaneously follows the laser field oscillations, and a drift term that depends linearly on time and whose gradient is determined by the ionization time t_i. The oscillatory term describes field-driven oscillations of the electron around the ion position with an amplitude a_o. Thus, the electron may (multiply) scatter off the ion two times a laser cycle. These scattering events are usually called recollisions and will be discussed in more detail below. For now let us focus on the electron's momentum and energy. The momentum given by (2.7) also consists of an oscillatory term $\dot{z}_o$ that follows the field oscillations and a drift term $\dot{z}_D$ that depends on the time t_i of the ionization

$$p_z(t, t_i) = \dot{z}_o + \dot{z}_D = -a_o\omega_o[\sin(\omega_o t) - \sin(\omega_o t_i)]. \tag{2.11}$$

After the laser pulse has faded, only the drift term remains (for not too short laser pulses). For electrons that do not recollide with the ion core, the so-called *direct electrons*, the final kinetic energy after the pulse, E_K^∞, is thus given by this drift term that can be recast into

$$E_\mathrm{K}^\infty = \frac{\dot{z}_D^2}{2} = \frac{a_o^2\omega_o^2}{2}\sin^2(\omega_o t_i) = 2U_p \sin^2(\omega_o t_i), \tag{2.12}$$

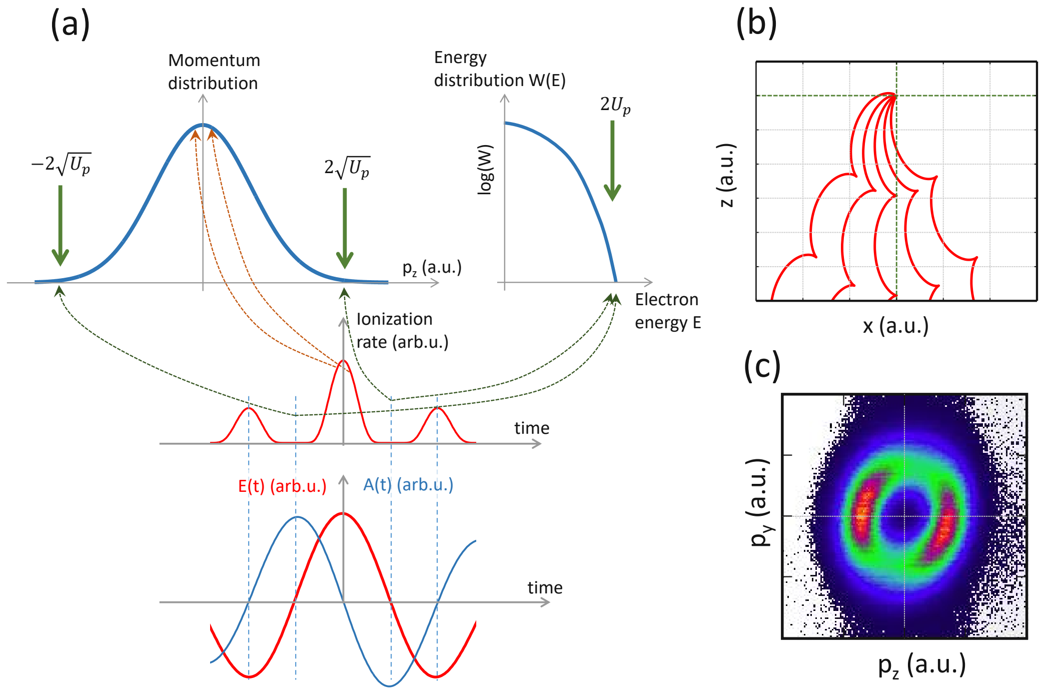

Figure 2.3: (a) The momentum and energy of an electron is determined by its release time t_i. In a linearly polarized laser field the momentum after the laser pulse is given by (2.8); it's maximum value $\boldsymbol{p}_{\max} = 2\sqrt{U_p}$ is reached for $t_i = 0$, see (2.12). The green and orange arrows visualize this dependence and the resulting electron momentum (top left) and energy distributions (top right). (b) Electron trajectories in a circularly polarized laser field for 5 different release times within $\pm 0.1T_o$ around the peak of the laser field, where T_o denotes the laser oscillation period. (c) Measured momentum distribution of electrons in the laser polarization plane released from helium atoms, adapted from Ref. **[190]**. As predicted by (2.16) the distribution resembles an ellipse (donut).

where we have introduced the *ponderomotive potential* $U_p = \frac{E_0^2}{4\omega_o^2}$. The ponderomotive potential is the average kinetic energy of the electron due to the oscillatory term of the velocity, $\dot{z}_o$, as can be seen by calculating the cycle-averaged electron energy

$$\bar{E}_\mathrm{K} = \frac{1}{T}\int_0^T \frac{\dot{z}^2(t')}{2}\mathrm{d}t' = U_p(1 + 2\sin^2(\omega_o t_i)) = U_p + E_\mathrm{K}^\infty, \tag{2.13}$$

where $T = 2\pi/\omega_o$ is the duration of one laser cycle. The final electron kinetic energy E_K^∞ thus crucially depends on the ionization time and its maximum is $2U_p$. This maximum energy, also called cut-off energy, is reached by electrons for which $\omega_o t_i = \pi/2$, i.e., for electrons where the electric field $E_0 \cos(\omega_o \pi/(2\omega_o)) = 0$ and therewith the ionization rate, as given by (2.2), is infinitely small. For electrons emitted at the peak of the electric field, i.e., at $\omega_o t_i = 0$, where the ionization rate is maximum, the final kinetic energy of the electron is zero, $E_\mathrm{K}^\infty = 2U_p \sin^2(\pi/2) = 0$. Thus, the kinetic energy distribution of the direct electrons shows maximum intensity at zero energy, and due to the exponential dependence of (2.2) on the field strength, the intensity exponentially decreases towards the cut-off value of $2U_p$. This is visualized in Fig. 2.3(a). Electron energies beyond the cut-off of $2U_p$ are still possible when the electron recollides with the ion core, as will be discussed below. The energy of these electrons can be quite large.

But also the energy of the direct electrons can be significant and typically exceeds the photon energy by far. For a laser peak intensity of $1 \times 10^{14}\,\mathrm{W/cm^2}$ and a laser wavelength of 800 nm (corresponding to a photon energy of 1.55 eV) $2U_p \approx 12\,\mathrm{eV}$. If in a photon picture an electron during ionization absorbs only the minimum number of photons necessary to overcome the ionization potential I_p, than its kinetic energy should at maximum only be one photon energy. In 1979 Agostini et al. observed electrons with an energy higher than one photon energy[153], i.e., with an energy above the ionization threshold. Subsequently this phenomenon was dubbed *above threshold ionization* (ATI) and was investigated extensively[17,155,171,224,225]. The electron energy spectra following from ATI exhibit clearly visible peaks spaced by the photon energy ω_o. Within the classical picture these peaks can be understood as interferences of EWPs released with a delay of one laser cycle $T = 2\pi/\omega_o$[226,227–229]. We will come back to the topic of interferences of EWPs in Section 6.2.

The dynamics of an electron driven by **circularly/elliptically polarized fields** is quite different from that in a linearly polarized field. A monochromatic laser field, elliptically polarized in the xz-plane, has the form $\boldsymbol{E}(t) = E_0 C_\zeta[\cos(\omega_o t)\boldsymbol{e}_z + \zeta \sin(\omega_o t)\boldsymbol{e}_x]$, where ζ denotes the ellipticity and $C_\zeta = 1/\sqrt{1+\zeta^2}$ is an ellipticity-dependent normalization factor of the field amplitudes. It ensures comparability of the field amplitudes with that of the linearly field from which the circular field is derived and is introduced during generation of an elliptical field with a waveplate, as during this process a linearly polarized field of amplitude E_0 is split into two orthogonal components along $\boldsymbol{e}_z$ and $\boldsymbol{e}_x$. For circular light the two components are equally large and amount to $E_0 \cos(\pi/4) = E_0/\sqrt{2}$; for arbitrary ellipticity ζ the amplitudes are $E_0 C_\zeta$ and $E_0 \zeta C_\zeta$, respectively. The vector potential of a such defined circular field reads $\boldsymbol{A}(t) = -E_0 C_\zeta/\omega_o[\sin(\omega_o t)\boldsymbol{e}_z - \zeta \cos(\omega_o t)\boldsymbol{e}_x]$. Inserting this expression for $\boldsymbol{A}(t)$ into (2.7) leads to the momentum of the electron,

$$\begin{aligned} p_z(t,t_i) &= -a_o \omega_o C_\zeta[\sin(\omega_o t) - \sin(\omega_o t_i)], \\ p_x(t,t_i) &= a_o \omega_o \zeta C_\zeta[\cos(\omega_o t) - \cos(\omega_o t_i)], \end{aligned} \tag{2.14}$$

from which the electron's trajectory can be obtained by integration as

$$\begin{aligned} z(t,t_i) &= a_o C_\zeta[\cos(\omega_o t) - \cos(\omega_o t_i) + \omega_o \sin(\omega_o t_i)(t - t_i)], \\ x(t,t_i) &= a_o \zeta C_\zeta[\sin(\omega_o t) - \sin(\omega_o t_i) - \omega_o \cos(\omega_o t_i)(t - t_i)]. \end{aligned} \tag{2.15}$$

The kinetic energy of an electron after an elliptically polarized pulse (i.e., for $t \to \infty$) is

$$E_\mathrm{K}^\infty = \frac{(p_z^2 + p_x^2)}{2} = 2U_p C_\zeta^2[1 - \cos^2(\omega_o t_i)(1 - \zeta^2)]. \tag{2.16}$$

From (2.15) we learn that an electron emitted in an elliptically polarized field is driven away from the parent ion on trajectories as depicted in Fig. 2.3(b) for different release times t_i. Equ. (2.14) shows that the momentum distribution of electrons (p_z, p_x) after the laser pulse resembles an ellipse, cf. the measured example momentum distribution in Fig. 2.3(c). There are no electrons with zero momentum (for large enough ellipticity ζ). For circular light ($\zeta = 1$), their energy is independent of the ionization time and has the well defined value $2U_p/2 = U_p$, cf. (2.16), where the factor $1/2$ is due to the $1/\sqrt{2}$ times smaller field amplitudes of a circular field as compared to the linear field from which it is derived (cf. explanation above). In reality, the electron energy distribution created with circular light does not resemble a narrow circular shape but shows some width around the value U_p determined by the tunneling momentum distribution[223] and the spatial intensity distribution in the focus of the laser beam[230].

2.2.3 Electron recollision

In Section 2.2.2 we have seen that for linearly polarized light an electron after ionization will oscillate in the field of the laser and may be driven back to the parent ion situated at $z = 0$ where it can

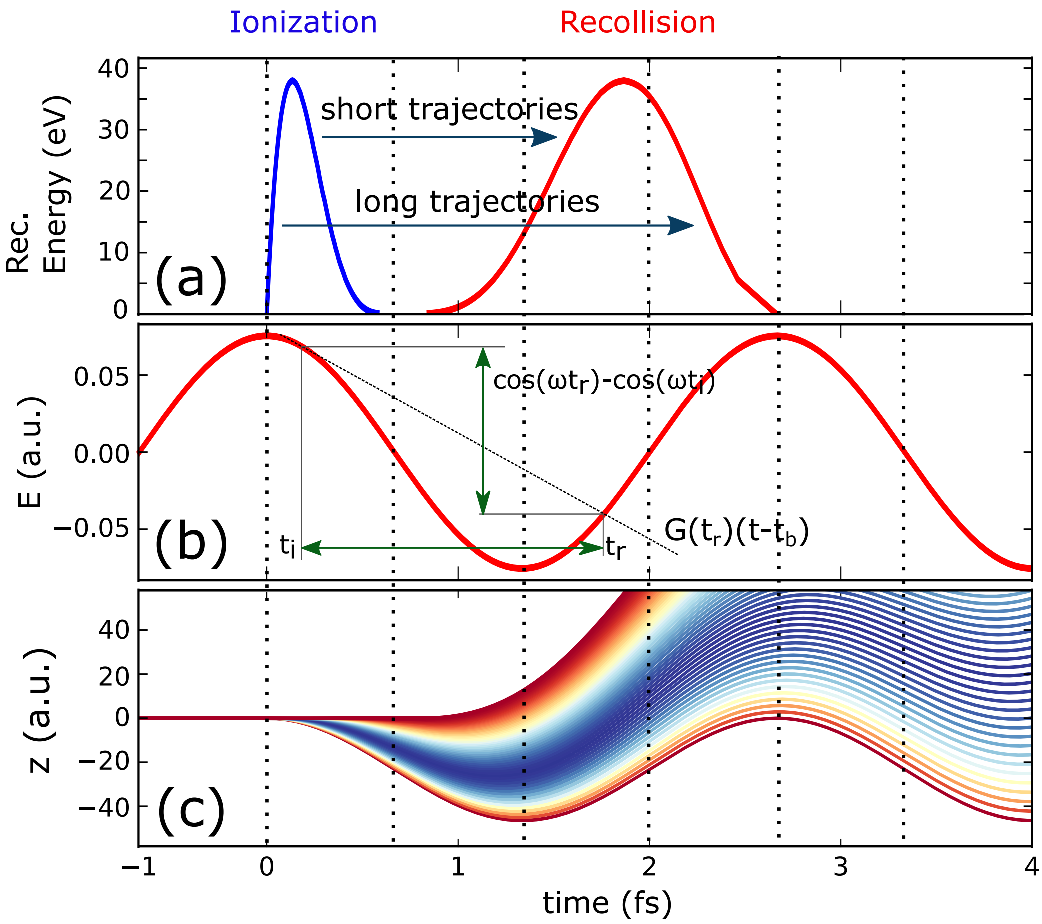

Figure 2.4: Recolliding electron trajectories. Depicted are the recollision energy (a) and propagation in space (c) of electrons emitted and driven by a strong laser field shown in (b). The relation between the times of ionization t_i and the times of recollision t_r are visualized in (b) using a graphical solution of the recollision condition given by (2.19), see text for details. The colors in (c) encode the recollision energy from lowest to highest in dark red to dark blue. Trajectories with the highest recollision energy (*cut-off* trajectories) recollide around the zero-crossing of the laser field during the next laser half-cycle. The two types of trajectories (long and short) are indicated in (a). The amplitude and frequency of the laser field in (b) correspond to a peak intensity of $2 \times 10^{14}\,\mathrm{W/cm^2}$ and wavelength of 800 nm, respectively.

recollide with it. For elliptically polarized light, in contrast, the electron will never return to the parent ion. Thus, all processes that build on this recollision process, which we will discuss below, are turned off with elliptical light. In reality, due to the EWP's finite momentum distribution (and the force exerted by the parent ion's binding potential on the emitted electron), parts of the EWP will still recollide for small values of the ellipticity. But for already quite small values of $\zeta \approx 0.2$ most processes induced by recollision are turned off[231].

Thus, to drive the electron back to the ion, linearly polarized light has to be used[‡]. From (2.10) the times $t = t_r$ at which the electron recollides in a linearly polarized field for a given t_i can be

---

[‡] Alternatively to linearly polarized light more complicated two-dimensional waveforms can be used[232,233,234–237]. Such waveforms and their applications will be discussed below starting with Chapter 3.

calculated by numerically solving

$$z(t_r, t_i) = 0 = a_o \left[\cos(\omega_o t_r) - \cos(\omega_o t_i)\right] + a_o \omega_o \sin(\omega_o t_i)(t_r - t_i) \tag{2.17}$$

for $t_r = t_r(t_i)$. For a given t_i there may be zero, one or more times t_r at which the electron returns to the parent ion. If it is neglected that the shape of the EWP might be modified by its re-encounter with the parent ion, e.g., by the Coulomb binding potential, then the overlap with the bound state of the ion decreases for every return due to the lateral spreading of the emitted EWP caused by its initial transversal velocity distribution. Thus, the first return is in many cases the most important one. A very descriptive solution of $t_r = t_r(t_i)$ can be obtained using a graphical method. For this we start from (2.17) and write it in the form

$$\cos(\omega_o t_r) - \cos(\omega_o t_i) = -\omega_o \sin(\omega_o t_i)(t_r - t_i) \tag{2.18}$$

by using the condition $z(t_r) = 0$. Equ. (2.18) can be recast into

$$\cos(\omega_o t_r) - \cos(\omega_o t_i) = \frac{\mathrm{d}}{\mathrm{d}(\omega_o t)} \cos(\omega_o t)\bigg|_{t=t_i} (\omega_o t_r - \omega_o t_i). \tag{2.19}$$

By identifying $G(t_i) = \frac{\mathrm{d}}{\mathrm{d}(\omega_o t)} \cos(\omega_o t)\Big|_{t=t_i}$ as the gradient of the electric field at the electron's release time, t_i, the right-hand-side of (2.19) describes a tangent to the electric field starting at t_i. The corresponding $t_r(t_i)$ is found where the tangent crosses the electric field again. Fig. 2.4(b) visualizes the described procedure for finding the relation $t_r = t_r(t_i)$. From the figure it becomes clear that for $0 < \omega_o t_i < 2\pi$ only for $0 < \omega_o t_i < \pi/2$ and $\pi < \omega_o t_i < 3\pi/2$ solutions of (2.19) exist and thus only electrons that are emitted within these limits can recollide. Consequently these are called the *recolliding electrons* or, if one wants to refer to the trajectories of these electrons, they are called the *recolliding trajectories*. In contrast, electrons born outside these ranges of t_i will not be driven back to the parent ion but leave the interaction zone on *direct trajectories* towards the detector.

The graphical solution of (2.17), depicted in Fig. 2.4, visualizes the strict sub-cycle mapping between ionization and recollision time. Moreover, the figure shows that the instants of the recollisions $t_r = t_r(t_i)$ vary substantially even for small changes of t_i, and that for emission times close to zero the travel-time of the electron, $\tau = t_r - t_i$, is significantly larger than for later emission times. This fact becomes apparent in Fig. 2.4(a) where the electron recollision energy $p^2(t_r)/2$ is plotted as a function of the recollision times $t_r = t_r(t_i)$, found by numerical solution of (2.19). It can be seen that the maximum recollision energy, roughly $3.17U_p$, is reached for electrons emitted at the phase $\omega_o t_i \approx 17^\circ$ after the laser field maximum. This value is called the *classical cut-off*. Later or earlier emission times lead to lower recollision energy, but the same recollision energy is reached by two different trajectories with large and small τ, respectively. Consequently, these two classes of trajectories are called the *long and short trajectories*, respectively. Fig. 2.4(c) depicts the two classes of recolliding trajectories and visualizes their recollision energies using a color scale. The cut-off recollision energy (blue) is reached for electrons recolliding around the zero-crossing of the laser field in the next laser half-cycle.

The maximum recollision energy $E_{r,\max} \approx 3.17U_p \propto E_0^2\lambda_o^2$ scales linearly with the laser intensity $I = E_0^2$ and quadratically with the laser wavelength $\lambda_o = 2\pi c/\omega_o$ (c is the speed of light), and can easily reach into the several 100's of eV or even into the keV range. For a laser wavelength of 800 nm and an intensity of $8 \times 10^{14}\,\mathrm{W/cm^2}$ $E_{r,\max} \approx 151\,\mathrm{eV}$. For the same intensity but a wavelength of $3\,\mu\mathrm{m}$ $E_{r,\max} \approx 2130\,\mathrm{eV}$, i.e., in the keV range. Long laser wavelengths are thus advantageous for reaching high recollision energies; and a high recollision energy $E_{r,\max} \propto E_0^2\lambda_o^2$ is useful for most of the processes that are induced by electron-recollision.

From the dependence of the recollision energy on laser-sub-cycle time, shown in Fig. 2.4, it becomes clear that a recolliding EWP passes the ion within a fraction of a laser-half-cycle. This is in particular true for those portions of the EWP that exhibit high recollision energy. Thus, recolliding EWPs can be used for probing dynamics in the parent ion with laser-sub-cycle resolution[146–149,170,238,239]. Beneficial for a high temporal resolution in such a scheme is furthermore the fact that the energy of the recolliding electron, $p^2(t_r, t_i)/2$, exhibits a well characterized chirp, as the recollision energy sweeps from zero to $3.17U_p$ within the ultrashort EWP, clearly visible as the slope of the recollision energy over time in Fig. 2.4(a). This energy sweep is called the *attochirp*. It establishes a mapping of time to recollision energy on laser-sub-cycle times and can be exploited for measurements, in particular using extreme ultraviolet or soft X-ray radiation emitted during the recollision via the process of high-harmonic generation[170,240,241].

In addition to the high temporal resolution provided by the recollision process, the recolliding EWPs can also probe the parent ion in space with Ångström resolution; a property that is most useful when applied to probing of molecular structure. The important property that allows probing of molecular structure with Ångström resolution is the small de Broglie wavelength $\lambda_e(t) = 2\pi/p(t_r)$ of the recolliding EWP at the instant of its recollision in the range of a few Å, which is facilitated by the high maximum recollision energy $3.17U_p$ and the correspondingly high electron momentum. Obtaining such high spatial resolution by light diffraction requires a photon energy in the keV range. This is because of the unfortunate dispersion relation of photons, $\lambda = 2\pi c/E$, with E their photon energy and c the speed of light. Additionally, such energetic photons mainly interact with the core electronic states rather than the valence shells. But it are the latter ones that are relevant for the molecular structure. Both, the short duration, chirp and the resulting high temporal resolution, as well as the small de Broglie wavelength and associated high spatial resolution of the recolliding EWPs establish the field of *recollision probing*, also referred to as *Attosecond-Ångström science*[147,149,170,238].

2.2.4 Basic processes induced by electron recollision

Section 2.2.3 discussed the possible electron trajectories and the properties of electron wavepackets that are driven back to the parent ion. It became clear that the recolliding EWP has a number of interesting properties in terms of its duration, energy composition and chirp which become important when considering the interaction of such EWPs with matter. Four basic processes induced by the recollision of an EWP can be distinguished:

Elastic electron scattering We have derived above that the direct electrons can acquire a maximum energy from the laser field of $2U_p$, and we have mentioned that for multi-cycle laser pulses the photoelectron energy distribution features prominent peaks spaced by the laser photon energy. For historic reasons these are called the ATI peaks (see explanation above). It is common to use the term ATI electrons for all photoelectrons resulting from direct ionization, and to refer to the corresponding portion of the photoelectron energy distribution as the ATI spectrum. Experiments have revealed that the photoelectron distribution does in fact not show a cut-off at $2U_p$ but features a plateau beyond this energy value[224,242]. It was found that this plateau extends up to a maximum energy of $10U_p$. Within the SMM this plateau can be explained by elastic scattering of a recolliding electron off the parent ion[171,172] as follows. After the electron has returned to the parent ion at t_r with a momentum $p(t_r, t_i)$ it is further accelerated by the laser field and acquires additional energy beyond $2U_p$, depending on t_r (and therewith on the ionization time t_i), and on the scattering angle. The highest energies can be reached for a scattering angle of 180°, i.e. for backwards-scattering against the recollision direction, such that the electron momentum after the scattering event reverses its sign. Then the final electron momentum after the laser pulse is given by

$$\begin{aligned} p(t\to\infty,t_i) &= -p(t\to\infty,t_r)+p(t_r,t_i)\\ &= -[A(t\to\infty)-A(t_r)]+[A(t_r)-A(t_i)]\\ &= 2A(t_r)-A(t_i). \end{aligned} \tag{2.20}$$

From the maximum momentum after the laser pulse,

$$p_{\max} = \max(t_i)\left|2A(t_r)-A(t_i)\right|, \tag{2.21}$$

where t_r and t_i are connected by (2.17), the maximum electron energy can be numerically obtained as

$$E_{\max} = \frac{p_{\max}^2}{2} \approx 10U_p. \tag{2.22}$$

The result is exactly $10U_p$ up to several digits after the comma.

Because the high-energy part of the ATI spectrum (HATI) is due to electron recollision, it sensitively depends on the times of ionization, t_i, and recollision, t_r, and therewith also on the evolution of the laser electric field which establishes the connection $t_r = t_r(t_i)$. It has thus been shown by experiments using tailored fields that the ATI spectrum is a very fine measure of the field evolution[155,243–246]. This can be exploited for measurement of the so-called carrier-envelope offset phase of few-cycle laser pulses[247–250]. We will come back to this point in Section 3.1.3.

In addition to the ATI peaks in the photoelectron spectrum with spacing of the laser photon energy, the electron momentum distribution after the laser pulse comprises also more complicated interference structures that originate in the interference of different portions of the emitted and recolliding EWPs[226,227,228,251]. These interference structures can be exploited for obtaining insight into the laser-driven electron dynamics on sub-femtosecond time-scales; we will come back to this point in Section 6.2.

A particularly interesting type of interference structure is the diffraction pattern created by the scattering of an EWP off a molecule, a process called laser-induced electron diffraction (LIED). It has been shown that this interference structure can be exploited for resolving molecular structure with Ångström resolution on few- to sub-femtosecond time-scales[252–255] facilitated by the short de Broglie wavelength and the short duration of the recolliding EWPs as described above. Thus, LIED is a method with a number of favourable properties. Unfortunately it is difficult to disentangle the different contributions to the measured data, see Section 6.1 for more detailed information.

Inelastic electron scattering The recolliding electron cannot only scatter elastically off the parent ion but also inelastically, thereby depositing part of its energy into the parent ion. As a result, one or more additional electrons might be emitted upon electron impact. This ionization mechanism is known under non-sequential double/multiple ionization (NSDI/NSMI). The term non-sequential distinguishes it from field-ionization via (2.2), where multiple electrons can be emitted one after another, i.e., sequentially. As in this case I_p increases with every ionization step, the ionization rate usually strongly decreases for every charge state. NSDI was discovered as a strong enhancement of the double ionization probability for low laser intensities as compared to that predicted by (2.2) in a sequential emission scenario[157,209,214]. Later it was confirmed by measuring the momentum of both emitted electrons in coincidence that this enhancement is due to impact ionization upon electron recollision[215]. In addition to direct impact double or multiple ionization promptly after the recollision event, usually called recollision ionization or impact ionization, the parent ion can also be excited upon electron impact, leaving an electron in a more loosely bound state from which it can ionize more easily during the next field maximum. This process is called recollision-induced excitation and subsequent field ionization (RESI)[158,159].

As the electron impact only takes a small fraction of a laser-half-cycle, NSDI (and NSMI) can serve as a testbed for the study of electron-electron correlation at ultrashort time-scales[175,256–261]. Moreover, since NSDI/NSMI is based on electron recollision, it shows a similar strong dependence on the laser field shape as the high-energy part of the ATI spectrum. Control over this process by tailoring the shape of the laser-field-cycle is thus possible[262,263], which permits detailed insight into and control over electron-electron correlation on attosecond time-scales[189], and also allows for control over molecular ionization-fragmentation processes using light fields[264].

High-harmonic generation (HHG)[18,19,160] In HHG the recolliding EWP interferes with the bound state of the parent ion according to its de Broglie wavelength $\lambda_e(t) = 2\pi/p(t_r)$ at the instant of its recollision and by that induces dipole oscillations. These dipole oscillations lead to emission of radiation at $\omega(t_r) \approx p^2(t_r)/2 + I_p$, with I_p the ionization potential of the parent atom/molecule[265]. Often, the generation process of this radiation is alternatively described as the radiative recombination of an electron into the original bound state at time t_r, whereby the kinetic energy of the electron, $p^2(t_r)/2$, plus the binding energy of the atom/molecule, I_p, that is gained during recombination, are converted into a photon which, due to energy conservation, must have the photon energy $\omega(t_r)$, see Fig. 2.1. The maximum generated frequency is proportional to the maximum recollision energy $3.17U_p$ and typically is in the extreme ultraviolet (XUV) or soft X-ray photon energy range, and may even extend into the keV regime. As for multi-cycle laser pulses the same frequency ω is generated twice per laser cycle (assuming HHG by only either the long or short trajectory class, as can be achieved by phase-matching[160,266–268]), the resulting spectrum is a comb of odd high-harmonics of the laser frequency, where the term 'high' means higher than the low order harmonics generated by perturbative nonlinear processes. This is what the name of this process refers to. The generated momentary frequency $\omega(t_r)$ is dictated by the strict relation $t_r = t_r(t_i)$ described above, cf. Fig. 2.4, and thus sweeps on a laser-sub-cycle time-scale. This by itself can be used for obtaining sub-cycle temporal resolution, see Section 7.1.2 for details. Moreover, the trajectory of the recolliding EWP and thus $p(t_r)$ can be influenced by shaping the laser field cycle, as we will discuss below. Therefore, the temporal emission pattern of the generated high-harmonic (HH) radiation can be controlled using tailored strong laser fields.

Non-radiative electron recapture Although it seems counter-intuitive, but there exists also notable probability that during the interaction of a strong laser field with an atom or molecule electrons are trapped in weakly bound Rydberg states that survive the high field of the laser pulse such that they can be detected after the pulse. Population of Rydberg states during strong field interaction has been predicted already roughly 30 years ago[269] and was experimentally confirmed by numerous experiments[161,270–274]. Recent measurements have shown that the population of Rydberg states in intense laser pulses can happen via a process dubbed *frustrated field ionization* (FFI)[49,50,162,275,276,163–165]. FFI applies to a substantial fraction of all field-ionizing electrons, and it has been shown that even more than one electron can be re-captured on an atom, molecule, or cluster[51,165]. In the FFI process, an electron, emitted by field ionization, does not gain enough drift energy from the laser pulse after ionization to overcome the Coulomb attraction of the nucleus and will eventually be recaptured by the Coulomb field of the ion. In order to get trapped after the pulse has faded, the electron has to be in the vicinity of the nucleus at the end of the pulse to ensure that the Coulomb potential energy is able to compensate the gained drift kinetic energy. Because the energy of the electron after the laser interaction should be very small, FFI can only be observed with (close to) linearly polarized light[164] (or with tailored waveforms that can drive the electron back to the nucleus with very low energy[163]). This is because, as explained in Section 2.2.2, elliptically polarized fields produce electrons with non-zero final energy, cf. (2.16). From (2.12) we infer that in linearly polarized fields negligible drift energy is imparted to those electrons that field-ionize close to the field maxima in each oscillation period, and thus it should be these electrons that are recaptured. This has been recently confirmed experimentally using the known field of few-cycle laser pulses as a sub-cycle driving force and temporal reference[165].

2.2.5 Semi-classical descriptions of important strong-field processes

So far we have restricted ourselves to a purely classical and phenomenological description of the various fundamental processes observed in the interaction of strong laser fields with atoms and molecules. Combined with the sub-cycle ionization dynamics in strong laser fields, Section 2.2.1, the classical trajectories obtained through solution of Newton's equations, Sections 2.2.2 and 2.2.3, can already provide a qualitative understanding of the most important phenomena taking place in strong laser fields such as ATI, HHG, NSDI, etc. that we described in Section 2.2.4. However, for interpretation of measured electron momentum distributions and high-harmonic spectra such a description is still insufficient. The most important shortcoming of the purely classical picture is that the phases of the EWPs and their evolution along their trajectories are neglected. Thus, interference phenomena are not captured by such a description which is, however, necessary for a quantitative understanding of essentially all abovementioned processes and applications of them.

Therefore, we will now sketch how the interaction of atoms and molecules with a strong laser field can be described quantum-mechanically, thereby providing the theoretical foundations for our discussions on the production of XUV/X-ray fields by HHG (Chapter 4), exploitation of EWP interferences in electron momentum spectra by holography, LIED and sub-cycle interferometry (Chapter 6), and retrieval of sub-cycle dynamical information from HH spectra (Chapter 7), etc. The key point that we want to highlight with this discussion is that from a thorough quantum-mechanical treatment, by making certain approximations, the classical trajectory picture described in the Sections above can be recovered and all conclusions that we made based on these trajectories stay qualitatively valid. As we will see, in the quantum picture the purely classical description given in the Sections above is amended by essentially two points, though: The electron trajectories (i) are weighted by amplitudes determined by the ionization probability at the ionization time; (ii) carry a phase that evolves due to the forces of the laser field and binding potential of the parent ion.

We start our discussion by considering the probability amplitude $M_{\boldsymbol{p}}$ for detecting an electron with drift momentum $\boldsymbol{p}$ that is emitted by irradiation of a system (atom, molecule) with a laser field $\boldsymbol{E}(t)$. The electron shall be in a certain state, e.g., in its ground state $|\psi_0\rangle = |\psi_0(\boldsymbol{r})\rangle e^{iI_pt}$, with $-I_p$ the energy of the ground state. This probability amplitude can be written in general and exact form as[171,277]

$$M_{\boldsymbol{p}} = \lim_{t\to\infty, t'\to\infty} \langle \psi_{\boldsymbol{p}}(t)|U(t,t')|\psi_0(t')\rangle, \tag{2.23}$$

where $U(t,t')$ is the time-evolution operator (propagator) of the Hamiltonian. Here we apply for the sake of simplicity the single active electron (SAE) approximation introduced above and consider the one-electron Hamiltonian (in length gauge)

$$H(t) = -\frac{1}{2}\nabla^2 + \boldsymbol{r}\cdot\boldsymbol{E}(t) + V_0(\boldsymbol{r}) \tag{2.24}$$

with the binding potential of the system $V_0(\boldsymbol{r})$. For convenience, we introduce the field-Hamiltonian that neglects the binding potential

$$H_f(t) = -\frac{1}{2}\nabla^2 + \boldsymbol{r}\cdot\boldsymbol{E}(t) \tag{2.25}$$

and the Hamiltonian describing the interaction with the laser field only

$$H_I(t) = \boldsymbol{r}\cdot\boldsymbol{E}(t). \tag{2.26}$$

With the latter, the equation for $M_{\boldsymbol{p}}$ (2.23) can be recast into

$$M_{\boldsymbol{p}}(t_f) = -i\int_{t'}^{t_f} \mathrm{d}\tau \langle \psi_{\boldsymbol{p}}(t)|U(t,\tau)H_I(\tau)|\psi_0(\tau)\rangle, \tag{2.27}$$

where t_f denotes some final time after the laser pulse. The propagator $U(t,t')$ in (2.27) can be formally decomposed as

$$U(t,t') = U_f(t,t') - i\int_{t'}^{t} \mathrm{d}\tau U_f(t,\tau)V(\boldsymbol{r})U(\tau,t'). \tag{2.28}$$

The expression (2.27) for $M_{\boldsymbol{p}}(t_f)$, which is still exact, can now be simplified by applying the *strong-field approximation* (SFA)[196,220,221]. To do so we replace the exact scattering states with the so-called Volkov states, $|\psi_{\boldsymbol{p}}\rangle \rightarrow |\psi_{\boldsymbol{p}}^V\rangle$, and the full propagator by that corresponding to $H_f(t)$ describing evolution in the laser field only, i.e., $U(t,t') \rightarrow U_f(t,t')$. The Volkov states $|\psi_{\boldsymbol{p}}^V\rangle$ are eigenstates of the time-dependent Schrödinger equation that only considers the laser field but not the binding potential,

$$i\frac{\partial}{\partial t}|\psi_{\boldsymbol{p}}^V\rangle H_f(t) = H_f|\psi_{\boldsymbol{p}}^V\rangle. \tag{2.29}$$

In length gauge, the Volkov states read

$$|\psi_{\boldsymbol{p}}^V(t)\rangle = |\boldsymbol{p}+\boldsymbol{A}(t)\rangle e^{-iS_{\boldsymbol{p}}(t)}, \tag{2.30}$$

where $|\boldsymbol{p}+\boldsymbol{A}(t)\rangle$ denote plane wave states $\langle \boldsymbol{r}|\boldsymbol{p}+\boldsymbol{A}\rangle = (2\pi)^{-3/2}\exp\left[i(\boldsymbol{p}+\boldsymbol{A})\cdot\boldsymbol{r}\right]$ and

$$S_{\boldsymbol{p}}(t) = \frac{1}{2}\int_{t'}^{t}\mathrm{d}\tau[\boldsymbol{p}+\boldsymbol{A}(\tau)]^2 \tag{2.31}$$

is the phase of the Volkov states, where $\boldsymbol{A}(t) = -\int_{-\infty}^{t}\boldsymbol{E}(t')\mathrm{d}t'$ is the vector potential of the laser field. By replacing in (2.27) the exact scattering states with the Volkov states and the full propagator with that of the field-only Hamiltonian, the influence of the Coulomb potential on the emitted EWPs is neglected and we obtain the SFA probability amplitudes

$$M_{\boldsymbol{p}}^{\mathrm{SFA},(d)}(t_f) = -i\int_{t'}^{t_f}\mathrm{d}t_0\langle\psi_{\boldsymbol{p}}^V(t_0)|H_I(t_0)|\psi_0(t_0)\rangle, \tag{2.32}$$

which are also known as Keldysh-Faisal-Reiss (KFR) amplitudes[196,220,221]. The physical content of expression (2.32) can be easily identified from its structure. Reading (2.32) from right to left we can interpret it as follows: Electrons are promoted into the continuum at times t_0 by the interaction with the laser field via $H_I(t) = \boldsymbol{r}\cdot\boldsymbol{E}(t)$. Then, from t_0 on, they no longer feel the binding potential and propagate as free electrons in the laser field until at time t_f the laser field is over. The integration runs over all ionization times t_0 at which electrons can be promoted into the continuum and ensures that their separate contributions are added up in the momentum distribution. The transition matrix element (2.32) corresponds to the **direct electrons** that we introduced in the Sections above, denoted by the index (d) in $M_{\boldsymbol{p}}^{\mathrm{SFA},(d)}$. A description of also the recolliding electrons necessitates that the additional term in (2.28) describing interactions with the binding potential is preserved. We will discuss this case below. Before, we would like to further simplify the KFR amplitudes and discuss some of their properties.

By explicitly inserting the expressions for the Volkov states and the Hamiltonian into (2.32) we obtain the SFA transition matrix element in its full form[171,277]

$$\begin{aligned} M_{\boldsymbol{p}}^{\mathrm{SFA},(d)}(t_f) = -i\int_{t'}^{t_f}\mathrm{d}\tau\langle\boldsymbol{p}+\boldsymbol{A}(\tau)|\boldsymbol{r}\cdot\boldsymbol{E}(\tau)|\psi_0(\boldsymbol{r})\rangle \\ \exp\left\{\int_{t'}^{\tau}\frac{1}{2}[\boldsymbol{p}+\boldsymbol{A}(t'')]^2 + I_p\mathrm{d}t''\right\}. \end{aligned} \tag{2.33}$$

Connection with the trajectory picture discussed in the Sections above can now be made by applying the stationary-phase method* to the integral in (2.33). By this procedure the full integral can be approximated as a sum over all stationary points s[171,277]

$$M_{\boldsymbol{p}}^{\mathrm{SFA},(d)} \approx \sum_s a(\boldsymbol{p}, t^s) e^{iS^s(\boldsymbol{p},t^s)} \tag{2.34}$$

with amplitudes $a(\boldsymbol{p}, t^s)$ and phase $S^s(\boldsymbol{p}, t^s) = \int_{t'}^{t^s} \frac{1}{2}[\boldsymbol{p} + \boldsymbol{A}(\tau)]^2 + I_p \mathrm{d}\tau$. For a given electron momentum and a given field-shape $\boldsymbol{A}(t)$ there exists a certain number of stationary points $t^s = t^s(\boldsymbol{p})$ that correspond to those times in (2.33), where the phase in the integral changes slowly. These points are those where the derivative of the phase is zero,

$$\frac{\mathrm{d}}{\mathrm{d}t^s}[S_{\boldsymbol{p}}(t^s)] = I_p + \frac{1}{2}[\boldsymbol{p} + \boldsymbol{A}(t^s)]^2 = 0. \tag{2.35}$$

The amplitudes $a(\boldsymbol{p}, t^s)$ in (2.34) are proportional to the matrix element $\langle \boldsymbol{p} + \boldsymbol{A}(\tau) | \boldsymbol{r} \cdot \boldsymbol{E}(\tau) | \psi_0(\boldsymbol{r}) \rangle$, i.e., to the amplitude of a field-mediated transition of the ground state into a Volkov state with momentum $\boldsymbol{p}$, which corresponds to the ionization probability. Obviously, the stationary points in (2.35) are complex for $I_p > 0$, i.e., for a binding potential. By applying the approximation $I_p = 0$ made in the simple man's model (SMM)[15–17,222] that we have mentioned above, we can make connection with the classical trajectory picture. Setting $I_p = 0$, we obtain from (2.35) $\boldsymbol{p} = -\boldsymbol{A}(t^s)$. Integration of this expression recovers the classical electron trajectory (2.9). This shows that (2.35) describes the quantum analog of the classical electron trajectories, usually called quantum trajectories or quantum orbits. Expression (2.34) thus shows that the electron momentum spectrum at each point $\boldsymbol{p}$ can be constructed as the interference of quantum trajectories that have a weight $a(\boldsymbol{p}, t^s)$ determined by the ionization probability at their release time. The trajectories are close to the purely field-driven classical trajectories whose properties we have discussed in detail in the Sections above. The interference of the quantum trajectories is determined by their phase, $S^s(\boldsymbol{p}, t^s)$, that evolves during the field-driven motion.

We now extend the description also to the **recolliding electrons** which are not considered in the electron momentum distribution described by the transition matrix element (2.34). To consider also recollisions the second term in (2.28) needs to be preserved[171,277]. This term is lost when replacing in (2.27) the full propagator, $U(t, t')$, with the one that only considers the interaction of the emitted EWPs with the laser field, $U_f(t, t')$. By also considering this term one obtains the full SFA transition amplitude,

$$M_{\boldsymbol{p}}^{\mathrm{SFA}} = M_{\boldsymbol{p}}^{\mathrm{SFA},(d)} + M_{\boldsymbol{p}}^{\mathrm{SFA},(r)}, \tag{2.36}$$

with $M_{\boldsymbol{p}}^{\mathrm{SFA},(d)}$ given by (2.32) and

$$M_{\boldsymbol{p}}^{\mathrm{SFA},(r)}(t_f) = -\int_{-\infty}^{t_f} \mathrm{d}t_0 \int_{t_0}^{t_f} \mathrm{d}t_1 \langle \psi_{\boldsymbol{p}}^V(t_1) | V(\boldsymbol{r}) U_f(t_1, t_0) H_I(t_0) | \psi_0(t_0) \rangle. \tag{2.37}$$

This expression constitutes a very comprehensible description of electrons recolliding with the parent ion and can again be easily interpreted analogously to (2.32) by reading it from right to left: At times t_0 electrons are promoted into the continuum by the interaction of the ground state $|\psi_0\rangle$ with the laser field via $H_I(t_0)$. Upon emission at t_0, the electron is propagated in the continuum by

---

*The *stationary-phase method*, also known as *method of steepest descent* or *saddle-point method*, is a method for approximating an integral that contains oscillating terms, see Ref. [278] for a short overview. The overall idea is that the dominant contributions to the integral comes from these points, where the oscillations of the integrand are slowest. Then, the integral can be approximated by a sum over the integrand evaluated at these most relevant points. In the literature on attosecond and strong-field science both *stationary-phase method* and *saddle-point method* are used equally. The relevant points and their defining equations are then called *stationary-phase points* and *stationary-phase equations* respectively *saddle-points* and *saddle-point equations*. Here and throughout this thesis we will use the terms *stationary-phase method*, *stationary-phase points* and *stationary-phase equations*.

the laser field until time t_1. This is described by the propagator $U_f(t_1, t_0)$. At times t_1 the electron encounters the parent ion's potential $V(\boldsymbol{r})$ and is elastically scattered into a Volkov state. From t_1 on it no longer interacts with the potential but is still moving in the laser field and can acquire additional energy. The integrals running over all emission times t_0 and all scattering times t_1 add up the contributions of all recolliding and scattering electrons. Expression (2.37) thus constitutes a quantum formulation of the three-step model and electrons that are described by it are observed as high-energy part of the ATI electron distribution with energies from $2U_p$ to $10U_p$. Application of the stationary-phase method to (2.37) leads to three equations for the stationary points $\boldsymbol{p}^s$, t_0^s and t_1^s

$$
\begin{aligned}
\frac{\left[\boldsymbol{p}^s + \boldsymbol{A}(t_0^s)\right]^2}{2} + I_p &= 0 \\
(t_1^s - t_0^s)\boldsymbol{p}^s &= \int_{t_1^s}^{t_0^s} \boldsymbol{A}(\tau)\mathrm{d}\tau \\
\frac{\left[\boldsymbol{p}^s + \boldsymbol{A}(t_0^s)\right]^2}{2} &= \frac{\left[\boldsymbol{p}^s + \boldsymbol{A}(t_1^s)\right]^2}{2} .
\end{aligned}
\tag{2.38}
$$

The first condition enforces energy conservation at the time of ionization t_0. The second condition is nothing but expression (2.9) for the electron's position and enforces that at time t_1 the electron returns to the parent ion's position $\boldsymbol{r} = 0$, i.e., it enforces $\boldsymbol{r}(t_1, t_0) = 0$. The third condition expresses that the electron, upon returning to the parent ion, scatters elastically. Thus, once again the classical description given in the Sections above can be recovered from the quantum description.

By extension of (2.37) to the two-electron case, described, e.g., in Refs. [175, 256, 257, 259], also double ionization by **inelastic scattering** (NSDI) can be described within the SFA by a transition matrix element of similar structure. It reads[175]

$$
M^{\mathrm{SFA}}_{\boldsymbol{p}_1,\boldsymbol{p}_2} = -\int_{-\infty}^{\infty} \mathrm{d}t_1 \int_{-\infty}^{t_1} \mathrm{d}t_0 \langle \psi^V_{\boldsymbol{p}_1,\boldsymbol{p}_2}(t_1) | V_{12} U_f^{(1)}(t_1, t_0) \otimes V U_f^{(2)}(t_1, t_0) | \psi_0(t_0) \rangle , \tag{2.39}
$$

where $\boldsymbol{p}_1$ and $\boldsymbol{p}_2$ are the momenta of the two electrons released by NSDI. The potential V is, as before, the binding potential of the system, and V_{12} is the electron-electron interaction through which the second electron is freed upon impact of the first. While expression (2.39) constitutes a quite formal solution for the transition matrix element, as in detail the two-electron momentum spectrum strongly depends on the exact shape of V_{12}, the different terms of this expression can be straightforwardly connected to the different phases of the three-step-model: Initially, the system is in the ground state $|\psi_0(t_0)\rangle$, which is a two-electron state approximated by $|\psi_0^{(1)}(t_0)\rangle \otimes |\psi_0^{(2)}(t_0)\rangle$. At time t_0 the first electron is released by the laser field, whereas the second electron remains bound. Subsequently, in between t_0 and t_1, the first electron propagates in the continuum as described by the propagator $U_f^{(1)}(t_1, t_0)$, thereby gaining energy from the field. At time t_1 it undergoes an inelastic collision with its parent ion and interacts with the second electron via V_{12}, thereby knocking out the second electron. The integrals in the matrix element (2.39) can again be approximated by application of the stationary-phase method, which now leads to three equations for the stationary times of the release of the first electron t_0^s and the second electron t_1^s, and for the momentum of the first electron in between ionization and recollision, $\boldsymbol{k}^s$. These equations read

$$
\begin{aligned}
\frac{\left[\boldsymbol{k}^s + \boldsymbol{A}(t_0^s)\right]^2}{2} + I_p^{(1)} &= 0 \\
\sum_{n=1}^{2} [\boldsymbol{p}_n + \boldsymbol{A}(t_1^s)]^2 &= [\boldsymbol{k}^s + \boldsymbol{A}(t_1^s)]^2 - 2|I_p^{(2)}| \\
\int_{t_0^s}^{t_1^s} [\boldsymbol{k}^s + \boldsymbol{A}(\tau)]\mathrm{d}\tau &= 0
\end{aligned}
\tag{2.40}
$$

The first and second equation express energy conservation at the times of ionization, t_0, and rescattering, t_1, respectively. The third equation determines the momentum of the first (recolliding) electron, $\boldsymbol{k}$, such that it returns to the ion at time t_1^s. By determining the three values t_0^s, t_1^s, and $\boldsymbol{k}^s$ from a certain set of momenta $(\boldsymbol{p}_1, \boldsymbol{p}_2)$, the matrix element (2.39) can be written as a sum of the form

$$M^{\mathrm{SFA}}_{\boldsymbol{p}_1,\boldsymbol{p}_2} \approx \sum_s a^s e^{iS^s}, \tag{2.41}$$

with the amplitudes a^s and the phase S^s, where the sum runs over all stationary points s.

Finally we turn to obtaining a semi-classical description of the process of **high-harmonic generation** (HHG). The standard description for this process is the so-called Lewenstein model[265]. Although this model describes the emission of photons, its results can still be recovered by using an approach as above for the description of electron momentum distributions. We start by recalling that by the laws of classical electrodynamics the observation of the emission of photons from a system, such as an atom or a molecule, is determined by the dipole acceleration. As described above, in HHG an oscillating dipole is induced by the interference of the ground state wave function with the wave function of the recolliding EWP. To describe this we start from the dipole expectation value of the system,

$$\boldsymbol{d}(t) = -\langle \psi(t)|\hat{\boldsymbol{r}}|\psi(t)\rangle, \tag{2.42}$$

with $\hat{\boldsymbol{r}}$ the dipole operator and the minus sign due to the electron's charge $q = -1$. The harmonic field $\boldsymbol{\epsilon}(t)$ that is emitted via the dipole acceleration then reads

$$\boldsymbol{\epsilon}(t) = -\frac{\mathrm{d}^2}{\mathrm{d}t^2}\langle \psi(t)|\hat{\boldsymbol{r}}|\psi(t)\rangle, \tag{2.43}$$

from which the harmonic spectrum can be obtained by Fourier transformation of (2.43),

$$\boldsymbol{\epsilon}(\omega) = -\int \mathrm{d}t e^{-i\omega t}\frac{\mathrm{d}^2}{\mathrm{d}t^2}\langle \psi(t)|\hat{\boldsymbol{r}}|\psi(t)\rangle = \omega^2\int \mathrm{d}t e^{-i\omega t}\langle \psi(t)|\hat{\boldsymbol{r}}|\psi(t)\rangle. \tag{2.44}$$

With the time-evolution operator $U(t,t')$ the dipole $\boldsymbol{d}(t)$ from (2.42) can be written as

$$\boldsymbol{d}(t) = -\langle \psi_0(t_i)|U(t_i,t)\hat{\boldsymbol{r}}U(t,t_i)|\psi_0(t_i)\rangle, \tag{2.45}$$

where we have assumed that at time t_i the electron starts in the state $|\psi(t_i)\rangle = |\psi_0\rangle$. Within the SFA, i.e., by making the replacement $U(t,t') \to U_f(t,t')$, expression (2.45) can be approximated as

$$\boldsymbol{d}(t) = -i\int_{t_i}^{t}\mathrm{d}t'\langle \psi_0(t')|H_I(t')U_f(t',t)\hat{\boldsymbol{r}}|\psi_0(t)\rangle + c.c., \tag{2.46}$$

with $U_f(t',t)$ the field-only propagator, $H_I(t)$ the Hamiltonian of the laser interaction from (2.26), and *c.c.* denoting the complex conjugated expression. Expression (2.46), which is the result of the Lewenstein model[265], describes ionization in the field at time t' (term $H_I(t')$), propagation in the laser field in between t' and t (term $U_f(t',t)$), and recombination, i.e., the emission of harmonic radiation, at time t (denoted by the dipole operator $\hat{\boldsymbol{r}}$). To obtain a description in terms of quantum trajectories we expand (2.46) as

$$\boldsymbol{d}(t) = -i\int_{t_i}^{t}\mathrm{d}t'\int \mathrm{d}^3\boldsymbol{p}\ \langle \psi_0(t')|\hat{\boldsymbol{r}}\cdot\boldsymbol{E}(t')|\boldsymbol{p}+A(t')\rangle\langle \boldsymbol{p}+A(t)|\hat{\boldsymbol{r}}|\psi_0(t)\rangle e^{iS(\boldsymbol{p},t_i,t)} + c.c., \tag{2.47}$$

with

$$S(\boldsymbol{p},t_i,t) = \int_{t_i}^{t}\frac{1}{2}[\boldsymbol{p}+\boldsymbol{A}(t')]^2 + I_p\mathrm{d}t' \tag{2.48}$$

the semi-classical action as above. In the representation (2.47) the dipole matrix elements for ionization

$$\boldsymbol{d}_{\mathrm{ion}}(\boldsymbol{p},t') = \langle \psi_0(t')|\hat{\boldsymbol{r}}\cdot\boldsymbol{E}(t')|\boldsymbol{p}+A(t')\rangle \tag{2.49}$$

and recombination

$$\boldsymbol{d}_{\mathrm{rec}}(\boldsymbol{p},t) = \langle \boldsymbol{p} + A(t)|\hat{\boldsymbol{r}}|\psi_0(t)\rangle \tag{2.50}$$

are easily identified. With that, the harmonic spectrum can be written as

$$\boldsymbol{\epsilon}(\omega) = -i\omega^2 \int \mathrm{d}t \int_{t_i}^{t} \mathrm{d}t' \int \mathrm{d}^3\boldsymbol{p}\; \boldsymbol{d}_{\mathrm{ion}}(\boldsymbol{p},t')\boldsymbol{d}_{\mathrm{rec}}(\boldsymbol{p},t)e^{iS(\boldsymbol{p},t_i,t)-i\omega t} + c.c. \tag{2.51}$$

To solve (2.51) the stationary-phase method is applied to the phase

$$\tilde{S}(\boldsymbol{p},t_i,t) = S(\boldsymbol{p},t_i,t) - \omega t = \int_{t_i}^{t} \frac{1}{2}[\boldsymbol{p} + \boldsymbol{A}(t')]^2 + I_p \,\mathrm{d}t' - \omega t, \tag{2.52}$$

which leads to three equations that correspond to the derivative of $\tilde{S}$ with respect to the three variables $\boldsymbol{p}$, $t' = t_i$, and $t = t_r$, where we have introduced the indices i for ionization and r for recombination. These three equations read

$$\begin{aligned} \int_{t_i^s}^{t_r^s} \boldsymbol{p}^s + \boldsymbol{A}(\tau)\mathrm{d}\tau &= 0 \\ \frac{[\boldsymbol{p}^s + \boldsymbol{A}(t_i^s)]^2}{2} + I_p &= 0 \\ \frac{[\boldsymbol{p}^s + \boldsymbol{A}(t_r^s)]^2}{2} + I_p &= \omega, \end{aligned} \tag{2.53}$$

and reflect the three conditions for the emission of a photon by HHG. The first equation dictates that the electron returns to the ion, and the second and third ones express the conservation of energy at the times of ionization and recombination. Solving these three equations yields triplets $(\boldsymbol{p}^s, t_i^s, t_r^s)$ that define the semi-classical analog of the classical trajectories that we discussed in Section 2.2.3.

For each frequency ω of the harmonic spectrum there exists a certain number of trajectories defined by the stationary-phase equations (2.53). These quantum paths or quantum orbits contribute to the dipole emission at these frequency. The exact number of quantum paths respectively stationary points depends on the shape of the laser field respectively its vector potential $\boldsymbol{A}(t)$. In Section 2.2.3 we have discussed the recollision process within a purely classical treatment for a sinusoidal field evolution. This leads to the expression (2.18) for $t_r = t_r(t_i)$. Solution of the stationary-phase equations (2.53) leads to a somewhat modified but conceptually similar correspondence between the ionization and recollision times of each quantum trajectory. In detail one needs to consider that they are complex because of the classically forbidden process of tunneling at time t_i. The different solutions s of the stationary-phase equations can be ordered by the real part of the time that the electron spends in the continuum between ionization and recollision, $\tau^s = t_r^s - t_i^s$. The first two trajectories $s = \{1, 2\}$ are then identified as the short and long trajectories that we have found in Section 2.2.3. Trajectories with larger s correspond to multiple returns of the electron to the parent ion. Having said this we can now write the harmonic spectrum as a sum over the discrete quantum trajectories s, which yields

$$\boldsymbol{\epsilon}(\omega) = -i\omega^2 \sum_s \frac{1}{(t_r^s - t_i^s)^{3/2}} \left[\det(\tilde{S}'')\right]^{-1/2} \boldsymbol{d}_{\mathrm{ion}}^s(\boldsymbol{p}^s, t_i^s)\boldsymbol{d}_{\mathrm{rec}}^s(\boldsymbol{p}^s, t_r^s)e^{iS(\boldsymbol{p}^s,t_i^s,t_r^s)-i\omega t_r^s}. \tag{2.54}$$

In most cases it is sufficient to only evaluate the first two members of this sum, i.e., the short and long trajectories, respectively. The first term in expression (2.54) accounts for the decrease of the intensity of the electron wavepacket during the time $t_r^s - t_i^s$ because of the spreading of the wavepacket. Because of the reduction of the wavepacket intensity with excursion time, the contribution of trajectories that spend longer time in the continuum decreases. The second term is the determinant of the 2 × 2 matrix of the second derivative of $\tilde{S}$ with respect to the variables t_i and t_r evaluated at the stationary points. The other terms are the ionization and recombination dipole matrix elements and the phase factor that accounts for quantum interferences of the different trajectories.

Summing up this Section, we found that the processes that were described above only phenomenologically (ATI, NSDI, HHG), based on classical electron trajectories, can be put onto a quantum mechanical footing. Although the semi-classical relations that we have discussed here provide a very useful and simple theoretical framework for the interpretation of measured spectra, one should not forget that they heavily rely on approximations. Quantitative agreement with measured data should therefore not be expected in general. The most important approximations that we made are the SAE (single active electron) approximation and the SFA. Currently, large efforts are made to add corrections to the semi-classical solutions that include the influence of the Coulomb potential[179,216–219] and many-body effects[173,177,179].

3

Tailored strong laser fields

The pronounced sensitivity of both the electron emission step and the subsequent field-driven electron motion that were discussed in Section 2.2 opens up the possibility to control the response of an atom, molecule and to a certain degree also other physical systems mentioned above, such as clusters, nanostructures and solids, on attosecond timescales by tailoring the sub-cycle evolution of the laser electric field. Examples of how this possibility can be exploited for research and applications will be discussed below. In this Chapter we will discuss different approaches for tailoring the electric field of ultrashort intense laser pulses. Historically, the first experiments that used tailored strong waveforms for studying the response of atoms[232,279–281] and molecules[282] to strong fields on laser-sub-cycle timescales applied the concept two-color waveform synthesis. We will discuss two- and also multi-color waveform synthesis in Section 3.2. Before, we will discuss in Section 3.1 concepts for gaining control over the field of broadband few-cycle laser pulses, although they were successfully implemented much later than two-color field-shaping. As we will see, these concepts are of crucial importance also for combining two- and multiple colors, though.

3.1 Reproducible strong few-cycle waveforms

For very short laser pulses whose duration approach the limit of only a few times the laser oscillation period $T_o = 2\pi/\omega_o$ (so-called *few-cycle pulses*), with ω_o the oscillation angular frequency of the laser pulse corresponding to the center wavelength of the laser spectrum, field-ionization and also the field-driven dynamics of the emitted electrons become strongly dependent on the shape of the laser-oscillations under the laser pulse envelope[21,149], see Figs. 2.2-2.4 and corresponding explanations. A correct description of the shape of a few-cycle laser field thus needs to reflect the relative positions of the field maxima with respect to the pulse peak. These are determined by the so called carrier-envelope phase (CEP), φ_{CE}. With that, the electric field of a laser pulse can be written as

$$\boldsymbol{E}(t) = F(t)\cos(\omega_o t + \varphi_{\mathrm{CE}})\boldsymbol{e}_z, \tag{3.1}$$

where we have assumed linear polarization along z. $F(t)$ is a pulse envelope function, for example a Gaussian, for which $F(t) = E_0 e^{-2\ln(2)(t/\tau)^2}$ with τ the full width at half maxium (FWHM) pulse duration and E_0 the pulse's peak electric field strength. This is a suitable description even for close to single-cycle laser pulses[283].

Although the variations of the electric field oscillations with φ_{CE} are relatively small even for near-single-cycle pulses [Fig. 2.2], their impact is huge and has numerous fundamental and practial consequences, e.g., in ionization[284] or XUV pulse generation[285]. The reasons for this strong dependence of various processes on the CEP are, on the one hand, that field-ionization depends exponentially on the field strength and, on the other hand, that the recollision energy depends strongly on the CEP. Chapters 6 to 8 will discuss numerous examples of CEP-related effects in the interaction of strong laser fields with atoms and molecules.

3.1.1 The carrier-envelope offset frequency

The value of the CEP $\varphi_{\text{CE},0}$ of a certain few-cycle laser pulse within the train of pulses emitted from a mode-locked laser cavity can, in principle, be measured using the information contained in photoelectron spectra generated by this pulse[247–250,286,287]. We will describe this method in greater detail below. However, due to the different values of the group, v_g, and phase, v_p, velocities in the optical components such as the laser crystal, dispersion compensation optics, etc., that are passed by the laser beam within a laser cavity, the CEP changes from one pulse to the next pulse by a value

$$\Delta\varphi_{\text{CE}} = \omega_o \sum_i \left(\frac{1}{v_{g,i}} - \frac{1}{v_{p,i}} \right) L_i, \tag{3.2}$$

where we labelled the different components by i and denoted the respective beam propagation lengths inside them by L_i. Denoting the cavity round trip time with T_r, which equals the time between the pulses in the pulse train, the pulse repetition rate becomes $\omega_r = 2\pi/T_r$. The rate at which the CEP changes from pulse to pulse is then given by $\omega_{\text{CE}} = \Delta\varphi_{\text{CE}}/T_r$. It is easy to show that in the frequency domain $\omega_{\text{CE}} < \omega_r$ appears as an offset frequency of the pulse train's frequency comb spectrum. To see that we write the field of the pulse train in the time domain and subsequently calculate its spectrum by applying Fourier transformation. In the time domain the field evolution of one pulse within the pulse train is in complex notation

$$E(t) = F(t)\exp(i\omega_o t + i\varphi_{\text{CE},0}), \tag{3.3}$$

from which the scalar electric field of (3.1) can be recovered by taking its real part. With (3.3) the complex electric field of the whole laser pulse train can be conveniently written as

$$\epsilon(t) = \sum_{j=-\infty}^{+\infty} F(t - jT_r)\mathrm{e}^{i[\omega_o(t-jT_r)+j\Delta\varphi_{\text{CE}}+\varphi_{\text{CE},0}]}. \tag{3.4}$$

To obtain the spectrum of the laser pulse train we apply Fourier transformation to (3.4) and obtain

$$\epsilon(\omega) = \mathrm{e}^{i\varphi_{\text{CE},0}} \sum_{j=-\infty}^{+\infty} \mathrm{e}^{i[j\Delta\varphi_{\text{CE}} - j\omega_o T_r]} \int F(t - jT_r)\mathrm{e}^{-i(\omega-\omega_o)t}\mathrm{d}t. \tag{3.5}$$

By using the relation $\sum_{k=-\infty}^{\infty} \mathrm{e}^{ikx} = 2\pi \sum_{q=-\infty}^{\infty} \delta(x - 2\pi q)$, $x \in \mathbb{R}$, for the Dirac delta function we can, together with the Fourier transform of the pulse envelope $\tilde{F}(\omega - \omega_o) = \int F(t)\mathrm{e}^{-i(\omega-\omega_o)t}\mathrm{d}t$, write (3.5) as

$$\epsilon(\omega) = 2\pi\mathrm{e}^{i\varphi_{\text{CE},0}}\tilde{F}(\omega - \omega_o) \sum_{q=-\infty}^{+\infty} \delta(\omega T_r - \Delta\varphi_{\text{CE}} - 2\pi q). \tag{3.6}$$

This is the well known comb spectrum of a mode-locked laser that consists of a series of teeth q spaced by the repetition rate $\omega_r = 2\pi/T_r$ under the spectral envelope $\tilde{F}(\omega - \omega_o)$. The important moment is that the whole comb spectrum is offset from zero by $\omega_{\text{CE}} = \Delta\varphi_{\text{CE}}/T_r$. To see this we explicitly write the frequencies ω_q of the comb teeth determined by the zero-values of the Dirac delta function,

$$\omega_q = 2\pi q \frac{1}{T_r} + \frac{\Delta\varphi_{\text{CE}}}{T_r} = q\omega_r + \omega_{\text{CE}}. \tag{3.7}$$

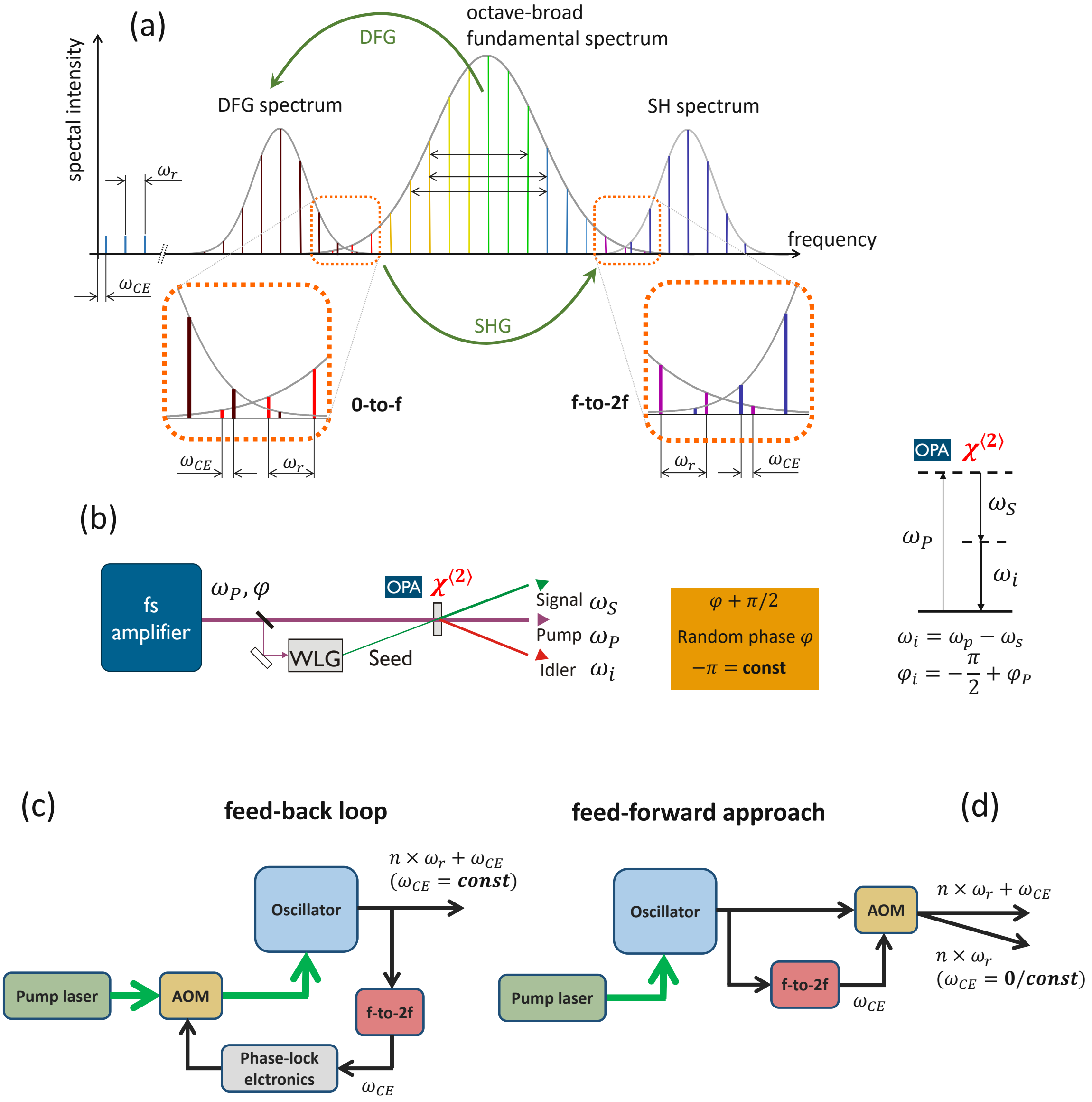

Figure 3.1: Measurement and stabilization of the carrier-envelope offset phase (CEP). (a) To determine the carrier-envelope offset frequency of a laser oscillator the f-to-2f or 0-to-f methods can be used. In these methods the beating of the wings of an octave-broad spectrum with the spectrum obtained via second-harmonic generation (SHG) or difference frequency generation (DFG), respectively, is analyzed. (b) Pulse trains with a constant carrier-envelope offset phase can be obtained by *passive CEP stabilization* during optical parametric amplification. WLG and OPA denote white light-generation and optical parametric amplification, respectively. Active CEP stabilization of an oscillator is possible by a feed-back (c) or feed-forward (d) approach. AOM denotes an acousto optical modulator. See text for further details.

3.1.2 CEP-stabilization for oscillators

From (3.7) it becomes apparent that the frequency comb spectrum of a mode-locked laser oscillator can be used as an optical frequency standard for high-precision measurements, provided the pulse repetition rate ω_r and the carrier-envelope (CE) offset frequency ω_{CE} can be controlled[288,289]. Controlling involves measuring and actively stabilizing these quantities. For achieving high precision, active stabilization is, in general, necessary due to fluctuations and drifts of the cavity mechanical setup caused by, e.g., temperature fluctuations and mechanical vibrations. The pulse repetition rate $\omega_r = 2\pi/T_r$ can be easily measured using, e.g., a photodiode. Stabilization of this quantity amounts to stabilization of the round-trip time T_r of the pulses in the cavity and therewith necessitates stabilization of the cavity length. For driving electronic dynamics with strong laser fields it is, however, not necessary to stabilize the pulse repetition rate $\omega_r = 2\pi/T_r$, because usually all interesting processes take place on a time-scale much smaller than T_r and each laser pulse starts the process under investigation anew. A jitter of the arrival time between the pulses, T_r, is therefore irrelevant. In contrast, precise control over ω_{CE} is of crucial importance. Methods for this will be explained in the following and are also visualized in Fig. 3.1.

CEP-stabilization with a feed-back loop Measurement (and therewith stabilization) of ω_{CE} is significantly more difficult than measurement of ω_r. Still, around the year 2000 several groups have achieved this crucial step using a technique that has been called f-to-2f CEP detection [Fig. 3.1(a)] and feedback control [Fig. 3.1(c)][290–293]. In this technique the spectrum $F(\omega)$ of a laser pulse train is broadened to more than one octave, e.g., by self-phase modulation in a nonlinear fiber. Subsequently the low-frequency (red) part of the spectrum is frequency-doubled in a nonlinear crystal and re-combined with the high-frequency (blue) part of the fundamental spectrum. If the spectrum covers a full octave this generates a beat frequency between the frequency-doubled red modes, $2(q\omega_r + \omega_{\mathrm{CE}})$, and the fundamental blue modes, $2q\omega_r + \omega_{\mathrm{CE}}$, exactly at the carrier-envelope offset frequency:

$$\omega_{\mathrm{CE}} = 2(q\omega_r + \omega_{\mathrm{CE}}) - (2q\omega_r + \omega_{\mathrm{CE}}). \tag{3.8}$$

As $\omega_{\mathrm{CE}} < \omega_r$ this beat frequency is for typical mode-locked laser oscillators within the radio-frequency range and therewith can be easily measured using standard electronics. The such generated electronic signal can then be used as a feed-back signal for stabilizing $\Delta\varphi_{\mathrm{CE}}$ via control of the difference between phase- and group velocity during a cavity round trip based on (3.2). This can for example by achieved by fine-scale rotations of mirrors, prisms or gratings inside the cavity[292] or via nonlinear modulation of the refractive index of the laser crystal via the pump intensity[25,294].

Note, that the actual value of the CEP cannot be determined by the f-to-2f method, only the rate at which the CEP changes from pulse to pulse. If, however, the CE offset frequency ω_{CE} is locked to the pulse repetition rate ω_r with a certain ratio, n, such that $n = \omega_r/\omega_{\mathrm{CE}}$, then every n-th pulse of the pulse train exhibits the same CEP φ_{CE}. This can be seen from $\omega_{\mathrm{CE}} = \Delta\varphi_{\mathrm{CE}}/T_r = \Delta\varphi_{\mathrm{CE}}\omega_r/(2\pi)$, and thus the CEP slippage from pulse to pulse is $\Delta\varphi_{\mathrm{CE}} = 2\pi\omega_{\mathrm{CE}}/\omega_r = 2\pi/n$. With this method, the CEP can therefore be fixed for every n-th pulse up to a constant, which is the value of the CEP of the initial pulse where the stabilization started. A typical value is $n = 4$[23,25].

Alternatively to the f-to-2f method, the carrier-envelope offset frequency ω_{CE} can also be measured using difference frequency generation (DFG)[295–297]. In this scheme ω_{CE} is generated as a beat signal between the low-frequency modes of the octave-spanning fundamental laser spectrum and the high-frequency modes of a spectrum generated by difference-frequency mixing of the high- and low-frequency wings of the laser spectrum, see Fig. 3.1(a). An interesting aspect in this scheme is that the spectrum generated by DFG between the high-frequency modes, $q_{\mathrm{high}}\omega_r + \omega_{\mathrm{CE}}$, and the low-frequency modes, $q_{\mathrm{low}}\omega_r + \omega_{\mathrm{CE}}$, is independent of the CE offset frequency: $q_{\mathrm{DFG}} = (q_{\mathrm{high}}\omega_r + \omega_{\mathrm{CE}}) - (q_{\mathrm{low}}\omega_r + \omega_{\mathrm{CE}}) = (q_{\mathrm{high}} - q_{\mathrm{low}})\omega_r$. In principle the DFG-beam could thus be directly used for seeding a laser amplifier for generating intense CEP-stabilized pulses[295]. Beating of the modes $q_{\mathrm{DFG}} = q\omega_r$ with those of of the laser spectrum, $q\omega_r + \omega_{\mathrm{CE}}$, generates ω_{CE} as the beat-frequency: $q\omega_r + \omega_{\mathrm{CE}} - q\omega_r = \omega_{\mathrm{CE}}$. Because the DFG-generated reference spectrum is independent of the CE offset frequency, this method is called 0-to-f method[295–297]. The such generated ω_{CE}-signal is equivalent to the one generated by the f-to-2f method and can also be used as a feed-back signal for CEP stabilization as described above.

Feed-forward approach for CEP-stabilization The CE offset frequency can, however, not only be stabilized by feedback of the measured ω_{CE}-signal but, conversely, also by a method that has been called the feed-forward approach[298–300], see Fig. 3.1(d). In that approach the cavity of a mode-locked oscillator is not locked to a certain signal but is kept freely running. Instead, the instantaneous, measured ω_{CE} is fed into an acousto-optical modulator (AOM) device, where it is subtracted from the spectrum of the pulse train via DFG between the optical signal and the acoustic signal. It has been shown that this method can very precisely stabilize ω_{CE}[298,299], in particular if it is combined with the feed-back method described above[301]. An interesting feature of this approach is that ω_{CE} can also be locked to 0 or 2π, such that every pulse in the pulse train exhibits the same value of the CEP.

3.1.3 CEP-stabilized intense laser pulse trains

Active CEP stabilization For producing intense CEP-stabilized laser pulses, the weak pulses from a mode-locked laser oscillator need to be amplified in a laser amplifier system to typically the milli-Joule (mJ) energy level per pulse. Generation of a train of amplified pulses with a constant CEP throughout the pulse train over an extended time in the minute-range was first demonstrated at TU Wien in 2003[23,25]. The key to producing amplified pulse trains with constant CEP is to synchronize the pulse-picking rate with the reproduction rate of the CEP in the oscillator pulse train, $n = \omega_r/\omega_{\mathrm{CE}}$. As mJ-class laser amplifiers, due to power limitations, are typically restricted to pulse repetition rates in the low kHz range (e.g., 0.1–50 kHz equivalent to 0.1–50 Watt output power for a typical pulse energy of 1 mJ), reduction of the MHz to GHz pulse repetition rate of oscillators to the kHz range by pulse-picking with, e.g., a Pockels cell, is inevitable. Thus, typically only one out of 10^6 pulses from the oscillator is amplified. If we denote the actual ratio by N, then the pulse-picker selects every N-th pulse for amplification from the oscillator pulse train, where the CEP reproduces itself every n-th pulse. If now N is chosen as an integer multiple of n, it means that every amplified pulse will have the same CEP.

Passive CEP stabilization An alternative method for obtaining a constant value of the CEP in a pulse-train of amplified pulses arises by the method of optical parametric amplification (OPA)[24,302,303]. Because of its possibility for generating wavelength-tunable intense pulses, OPA is a particularly attractive method for waveform synthesis, as we will see below. If in OPA the seed pulse is derived from the non-CEP-stabilized pump pulse, e.g., by white-light generation, then the idler-pulse generated automatically during OPA to satisfy the energy conservation law exhibits constant CEP, i.e., every pulse within the pulse train has the same CEP, see Fig. 3.1(b) for a visualization of the concept called *passive CEP-stabilization*. This automatic stabilization of the idler's CEP is because the process of white-light generation preserves the CEP. Thus, the signal-pulse exhibits the same random CEP as the pump-pulse (up to a constant). Because in OPA the idler-pulse is generated by DFG between the pump and signal pulses, its CEP is also the difference between their respective CEP values. As they are identical (up to a constant), the CEP of the idler is also constant. This is the identical concept that is also exploited in the 0-to-f method described in Section 3.1.2.

CEP-tagging Stabilization of the CEP of a train of intense laser pulses is necessary if in an experiment a CEP-sensitive quantity needs to be accumulated over many laser shots to obtain sufficient statistics. In certain types of experiments, data accumulation periods can be very long and may reach several days, for example in experiments that use coincidence detection technologies for electrons and/or ions[304–307], see Section 5.2 for details. However, it is challenging to keep the CEP constant with high precision over such long times by active or passive stabilization techniques. It is therefore more convenient and potentially also more precise to exploit instead to ones advantage the fact that these experiments work on the basis of a single laser shot. Indeed, in these experiments one tries to detect all ions/electrons that are generated by a certain laser pulse and stores all relevant information derived from them, tagged with a unique laser-shot number. In this case, if the CEP-value of exactly this laser pulse that generates the detected ions/electrons can be determined, it can be stored together with the information obtained from the ions/electrons as an additional parameter. Thus, knowledge of the CEP for each and every laser-shot is sufficient to plot measured quantities for certain values of the CEP in the off-line data analysis. Stabilization of the CE offset frequency is not required. This concept is known as *CEP-tagging* and is now routinely used in experiments[**190**,**264**,286,308].

Although the CEP-tagging concept obviates the need for long-term CEP stabilization, it necessitates that the CEP is measured for each and every pulse within a pulse train at kHz rates. Such single-shot CEP-measurement became possible with the finding that photoelectron spectra in the regime of above threshold ionization (ATI)[17,155,171,224,225] generated by few-cyle laser pulses are highly sensitive to the CEP[243,245]. Measurement of photoelectron spectra into two opposing directions with two detectors, i.e., in a *stereographic ATI photoelectron measurement*, reveals an asymmetry between spectra measured to the left and to the right, in particular for certain energy ranges[243,245]. The asymmetry is strongest for the high-energy part of the ATI spectra that is generated by electron-recollision[171]. Determined by the sub-cycle timing of the field-driven electron-recollision process, the left-right asymmetry in this high-energy range shows a different dependence on the CEP for different spectral portions[171]. This pronounced dependence of the spectral asymmetry can be exploited to retrieve the CEP from it[243,245]. Retrieval of the CEP (up to a constant) from photoelectron spectra in a single laser shot has been demonstrated using a stereo-ATI spectrometer (also known as a *phase-meter*)[247–250]. Using this device the CEP-dependence of the asymmetry can be visualized using a parametric plot, where the asymmetry in the highest energy range is plotted versus the asymmetry in the lower energy range for each and every laser shot. For a large number of laser-shots with random CEP an almost circular shape (commonly referred to as a *phase-potato*) is obtained due to a $\pi/2$-phase offset between the CEP-dependences of these two spectral portions. Since the field-driven electron-recollision dynamics underlying the measured asymmetry is precisely known[171], with this method it should in principle be possible to obtain the absolute CEP-value, as opposed to only a relative value that can be obtained by the f-to-2f or 0-to-f methods. However, the force exerted by the parent ion onto the electron during the ATI process leads to a shift of the measured CEP from its actual value. To obtain absolute CEP values with a *phase-meter* this shift, thus, needs to be calibrated. It has been shown that for ATI electrons emitted from argon (with a certain minimum energy) by circularly polarized laser pulses such calibration is possible by comparison to ATI spectra obtained by CTMC simulations that take the influence of the parent ion into account [287]. CEP-tagging with a phase-meter, thus, allows for offset-free CEP-measurements.

3.2 Two- and multi-color waveform synthesis

The previous Section discussed how the sub-cycle evolution of the laser electric field of few-cycle pulses can be determined by gaining control over their CEP. Although the difference in the shape of the field between $\varphi_{\mathrm{CE}} = 0$ and $\pi/2$ is quite small, this small difference can lead to comparably large effects during the interaction of such fields with matter. This is because of the strongly nonlinear character of the interaction of intense pulses with matter. Chapters 6 to 8 will discuss several examples where the CEP strongly affects the outcome of the interaction of few-cycle pulses with atoms and molecules. Although for some applications the CEP is an important pulse parameter also for longer pulse durations (as we will see in the following), it is the CEP-dependent breakage of the symmetry of the laser-matter interaction that is in the end responsible for observing CEP-effects with few-cycle pulses. This asymmetry in the interaction progressively averages out when the pulse duration in number of laser-cycles increases and eventually vanishes completely. However, CEP-controlled few-cycle pulses are not the only waveforms that can break the symmetry of the light-matter interaction process. In fact, even stronger symmetry-breaking can be induced with pulses whose waveform is not asymmetric with respect to their envelope, but instead on the basis of a single laser cycle. If the shape of each and every laser cycle shows asymmetry, then the overall asymmetry becomes independent of the number of cycles and also long, multi-cycle laser pulses can be used for control of dynamical processes with the shape of the laser field. Such waveforms can be obtained by coherently combining laser pulses with different colors and with adjustable relative phases, a concept that can be called *waveform synthesis*. This Section shall briefly review the most important concepts for obtaining linearly polarized tailored strong laser fields by waveform synthesis, see sketches in Fig. 3.2 for an overview.

Two-color pulses

The simplest type of waveform synthesis is coherent superposition of a linearly polarized laser pulse with its second harmonic pulse,

$$E(t, \Delta\varphi) = F_{\omega}(t)\cos(\omega t + \varphi_{\mathrm{CE}}) + F_{2\omega}(t)\cos(2[\omega t + \varphi_{\mathrm{CE}}] + \Delta\varphi), \tag{3.9}$$

where $\Delta\varphi$ is the relative phase between the two pulses, cf. Fig. 3.2(a) Here we consider ω and 2ω pulses that consist of multiple cycles and exhibit a bandwidth significantly less than an octave such that the two spectra do not overlap. Such pulses, usually called $\omega/2\omega$ pulses, have been applied in strong-field experiments for almost thirty years[279–281,309]. Generation of the pulse at 2ω can be straightforwardly done by second harmonic generation (SHG) in a suitable nonlinear crystal. By variation of $\Delta\varphi$ the waveform $E(t, \Delta\varphi)$ can be varied from an asymmetric shape of the laser-cycle for $\Delta\varphi = 0$ over a symmetric shape at $\Delta\varphi = \pi/2$, and for $\Delta\varphi = \pi$ the waveform becomes inverted, i.e., $E(t, \Delta\varphi = \pi) = -E(t, 0)$. Two schemes for variation of $\Delta\varphi$ are possible: Using an in-line geometry, or with the help of an interferometer. In the in-line geometry $\Delta\varphi$ can be varied by introducing adjustable amounts of transparent material into the combined beam. Variation of the amount of material results in adjustment of $\Delta\varphi$ due to the difference in phase and group velocity within this material at the two frequencies. Using an interferometer the two pulses are spectrally separated and recombined. Fine variation of the path length between the two arms results in tuning of $\Delta\varphi$.

An important property of SHG is that both the carrier frequency and CEP are doubled, see (3.9). Thus, even if the CEP of the fundamental beam at ω is evolving from pulse to pulse, the relative phase of the two colors stays constant and the shape of the field's cycle is independent of the CEP of the fundamental pulse. The only effect of a freely evolving CEP of the fundamental pulse is that the combined waveform slips under the pulse envelope, which for long pulses is irrelevant. More generally even, this convenient property holds for any case of sum frequency generation or n^{th} harmonic generation. This can be seen if we write the two-color waveform in the form

$$E(t, \Delta\varphi) = F_{\omega_1}(t)\cos(\omega_1 t + \varphi_{\mathrm{CE}}) + F_{\omega_2}(t)\cos(\alpha\omega_1 t + \beta\varphi_{\mathrm{CE}} + \Delta\varphi). \tag{3.10}$$

For $\alpha = \beta = 2$ the $\omega/2\omega$-case is recovered. For nth harmonic generation $\alpha = \beta = n$. Thus, the slippage of the waveform under the pulse envelope with the CEP of the ω_1-pulse takes place for

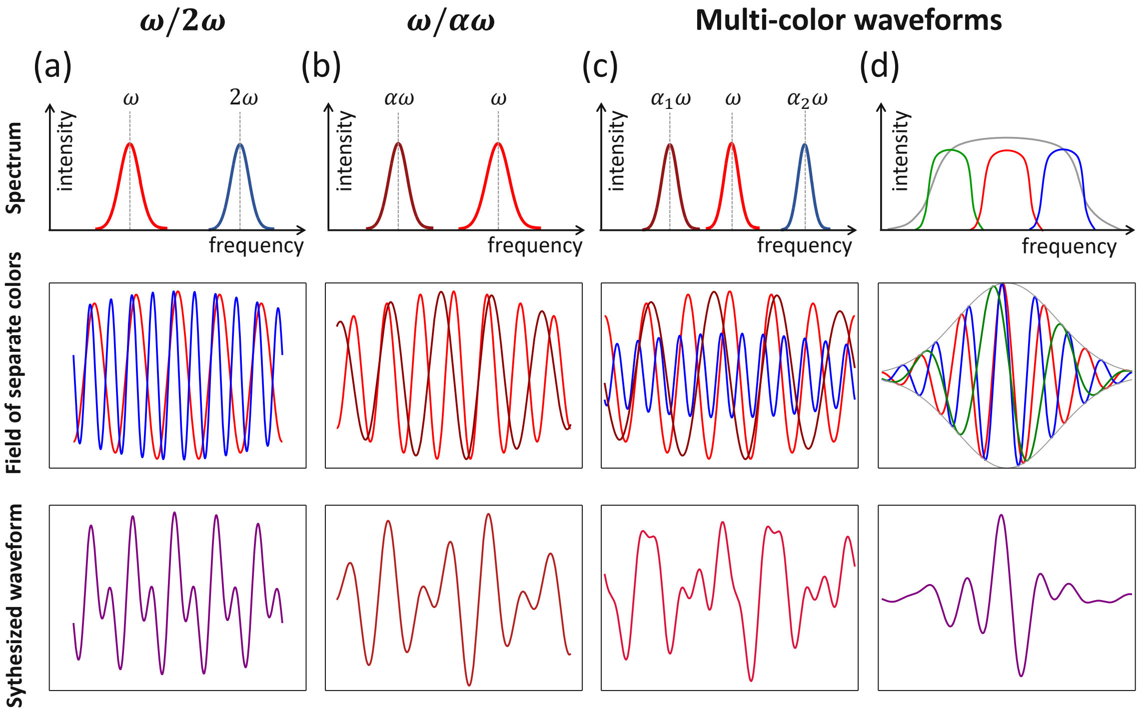

Figure 3.2: Concepts of waveform synthesis for obtaining tailored strong laser fields. Depicted are the coherent superposition of two laser spectra with integer (a) and non-integer frequency ratios (b), and the synthesis of pulses with three separated spectra (c) or frequency bands derived from one broad spectrum (d). The top row sketches the spectra of the coherently combined pulses, the center row depicts several cycles of the corresponding laser fields (encoded in color to match the spectra), and the bottom row shows the laser waveforms generated by coherently combining these laser fields. The frequency ratios and phases φ of the fields shown in the center row are (a) ω (red) and 2ω (blue); $\varphi_\omega = 0$ and $\varphi_{2\omega} = 0.4\pi$, (b) ω (red) and $2/3\omega$ (dark red); $\varphi_\omega = 0$ and $\varphi_{2/3\omega} = 0.5\pi$, (c) ω (red), $2/3\omega$ (dark red), and 2ω (blue); $\varphi_\omega = 0$, $\varphi_{2/3\omega} = 0.5\pi$, and $\varphi_{2\omega} = 0.8\pi$, (d) ω (red), 0.6ω (green), and 1.25ω (blue); $\varphi_\omega = 0.2\pi$, $\varphi_{0.6\omega} = 0.4\pi$, and $\varphi_{1.25\omega} = 0.3\pi$.

both waveforms (as for the case $\alpha = \beta = 2$) such that the relative phase between the two colors is preserved.

Waveform synthesis with non-integer frequency ratios

More complicated tailored waveforms than those obtained by $\omega/n\omega$ pulse-synthesis discussed in the previous paragraph can be generated by coherent combination of two pulses whose spectra exhibit non-integer center frequencies[‡]. As before, we consider two pulses that consist of multiple cycles and exhibit well separated spectra, see Fig. 3.2(b). Waveforms composed of spectra with non-integer center frequencies feature complex cycle-shapes with a non-trivial repetitive pattern which

---

[‡] In the literature of ultrafast photonics, often the term non-*commensurate* is used to state that two frequencies exhibit a non-integer frequency ratio, e.g. in Refs. [302, 310]. Two non-zero real numbers a and b are said to be commensurate if a/b is a rational number. Then, a and b can be written as $a = mc$ and $b = nc$ with $c \in \mathbb{R}$ and $m, n \in \mathbb{N}$. Thus, a ruler, marked off in units of length c, can be used to measure out both a line segment of length a, and one of length b[311]. According to this strict mathematical definition, almost all frequency ratios used in practice (e.g., 2/3, 1.253, etc.) would actually be commensurate (only frequency ratios of irrational numerical value are non-commensurate). To avoid confusions we will therefore avoid the term *(non-)commensurate* altogether and will instead throughout use the term *non-integer* for characterizing the ratio of two frequencies $\omega_a/\omega_b \notin \mathbb{N}$.

in particular can be applied to the improved generation of XUV/X-ray or THz pulses[26,312–314], as will be discussed in detail in Sections 4.1 and 4.3.

To generate a waveform from two pulses that exhibit an arbitrary tunable frequency ratio α in (3.10), optical parametric amplification (OPA) can be used, for example seeded by a white light super continuum[26,315,316]. In this scheme the CEP of the amplified signal pulse is inhereted from that of the pump pulse[23,24] and $\beta = 1$, independent of the tunable α. Thus, the relative phase between the two colors is affected by the CEP-slippage of the seed pulse. In order to get a reproducible shape of the coherently combined waveform, active stabilization of the CEP of the pump and signal pulses of the OPA is necessary. However, since the seed for the signal pulse is derived from the pump pulse, it is enough to stabilize the CEP of the driving laser in order to get all the waves of the OPA phase-locked together. Similar considerations and the necessity to stabilize the CEP of the pump and/or signal pulses also arise in different OPA schemes for coherent waveform synthesis[28,29,312,313,317].

Multi-color waveform synthesis

The generation of very complex waveforms with a large freedom to engineer the shape of the cycle requires a very large coherently locked bandwidth of optical frequencies and tunability of the frequencies of the separate spectral components. Such large bandwidth in excess of two octaves requires the coherent combination of multiple spectra associated with multiple pulses, for example the pump, signal and idler pulses in an OPA scheme, and possibly additional pulses derived from them by sum-frequency generation. Coherent combination of three, four or even more of such pulses with an OPA multi-pulse waveform synthesizer, an example of which is shown in Fig. 3.2(c), provides ample possibilities to adjust their relative phases (on top of the CEP of the fundamental pulse). In combination with tunability of the frequencies of the signal and idler pulses this allows very fine adjustment of the tailored output waveform and the generation of cycle shapes that may exhibit large slopes and dominant features or spikes that markedly stick out from the rest of the cycle evolution. With such freedom to shape the laser cycle it becomes possible to engineer waveforms capable of driving electronic wavepackets on very specific trajectories with the aim of optimizing, e.g., the HHG process[26,318] as will be discussed in detail in Section 4.1.

Waveform synthesis with multiple pulses and coherently locking their spectra to obtain a large combined bandwidth with the aim of generating strong tailored waveforms of almost arbitrary shape for pulse generation in the X-ray and/or THz regime is currently an important route of research[26,28,29,315–317,319]. It has been shown that waveforms generated by coherent combination of multi-cycle pulses with carefully chosen frequencies can confine the interaction with matter to dominantly the central cycle of the waveform[312–314], which for certain applications such as HHG effectively makes them equivalent to a single-cycle laser pulse. For some applications it might, however, still be necessary to generate waveforms that consist of only one or few repetitions of the combined-waveform cycle. This is possible by coherent combination of few-cycle pulses[28,29,317]. This approach can generate waveforms with peaks of sub-femtosecond duration for which the name *light transients* has been suggested[27,320]. Such light transients have been generated by coherent combination of few-cycle pulses that are obtained by spectral division of a very broad continuum spectrum[27,320]. As depicted in Fig. 3.2(d), a broadband spectrum is divided into different spectral portions. Subsequently, each of these portions are compressed to few-cycle durations. Coherent combination of these separate few-cycle pulses may result in a sub-femtosecond light transient. While it is difficult to scale this approach to high pulse energies, energetic light transienst might be generated by waveform synthesis of few-cycle pulses generated by OPA schemes[28,29,317].

3.3 Two-dimensional waveform synthesis

Section 3.2 described how waveform synthesis using laser pulses of different colors can be used for generating strong cycle-shaped laser fields with almost arbitrary evolutions. With such laser fields it becomes possible to precisely control the sub-cycle timing of the emission of electrons by field-ionization and to drive them on designed trajectories that are highly optimized for a particular application such as the generation of attosecond pulses by HHG[26,314] or the enhancement of interference structures in electron spectra[226]. Many important applications, e.g., HHG, NSDI, or laser-induced electron diffraction[252,255], which we will discuss in more detail in Section 6.2.4, build on electron recollision. From what we were discussing in Section 2.2.2, we know that electron recollision necessitates linearly polarized light. Already for small values of the ellipticity of light of a certain frequency ω_0, emitted electrons are spiralled away on trajectories given by (2.15) and recollisions are inhibited[231].

Thus, it seems that only linearly polarized is useful for recollision-based applications. For laser light of a given frequency ω_0 this is indeed the case, and recollisions are restricted to occur exclusively along the laser polarization direction and from the same direction the electron wavepacket was initially ejected. It was shown, however, that using pulses consisting of two different colors the trajectories of field-ionizing electron wavepackets can be shaped in space with great flexibility, such that recollisions can occur from different directions. Two different schemes, both offering different advantages, for superposing pulses with different colors have been introduced as will be discussed in the following, also cf. Fig. 3.3.

3.3.1 Orthogonally polarized two-color fields (OTC)

The possibility of steering attosecond electron wavepackets in time and space using OTC fields was suggested by the author based on classical trajectory simulations[234,235]. Since then, OTC pulses have been applied in a large number of works based on HHG[236,237,321–325] or electron/ion detection[151,189,326–331]. A selection of these works and the possibilities opened up by the use of OTC pulses will be discussed in detail in Section 6.1.2.

OTC pulses consist of two linearly polarized laser pulses of two different colors that are superposed orthogonally with each other such that the combined laser electric field in the polarization plane xz can be written as

$$\begin{aligned} E_x(t) &= E_{0,x} f_x(t) \sin(\omega_x t + \varphi_{\mathrm{CE},x}) \\ E_z(t) &= E_{0,z} f_z(t+\Delta t) \sin(\kappa[\omega_x (t+\Delta t) + \varphi_{\mathrm{CE},z}]), \end{aligned} \tag{3.11}$$

with ω_x the laser frequency and $E_{0,x}$ the peak electric field strength, both in x-direction, $\varphi_{\mathrm{CE},x}$ and $\varphi_{\mathrm{CE},z}$ are the carrier-envelope (CE) phases in x and z direction, and $\kappa = \omega_z/\omega_x$ is the frequency ratio between the two linearly polarized pulses in x and z, respectively. The pulse envelopes are given by $f_{x,z}(t)$, and Δt denotes a time-delay between the pulse in z and the one in x. Pulses of two different frequencies in x and z can be generated using nonlinear frequency conversion techniques as discussed in Section 3.2.

A frequency ratio $\kappa = 2$ can be obtained straightforwardly using second-harmonic generation, which is the case used in most works so far. Two approaches for generating OTC pulses are common; either using an in-line configuration or with an interferometer. In the in-line configuration the fundamental and second-harmonic pulse propagate through the same pieces of optics. The different group delays experienced by the two colors must be compensated for by using birefringent plates such that Δt in (3.11) is a value suitably close to zero ensuring temporal overlap of the two pulses at their peaks. The sub-cycle evolution of the laser electric in the polarization plane can be controlled by adjusting the overall phase difference between the two fields

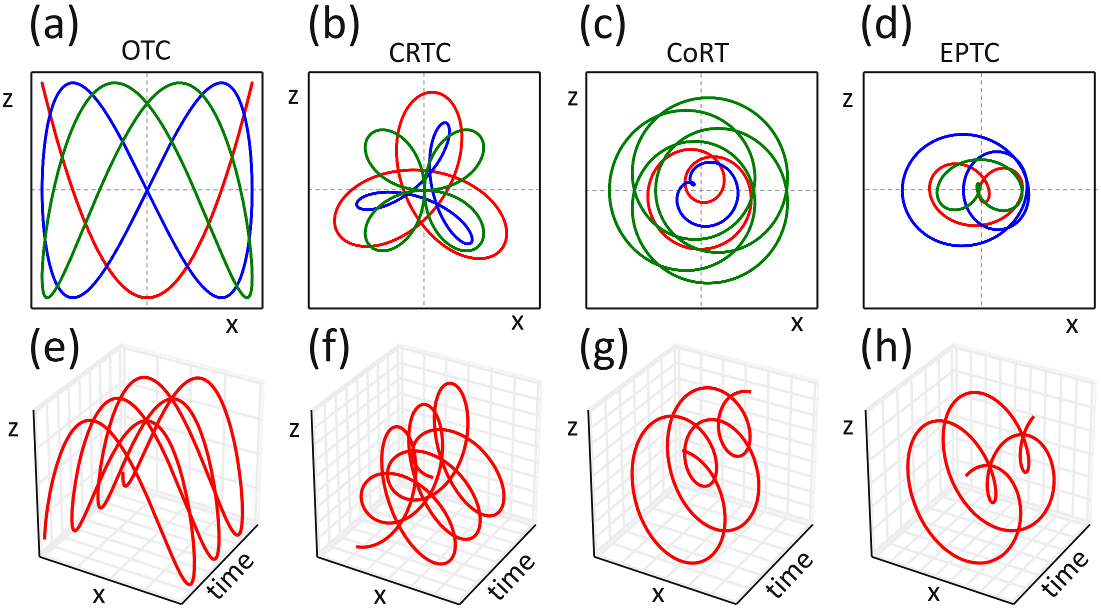

Figure 3.3: Two-dimensional waveform synthesis. The columns visualize the electric fields of four different waveforms. (a) OTC, orthogonal two-color; (b) CRTC, counter-rotating two-color; (c) CoRTC, co-rotating two-color; (d) EPTC, elliptically polarized two-color. The top row depicts the evolution of the electric field vectors in the laser polarization plane for different frequency ratios, relative phases and intensity ratios. The bottom row shows field evolutions over time (for one of the cases depicted in the corresponding panels in the top row). The parameters of the depicted OTC fields in (a) are ω along x, 2ω along z; equal intensities of the two colors; $\Delta\varphi = 0/0.5/0.8\pi$ for red/blue/green. The waveform in (e) corresponds to the green shape in (a). The red, blue and green CRTC field evolutions in (b) are generated by two counter-rotating circularly polarized fields 1 and 2 with the following parameters, respectively: $\omega_2 = 2\omega_1$, $\omega_2 = 2\omega_1$, $\omega_2 = 3\omega_1$. Their intensities I_1 and I_2 are related as: $I_2/I_1 = 1.5, 0.8, 1$. The relative phases are $\Delta\varphi = 0.6\pi$, 0.8π, π. The waveform in (f) corresponds to the red shape in (b). The red, blue and green CoRTC field evolutions in (c) are generated by two co-rotating circularly polarized fields 1 and 2 with the parameters: $\omega_2 = 2\omega_1, \omega_2 = 2\omega_1, \omega_2 = 4\omega_1$. Their intensities I_1 and I_2 are related as: $I_2/I_1 = 1.5$, $0.6, 3$. Their relative phases are $\Delta\varphi = 0.6\pi, 0.2\pi, \pi$. The waveform in (g) corresponds to the red shape in (c). The red, blue and green EPTC field evolutions in (d) are generated by two fields 1 and 2 with $\omega_2 = 2\omega_1$ for all cases. Their intensities I_1 and I_2 are related as: $I_2/I_1 = 1, 2, 0.8$. Their relative phases are $\Delta\varphi = 0.6\pi, \pi, 1.5\pi$. The waveform in (h) corresponds to the red shape in (d).

$\Delta\varphi = \varphi_{\mathrm{CE},x} - \kappa(\omega_x \Delta t + \varphi_{\mathrm{CE},z})$ by introducing small amounts of suitable glass into the beam path. In the interferometer-based configuration the fundamental pulse is split into two portions, the second color is generated in one arm of the interferometer, and the two pulses are recombined with a certain controllable phase-delay $\Delta\varphi$. The former configuration is quite robust against mechanical vibrations, while the latter needs active mechanical stabilization of the interferometer.

Tuning of the phase-delay between the two pulses results in variations of the two-dimensional evolution of the laser electric field within the polarization plane, see Figs. 3.3(a) and 3.3(e). By virtue of (2.8), i.e., $\boldsymbol{p}^{\infty} = -\boldsymbol{A}(t_i)$, the contributions of wavepackets emitted at certain times t_i can be observed in different regions within the emerging two-dimensional electron momentum distribution. This mapping can be exploited for performing measurements on sub-cycle times[151]. At the same time the recolliding electron trajectories can be finely shaped by tuning $\Delta\varphi$, and it is possible to control (within certain limits) the travel time of a certain trajectory $\tau = t_r - t_i$ between emission and recollision, the angle between the emission and recollision direction, and also the range of recollision energies[234]. These quantities are, however, not independent of each other and are in fact locked to each other on a sub-cycle time scale by the laser field, a property which in turn can be exploited for measurements and control of HHG, NSDI, etc.[236,237]. Examples of opportunities opened up by OTC pulses for measurements and recollision control can be found throughout this thesis, for example in Sections 6.1.2 and 7.2.

3.3.2 Counter- and co-rotating circular and elliptical two-color fields

Cycle-shaped two-dimensional waveforms can not only be generated by combination of two pulses with linear polarization (as is done for generating OTC pulses) but also using pulses that exhibit circular polarization. This way counter- (CRTC) and co-rotating (CoRTC) circular two-color fields can be generated. For the former, the electric field vectors of the two circularly polarized pulses that are combined are counter-rotating in the polarization plane, for the latter they are co-rotating. Experimentally, such fields can for example be generated straightforwardly using an optical setup based on a two-color interferometer as described above for the generation of OTC pulses. A waveplate in each of the two interferometer arms ensures that the pulses of different color have circular polarization before recombination. The helicity of each of the circular pulses and therewith whether they are counter- or co-rotating can be adjusted simply by the rotation angle of the waveplate. Different CRTC and CoRTC waveforms are depicted in Figs. 3.3(b,f) and Figs. 3.3(c,g), respectively.

For applications the most important difference between the counter- and co-rotating circular two-color fields is that for the counter-rotating case the trajectories of emitted electron wavepackets may return to the parent ion, i.e., the electron wavepackets can be made to recollide, while for the co-rotating case the electron trajectories do not recollide[332,333]. Thus, for applications that build on electron recollision, such as HHG, NSDI, etc., counter-rotating circular two-color (CRTC) have to be used. For example, it has been shown recently that a CRTC field can control the NSDI process[332,334]. But also CoRTC are useful tools, e.g., for controlling molecular fragmentation reactions, see Section 8.6.2 for examples of applications.

A two-dimensional field shape that can also be synthesized from two pulses of different color, even in an in-line geometry, are elliptically polarized two-color (EPTC) pulses[335]. Similar as for elliptical light of one color, with EPTC fields recollisions are suppressed. The advantage of EPTC light is that the polarization ellipse exhibits an asymmetry with respect to zero, and this asymmetry and the helicity of the field vector rotation can be adjusted by the relative phase $\Delta\varphi$ between the colors, see Figs. 3.3(d,h). Such field shapes can be used to study the phase-dependent directional dissociative ionization of molecules[336,337], see Section 8.6.2 for examples of applications and results.

Let us return to CRTC fields and discuss a few properties and applications of them in greater detail. For such fields the electric field vector performs rotations in the polarization plane such that it forms symmetric petals whose number is defined by the frequency ratio of the two pulses (for integer ratios n the number of petals is $n+1$), see Fig. 3.3(b). As the number of petals determines the number of possible recolliding trajectories, recollisions can occur from different directions within the polarization plane. The intensity ratio of the two pulses determines at what distance the electric field misses the zero value during its rotation, i.e., determines the center-opening of the petal shape. A very interesting property of CRTC fields is that a change in the relative phase between the two colors, $\Delta\varphi$, simply results in a rotation of the petal shape; the overall field-shape in the polarization plane is unaffected by a phase-shift, though. This property is convenient for example in HHG, where over extended distances a phase-shift between the two colors could be introduced during propagation of the pulses in the generation medium[338].

CRTC fields were in fact introduced already in 1995 by Eichmann et al. in the context of the generation of circularly polarized light in the XUV/soft X-ray wavelength range using HHG[232]. Since then this application has been extensively studied experimentally[338–341] and theoretically[233,342–347]. The generation of circularly polarized harmonics by HHG with CRTC pulses can be explained by arguments based on the conservation of energy and spin angular momentum of the laser and HHG photons[339]. Since the photons of the two counter-rotating circularly polarized laser pulses carry spin angular momentum, they can add up in large numbers to generate XUV/soft X-ray photons that carry a net spin angular momentum, i.e., result in harmonics with a net circular polarization.

Circularly polarized XUV/soft X-ray light can be used to probe the magnetic state of a sample[341], which is an application of high practical relevance. Generation of circularly polarized XUV/soft X-ray pulses is therefore an important problem in ultrafast intense laser science. Several schemes have been proposed and implemented, the application of CRTC pulses being one of the most heavily studied ones. The author has also proposed a method for the generation of circularly polarized XUV/soft X-ray pulses[348]. This method that is based on exploiting initial states with a net angular momentum can, in contrast to existing schemes based on CRTC pulses, also generate isolated attosecond pulses with circular polarization. A more detailed discussion of the problem of generating circularly polarized XUV/soft X-ray pulses will be provided in Section 4.2.

4

Generation of secondary radiation with tailored strong laser fields

Chapter 3 discussed different methods for the generation of strong tailored waveforms. The availability of such waveforms opens up the generation of radiation with intriguing properties in wavelength ranges, where it is difficult to generate radiation by other means due to the lack of suitable materials. These wavelength ranges are those with very small photon energy in the THz frequency range, and with very high photon energies in the XUV and X-ray regime. As both types of radiation, THz and XUV/X-ray, are generated by (down- respectively up-) conversion of photons from the tailored laser waveform to lower respectively higher frequencies, these types of radiation are often referred to as *secondary*.

Generation of pulses in the XUV/X-ray regime by the process of HHG is one of the most frequently explored applications of strong laser fields and constitutes one of the forefronts of research in attosecond physics. See recent reviews and references in them for a comprehensive overview over this field[8,30,33,285,349,350]. Using strong tailored waveforms for driving the HHG process enables to produce XUV/X-ray pulses with great flexibility and very specific properties, as will be discussed in Sections 4.1 and 4.2.

The research on the generation of THz-waves with strong laser fields—despite the importance of such waves for applications, e.g., in scanning, imaging and probing of dynamics in semiconductors—has, until recently, not received equal attention as that on XUV/X-ray pulse generation. However, with the recent possibilities to generate strong multi-color waveforms, this application has shifted into the focus of attention. Section 4.3 will briefly discuss a few examples of THz-generation with strong tailored waveforms.

4.1 Attosecond XUV and X-ray pulse generation

Generation of XUV/X-ray radiation by the process of HHG—driven by the prospect of obtaining probe pulses for electronic dynamics in atoms, molecules, solids, etc.[31–33,35,284,351,352]—has ever since the discovery of the HHG conversion-process focused on its optimization with respect to the following parameters: (i) isolation of a single pulse from the pulse-train generated by HHG, (ii) decrease of the duration of these pulses to the atomic unit of time and beyond, (iii) increase of the XUV/X-ray pulse energy, (iv) generation of pulses at high photon energies (100's of eV to keV) for reaching atomic absorption edges, (v) generation of attosecond XUV/X-ray pulses with polarization states different from linear. The optimization of all these parameters benefits from the use of tailored waveforms. In this Section we will discuss selected works to exemplify how tailored waveforms can be applied to the generation of isolated XUV/X-ray pulses with high pulse energies and with adaptable photon energies. Section 4.2 will show examples that concern point (v).

The generation of isolated XUV/X-ray pulses can essentially be boiled down to the problem of selecting a single pulse out of the train of pulses that is generated by HHG even with few-cycle pulses. A number of methods for the selection of one pulse, often referred to as *gating*, have been invented and are now applied successfully in experiments. The most frequently used methods are based on gating in the spectral domain, called *amplitude gating* or *cut-off selection*[168,353,354,355], gating by shaping the evolution of the polarization state of the drive laser pulse, called *polarization gating*[356–358], or gating in the time-domain by directly shaping the evolution of trajectories of recolliding electron wavepackets in time and space. Tailored waveforms are particularly suitable for the latter type of gating.

$\omega/2\omega$ pulses As discussed in Chapter 3, the simplest method for tailoring the laser waveform is to coherently add a second-harmonic pulse to the fundamental pulse, thereby obtaining the so-called $\omega/2\omega$ pulses. Already a small 2ω-component breaks the symmetry of the HHG process and leads to the generation of not only odd but also even harmonics. Thus, XUV/X-ray pulse-trains with a temporal spacing of twice the temporal separation, i.e., T instead of $T/2$, between the pulses can be generated[359], where $T = 2\pi/\omega$ is the laser oscillation period of the fundamental carried at frequency ω. The twice increased temporal spacing of the pulses within the pulse-train makes it easier to select one of them by temporal gating, e.g., by using a polarization gate[360,361].

Two-color tailored waveforms Increasing the temporal separation between the individual pulses within the XUV/X-ray pulse train by optimization of the waveform of the strong drive laser pulse is in fact a very efficient and also scalable route for the generation of isolated, intense attosecond pulses. An increase of the temporal separation between the individual XUV/X-ray pulses beyond the oscillation period of the fundamental can be elegantly achieved with two pulses carried at frequencies ω_0 and ω_1, respectively, if their frequency ratio $\kappa = \omega_1/\omega_0 < 1$ is a non-integer number with a specifically chosen numerical value[312,313,362–364]. To see this we write the coherent superposition of the two waves in the form

$$\cos(\omega_0 t + \varphi_0) + \cos(\omega_1 t + \varphi_1) = \underbrace{2\cos\left(\frac{\omega_0 - \omega_1}{2} t + \varphi_{\text{env}}\right)}_{\text{"envelope"}} \underbrace{\cos\left(\frac{\omega_0 + \omega_1}{2} t + \varphi_{\text{car}}\right)}_{\text{"carrier"}}, \tag{4.1}$$

with $\varphi_{\text{env}} = \frac{\varphi_0 - \varphi_1}{2}$ and $\varphi_{\text{car}} = \frac{\varphi_0 + \varphi_1}{2}$. This shows that the coherent superposition of two waves of different colors leads effectively to a beat waveform that can be understood as the modulation of a high-frequency "carrier" wave, with a low-frequency part that can be interpreted as the "envelope" of multiple sub-pulses. This is visualized in Fig. 4.1(a) for the example of combining two laser pulses with wavelengths 800 nm and 1300 nm in comparison with a 5 fs-pulse at 800 nm. It can be seen that, indeed, the two-color waveform closely resembles a train of pulses consisting of multiple sub-pulses ("envelopes") determined by the difference-frequency term, and a fast oscillating "carrier" determined by the additive term. The temporal spacing between the multiple sub-pulses is determined by the beat period of the two waveforms and is $2\pi/(\omega_0 - \omega_1)$. Additionally, the field-evolution within the sub-pulse resembles that of a much shorter, near single-cycle pulse.

The peak field strength of the sub-pulses decreases with their distance from the peaks of the two coherently combined laser pulses with ω_0 and ω_1 due to their respective pulse envelopes, as given by their durations τ_0 and τ_1, respectively. For the generation of isolated XUV/X-ray pulses with a waveform given by (4.1), the ratio of the combined carrier frequency $\frac{\omega_0 + \omega_1}{2}$ to the duration of the sub-pulses is an important parameter. The latter parameter is determined by the beat period. If the duration of each sub-pulse is roughly only one cycle of the carrier wave, only one dominant

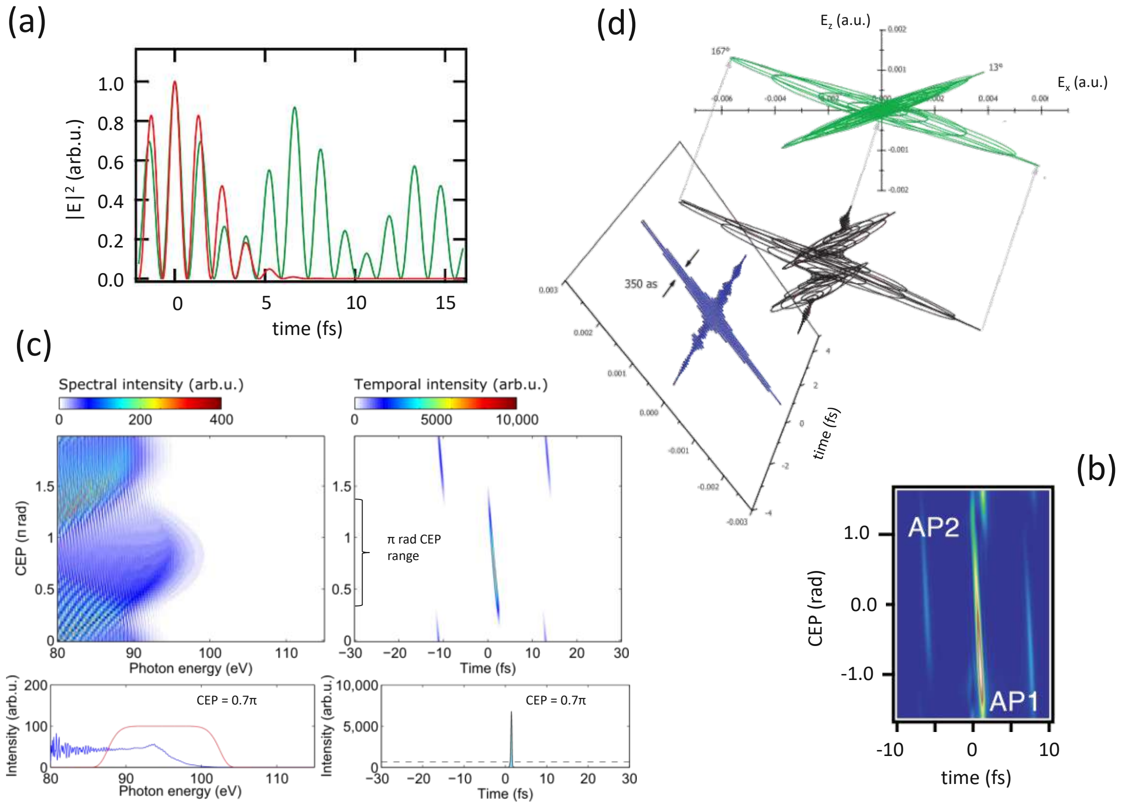

Figure 4.1: Attosecond pulse generation with tailored waveforms. (a) The green line shows the square of the laser field obtained by the superposition of two laser pulses with wavelengths 800 nm and 1300 nm in comparison with a 5 fs-pulse at 800 nm (red). The phases of the pulses are as follows: in the synthesized waveform the CE-phase of the 800 nm pulse is $\varphi_{\mathrm{CE}} = 0.15$ rad and the 1300 nm exhibits a relative phase $\Delta\varphi = 0$ rad to the 800 nm pulse. The CE-phase of the 5 fs-pulse at 800 nm is 0. (b) Attosecond pulses (AP) generated with the green waveform from (a) as a function of the CEP of the 800 nm pump pulse. Panels (a) and (b) are adapted from Ref. [313]. (c) Simulated high-harmonics generated with a three-color pulse consisting of wavelengths 1.44 µm, 1.03 µm, and 0.515 µm as a function of the CEP of the 1.03 µm pump pulse (top left). Spectral selection leads to an isolated attosecond pulse carried at a center photon energy of roughly 95 eV for a large range of CEP-values. Adapted from Ref. [314]. (d) Attosecond pulse generation with an OTC field, see text for details. Adapted from Ref. **[237]**.

XUV/X-ray pulse with high photon energy will be generated per sub-pulse. If additionally the delay between the sub-pulses is large enough and the pulse envelopes determined by $\tau_{0/1}$ have sufficiently decayed during this time such that ionization and electron acceleration during the next sub-pulse is negligible, effectively only one pulse will be generated by the combined waveform (4.1). The parameter

$$N = \frac{\omega_0 + \omega_1}{\omega_0 - \omega_1} = \frac{\omega_{\mathrm{car}}}{\omega_{\mathrm{env}}}, \tag{4.2}$$

which compares the sub-pulse spacing to the combined carrier frequency in combination with $\tau_{0/1}$ can be used for a quantitative optimization of these conditions.

To generate a two-color waveform with non-integer frequency ratios where (at least) one of the two pulses has a wavelength in the mid-infrared regime, optical parametric methods as discussed in Section 3.2 can be used. Because, as discussed above, for such type of waveform synthesis the laser electric field of the pulse obtained by coherent combination depends on the CEP value of the pump-pulse (in contrast to waveform synthesis with integer frequency ratios), CEP-variations of the pump will affect the XUV pulse generation. This effect is shown in Fig. 4.1(b), which shows the dependence of the generated XUV pulse-train on the CEP of the pump[313] for the case of coherently combined pulses with wavelengths 800 nm and 1300 nm and durations of 30 fs and 40 fs, respectively, that we discussed above. Although, for a small range of CEP-values two XUV pulses are generated, for most CEPs the XUV temporal structure is dominated by only one pulse around time zero, with small satellites around ±8 fs. Using this two-color scheme with non-integer frequency ratios, Takahashi et al. recently succeeded in the generation of quasi-isolated XUV pulses at a photon energy of 30 eV similar to those in Fig. 4.1(b) with a record pulse energy of 1.3 µJ[312].

Multi-color tailored waveforms The generation of isolated XUV/X-ray pulses using tailored waveforms can be further refined by extending the scheme described above for the case of two coherently combined pulses to the multi-color case. The combination of multiple pulses with different colors was discussed in Section 3.2. By the coherent superposition of multiple laser fields of different colors strong tailored waveforms with stunningly complicated field-evolutions can be generated. Recently, Haessler et al. coherently combined three different colors derived from an Yb-laser system by optical parametric methods (1.5 µm, 1.0 µm, and 0.5 µm)[26]. The CEP of the pump laser was stabilized. In that work, a waveform that resembles the *perfect wave* for HHG[318] was generated by adjusting the relative phases of all three colors. The *perfect wave* optimizes the trajectory of the recolliding electron wavepacket with respect to optimal conditions for HHG. Such a trajectory should have small excursion amplitude in order to minimize wavepacket spreading for a high recombination cross-section, and should nevertheless return to the ion with a high recollision energy. It could be shown that a drive laser field whose cycle-shape resembles a triangle, offset from zero, optimizes these requirements[318]. Hässler and co-workers implemented this scheme experimentally and could show that the experimentally generated ”perfect wave” indeed leads to a strong increase of both the high-harmonic cut-off energy and XUV flux[26]. They observed an increase of about 140 times within the photon energy range 55-65 eV as compared to the single-color pulse at 1.5 µm.

From the periodicity of the harmonics in the measured HH spectrum[26] and from simulations it could be inferred that with the three-color tailored waveform a single attosecond pulse per 10.3-fs period is formed. Thus, by multi-color waveform synthesis the sub-pulse spacing (and therewith the periodicity of the XUV pulse-train) can be enormously increased as compared to the case of two-color synthesis described by (4.1). Simulations have indeed shown[314] that by the coherent combination of three colors and careful optimization of their frequency ratios, relative phases and intensities an isolated attosecond XUV pulse can be generated with an Yb laser system and drive pulse durations as long as 180 fs. Fig. 4.1(c) shows the results of these simulations for a combination of pulses with wavelengths and 1.44 µm, 1.03 µm, and 0.515 µm as a function of the CEP of the pump pulse. Spectral selection leads indeed to an isolated attosecond pulse carried at a center photon energy of roughly 95 eV for a large range of CEP-values.

Multi-color light transients As outlined in Section 3.2, multi-color waveform synthesis with few-cycle laser pulses of different colors can generate pulses that may be seen as the optical analogue of half-cycle pulses with nanosecond duration generated by electronic circuits used for steering Rydberg electron wavepackets[365]. Similar to those nanosecond pulses, the optical tailored waveforms can be generated such that they feature only one dominant peak of the laser electric field within the duration of the constituent few-cycle pulses. In contrast to the nanosecond pulses this peak may, however, exhibit a sub-femtosecond duration[27,29,317,320]. Thus, the name *light transients* was suggested for this type of tailored waveforms. Although these waveforms have so far only been generated with lower pulse energies than those obtained by coherent combination of multi-cycle pulses, high-harmonics could still be generated with them[27,46,366]. In these experiments the main purpose of generating high-harmonic radiation with light transients was, however, not the production of XUV/X-ray beams for further applications, but rather to obtain insight into the electronic dynamics underlying their generation by analysis and careful interpretation of the emitted HH radiation. This approach for studying electronic dynamics will be discussed in greater detail in Chapter 7. HHG with light transients has for example been used to study attosecond electronic dynamics in krypton atoms[366] or in solid SiO_2[46].

Two-dimensional tailored waveforms Isolation of a single attosecond XUV pulse from a train of pulses is also possible with two-dimensional tailored waveforms introduced in Section 3.3. As an example, Fig. 4.1(d) shows a method suggested by the author that uses a few-cycle OTC pulse for this purpose[236,237], also see **Paper 2** and **Paper 3**. The few-cycle pulse leads to the emission of only three main ionization bursts. Owing to the two-dimensional field-evolution of the OTC pulse, the electron wavepackets emitted during these three bursts are driven on two-dimensional trajectories that return to the parent ion under an angle that is different from their emission angle. Two of these trajectories return from the same side and under the same angle, whereas the wavepacket emitted during the strongest burst recollides under a different angle from the opposite side with the parent ion. In HHG from spherically symmetric systems such as atoms the recollision angle determines the polarization direction of the emitted HH radiation. Therefore, the XUV burst generated during the recollision of the strongest burst is polarized under a different angle than the two other bursts. By passing the XUV radiation through a suitable polarizer the two weaker pulses can be filtered away and the strongest XUV burst can be extracted, i.e., an isolated attosecond pulse can be obtained, see Fig. 4.1(d). The usage of the lossy XUV polarizer could be avoided by angle-resolved detection of photoelectrons emitted by the two-dimensional pulse train[236,237]. On a more fundamental basis, this example shows that OTC pulses establish a mapping of time into polarization. We will discuss in Chapter 7 how this mapping can be exploited for attosecond measurements. Other works have shown that high-harmonic generation with OTC pulses may also lead to stronger XUV emission[321,367].

4.2 Generation of circularly polarized XUV pulses

The table-top generation of circularly polarized XUV/X-ray pulses by HHG has been on the agenda of strong-field research ever since the discovery of the HHG process. This is due to the importance of circularly polarized XUV/X-ray fields for a number of methods that probe the properties of matter. For example, circularly polarized XUV/X-ray fields can be used for probing the electronic structure of complex systems using angle-resolved photo-emission spectroscopy (ARPES)[368], for studying the electronic origin of magnetic properties of matter using X-ray magnetic circular dichroism (XMCD)[369], or for the investigation of chirality in molecules using photoelectron circular dichroism (PECD)[370].

Unfortunately, it is not straightforward to generate circularly or elliptically polarized XUV/X-ray light by HHG, as it is difficult to impart spin angular momentum (SAM)—which is the component of angular momentum of light that can be associated with a wave's circular or elliptical polarization state—to the generated photons. Imparting SAM to the harmonic photons by simply using elliptical/circular light for driving the HHG process fails because electron recollision and therewith harmonic generation is suppressed already for quite small ellipticity, see Section 2.2.3. Thus, synchrotron radiation has been the main light source for experiments that rely on elliptical/circular XUV/X-ray light, which impedes probing dynamic processes on time-scales below about 100 fs which, however, would be required for many processes. Therefore, generation of elliptically/circularly XUV/X-ray pulses of few-femtosecond or attosecond duration generated by HHG is at the forefront of contemporary research and has been investigated intensely both experimentally[232,338–341,371–375] and theoretically[348,233,322,342–347,376–379]. For example, it has been predicted theoretically that OTC pulses can to some extent be applied for the generation of elliptically polarized XUV light[322]. Also it has been shown that molecules aligned with an angle to the laser polarization emit elliptical XUV light[375].

A method that is currently applied in many experiments builds on the use of CRTC pulses introduced in Section 3.3. This method was, in fact, introduced as early as 1995 by Eichmann et al.[232] who have produced harmonics in argon using $\omega/2\omega$ CRTC pulses generated with a Titanium-Sapphire laser system. The measured spectra were in agreement with theoretical results[233,342,379], which showed that circularly polarized harmonics can be produced with CRTC pulses. The underlying process can be understood as the generation of an XUV photon by superposition of different numbers of photons from the left respectively the right circularly polarized pulses that form the CRCT waveform, such that in total one quanta of SAM is transferred to the generated XUV photon, see the sketch in Fig. 4.2(a). Thus, intuitively, the generation of circularly polarized harmonics is possible with CRTC pulses because the petal-shaped two-dimensional evolution of the CRTC field, on the one hand, can drive electron recollisions (in contrast to circularly polarized pulses of only one color) and, on the other hand, the SAM of the drive photons can add up during the generation process.

In a more thorough way the generation of circularly polarized harmonics by CRTC fields can be understood by considering the conservation of energy and SAM during the production of a photon[338–341]. For CRTC pulses consisting of two circularly polarized pulses with frequencies ω_1 and ω_2, respectively, energy conservation dictates that the circular harmonics (denoted as ch) are observed at frequencies

$$\omega_{ch} = n_1\omega_1 + n_2\omega_2, \tag{4.3}$$

where n_1 and n_2 are the numbers of photons absorbed at ω_1 and ω_2, respectively. The conservation of SAM during the HHG process can be expressed as[339]

$$\sigma_{ch} = n_1\sigma_1 + n_2\sigma_2, \tag{4.4}$$

where $\sigma_1 = \pm 1$ and $\sigma_2 = \mp 1$ is the SAM of the photons at ω_1 and ω_2, respectively. For the generation of a circular harmonic, i.e., to obtain $\sigma_{ch} = \pm 1$, the number of absorbed photons must obviously satisfy the condition $n_1 = n_2 \pm 1$. Inserting this into the relation of energy conservation (4.3) leads to $\omega_{ch} = (n_2 \pm 1)\omega_1 + n_2\omega_2$. Thus, the HH spectrum consists of pairs of harmonics that are separated by $\omega_1 - \omega_2$, and each pair is separated from the adjacent one by $\omega_1 + \omega_2$. For the case of $\omega/2\omega$ CRTC pulses, where $\omega_2 = 2\omega_1$, it follows that $\omega_{ch} = (n_2 \pm 1)\omega_1 + n_2 2\omega_1 = (3n_2 \pm 1)\omega_1$, and harmonics $q = \omega_{ch}/\omega_1$ are observed at $q = 3n_2 + 1$ and $q = 3n_2 - 1$. Harmonics at $q = 3n_2$ are forbidden, i.e., every third harmonic is missing in the HH spectrum for $\omega_2 = 2\omega_1$. For CRTC pulses with a different frequency ratio a similar harmonic structure but with different periodicity emerges, cf. Fig. 4.2(b) which depicts a HH spectrum generated with $\omega_1 \approx 0.6\omega_2$.

An important point is the polarization state of each peak in the HH spectrum. This point can be intuitively understood for the case $\omega_2 = 2\omega_1$ for which the CRTC field shows a three-fold symmetry with a polarization rotation of 120° every $T_1/3$, where $T_1 = 2\pi/\omega_1$ is the optical cycle of the pulse at ω_1, see Fig. 3.3(b). This dynamical change in the symmetry is imparted to the harmonics, resulting in circular harmonics where peaks at $q = 3n_2 + 1$ rotate in the one and peaks at $q = 3n_2 - 1$ in the other direction. Similar considerations for different ratios ω_2/ω_1 lead to the equivalent result, i.e., the pairs of harmonic peaks exhibit opposite circularity[340,341]. Related to these symmetry considerations is the fact that, although the harmonics feature circular polarization, in the time domain the XUV field consists of linearly polarized bursts whose polarization direction is rotated according to the symmetry of the CRTC field. Thus, application of the circular harmonics for measurements necessitates a ”spectral approach” such as magnetic circular dichroism[341].

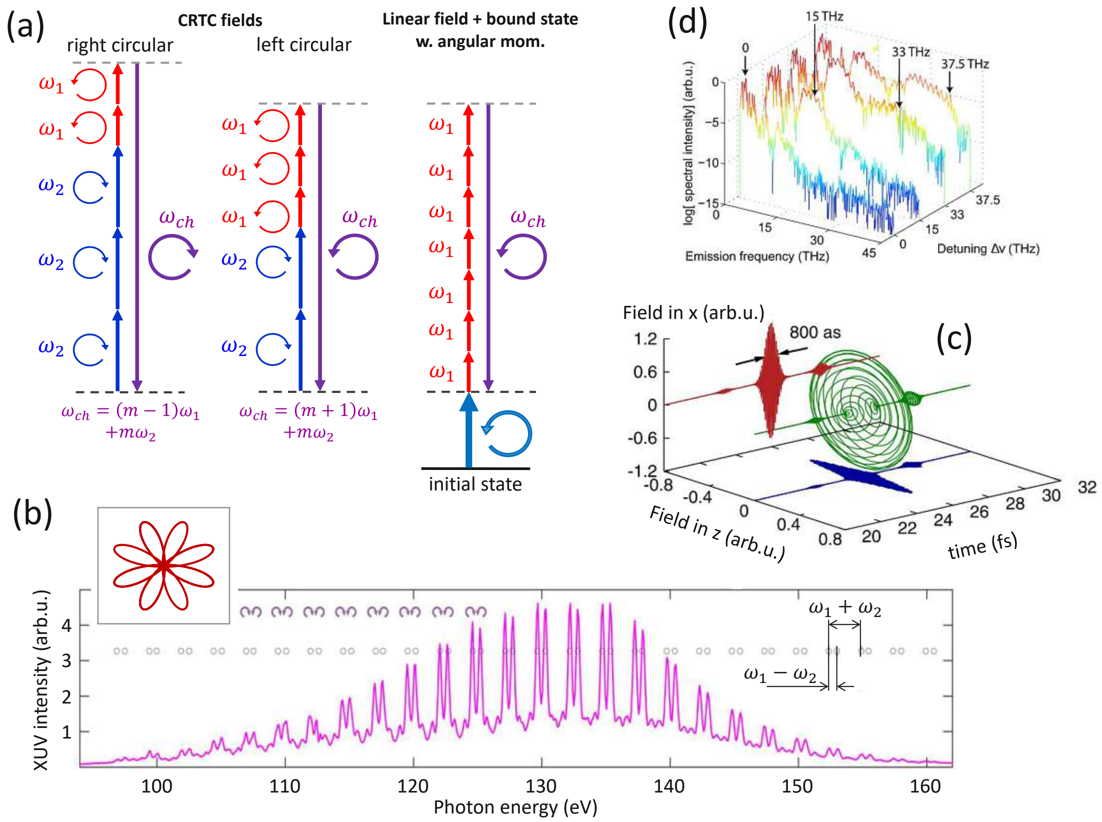

Figure 4.2: Tailored waveforms for the generation of circularly polarized high-harmonic fields and THz radiation. (a) Energy conservation during the generation of high-harmonic photons (violet) with spin angular momentum (SAM) by adding photons from the circularly polarized two colors of a CRTC field (left and center). The rightmost scheme shows the generation of high-harmonic photons with SAM by using a bound state that exhibits angular momentum[348]. See text for details. (b) Measured high-harmonic spectrum generated with a CRTC field shown in the inset. Figure adapted from Ref. [341]. (c) Isolated attosecond pulse generated with the rightmost scheme in (a). Figure adapted from Ref. [**348**]. (d) Spectra of THz pulses experimentally generated using a two-color scheme where the frequency of the second color is detuned from the ratio of 2 to the frequency of the first color by an amount given in the figure. Figure adapted from Ref. [316].

A number of works has investigated possibilities for gaining more intricate control over the production process of circular harmonics with CRTC pulses. For example it has been suggested to use molecules for HHG whose symmetry matches that of the CRTC field[347], or using phase-matching of the HHG process for enhancing one of the two polarization directions[338,341]. Production of harmonics with a specific circular polarization state and the creation of an isolated, circularly polarized XUV pulse is probably the most important goal for future research. A promising route seems HHG with few-cycle CRTC pulses in a non-collinear geometry[372].

The first work that predicted an isolated, circularly polarized XUV attosecond pulse actually used a different method, though. This method, proposed by the author and co-workers[348], suggested to use ring-current states[380] for providing angular momentum to the HHG process, see **Paper 6** for details. In short, the method works as follows: Instead of imparting SAM to the generated XUV photons by the generating laser light, as it is done when using CRTC fields, the angular momentum is first transferred to the system by any suitable method, e.g., by a (weak) circularly polarized optical preparation pulse. Then the angular momentum is ”readout” by the returning electron wavepacket in strong-field recollisions driven by linearly polarized laser light, see the rightmost sketch in Fig. 4.2(a). Thus, in this scheme one quanta of SAM imparted to the bound state by the preparation pulse is up-shifted to the XUV/X-ray regime by the HHG process, while with CRTC fields many quanta of SAM are involved in the HHG process. The functionality of the method was demonstrated by simulations[348] which predicted that an isolated circularly polarized attosecond pulse as the one shown in Fig. 4.2(c) can be obtained by this method.

4.3 THz pulse generation

Generation of ultrashort pulses in the THz frequency range is an application of intense laser pulses with increasing importance. The high relevance of THz radiation foots on the fact that it covers many important resonances in molecules (vibrational and rotational resonances) and solids (phonon and plasmon resonances, impurity transitions) and, thus, is a unique tool for probing in both fundamental research and industrial environments. In research it allows, e.g., ultrafast probing of material properties and performance of electronic devices[381] or enables biomedical sensing[382]. Applications include probing and imaging in the food and drug industry[383] or the construction of sensor devices for imaging and communication[384]. An important step in the research on THz generation with strong laser fields was the demonstration of intense THz pulses emitted from air ionized with an $\omega/2\omega$ laser field by Cook and Hochstrasser[385]. Since then this method of THz generation has been studied and applied in many works, e.g. in Refs. [386–389], motivated by its potential as a source of *intense single-cycle* THz pulses. The possibility of generating high THz fields with a large bandwidth with this method is facilitated by the fact that no (crystalline) material subject to damage is necessary.

The mechanism underlying the THz generation with $\omega/2\omega$ laser fields was initially interpreted as a parametric four-wave difference frequency mixing process[385,390]. Later experimental and theoretical work showed, however, that the THz emission can be readily understood by considering the continuum motion of electrons emitted in the strong laser field by field-ionization[315,316,386,387,391–393]. In this scheme the emission of the THz electromagnetic field from the plasma is due to the radiation of the accelerated charge of the electrons that are emitted in and driven by the laser field $E(t)$. This radiation is proportional to the derivative of the induced current density, $J(t)$, and therefore the THz field can be written as $E_{\text{THz}} \propto \mathrm{d}J(t)/\mathrm{d}t$. Classically, the macroscopic current density can be calculated as $J(t) = -\rho_e(t)v_e(t)$, with $\rho_e(t)$ the density of electrons and $v_e(t)$ the classical expectation value of the electron velocity given by (2.6). This mechanism was first described by Brunel[394] and therefore the associated radiation is usually called *Brunel radiation*[‡]. The spectrum of radiation emitted by field-driven electrons is very broad. Brunel radiation can therefore extend from the THz regime into the VUV photon energy range. Because the Brunel radiation is determined by the derivative of the macroscopic current $J(t)$, a prerequisite for observing Brunel radiation is that its symmetry is broken, i.e., that the electrons' motion exhibits a bias into a certain direction. Thus, to generate Brunel radiation, one needs asymmetric driving fields, e.g., an $\omega/2\omega$ field or a CEP-stable few-cycle pulse[393]. In a single-color periodic driving field the Brunel radiation vanishes. The necessity for symmetry-breaking of the electronic motion for THz production with the Brunel mechanism can be intuitively understood also by the near-DC spectral range of the THz radiation. To generate near-DC radiation, the electronic motion responsible for its emission should have a low-frequency or DC component, which is equivalent to a bias towards a certain direction.

The spectrum of the THz radiation generated by a tailored waveform can be obtained from a semi-classical derivation[315,316] that calculates the macroscopic emitted field from the acceleration

---

[‡] Initially Brunel aimed at describing high-harmonic radiation by this mechanism. The essential step for describing HHG, namely the recombination step is, however, not included in Brunel's derivation.

of the induced dipole moment, $E_{\mathrm{THz}} \propto \ddot{d}(t)$. The dipole velocity $\dot{d}(t)$ can be written as $\dot{d}(t) = \langle \Psi_c(t)|\hat{\boldsymbol{p}}|\Psi_c(t)\rangle$, with $\Psi_c(t)$ the wavefunction of an electron moving in the continuum and $\hat{\boldsymbol{p}} = i\boldsymbol{\nabla}$ the momentum operator. The continuum wavefunction $\Psi_c(t)$ can be expressed as a superposition of the wavepackets emitted into the continuum at times t_i and moving on classical trajectories $\boldsymbol{r}(t, t_i)$, i.e., $\Psi_c(t) = \sum_{t_i} \psi[\boldsymbol{r}(t, t_i), t]$. Using plane waves for $\psi[\boldsymbol{r}(t, t_i), t]$, the dipole velocity can be written as

$$\dot{d}(t) = \int_{-\infty}^{t} \Gamma(t_i)\bar{v}(t, t_i)\mathrm{d}t_i, \tag{4.5}$$

with $\bar{v}(t, t_i)$ the average velocity of the wavepacket $\psi[\boldsymbol{r}(t, t_i), t]$ and $\Gamma(t_i)$ the ionization rate at time t_i. From (4.5) the dipole acceleration can be calculated by taking the derivative with respect to t, which, by neglecting the small initial velocity of the wavepacket after tunneling and the influence of the ion's Coulomb potential on the motion of the wavepacket, gives

$$E_{\mathrm{THz}} \propto \ddot{d}(t) = E(t) \int^{t} \Gamma(t_i)\mathrm{d}t_i. \tag{4.6}$$

Thus, the THz emission is proportional to the driving laser field $E(t)$ multiplied by the ionization steps $\int^t \Gamma(t_i)\mathrm{d}t_i$. The spectrum of the emitted radiation is then simply given by Fourier transform of (4.6), i.e.,

$$E_{\mathrm{THz}}(\omega) \propto E(\omega) \star \mathscr{F}\left[\int^{t} \Gamma(t_i)\mathrm{d}t_i\right](\omega). \tag{4.7}$$

Equ. (4.7) reveals that the spectrum of the emitted THz radiation is determined by the convolution of the laser field spectrum and the spectrum of the ionization steps.

This result shows that the spectrum of the generated THz radiation can be controlled by variation of the spectrum of the tailored drive laser field. Fig. 4.2(d) shows an example where this has been exploited for shaping the spectrum of THz radiation created in ambient air with a tailored two-color $\omega_s + \omega_p$ driving field[315,316]. The two pulses used for this waveform were the signal (s) and pump (p) pulse of a near-degenerate optical parametric amplifier driven by an actively CEP-stabilized Yb:KGW regenerative amplifier system. The wavelength of the pump pulse was $\lambda_p = 1030\,\mathrm{nm}$, the signal wave was tunable in the range $\lambda_s = 1800 - 2100\,\mathrm{nm}$. Because the two colors used for the waveform synthesis exhibit non-integer frequency ratios, stabilization of the CEP is essential, as discussed in Section 3.2. If the CEP-locking is turned off, the THz waveform measured by electro-optic sampling vanishes[316]. Fourier transform of the measured THz waveforms leads to the spectra shown in Fig. 4.2(d). In agreement with (4.7) it can be clearly seen in these spectra for various values of the signal wavelength $\omega_s = (\omega_p + \Delta\nu)/2$, that detuning the optical parametric amplifier by $\Delta\nu$ from the degeneracy point, leads to a significant change of the generated THz spectral range.

This shows that tailored waveforms can be used for THz production with tunable properties. Thanks to the enormous recent progress in waveform synthesis with energetic laser pulses (Section 3.2), and motivated by the high practical importance of this type of radiation, the production of short THz pulses with high peak powers and tunable spectrum from gas plasmas by the Brunel mechanism outlined above has become a very active field of research. Because the conversion efficiency from the optical to the THz regime is small, the availability of energetic tailored waveforms for driving the plasma process will further boost this field. A particularly interesting theoretical finding in this context is that the THz generation process can be seeded[395], which opens up the possibility of amplification of THz pulses by iterative application of the Brunel plasma process.

5

Detection techniques

An important goal of Ultrafast Photonics is the measurement and control of ultrafast processes in atoms, molecules and other types of matter on attosecond temporal and Ångström spatial scales, the fundamentals of which were discussed in Section 2.2. Such precise control can be obtained using the light oscillations of strong tailored waveforms (introduced in Chapter 3) as the driving force. Measurement of the induced dynamics with the same precision is possible by utilizing the attosecond-scale oscillations of the strong laser electric field as a reference, which establishes a mapping between time and space on the one hand and accessible observables such as photoelectron/-ion momentum or photon energy on the other hand, as will be discussed in detail in Chapter 6. Retrieval of the spatio-temporal information encoded in these observables requires, obviously, their detection. Measurement of the momenta of photoelectrons and/or photoions generated during the interaction process or, likewise, measuring the spectrum and/or polarization state of emitted XUV/X-ray radiation or also of emitted THz radiation, is thus key to understanding the induced dynamics. Detection of the reaction products (electrons, ions, photons) and measurement of (some of) their properties is therefore of paramount importance for understanding the interaction of strong laser fields with matter.

XUV/X-ray radiation can be characterized using spectrometers, see Section 5.1 below. Analysis of the (spectral, temporal) properties of emitted THz radiation is possible even without any elements for spectrally dispersing the radiation, since the emitted THz field can be measured directly in the time-domain by electro-optic sampling[316]. While the analysis of the radiation emitted during the interaction process is relatively simple, the measurement of the momenta of photoelectrons/-ions requires substantial effort – in particular when two or more particles need to be detected in coincidence. Two main techniques for obtaining momentum distributions of emitted particles are applied in experiments: *reaction microscopy* (REMI) and *velocity map imaging* (VMI). Most of the measured photoelectron/-ion distributions that will be discussed in Chapters 6 and 8 were obtained either by REMI or VMI. Each of the two methods has specific advantages and disadvantages which define their respective fields of typical applications. Still, REMI is a much more versatile and complex method and all experimental data of the author and co-workers shown in Chapters 6 and 8 were obtained with a home-built reaction microscope, a schematics of which is displayed in Fig. 5.1(a). Therefore, the REMI method is more important for the research contained in this thesis and consequently will be described in greater detail in the following, while we will content ourselves with a short overview over the functionality of VMI and its differences to REMI.

5.1 XUV/X-ray spectrometry

Usually, when one talks about the detection of XUV or X-ray radiation, one actually means the measurement of its spectral intensity distribution. In most cases it is not even necessary to measure this distribution in absolute intensity values. Arbitrary intensity values, normalized to some reference value, are usually sufficient, in particular when comparing them to calculated spectra. However, as outlined in Chapter 4, other parameters of XUV/X-ray radiation generated by the process of high-harmonic generation (HHG), in particular its spectral phase, its polarization properties or the spatial emission profile, also contain valuable information. While measurement of the spectral intensity distribution and the spatial profile are relatively straightforward tasks, as will be outlined in this Section, measurement of the phase and polarization properties requires much more involved techniques. A selection of available techniques for the measurement of phase and polarization of XUV/X-ray radiation generated by HHG will be discussed in Section 7.1.3.

In the following we will focus on the measurement of the spectral and spatial intensity distributions of XUV/X-ray beams generated by HHG. This task can be accomplished using spectrometers that consist (in their simplest form) of a slit, a grating and an imaging system (e.g., an XUV/X-ray sensitive camera, or micro-channel plates coupled to a phosphor screen in combination with a simple camera for visible light). This approach using gratings works well until a photon energy of about 2 keV, above which the necessary groove density of the grating would be too high. Above a photon energy of about 6 keV it is possible to employ Bragg reflection from crystal surfaces for spectral measurements. The difficult photon energy range, where the availability of diffractive elements is sparse, is the one in between. Here, we will limit our discussion to photon energies well below 2 keV and the application of XUV/X-ray grating spectrometers. As will be described in greater detail in Section 7.1.3, they can be amended with (rotatable) polarizing elements such as metal mirrors under grazing incidence, and then also allow for the analysis of the polarization state of the XUV/X-ray radiation[339,375,396].

Technically, the state-of-the-art for measuring the spectral intensity distribution of XUV/X-ray radiation are concave gratings, used in grazing incidence geometry to achieve a high reflectivity, that exhibit a varying groove density along their surface[397,398]. Such gratings focus the spectrum along a straight line (within the spectral bandwidth the grating is designed for). Together with the focusing achieved in the orthogonal direction by the concave shape of the grating, this leads to so-called *flat-field* conditions, i.e., the spectrum and the spatial profile of the XUV/X-ray beam are imaged onto a *plane*. This enables the use of plane detectors (CCD chips, micro-channel plates) that can be conveniently placed along the focal plane to measure both the spectrum in the tangential direction and the beam shape in the transversal direction. The additional information about the spatial intensity distribution can provide important information about the high-harmonic generation process[399]. If the groove density of the grating were constant, the different photon energies within the XUV/X-ray spectrum would be focused onto different points that lie on the so-called Rowland circle[400]. That is, the highest spectral resolution is achieved at different points for different photon energies, which may usually prohibit measuring the spectrum in single-exposure mode with a flat detector. In this case, the detector is often moved along the Rowland circle and the spectrum is measured in scanning mode by selecting small spectral portions with a slit.

In high-harmonic generation, the laser beam that drives the HHG process and the generated XUV/X-ray beam co-propagate. The divergence of the XUV/X-ray beam is much smaller than that of the laser beam. To measure the intensity spectrum of the HH radiation, the orders of magnitude stronger laser light needs to be filtered out. This is usually done using thin metal filters that far from material resonances exhibit decent transmittance for the HH radiation and a strong suppression for laser light. Additionally, the HH radiation that for a given diffraction order (e.g. the first) is reflected off the grating under a certain angle determined by the groove density and the blaze-angle of the grooves, can be spatially separated from the laser beam that is reflected off the grating under the incoming angle (zeroth diffraction order). Still, because the laser light is stronger by many orders of magnitude, its sufficient suppression can be challenging. This is particularly true for stray light reflected off the walls of the spectrometer chamber. With respect to stray light rejection, detectors consisting of stacks of micro-channel plates (MCPs) and a phosphor screen assembly, with their relatively smaller detection efficiency for the small photon energies of laser light, are therefore advantageous over semi-conductor XUV/X-ray detectors that exhibit high detection efficiency already for visible photons. However, MCPs are inferior as compared to CCD sensors with respect to spatial resolution. Typical values for the spatial resolution, which together with the resolution of the grating determines the spectral resolution of the whole spectrometer, are about 40 to 50 μm with a single-stage MCP and about 80 to 100 μm with a double-stage MCP. The pixel size of XUV/X-ray CCD sensors, in comparison, can be as small as roughly 10 μm.

5.2 Reaction microscopy (REMI)

The development of reaction microscopy was initiated by work in the group of H. Schmidt-Böcking at the University of Frankfurt am Main in collaboration with L. Cocke from Kansas State University. The original idea was to circumvent the difficult task of directly measuring the momentum of fast electrons by instead measuring the recoil of the ion. To express this idea, the method was called RIMS (recoil ion momentum spectroscopy)[401]. Soon it became clear, however, that the uncertainty in the velocity of the target due to its thermal energy limits the resolution of the method. This is because the uncertainty in thermal target velocity is consumed to the largest degree by the recoil ion rather than the electron. To see this, consider that before the electron separates from the ion, their velocities are the same, $\boldsymbol{v}_R = \boldsymbol{v}_e = (\boldsymbol{v}_T + \Delta\boldsymbol{v}_T)$. Here we have used the indices R, e and T for recoil, electron and target, respectively, and have additionally formally separated the statistical thermal velocity spread of the target, $\Delta\boldsymbol{v}_T$, from its well defined, directional mean velocity $\boldsymbol{v}_T$ that can be calibrated in the experiment. If we consider the momenta of the particles right before they separate, we obtain for the momentum uncertainties of the recoil ion and electron, respectively, $\Delta\boldsymbol{p}_R = m_R\Delta\boldsymbol{v}_T$ and $\Delta\boldsymbol{p}_e = m_e\Delta\boldsymbol{v}_T$. Because of the much higher mass of the recoil ion than that of the electron, $m_R \gg m_e$ (by about a factor of $M \times 1836$ for targets with mass number M), the recoil ion takes almost the complete uncertainty in momentum. Therefore, to improve the accuracy of a RIMS measurement, the uncertainty $\Delta\boldsymbol{v}_T$ due to the thermal energy of the target must be minimized, which is possible by cooling the target. Cold targets can be obtained by, e.g., super-sonic expansion of pressurized gases through a nozzle with small diameter. By the use of cold targets, which extends RIMS to COLTRIMS (cold target recoil ion momentum spectroscopy), the obtained momentum resolution could indeed be strongly improved[304,401,402]. Targets in the form of a thin, internally cold jet produced by super-sonic expansion are now standard. Subsequently, several conceptual improvements of the method were made, e.g., by the introduction of an additional detector for electrons that opened up the possibility to detect electrons and ions in coincidence, by extending the detectors with spatial resolution, or by introducing magnetic fields for detection of electrons within a full solid angle of 4π, etc., thereby turning a COLTRIMS apparatus into a full-fledged microscope for imaging reactions. To reflect this, nowadays a COLTRIMS apparatus is often called a *reaction microscope* (REMI).

REMI apparatus A schematics of an example for a REMI, built by the author and co-workers, is shown in Fig. 5.1(a). A thorough overview over its components and over reaction microscopy in general can be found in Ref. [403]. The REMI apparatus sketched in Fig. 5.1(a), like most other modern REMIs for the measurement of momentum distributions of photoelectrons/-ions generated by a strong laser field, consists of the following main components: The target is provided in the form of a thin gas jet that is produced by ultra-sonic expansion through a nozzle with small diameter (typically 5-50 µm). Additionally, the gas-nozzle can be pre-cooled to cryogenic tem-

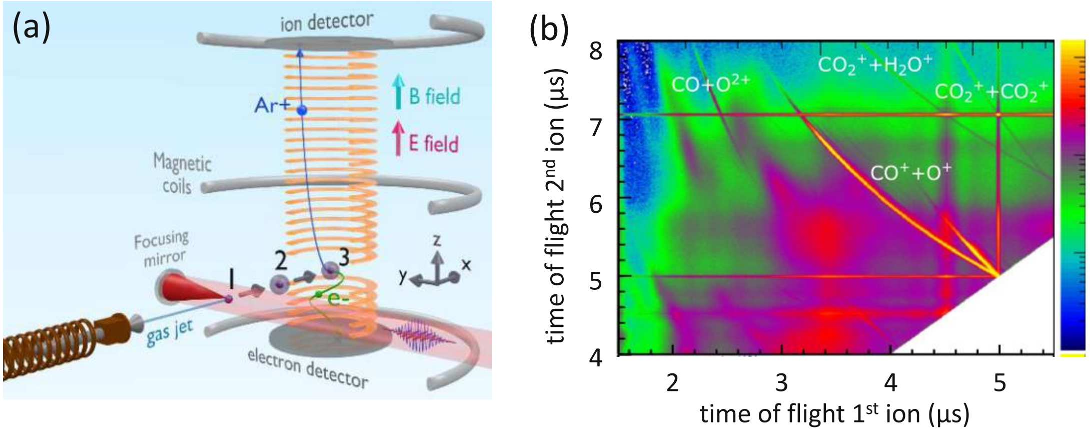

Figure 5.1: Coincidence momentum imaging–reaction microscopy. (a) Schematics of the REMI apparatus used for all electron-ion experiments in the papers given in the Appendix. Shown are the nozzle and skimmer used to produce the ultrasonic gas jet, the copper plates (in yellow) that generate a homogeneous electric field, the coils used to produce a homogeneous magnetic field, the two detectors and the focusing mirror. The example shows the experiment described in Ref. [163], in which an OTC pulse is used to control the localization of Rydberg electron wavepackets produced in argon atoms by the process of frustrated field ionization described in Section 2.2.4. In the figure, the OTC pulse impinges from the right onto the focusing mirror, which focuses it onto an argon atom (1) whereby a Rydberg atom is created (2). After some time the Rydberg atom becomes ionized (3) and the Rydberg electron and Ar^+ ion are guided to the electron respectively ion detector by the electric and magnetic spectrometer fields, where they generate electronic signals used for determining their momentum vectors. (b) Example of a photoion-photoion-coincidence (PIPICO) plot based on data measured with the REMI shown in (a). The example depicts pronounced coincidence lines (cf. the color scale) arising from an experiment performed on $\mathrm{CO_2}$ mixed with water. Indicated are break-ups of the $\mathrm{CO_2}$ monomer, the $\mathrm{CO_2}$ dimer and the hetero-dimer $\mathrm{CO_2}$-$\mathrm{H_2O}$. The physical origin of the appearance of these sharp lines is described in the text.

peratures (e.g. with liquid nitrogen) to achieve very cold gas temperatures and therewith small momentum uncertainty. The atoms or molecules in the jet are intersected by the laser pulse which drives the interaction and generates electrons and ions. The interaction point is in the center of a spectrometer consisting of a number of copper plates. Because the interaction with the laser must take place in vacuum, the spectrometer is placed in an ultra-high vacuum chamber (base pressure typically 1×10^{-10} mbar or even below). As we will see below, extremely good vacuum conditions are necessary for performing coincidence measurements, which is the key capability of a REMI. The spectrometer generates a weak, homogeneous electric field (typically 1-100 V/cm) that guides the electrons and ions generated during the interaction with the laser pulse to the detectors. Additionally, coils are used for the generation of a weak, homogeneous magnetic field, $\boldsymbol{B}$, typically of the order of one mT. The magnetic field, that is parallel to the electric field of the spectrometer, enables the collection of electrons within a full solid angle of 4π. This is because electrons that exhibit a velocity $\boldsymbol{v}$ perpendicular to the spectrometer axis, will be guided towards the detector on spirals due to the Lorentz force $q(\boldsymbol{v} \times \boldsymbol{B})$. Detection of the electrons and ions takes place by multi-hit-capable position- and time-sensitive detectors. Typically, as in the example in Fig. 5.1(a), there are two detectors situated on either side of the spectrometer. The multi-hit capability of the detectors opens up the possibility to detect multiple charged particles in coincidence. Position-sensitivity is important because it allows to reconstruct the momentum of the detected particles also along the directions perpendicular to the spectrometer axis and therewith allows measuring their momenta in all three spatial directions. Additionally, fast electronics (multi-channel amplifiers, constant fraction discriminators and time-to-digital converters with a resolution of, nowadays, on the order of 50 ps) is necessary for feeding the information about the impact position and time-of-flight of the different particles that are detected into a computer for further data analysis and storage (not shown in Fig. 5.1(a)). From the times when the electrons and ions are detected and from their impact positions on the detectors, their three-dimensional momentum vectors can be reconstructed. For a spectrometer with a homogeneous electric field, E, along the spectrometer axis (assumed in z-direction of the lab-coordinate system in the following), the flight time, t_F, of a particle with charge q and mass m from the interaction with the laser pulse to the detector reads

$$t_F = -\frac{v_z}{a} + \frac{1}{a}\sqrt{v_z^2 + 2La}, \tag{5.1}$$

where v_z is the initial velocity of the particle along z that it gained during the laser-interaction, L is the spectrometer length, and $a = \frac{qE}{m}$ is the acceleration of the particle in the spectrometer field. From (5.1) the value v_z can be obtained, and from this one obtains the particle's momentum $p_z = mv_z$. The particle's momenta in the plane perpendicular, p_x and p_y, can be easily obtained as $p_x = mx/t_F$ and $p_y = my/t_F$, respectively, where (x, y) is the point where the particle is registered on the detector. For electrons these relations are valid with $m = 1$ and $q = -1$. If a magnetic field $\boldsymbol{B} = B\boldsymbol{e}_z$ is used for enhancing the solid detection angle, the calculation of perpendicular momenta additionally needs to consider the gyration of the electrons in the magnetic field[403].

Coincidence detection The key capability of a REMI, as was already mentioned, is that it allows the detection of several particles in coincidence. Coincidence detection means, in descriptive terms, that individual fragments produced by the same reaction are detected. Under this condition, it is possible to exploit the common information that is shared by these individual fragments, e.g., the information that an electron is ejected from an ion with a certain mass, or that the electrons and ions must fulfil momentum conservation. A thorough description of coincidence detection and an analysis of its limits can be found in Refs. [306, 307]. Historically, coincidence detection was invented as early as in the 1920's by H. Geiger and W. Bothe. In 1954 Bothe received the Nobel Price in Physics "for the coincidence method and his discoveries made therewith". A well-known example of a coincidence measurement is photoelectron-photoion coincidence (PEPICO). In PEPICO, the ion and the electron of a certain photo-induced reaction are detected in coincidence. This allows obtaining photoelectron energy distributions for different fragmentation reactions which, in turn, can provide insight into the pathways that lead to the fragmentation[404,405,406]. Additional possibilities for coincidence measurements and analyses arise when momentum conservation conditions in all three spatial dimensions, either between the photoelectrons and the photoions, or also between individual photoions, can be exploited, as it is possible with a REMI (see below).

The crucial point for being able to detect different particles generated during the same reaction and to apply coincidence analysis to the measured data, is that the particles must originate from the same target atom or molecule. Thus, for the study of the interaction of the target atoms or molecules with a laser pulse, it must be ensured that at maximum one atom or molecule interacts with one laser pulse. In practice this number should be kept well below one and experiments are typically carried out in a regime where on average significantly less than one atom or molecule becomes ionized per laser pulse. If too many particles are generated, coincidence detection can no longer be ensured and false coincidences are generated, compromising the validity of the measured data[306,307].

Demands on a coincidence experiment From the requirement that at maximum one atom or molecule interacts with one laser pulse it follows that, first, obtaining a low count-rate of generated ions requires a low target density, i.e., a low density of the gas jet for COLTRIMS, or a small target background density if no jet is used (as is often the case in conventional PEPICO time-of-flight spectrometers). Since the ionization rate strongly increases with laser intensity, the target density needs to be the lower the higher the laser intensity is. In order to avoid contributions to the data from the background vacuum, the requirement of a small target density immediately means that the quality of the background vacuum must be very high. Ultra-high vacuum with a background pressure of about 1×10^{-10} mbar or less is typically required.

The second important point that follows from the coincidence requirement that demands the detection of at maximum one set of hits on the detector per laser pulse, i.e., one set of hits every nth pulse, is that the repetition rate of the laser pulses should be high. To visualize the importance of the repetition rate, denoted as f_r, we can estimate the necessary measurement time for an example measurement as a function of $f_r = 1/T_r$, with T_r the time in between the pulses in the laser pulse train. Let us consider the measurement of the momentum distribution of one of the two electrons emitted during fragmentation upon double ionization of some molecule, $\mathrm{AB}^{2+} \rightarrow \mathrm{A}^{+} + \mathrm{B}^{+} + 2e^{-}$. Assume that the overall probability for the ionization and fragmentation process is $P_f = 10^{-2}$ per pulse. To measure the electron momentum distribution we need to detect the two ions and one electron in coincidence. The probability for detection of a particle shall be, for simplicity, equal for electrons and ions, $P_d = 0.5$. The overall probability per laser pulse to detect the three particles is therefore $P = P_f \times P_d^3 = 10^{-2} \times 0.5^3 = 1.25 \times 10^{-3}$. Now assume that for obtaining a certain statistical significance, the electron momentum distribution shall contain N electrons. To measure this distribution it, thus, takes $n \times N/P$ laser pulses, when only every n^{th} pulse a set of recoils and electrons shall be produced. This ensures suppression of wrong coincidences. Expressed in time this means one needs to measure for $T_{\text{meas}} = T_r \times n \times N/P = n \times N/(P \times f_r)$ seconds. Assuming, for example, $N = 3 \times 10^4$ and $n = 4$ one obtains $9.6 \times 10^7/f_r$ seconds or roughly $27 \times 10^3/f_r$ hours. This shows that a laser pulse repetition rate of at least a few kHz is in practice necessary for REMI measurements. With $f_{\text{rep}} = 1\,\text{kHz}$ one could measure the spectrum in 27 hours, which is doable but challenging. Typically, laser systems for REMI measurements have repetition rates of several kHz, say 10 or even 100. With the latter one could measure our example distribution in roughly a quarter of an hour.

Phase-tagging Although REMI measurements are obviously time-consuming and therefore put high demands on the long-term stability of the laser setup and all other components involved in the experiment, this penalty comes with a number of unique advantages. One of these advantages is that data collection on the basis of single laser pulses opens up the possibility to correlate the electron-ion data with any other data that is measured for the same pulse. For example, REMI can be ideally combined with a stereo-ATI phasemeter that measures the CEP of a few-cycle laser pulse for each and every laser pulse within the laser pulse train, described in Section 3.1.3. Storage of the measured CEP together with the electron-ion data obtained for the same laser pulse makes it unnecessary to actively stabilize the CEP of the laser pulse train. Instead, the measured momentum data can in the off-line data analysis simply be linked to the CEP-data, which results in higher precision and better long-term stability. This method of obtaining CEP-sensitivity has been introduced in Section 3.1.3 as *CEP-tagging*, often only called *phase-tagging*[250,308], and has been applied in a number of experiments, e.g., in Refs. [**190**, **264**]. More examples can be found in Chapters 6 and 8.

Coincidence selection The temporal and spatial resolution and multi-hit capability provided by the detectors of a REMI allow to retrieve the three-dimensional momentum of each particle that hits the detector. In practice, the number of particles that can be detected per laser shot is limited to a few (typically ≤ 5 for ions and $\leq 2-3$ for electrons). Electrons are more difficult to detect separately because they typically arrive at the detector within a short time on the nanosecond scale. The different mass of ions and their longer flight times makes it easier to distinguish them. Under coincidence conditions, sophisticated and powerful coincidence selections between the different ions, the detected electrons and also between electrons and ions can be performed. At the heart of such coincidence analysis lies the requirement for the conservation of momentum between all particles emerging from a photon-induced reaction. The conservation of momentum can be expressed as

$$\sum_i \boldsymbol{p}_R^i + \sum_j \boldsymbol{p}_e^j + \sum_k \boldsymbol{p}_p^k = \boldsymbol{p}_T + \Delta \boldsymbol{p}_T, \tag{5.2}$$

where again the indices R, e and T for recoil, electron and target are used, respectively. The photons absorbed during the interaction with the light are denoted by the index p. The sums in (5.2) run over all particles generated respectively absorbed in the reaction. Because the momentum of a photon $p_p = \hbar\omega/c$ is very small for laser light in the visible to infrared wavelength ranges, the contribution of the photons can be neglected. As mentioned above, the constant momentum of the target before the reaction, $\boldsymbol{p}_T$, can be calibrated in the experiment and, thus, can be subtracted during analysis. We can therefore, without compromising generality, set it to zero here and obtain

$$\sum_i \boldsymbol{p}_R^i + \sum_j \boldsymbol{p}_e^j = \delta \boldsymbol{p}. \tag{5.3}$$

Here $\delta \boldsymbol{p}$ denotes the momentum uncertainty along different directions in the lab coordinate system. This uncertainty is determined by the finite temperature of the jet, $\Delta \boldsymbol{p}_T$, and and by the imprecision in determining the time-of-flight and impact positions on the detectors of the electrons and ions.

To estimate the measurement precision achieved in an experiment that exploits electron-ion coincidences along different spatial directions, one can evaluate the width of the sum momentum distribution of one electron and one ion generated during single ionization of the target,

$$\boldsymbol{p}_R + \boldsymbol{p}_e = \delta \boldsymbol{p}^{(1)}, \tag{5.4}$$

where the super-script indicates that this precision is obtained for one electron and one ion. The precision varies strongly for different directions in the lab coordinate system. This is, on the one hand, because the uncertainty due to the finite jet temperature, $\Delta \boldsymbol{p}_T$, is lowest perpendicular to the jet's propagation direction and usually much higher along the propagation direction. On the other hand this is because the measurement of the time-of-flight can be performed with much higher precision than that of the impact position of the fragments on the detector. Example values for a good resolution in electron-ion coincidence in atomic units of momentum are 0.02 along the spectrometer axis, and 0.1 respectively 0.5 in the perpendicular planes[261,407]. The higher value along the jet's propagation direction is mainly due to the finite jet-temperature. Better resolution can be obtained if only the electrons are measured, as in this case the uncertainty due to the jet-temperature is very small.

Equ. (5.3) also shows, along the original ideas of the (COLT)RIMS method, that the sum momentum of the electrons is the negative sum momentum of the ions (within the achieved momentum resolution). An example where this relation between electrons and ions can be advantageously exploited is double ionization of an atom or molecule. As it is difficult to detect both electrons, one analyses only the momentum of one electron, $\boldsymbol{p}_{e,1}$, and that of the doubly charged ion, $\boldsymbol{p}_r$, and obtains the momentum of the second electron by means of momentum conservation[261,407],

$$\boldsymbol{p}_{e,2} = -\boldsymbol{p}_r - \boldsymbol{p}_{e,1}. \tag{5.5}$$

Along the same idea, for obtaining insight into the momenta of the electrons, it is also possible to only measure the momentum of the recoil ion. This is helpful when high laser intensities are used, for which a high rate of electrons is already produced from the background gas. Such a strategy has, e.g., been taken in Ref. [190], where attosecond double ionization of helium with few-cycle circularly polarized pulses has been investigated. As the momentum of the recoil ion, $\boldsymbol{p}_r = -(\boldsymbol{p}_{e,1} + \boldsymbol{p}_{e,2})$, carries the combined information of both electrons, detailed insight into the ionization dynamics of both electrons can be obtained, as will be explained in greater length in Section 6.1.1.

Coincidences can, however, not only be exploited between electrons and ions, but also between ions and ions. This is particularly useful for the investigation of molecular fragmentation reactions, e.g., as in the example reaction $AB^{2+} \rightarrow A^{+} + B^{+} + 2e^{-}$ discussed above. In a molecular fragmentation reaction the recoil ions obtain large momenta due to their strong Coulomb repulsion that may easily exceed 100 atomic momentum units. In contrast, the electrons acquire their momenta dominantly from the laser field only. Thus, for the largest share of electrons that do not rescatter from the ion (direct electrons), their maximal momenta are $2\sqrt{U_p}$, cf. Fig. 2.3. This value is typically on the order of few atomic momentum units and, thus, is much smaller than the momenta of the ions. In this case (5.3) can be approximately written as

$$\sum_i \boldsymbol{p}_R^i = -\sum_j \boldsymbol{p}_e^j \approx 0. \tag{5.6}$$

For a two-body fragmentation reaction with generated fragments $i = \{A^+, B^+\}$ this can be simplified to $\boldsymbol{p}_{A^+} = -\boldsymbol{p}_{B^+}$. Thus, the conservation of momentum between the two ions A^+ and B^+ appears as a narrow distribution along the anti-diagonal in momentum space when plotting $p^a_{B^+}$ over $p^a_{A^+}$ with $a = \{x, y, z\}$. From (5.1) it can be seen that for large initial velocities along the direction of the spectrometer axis, the momenta scale nonlinearly with the flight time t_F. Thus, the straight momentum conservation distribution in the direction of the spectrometer axis, z, appears as a curved distribution when plotting the flight time of ion B^+ versus that of ion A^+. An example of such a photoion-photoion (PIPICO) plot is shown in Fig. 5.1(b) for different fragmentation reactions of the CO_2 monomer, the CO_2 dimer and the hetero-dimer CO_2-H_2O into two fragment ions. Typically, molecules exhibit several different break-up channels. Each of these break-up reactions leads, due to momentum conservation, to a line in the PIPICO plot around the point where both particles are generated with zero momentum, $(t^0_{F,A^+}, t^0_{F,B^+}) = \sqrt{\frac{2L}{E}}\left(\sqrt{\frac{m_{A^+}}{q_{A^+}}}, \sqrt{\frac{m_{B^+}}{q_{B^+}}}\right)$. This shows that coincidence detection of two (and also of more) photoions can be used to select certain fragmentation channels, characterized by the mass m and charge q of the fragments, during the offline data analysis. Examples of experiments where this was applied successfully will be discussed in Chapter 8.

5.3 Velocity map imaging (VMI)

The previous Section has described REMI as an extremely powerful method for measuring electron and/or ion momentum distributions. The key advantage of REMI, as compared to other methods, is the possibility to perform sophisticated three-dimensional coincidence data analysis. This capability is facilitated by multi-hit particle detection in combination with low count-rates to achieve coincidence conditions. This results in long data acquisition times with REMI. In contrast, electron/ion imaging techniques such as VMI detect many charged particles per laser shot. The momentum distribution of electrons/ions generated during the laser interaction right after the laser pulse is imaged onto position sensitive detectors using suitable electron/ion optics. The number of electrons/ions generated during the interaction is ultimately only limited by space-charge effects that lead to measurement errors because of distortions of the particle trajectories due to the Coulomb forces of neighbouring particles, and by the damage threshold of the detector. Thus, this way an electron/ion momentum distribution can be obtained much faster than with a REMI.

This advantage comes, however, with a number of limitations. The most important one of them is certainly that, obviously, coincidence selections during offline data analysis are inherently impossible. Thus, obtaining, e.g., an electron momentum distribution for a certain molecular break-up channel, possibly correlated with a certain fragmentation direction of the molecular moieties, as can be measured with a REMI, is not straightforwardly possible. It is possible, though, to obtain electron momentum distributions for certain ion species by gating the detector's high-voltage (HV) with a fast HV switch based on ion flight times[408]. Also, it has been shown that single-shot measurements of momentum distributions are feasible, which opens up the possibility to run them in phase-tagging mode (see Section 3.1.3) similar to a REMI[409]. Another limitation is that only a two-dimensional (2D) projection of the three-dimensional (3D) momentum distribution is obtained. However, in the case of cylindrical symmetry of the electron or ion emission, the 3D momentum distribution may be recovered from a 2D projection by Abel inversion, e.g., using an iterative inversion procedure[410]. Thus, VMI is less powerful than REMI, but also less complicated and facilitates much faster measurements. For applications that investigate processes with a low cross-section, such as ionization of atoms/molecules with weak XUV pulses, this is a decisive advantage, as one XUV pulse can be allowed to interact with many target atoms/molecules facilitated by a high target density. This way, an acceptable electron/ion count-rate can be obtained despite the low probability of the process for a single target atom/molecule. This, in turn, might make it possible to conduct a certain experiment with a VMI that would be practically impossible to be conducted with a REMI due to extremely long data acquisition times. VMI can therefore be applied complementary to REMI.

Technically, the electron/ion optics of a VMI apparatus typically consist of repeller, extractor, and grounded plates. The static electric field E between the repeller and extractor plates is much higher than the spectrometer field in a REMI. The spectrometer lens generated by the plate configuration projects the initial momentum distributions of electrons or ions produced during the interaction of the laser pulse with the target (atoms, molecules, clusters, nano-particles, etc.) onto the detector. The detector usually consists of a micro-channel plate (MCP) arrangement paired with a phosphor screen. To distinguish different ionic species the high voltage across the MCP arrangement can be gated with a laser-triggered fast high-voltage switch based on the time-of-flight of the desired ion species[408]. A camera behind the phosphor screen records images of the phosphor luminescence resulting from the particle impact on the MCP arrangement and this way records two-dimensional projections of the three-dimensional momentum distributions. For single-shot detection a very fast camera is necessary.

6

Laser-sub-cycle mapping of attosecond electron dynamics

Sections 2.2.2 and 2.2.3 showed that the trajectories of electrons emitted by strong-field ionization can be controlled by a strong laser field with attosecond temporal and Ångström spatial precision. As was already indicated and will be further detailed below, this opens up superb opportunities for inducing and probing dynamics in atoms, molecules, clusters, etc., with matchless precision and — in particular when laser pulses with tailored evolutions of the field-cycle are used — also with enormous flexibility. This, in turn, builds the basis for a number of novel applications in, e.g., the control of molecular dynamics or the generation of XUV or X-ray pulses with unparalleled properties.

However, even if we know from theory that laser pulses can drive and reference dynamics on laser-sub-cycle time-scales, and that there exists a very precise relation between the emission time of an electron and its final momentum, recollision time, recollision energy, etc., that are mediated by the sub-cycle evolution of the laser electric field, it still needs methods for extracting this sub-cycle information from observables amenable to measurements. Unfortunately, all detection methods, be it for charged particles (electrons, ions) or photons, are orders of magnitudes slower than femtosecond laser pulses, let alone the period of light oscillations. Ultimately this limitation arises from the speed limit of electronic circuits in the picosecond range. Thus, it needs methods that are capable of mapping sub-cycle time (and potentially also Ångström space) onto some observables that are also available in time-integrating experiments, as for example electron momenta, photon energies or light polarization states.

A number of methods for laser-sub-cycle mapping have been developed and are now commonly used in experiments. A very versatile mapping is provided by the relation $\boldsymbol{p}^{\infty} = -\boldsymbol{A}(t_i)$ given by (2.8), valid within the SFA, that relates the momentum of an electron measured (long) after the laser pulse to the value of the vector potential at the emission time of the electron, t_i (which is directly linked to the electric field strength at this time). Under the assumption that the SFA is valid, for a given field shape this relation provides a direct mapping between the sub-cycle evolution of the electron emission to the momentum space, as is visualized in Fig. 2.3(a). Thus, from measured electron momentum spectra, insight into the laser-driven sub-cycle electron emission dynamics can be obtained. More generally, electron momentum spectra not only contain information about the electron emission but also about the complete interaction of the emitted electron with the laser field. These dynamics can be retrieved by suitable models; in certain cases using the SFA transition matrix element (2.33) or its stationary-phase approximation (2.34).

Mapping the emission time of an electron to a measurable quantity with the help of a strong electric field bears strong similarity to a conventional *streak camera*. Such a device uses a time-varying electric field to deflect electrons emitted at different times onto different positions of a detector, which allows measuring processes with picosecond or even sub-picosecond precision[411]. Because of this reminiscence, the mapping provided by the relation $\boldsymbol{p}^{\infty} = -\boldsymbol{A}(t_i)$ is usually called *electron streaking* or also *attosecond streaking*, in particular when it is applied to the measurement of attosecond light pulses generated by HHG[412,413].

Another frequently exploited mapping of sub-cycle time onto an experimentally accessible observable is available in high-harmonic (HH) spectra, as will be described in detail in Chapter 7. In this scheme the strict dependence between the recollision time of an electron, t_r, and its recollision energy, $p^2(t_r)/2$, is exploited. As in HHG photons are emitted with an energy $\omega(t_r) \propto p^2(t_r)/2$, the HH intensity spectrum at the frequencies $\omega(t_r)$ contains information about the photon emission probability (the recombination dipole matrix element) multiplied by the electron emission probability (the ionization rate) at $t_i = t_r^{-1}(t_i)$. This commingling of the ionization and recombination probabilities is a well-known problem in mapping-methods that exploit the process of HHG. However, as will be shown in Chapter 7, if the ionization rate can be obtained by a separate gauge measurement, HH spectra can be used to extract dynamical information with attosecond precision of strong-field induced process such as nuclear dynamics in molecules[241], electronic beating dynamics[414], or even the evolution of molecular orbitals[238,415].

Because both processes, electron emission and recollision, are sensitive to the laser electric field, for linearly polarized light they repeat itself two times per laser cycle – one time for the positive and another time for the negative laser half cycle, cf. Figs. 2.3 and 2.4. This leads to an ambiguity in mapping electron emission and recollision processes to electron momenta or HH spectra. In addition to this half-cycle-ambiguity, the straightforward exploitation of the mapping inherent to the electronic processes driven by the strong laser field that we discussed in Section 2.2 allows obtaining insight into sub-laser-cycle processes for only quite short times. This is on the one hand because electron emission is confined to very short time intervals around the peaks of the field within a laser half-cycle, and on the other hand because the recollision event itself – depending on the considered range of recollision energies – lasts for only a fraction of a laser half-cycle. If electron recollision is understood as a pump-probe method in which the role of the pump and probe pulses are taken by the ionization and recollision events[416], the useful pump-probe range is only a fraction of a laser half-cycle. This limitation applies to both, HHG[170,238,417] and all processes induced by electron scattering upon recollision[147,416,418]. Fortunately, a number of approaches have been developed that overcome these limitations for certain processes and in specific parameter ranges.

In the following we will describe the most important mapping methods that can be exploited in the interaction of strong laser fields with isolated objects in the gas phase such as atoms, molecules, clusters, nano-particles, etc. For each method we will exemplarily review some noteworthy results obtained with it. We shall group the different approaches into two classes of mapping methods. The first class is based on measuring the momenta of electrons emitted during the ionization and/or rescattering process. From the momenta insight into the emission and rescattering timing and, by comparison to models, also into the state of the ion might be gained. The second class is also based on measuring electron momenta but exploits fine structures in the measured momentum distributions that are due to interferences of emitted electron wavepackets. We will discuss how dynamical and also structural information can be obtained from them. Approaches that exploit the photons emitted during HHG to obtain insight into dynamical processes on sub-laser-cycle time scales, which would be the third class of mapping methods, will be discussed in Chapter 7.

6.1 Electron momentum mapping

Measured momentum distributions of photoelectrons emitted during strong-field ionization contain a plethora of information about the ionizing laser field, the target, and ultrafast processes that may take place during the interaction of the laser field with the target. If it is possible to disentangle these different contributions, it may be possible to use photoelectron momentum distributions to image the entire ionization dynamics and the structural information convoluted into it. As in many cases the strong-field ionization dynamics can be analyzed in terms of semi-classical electron trajectories (see Section 2.2) the complex features in photoelectron momentum distributions that contain structural and dynamical information can often be explained in simple and intuitive terms. This Section provides an overview over different approaches to extraction of the information contained in photoelectron momentum distributions that exploit the mapping provided by the driving laser field in combination with a description of the underlying dynamics in terms of semi-classical electron trajectories.

The goal is to exploit this mapping such that from the measured electron momentum distributions information about the object under study can be obtained with (i) attosecond temporal resolution and ideally (ii) for extended periods of time, (iii) without ambiguity introduced by the different contributions originating from different laser half-cycles, and (iv) with Ångström spatial information. In practice it might, however, not be possible to satisfy all goals (i)-(iv) for all investigated processes. As the mapping, within the SFA, is eventually established by $\boldsymbol{p}^{\infty} = -\boldsymbol{A}(t_i)$ and therewith by the vectorial evolution of the strong laser electric field, a key ingredient in most mapping methods is the generation of specifically tailored strong laser fields using methods described in Chapter 3. In the following we will discuss different established mapping methods and examples of processes that have been investigated with them.

6.1.1 Angular streaking – the attoclock concept

The method of angular streaking exploits the fact that for circularly/elliptically polarized laser light the electric field vector $\boldsymbol{E}$ performs a rotation over an angle of 2π rad within one laser oscillation period T, i.e., with an angular frequency $\omega_o = 2\pi/T$. From Section 2.2.2 we know that in a circularly/elliptically polarized field an electron emitted at time t_i is driven away from the ion on a non-recolliding trajectory, cf. Fig. 2.3(b). Because for monochromatic light the electric field $\boldsymbol{E}$ and the vector potential $\boldsymbol{A}$ exhibit a phase offset of $\pi/2$, within the SFA the electron's momentum after the laser pulse, $\boldsymbol{p}^{\infty} = -\boldsymbol{A}(t_i)$, points 90° to the instantaneous angle of the electric field at time t_i. Thus, the emission time of an electron t_i is mapped into the direction of the vector $\boldsymbol{A}(t_i)$ at this time within the polarization plane of the laser field, see Fig. 6.1 for a visualization. Measurement of the vectorial electron momentum in the laser polarization plane with, e.g., a reaction microscope (Section 5.2) thus allows reading out this mapping. Because in this concept, originally introduced in Ref. [419], the electron emission time is *streaked* into the angular direction of the electron momentum plane parallel to the laser polarization plane, this mapping method is known as *angular streaking*.

The temporal resolution of the method is very high, as can be seen by considering the example of the frequently used Titanium-Sapphire laser, for which at 800 nm $T = 2.67$ fs, and thus the theoretically achievable precision amounts to 7.4 as/°. Of course, in practice the experimental uncertainty for measuring $\boldsymbol{p}^{\infty}$ leads to a somewhat reduced precision. The fast attosecond-scale rotation of the electric field vector bears some similarity to the minute hand of a clock. An hour hand of this clock can be associated with the femtosecond-scale variations of the magnitude of the electric field vector due to gradual increase and decrease of the pulse's envelope before and after the laser peak field strength. Because of these similarities the method is also known as the *attoclock*. Fig. 6.1(a) visualizes the principle and the hour and minute hands of the clock. An-

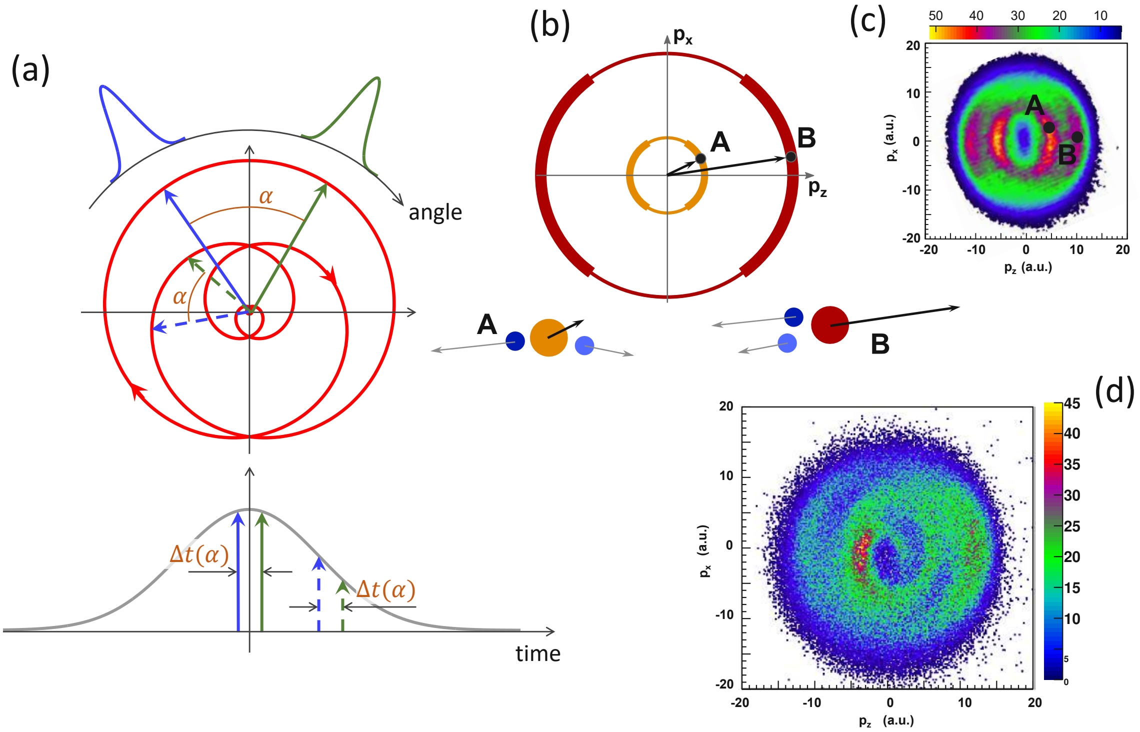

Figure 6.1: Visualization of the attoclock concept based on angular streaking of ionizing electron wavepackets. (a) The attoclock consists of an hour hand determined by the pulse envelope, and a minute hand given by the fast rotation of the electric field vector. See text for details. (b) In double ionization the momenta of the two emitted electrons add up vectorially to the ion momentum. An ionization-delay of an odd (even) number of half cycles results in electron emission into the opposite (same) hemisphere and, therewith, in a small (large) ion momentum (case A vs. B). This leads to rings in the ion momentum distribution (c) with a small (large) diameter. For few-cycle pulses the ion momentum distribution becomes sensitive to the CEP. Panel (d) shows a measured ion momentum distribution (adapted from Ref. [190], also see **Paper 7**) for a certain value of the CEP. The sub-cycle evolution of the ionization dynamics is clearly visible as spiral-shaped features reminiscent of the laser field-evolution in (a).

gular streaking has been applied to time-resolving the electron emission process in single[420–424], double[190,191,419,425–427] and multiple[427] ionization of different atoms, and has also been applied to the investigation of the electron dynamics underlying electron emission and fragmentation processes of molecules upon strong-field ionization[428–434].

Taking advantage of the very high temporal resolution achievable with the angular streaking method, a number of the experiments on atomic single ionization were dedicated to investigating the timing of the ionization process, e.g., in Refs. [420, 435, 436]. The question asked by these experiments is whether the tunneling process takes some small amount of time, i.e., whether there exists some tunneling delay with respect to the field maxima. Motivation for this question comes from Keldysh's theory that defines a hypothetical transit time for an electron passing through the field-tilted Coulomb barrier as given by (2.4). The observable in the experiments is the electron streaking angle with respect to the main axis of the laser field's polarization ellipse which, after removing the streaking angle introduced by the laser field and an additional offset introduced by the ion's Coulomb potential, shows a small remaining intensity dependent angle that is interpreted as a tunneling delay[420,435,436]. Depending on the physical picture used for the interpretation, some theoretical works dispute the existence of a delay[437,438], while others interpret this offset as a genuine tunneling delay[435,436,439]. The interpretation of the measured angular offset also depends on the applied model and coordinate system[435–437,440].

Using coincidence detection – as introduced in Section 5.2 – of electrons and ions emitted upon dissociative ionization of molecules, angular streaking can also be used to probe the fast laser-driven electron dynamics underlying the molecular dissociation process. This opportunity has been exploited for the investigation of one of the most studied process in strong-field laser interaction, namely the dissociative ionization of the hydrogen molecule, H_2, into a proton, a hydrogen atom and an electron, $H_2 \xrightarrow{laser} H_2^+ + e^- \rightarrow H^+ + H + e^-$. For this process (or the corresponding one in D_2) it has been shown by numerous works that laser pulses that break the inversion symmetry can be used to determine the localization of the remaining electron and therewith can achieve an energy-dependent forward-backward asymmetry in the emission of the proton H^+, see Refs. [441–446]. Using angular streaking with multi-cycle single-color laser pulses Wu et al. could show[430,434] that the observation of an asymmetry in this process does in fact not necessitate breakage of the inversion symmetry by the laser pulse, but that the asymmetry emerges as a result of the timing of the electron emission within a laser cycle. The laser-sub-cycle timing of the electron emission in the molecular frame of reference provided by angular streaking in combination with electron and ion coincidence detection reveals the influence that the phase of the laser electric field at the instant of the electron emission has on the asymmetry of the molecular dissociation process. Variants of this experimental approach have been used to investigate the ionization and fragmentation processes in different molecules such as acetylene[431], N_2[432], CO[428], and also in small atomic clusters[53,429].

If two electrons are released during the laser interaction in a circularly polarized pulse, the question of their relative emission timing arises. As for such laser fields recollisions are suppressed, the two electrons are expected to ionize strictly sequentially and independently of each other. However, probing this process of sequential double ionization (SDI) on very short time-scales might reveal deviations from this assumption and one may wonder whether electron-electron correlation could play some role in the dynamics of the double ionization process. Investigation of this question for atomic double ionization was actually the motivation for the invention of the method of angular streaking by Maharjan et al. who applied it to double ionization of argon and neon atoms[419]. It was found that the emission of two electrons can take place within one laser cycle. Analysis on shorter time-scales was not possible in this experiment. Pfeiffer et al. further investigated SDI of argon using angular momentum streaking and found features in the measured momentum distributions and yields as a function of laser peak intensity that were interpreted as evidence for the break-down of the independent particle approximation during double ionization on short time-scales[425,426]. Simulations using the classical trajectory Monte-Carlo (CTMC) method showed, however, that the experimental observations may not necessarily be a signature of electron-electron correlation, but can also be ascribed to the various possible combinations of laser-sub-cycle electron ionization times of the two electrons[193,447] whose existence have been predicted using CTMC[448].

An unambiguous experimental characterization of this sub-cycle two-electron emission dynamics for the benchmark process of double ionization from the strongly correlated ground state of helium with the angular streaking method has been performed by the author and co-workers using sub-two-cycle intense laser pulses with a well-characterized CEP, see Ref. [190] and **Paper 7**. Fig. 6.1(b) visualizes how the double ionization dynamics is mapped into the angular momentum distributions of He^{2+} that were measured in the experiments. The measured He^{2+} momentum distribution [Fig. 6.1(c)] is dominated by a double-segment ring structure that is due to the different possible combinations of the vectorial sum momentum of the two sequentially emitted electrons. Depending on their emission times t_i the two electrons ($i = 1, 2$) may be emitted into different directions and gain different momenta in the laser field. Neglecting the influence of the ion's Coulomb potential, the electrons' momenta gained in the laser field are given by the laser vector potential at their release times, i.e., $\boldsymbol{p}_i^e = -\boldsymbol{A}(t_i)$. Thus, the structures in the He^{2+} momentum distribution reflect the distributions of the release times of the two electrons. Depending on whether the delay between the first and second emission is an even or odd number of half-cycles, the two electrons are emitted either into the same or into opposite directions, cf. Fig. 6.1(b). As due to momentum conservation the He^{2+} ion momentum is the negative sum of the two electron momenta, $\boldsymbol{p}_{\mathrm{He}^{2+}} = -\left(\boldsymbol{p}_1^e + \boldsymbol{p}_2^e\right)$, this results in either a large (for emission into the same direction) or a smaller sum momentum (for emission into opposite directions), which is the reason for the appearance of the two ring segments in the measured distributions. Two situations that lead to a sum momentum within two different ring segments, marked by A and B, are shown in Figs. 6.1(b) and (c).

Sub-cycle and even sub-half-cycle temporal resolution is obtained if the different contributions to the He^{2+} momentum distribution from the separate half-cycle ionization bursts can be disentangled. The momentum distributions of He^{2+} in the laser polarization plane obtained with sub-two-cycle laser pulses with a known carrier-envelope offset phase (CEP) show rich structure and a strong dependence on the duration, peak intensity, and CEP of the pulses. As could be shown, the separate bursts and their attosecond evolution can be clearly identified in the CEP-resolved He^{2+} momentum distributions, as depicted in Fig. 6.1(d) for a particular value of the CEP and an intensity of 1×10^{16} W/cm^2. In this figure it can be seen that the He^{2+} momentum distributions for a given CEP consist of two spirals; one coiling counter-clockwise from the center outwards, the other one coiling clockwise. The spirals in Fig. 6.1(d) reflect the rotating evolution of the laser field vector in the polarization plane which establishes a unique attosecond timing reference in the angular direction[419].

By exploiting this timing reference the emission times t_1 and t_2 of the first and second electron could be unambiguously retrieved from the measured CEP-resolved He^{2+} momentum distributions. Thus, Ref. [**190**] succeeded for the first time in resolving the different contributions of the half-cycle ionization bursts[448] to the overall momentum distribution. This achievement, on the one hand, revealed two thus far unreported cases of two-electron emission dynamics, and, on the other hand, allowed studying in detail their dependence on pulse intensity and duration. The first interesting finding is that for the shortest laser pulses and for relatively low peak intensity the two electrons are emitted most probably with a mere delay of about one laser-half-cycle. The second notable finding is that for few-cycle pulses the two electrons may also be emitted very likely in between the peaks of the electric field oscillations.

6.1.2 Momentum mapping with tailored waveforms

In Sections 3.2 and 3.3 a number of types of tailored waveforms composed of two and also multiple pulses of different colors were introduced, and a few applications of them were mentioned. Here we will now discuss in detail how such tailored waveforms can be applied to map the sub-cycle dynamics of single and multiple ionization into the electron momentum, and how these dynamics can be retrieved from the measured electron momentum distributions. We will see that by tailoring the laser electric field one cannot only obtain insight into the ionization process, but that one can even control the electron emission dynamics on attosecond time scales. A very similar mapping for sub-cycle electronic processes can also be established for photons from HHG rather than electrons. Such mapping and control techniques in the XUV/soft X-ray regime based on the use of strong tailored waveforms will be discussed in Chapter 7. Furthermore, since the emission of electrons may be the trigger for the dissociation of a molecule, by gaining control over the ionization process it becomes possible to determine molecular processes. This opportunity and successful implementations of this idea will be discussed in Chapter 8 below.

Historically, the first experiments that showed control over strong-field processes were per-

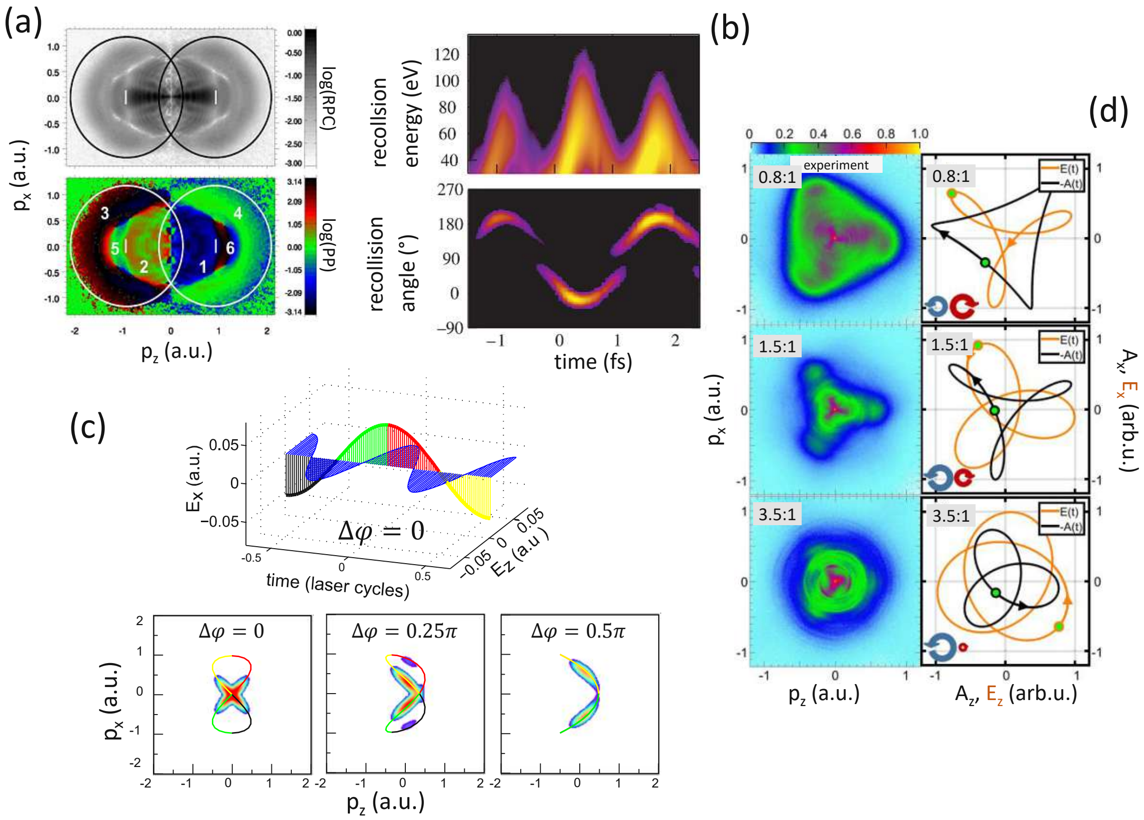

Figure 6.2: Momentum mapping with tailored waveforms. (a) Relative phase contrast (RPC, top) and the "phase of the phase" (PP, bottom) obtained from measured photoelectron momentum distributions emerging during single ionization of argon with an $\omega/2\omega$ field. Adapted from Ref. [449]. (b) Recollision energy (top) and recollision angle (bottom) simulated for an $\omega/2\omega$ OTC field. See text for details. Adapted from Ref. [237]. Also see **Paper 3**. (c) Visualization of the two-dimensional mapping in electron momentum spectra established by OTC fields. Depending on the relative phase $\Delta\varphi$ of the OTC field, electrons released during different quarter-cycles of the OTC field (top) are mapped into different regions of the electron momentum plane (bottom). Adapted from Ref. [151]. Also see **Paper 4**. (d) Electron momentum mapping with $\omega/2\omega$ CRTC pulses. Shown are momentum distributions of photoelectrons from single ionization of argon (left) measured with the CRTC fields shown in the right column. The intensity ratio of the 2ω to the ω fields is indicated in the panels. Adapted from Ref. [334].

formed with **linearly polarized two-color fields**[279–281]. In these works electron emission from atoms was controlled with strong fields composed of a fundamental pulse and its second harmonic in the so-called $\omega/2\omega$ configuration (cf. Sections 3.2 and 3.3). The effects of changing the sub-cycle field evolution by varying the relative phase, $\Delta\varphi$, between the two colors were observed in measured ATI photoelectron spectra. These experiments established a sensitivity of the different photoelectron energy peaks in ATI spectra to the laser field's evolution. This sensitivity can be understood within a picture that employs interferences between electron wavepackets emitted during different cycles of the laser field[226,227,228]. Interference structures in electron spectra are thus a method of obtaining sub-cycle timing, as will be discussed in detail in Section 6.2.

Linearly polarized two-color pulses in the $\omega/2\omega$ configuration have been frequently used to explore and control the electron emission dynamics. An interesting approach that builds on the variation of the relative phase $\Delta\varphi$ has been introduced recently[449]. In this approach one performs a Fourier transform of measured electron momentum distributions with respect to the periodically varying $\Delta\varphi$ and analyzes the absolute and phase values of the emerging complex Fourier transform, which are the relative phase contrast (RPC) and the ”phase of the phase” (PP), see Fig. 6.2(a) for an example of RPC and PP distributions. These quantities show very interesting properties: The overall structure of the PP distributions is largely independent of the target atom/molecule and displays features that can be assigned to certain electron trajectories, thus, establishing a possibility to extract sub-cycle timing from them. On fine scale, both RPC and PP distributions show target-dependent detailed features and therefore can be used to obtain structural and even dynamical information from them.

Observing the sensitivity of different observables or distributions on the shape of the $\omega/2\omega$ field as determined by $\Delta\varphi$ is thus a viable way of mapping the influence of certain structural or dynamical influences on the purely field-driven dynamics into electron momentum distributions and facilitates, in turn, the recapture of this influence from measured distributions. The author and co-workers have used this approach for experimentally tuning and probing the influence of the parent ion’s Coulomb field on the trajectories of strong-field-driven wavepackets[150], see **Paper 10** for details. Measuring the influence of the Coulomb potential is of importance, since inclusion of this influence into the theoretical description is all but straightforward, and the interpretation of photoelectron distributions relies to a large extent on the applicability of the SFA in which the influence of the ionic field on electron trajectories is neglected. By comparison of measured photoelectron distributions as a function of $\Delta\varphi$ with predictions of the three-dimensional time-dependent Schrödinger equation and of a semi-classical trajectory model it was possible to trace back the influence of the Coulomb field to the timing of the wavepacket release with sub-cycle precision.

Still more information about the structural dynamics taking place in the target during the interaction with the laser field can be extracted from electron momentum distributions generated by two-dimensional tailored fields that were introduced in Section 3.3. Also, such two-dimensional fields open up largely enhanced possibilities for controlling this dynamics. We will first discuss the case of **orthogonally polarized two-color (OTC) fields**. This waveform was introduced by the author in 2005 for controlling the trajectories of field-ionizing electrons[234,235], see **Paper 1**. Using a semi-classical trajectory model the author could show that, depending on $\Delta\varphi$, electrons can be steered back to the parent ion such that they recollide under an angle that is different from the ejection angle. This way, targets can be probed by the rescattering electron wavepacket from adjustable angles. Moreover, and this is crucial, the recollision angle and the recollision energy sweep on an attosecond time-scale synchronized with the oscillations of the OTC field, as visualized in Fig. 6.2(b). Thus, laser sub-cycle time, energy and angle are strictly locked to each other by the laser field oscillations, which establishes an attosecond reference in the angular direction[236,237], see **Paper 2** and **Paper 3** for details. As time is mapped into angle and energy, this is somewhat reminiscent of the attoclock method discussed above. However, it is of uttermost importance to note that the mapping established by OTC fields exists for recolliding electron trajectories and, thus, in contrast to the attoclock, can be exploited for time-resolving (and also controlling) the processes of NSDI (see this Section, below), self-diffraction imaging (LIED) (see Section 6.2.4) and HHG (see Chapter 7). Moreover, the details of this mapping can be controlled by $\Delta\varphi$, and the duration of the recolliding wavepackets can be significantly shorter than for linearly polarized light[234].

OTC fields can, however, not only be employed for the investigation or control of processes that rely on electron recollision. Based on the two-dimensional structure of the laser field oscillations in the polarization plane, by virtue of $\boldsymbol{p}^\infty = -\boldsymbol{A}(t_i)$ electron wavepackets detached by the OTC field within different laser quarter cycles are observed in different momentum regions in the polarization plane[236,237], see Fig. 6.2(c). The author and co-workers were investigating the applicability of this sub-cycle time-to-momentum mapping with respect to the influence of the parent ion[151], see **Paper 4** for details. By comparison of experimental photoelectron distributions of neon recorded by coincidence momentum imaging with corresponding simulated distributions obtained by semiclassical and numerical solutions of the time-dependent Schrödinger equation, it was established that a resolution of a quarter optical cycle in the photoelectron trajectories can be achieved. Furthermore, it was found that depending on their sub-cycle birth time the trajectories of photoelectrons are affected differently by the ion's Coulomb field. While recollision trajectories are focused, direct trajectories are defocused or strongly scattered.

The influence of the Coulomb field on the trajectories of emitted electrons was also investigated in other theoretical[450] and experimental work[451]. In that experiment, OTC pulses with a substantially weaker 2ω pulse were used to streak photoelectrons depending on $\Delta\varphi$, rather than to really drive photoelectrons in two-dimensional space. This $\Delta\varphi$-dependent streaking with OTC fields was also employed in experiments that measured photons generated by HHG in order to obtain insight into the attosecond timing of the field-ionization process[452,453] (see further details on this subject in Chapter 7). Theory work showed that this problem can also, potentially more efficiently, be investigated by measuring photoelectrons streaked by an OTC field[454].

We now turn from the investigation of single ionization dynamics to controlling the emission of two electrons. For this process the author and co-workers could show that with OTC pulses it becomes possible to control the correlation between the two emitted electrons[189], see **Paper 5**. Electron correlation is of fundamental importance in physics, chemistry, and biology. For example, it is central for the formation of molecular structure, acts as a driving force behind chemical reactions, determines the (dynamical) behavior of solid-state materials, and also plays an essential role in biological processes such as radiation damage or light harvesting. The process of NSDI has been serving as a testbed for the investigation of electron correlation since its discovery[175]. In NSDI the two electrons can be ejected either via a correlated scenario, where both electrons are emitted into the same hemisphere, or via an anticorrelated scenario, where both electrons are preferentially emitted into opposite hemispheres. Using coincidence momentum imaging the author and co-workers could show experimentally that by tuning the shape of the electric field of the OTC pulses on the sub-cycle scale it is possible to control the two-electron emission dynamics in NSDI, and to dictate whether the two electrons are predominantly emitted in a correlated or anticorrelated manner. With the help of simulations based on a semiclassical trajectory model[328,330] it was possible to qualitatively explain the experimental results by sub-cycle changes of the recollision time that depend on the relative phase of the two colors.

Control over the recollision process in NSDI can also be gained with yet another type of two-dimensionally tailored fields, namely **counter-rotating two-color (CRTC) fields**, introduced in Section 3.3. Such control has been shown both experimentally[332,334] and theoretically[455]. Similar to OTC fields and in contrast to linearly polarized light, CRTC fields offer the possibility to control the recollision direction, and they also support control over the energy distribution of the recolliding electron wavepackets[334,456]. Examples of measured electron momentum distributions generated with CRTC fields are shown in Fig. 6.2(d). CRTC fields have so far been mainly used in HHG for the generation of higher harmonics with circular polarization[338]. But an exciting future application could be the generation of spin polarization of the emitted electrons[457,458] based on the fact that at the time the electron is set free, the field vector rotates as in circularly polarized light. The experiment shows that CRTC fields are highly efficient in generating such electrons by electron impact ionization[334] opening up opportunities for attosecond time-resolved collision studies with spin-polarized electrons.

Finally, we would like to mention that **elliptically polarized two-color (EPTC) fields** introduced in Section 3.3 can also be used to map details of the ionization process into the measured electron momentum distribution. One example is the observation of a Coulomb asymmetry in the multiple ionization of nitrogen molecules[335].

6.2 Attosecond electron wavepacket interferometry

One of the most powerful techniques in the optical sciences is interferometry. Its importance roots in the possibility to retrieve the relative phase of the interfering waves from interference structures recorded in an interferogram. The interferogram thus represents a mapping of the phase of the interfering waves into frequency and/or real space. Interferometry is certainly not limited to the optical domain and can also be exploited with matter waves, e.g., with neutrons[459] or electrons. Interferometry with electrons can be employed for obtaining sub-cycle temporal and also structural information about the ionization dynamics and therewith about the target from strong-field driven electron wavepackets (EWPs). The interference structures that are imprinted on measured electron momentum distributions contain phase-sensitive dynamical and structural information about the target (atom, molecule, etc.). This is because this information is encoded in the phases and amplitudes of the EWPs emitted during the ionization process[**226**]. The interference structures contained in the electron momentum distribution measured for a certain driving field can be easily calculated approximately within the strong-field approximation using semi-classical trajectory models as those discussed in Section 2.2.5. As with most other mapping methods, the biggest challenge is disentangling the different contributions to the interference structures and interpreting the information contained in them since, unfortunately, the structures corresponding to different types of interferences often overlap in momentum space.

Nevertheless, as compared with other techniques, EWP interferometry (EWPI) has its unique advantages. First, it grants access to the phase of EWPs and therewith to the phase of the bound states from which the EWPs are split off coherently during field-ionization[**226**]. As the phase is an elusive quantity, this information is difficult to obtain with any other method. Secondly, in EWPI not only the information contained in the rescattering EWPs can be exploited, but also those of the direct EWPs that are not driven back to the parent ion. This is a major advantage as compared to high harmonic spectroscopy. Thirdly, although high harmonic spectroscopy has been successfully used in obtaining structural dynamical information, such as attosecond multi-electron dynamics in molecules[414] or the shape of bound-state orbitals using molecular orbital tomography[415,460], obtaining phase-information from high-harmonic radiation is not straightforward and requires multiple observables[461]. In contrast, phase-information is *directly* available via interference structures from EWPs. Fourth, because electron momentum distributions are usually recorded using devices that also allow for simultaneous ion detection, e.g., a reaction microscope[401,462], in experiments electron interference structures can be easily obtained for a certain molecular fragmentation or dissociation channel, which allows in-depth investigations of multi-electron dynamics in molecules and disentangling the contributions of different molecular orbitals to the photoelectron spectrum[404].

In the following, we will in Sections 6.2.1 and 6.2.2 discuss the different types of interference structures that can be observed in electron momentum distributions. Section 6.2.3 will then discuss how phase-information can be obtained from measured EWPI structures.

6.2.1 Interference structures in electron momentum distributions

Although interferometry with electron wavepackets generated by multi-photon or single-photon ionization during sequences of delayed laser[463,464] and/or XUV[465–468] pulses has been considered for decades, exploitation of the interference structures that are caused by EWPs emitted on laser-sub-cycle times in a strong laser field is a relatively recent topic. Interestingly, the first experimental observations of such interferences were made using elliptically polarized light[154,469]. Later experiments with linearly polarized light, e.g. Refs. [470, 471], benefited from the availability of an improved resolution for measuring electron momentum and revealed various fine-scale structures throughout the measured three-dimensional electron momentum distributions. Rich structure in the electron momentum distributions was also shown by simulations[252,472,473]. Moreover, the simulations could also attribute several of the structures to certain dynamics, e.g., to diffraction of recolliding electron wavepackets on the ion's Coulomb potential. With the emerging capability of measuring electron spectra for certain CEP-values of few-cycle laser pulses it could be shown experimentally that a certain type of interference fringes are due to EWPs released during adjacent half-cycles within one pulse[474] — a configuration that has become known as the *attosecond double slit* because of its temporal analogy to Young's double slit in space.

The interference structures caused by the EWP emission in the attosecond double slit represented by two-cycle fields were investigated by Arbó and co-workers using semi-classical theory[229]. In 2010 this group of authors pointed out in a seminal paper[228] that the same type of interference structures should also be visible in electron momentum distributions generated by multi-cycle laser pulses. In that and subsequent papers[152,475] the authors could establish a unifying picture for the different types of interference structures based on the emission timing of the interfering EWPs in different half-cycles within one laser pulse. As the emerging equations bear a strong analogy to those that describe diffraction of a light pulse off a grating, this concept was called *the time grating*.

According to the time grating concept the sharp ATI peaks in the photoelectron energy spectrum that are spaced by the photon energy $E_0 = \hbar\omega_0$ are due to interferences of EWPs released with a time-delay of exactly one laser cycle $T = 2\pi/\omega_0$, i.e., with a frequency of ω_0. Thus, the well-known ATI peaks can be understood as interference fringes caused by pairs of EWPs released during different laser cycles. They are therefore also named **intercycle interferences** synonymously with the term ATI peaks (in electron energy spectra) or ATI rings (in two-dimensional electron momentum distributions). In addition to the intercycle fringes there also exist structures that are caused by interference of EWPs released during adjacent half-cycles within one laser cycle, called **intracycle or sub-cycle interferences**. As these EWPs are released with a much shorter delay than those leading to the intercycle peaks, the corresponding fringes are space more widely in energy. In an experiment both types of interferences are observed concomitantly, and thus the intercycle peaks are modulated by the intracycle fringes. Fig. 6.3(a) visualizes the emergence of these two types of interferences.

An experiment[476] similar to the one by Lindner et al.[474] used near-singe-cycle laser pulses with a stabilized CEP to realize a "true" attosecond double slit with only two contributing laser half-cycles and reported observation of the intracycle interferences based on their different momentum spacing as compared to that of the ATI peaks. A clear experimental separation of the inter- and intracycle peaks was realized in an experiment performed by the author and co-workers[226], see **Paper 8** for details. In this experiment tailored two-color pulses in $\omega/2\omega$-configuration were used to distinguish the contributions of the inter- and intracycle interferences to the electron momentum distribution based on their different sensitivity to the field-shape controlled by the relative phase $\Delta\varphi$ of the two colors: Because the energetic positions of the intercycle peaks that are caused by interference of EWPs released every laser cycle only depend on the oscillation period of the laser field, which is independent of $\Delta\varphi$ always $T = 2\pi/\omega_0$, their position in the momentum distribution stays constant with $\Delta\varphi$. In contrast, since the energies of the intracycle fringes are determined by the relative emission timing of the interfering EWPs *within* a laser-cycle, which varies as the sub-cycle evolution of the field-shape is changed by variation of $\Delta\varphi$, their positions strongly depend on $\Delta\varphi$. This is exactly what was observed in the author's experiment[226], see the experimental data in Fig. 6.3(b) and Refs. [**477**] and [478] for a theoretical analysis of the experiment.

Intercycle and intracycle fringes are not the only interference structures that can be observed in electron momentum distributions. In fact, there exists a whole family of different interference structures due to the many different combinations of pairs of quantum trajectories that end up at the same momentum and therewith can interfere, depending on their relative emission timing within the laser field oscillations and their subsequent field-driven dynamics. Huismans et al. reported[251]

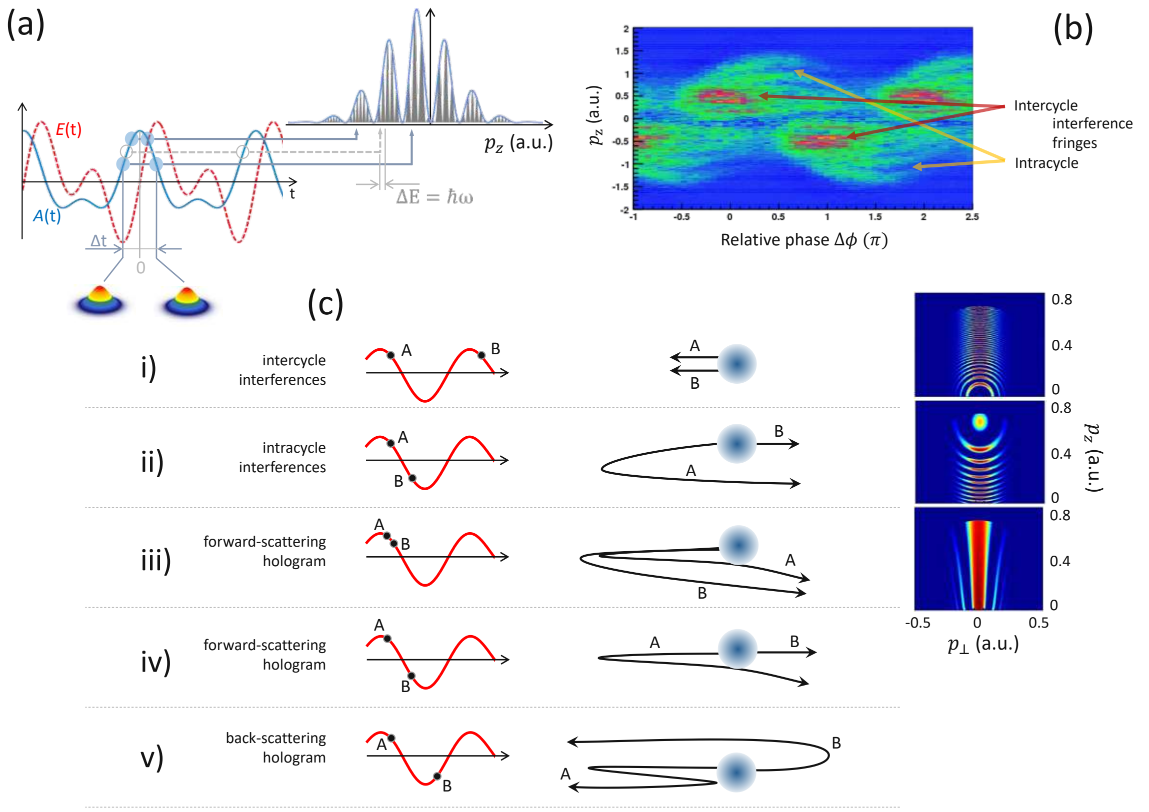

Figure 6.3: Depending on their emission time and trajectories electron wavepackets emitted by field ionization may interfere with each other and lead to interference structures in electron momentum distributions. (a) Visualization of the emergence of intercycle and intracycle interference structures. See text for details. (b) Measured electron momentum distributions along the laser polarization direction of a linearly polarized $\omega/2\omega$ field as a function of its relative phase $\Delta\varphi$. The dependence of the intracyle interference structures on the laser field shape allows to unambiguously disentangling them from the intercycle structures that do not depend on the field's shape. Adapted from Ref. [226], see **Paper 8** for details. (c) Trajectories of pairs of electron wavepackets leading to intercycle (i), intracycle (ii) and holographic (iii-v) interference structures. The left column indicates the wavepackets' emission times (denoted as A and B, respectively). The center column sketches their trajectories in space (the large blue dot indicates the photoion). The right column sketches examples of the corresponding electron momentum distributions for the intercycle (top), intracycle (center) and forward-scattering hologram (bottom) adapted from Ref. [251].

interferences that can be interpreted as a hologram. The existence of **holographic structures in electron momentum distributions** had actually been already predicted in 2004[252], and experiments on helium, neon and argon also showed holographic structures[470,471]. Later, holograms were studied, recorded and even exploited for measurements of structural dynamics in numerous experimental and theoretical works using linearly polarized[479–487] and circularly polarized[488] pulses, and even using OTC pulses[489].

Holography was invented in 1947 by Dennis Gábor[490]. Its central idea is to record an interference structure between a signal and a reference wave from which the object can be reconstructed upon illumination with another coherent wave. There exist several possibilities to obtain a hologram in the electron momentum distribution. The different types of holograms can be distinguished by the emission times and pathways of the signal and reference trajectories[251,479–487]. Fig. 6.3(c) sketches several possible trajectory configurations [labeled iii) to v)] that result in holographic structures and compares them to the trajectories leading to inter- [i)] and intracycle structures [ii)]. One possibility of obtaining a holographic structure is when both the signal and reference EWP are emitted within the same laser quarter cycle after the field maximum [iii)]. In that case the reference EWP follows a trajectory that after ionization starts with nonzero transverse momentum and reaches the detector without interaction with the ion core. The signal EWP follows a trajectory that starts with zero or very small transverse momentum and acquires non-zero transversal momentum upon rescattering with the ion core, after which it drifts to the detector. The interference of these two EWPs with the same final momentum produces a structure in which the interference fringes appear along the laser polarization direction and form a ”spider-like” or ”fork-like” structure[251,479–485], see momentum distribution in the right column in Fig. 6.3(c). As this holographic structure is caused by a signal-EWP that is scattered into its field-driven propagation direction, this possibility is called **forward scattering holography**. Another possibility for forward scattering holography that results in a different interference structure is that where the signal EWP follows a recolliding trajectory, but the reference EWP is emitted during the next laser quarter cycle and reaches the detector on a direct trajectory that does not reverse its direction [configuration iv) in Fig. 6.3(c)].

Analogously, holographic structures can also be observed when the signal EWP follows a back-scattering trajectory[480,486,487], see configuration v) in Fig. 6.3(c). The advantage of this **back-scattering holography** is that it is very sensitive to the structure of the scattering potential and can therefore be used to retrieve, e.g., the structure of a molecule[486,487]. This is in contrast to the forward scattering case, where the signal EWP contains dominantly information about the long-range Coulomb potential and therewith the hologram is of limited use for the reconstruction of finer structures contained in the the scattering potential. However, to extract the backscattering interference, the structure due to forward scattering needs to be overcome. Haertelt et al. have succeeded in this endeavour and extracted the different nuclear dynamics between H_2 and D_2 with sub-Ångström spatial and sub-cycle temporal resolution from measured holograms[487].

Other types of interferences Although so far only the intercycle (e.g. in Ref. [491]), intracycle (e.g. in Ref. [**226**]), and holographic structures (e.g. in Ref. [487]) have been exploited for measurements of attosecond timing, there exists still a large number of other possible combinations of EWP trajectories that cause interference structures in electron momentum distributions which could in principle be exploited for extracting temporal and/or structural information from them. A very instructive tool to visualize within the strong-field approximation the many types of interferences generated by linearly polarized light is the *Simpolator* applet written by Manfred Lein from the University of Hannover[492] that uses semi-classical trajectory models similar to those discussed in Section 2.2.5.

6.2.2 Interferences driven by tailored and two-dimensional fields

As both the intracycle and holographic interference structures are determined by the sub-cycle evolution of the driving laser field, tailored fields can be used to potentially suppress or enhance certain contributions. Above, we already mentioned a work by the author and co-workers[226] where the advantages of $\omega/2\omega$ **linearly polarized tailored waveforms** were exploited for enhancing and controlling intracycle interferences, see **Paper 8**. Additionally, the $\omega/2\omega$ field does not only allow for control over the relative timing of the interfering EWP by tailoring the laser-cycle-shape with the relative phase of the two colors, but it also leads to an $\Delta\varphi$-dependent pronounced asymmetry in the electron momentum distribution relative to zero momentum. This asymmetry allows to observe the interferences in momentum regions where the overlap with low-energy reso-

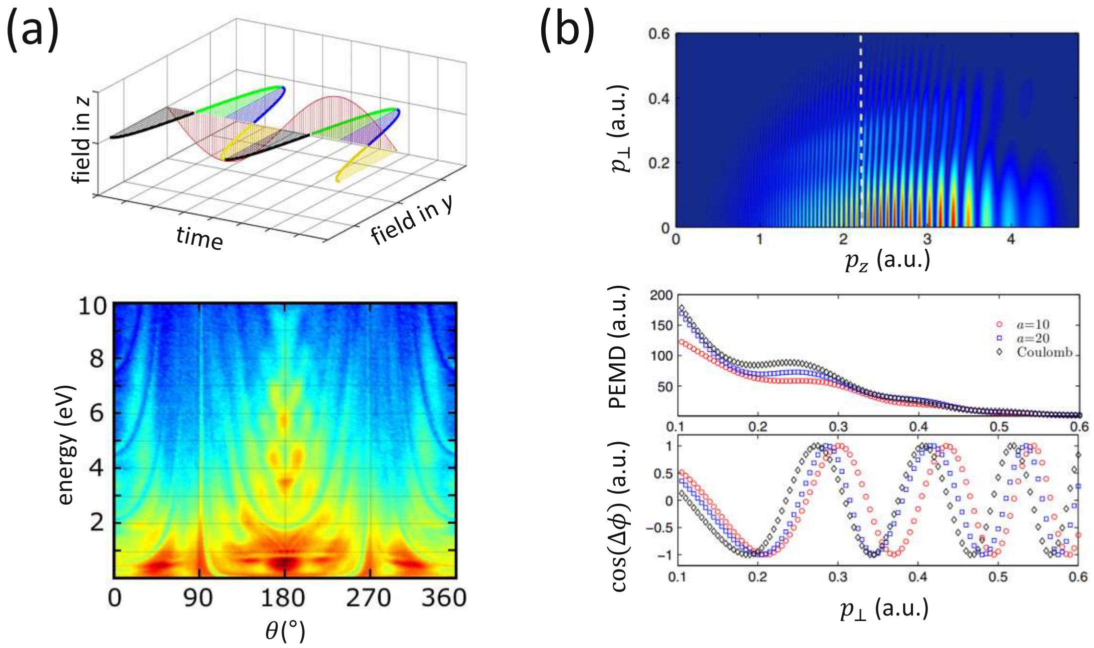

Figure 6.4: Controlling and reading electron wavepacket interference structures. (a) Interference structures observed and controlled with an OTC field. The top panel shows an OTC field composed of a field ω and its second harmonic 2ω with a certain relative phase of the two colors. Pairs of electron wavepackets released during certain quarter cycles of the field (encoded in color) interfere in certain quadrants of the electron momentum plane determined by the polar angle θ in the bottom panel. The structures visible around $\theta = 180°$ are due to intracycle interferences of electron wavepackets emitted during different quarter cycles of the OTC field (encoded in black and yellow in the top panel). The interferences can be turned on and off using the relative phase of the OTC field. Adapted from Ref. [**495**]. See **Paper 9** for details. (b) Phase-retrieval from a forward-scattering holographic interference structure. The holographic structure is clearly visible as modulations of the electron momentum distribution (top panel) along $p_\perp$, the direction perpendicular to the laser polarization direction [compare to the trajectories and momentum distribution of row iii) in Fig. 6.3(c)]. The center panel plots the modulation of the photoelectron momentum distribution (PEMD) due to the holographic wavepacket interference structure along a certain p_z (white line in top panel) for different parameters/shapes of the parent ion's binding potential. The bottom panel shows the phase oscillations across the hologram structure extracted from the PEMD from which the relative phase of the two interfering wavepackets can be extracted. The sensitivity of the interferogram to the shape of the potential is clearly visible in this plot. Adapted from Ref. [485].

nance structures ("Freeman resonances"[493]) can be avoided and leads to a broad spectral detection range and improved time resolution[**226**]. Combined with coincidence detection it is also possible to obtain interference structures for an ionization process controlled by $\Delta\varphi$ that eventually leads to a specific molecular fragmentation as the author and co-workers could recently show[**494**]. In the future this approach could be applied to obtain detailed information about the light-driven electron dynamics underlying molecular fragmentation, and thus should lead to improved capabilities for strong-field control of molecular fragmentations, see Section 8.6.

A still higher degree of beneficial control over the EWP trajectories and the corresponding interferences can be achieved with **two-dimensionally tailored waveforms**. In particular the two-dimensional character of OTC fields can be exploited beneficially. A number of theoretical works has investigated control over EWP interferences with OTC pulses. For example, it has been shown that with such pulses the back-scattering holographic structure can be enhanced[489]. It has also been shown that certain details of the ionization process such as the nonadiabaticity of the ionization rate and the nonzero initial velocities at the tunneling exit can be observed in the interferences[496]. Finally, it has been shown that by a Fourier transform of the interference structures in the electron momentum distribution different processes such as the excitation of valence electrons by the ionization process or the influence of the long-range Coulomb potential can be disentangled[497]. Control over interferences has also been investigated experimentally. For example, it has been shown that intracycle interference structures driven by OTC fields can be turned on and off using $\Delta\varphi$ as a control parameter[451]. In an experiment by the author and co-workers**[495]** OTC fields were used for disentangling a previously unobserved type of intracycle interference, where the interfering quantum pathways originate in non-adjacent quarter-cycles within a single cycle of the optical field, see Fig. 6.4(a) for a visualization of this interference structure. Variation of $\Delta\varphi$ allows to gradually turn on and off these structures and to move them to the other side of the momentum distribution, see **Paper 9** for details. The advantage that different types of interference structures can be distinguished by their different dependence on $\Delta\varphi$ has also been exploited in an experiment that succeeded in extracting time-delays in the emission of electrons that originate from different levels and hit a resonance during the ionization process[498].

Interference structures can also be observed in electron momentum distributions recorded with **elliptically/circularly polarized waveforms**. In fact, as mentioned above, the first experimental demonstration of interferences were made using elliptically polarized light[154,469]. Theoretical work predicts that these interferences created with circularly polarized pulses should exhibit a pronounced dependence on the CEP of few-cycle laser pulses[244]. So far, however, this CEP-dependence was not experimentally observed. Recent simulations[488] suggest that holograms recorded with circularly polarized laser pulses contain information about the molecular spatial structure and may even have a number of advantages over holograms recorded with linearly polarized pulses, e.g., enhanced clarity and easier discrimination from other structures.

6.2.3 Attosecond phase-retrieval from interference structures

While it is, in general, comparably easy to measure the intensity distribution of a wavepacket (optical, electron, etc.), it is very difficult to measure its phase. The interference structures observed in electron momentum distributions that we have discussed in Sections 6.2.1 and 6.2.2 contain information about the difference of the phases of the two interfering EWPs that they acquire during their respective emission and field-driven propagation processes until they eventually interfere at the detector. The interference of two EWPs $W_{1,2} = W_{1,2}(\boldsymbol{p}) = |W_{1,2}(\boldsymbol{p})|e^{i\alpha_{1,2}(\boldsymbol{p})}$ in the momentum space leads to an interference pattern

$$\begin{aligned} P(\boldsymbol{p}) &= |W_1(\boldsymbol{p}) + W_2(\boldsymbol{p})|^2 \\ &= |W_1|^2 + |W_2|^2 + 2|W_1 W_2| \cos(\Delta\alpha(\boldsymbol{p})) \\ &\propto |W_1(\boldsymbol{p})||W_2(\boldsymbol{p})| \cos^2\left(\frac{\Delta\alpha(\boldsymbol{p})}{2}\right) \end{aligned} \tag{6.1}$$

with $\Delta\alpha(\boldsymbol{p}) = \alpha_1(\boldsymbol{p}) - \alpha_2(\boldsymbol{p})$ the phase-difference of the two EWPs. Because $\boldsymbol{p}$ is to a large degree dominated by the strong driving laser electric field and can, within the SFA, be calculated as $\boldsymbol{p}_{1,2} = -\boldsymbol{A}(t_{1,2})$, where $t_{1,2}$ are the electron emission times, a certain interference structure $P(\boldsymbol{p})$ associated with a specific trajectory evolution contains phase-sensitive information on laser-sub-cycle times about the ionization and field-interaction process. Based on a suitable model this information can be extracted from measured distributions for a given laser field evolution and for a certain trajectory evolution. Additionally, since different types of trajectories sample different regions in momentum space and may probe the parent ion in different ways, as discussed in Sections 6.2.1 and 6.2.2, interference structures in the electron momentum distribution may contain also structural information about the target atom or molecule. Moreover, once the phase of the EWP is reconstructed, it might even be possible to obtain information about the bound-state from which the EWP is split off during ionization[226], as we will discuss in the following.

In principle, any type of suitable trajectory evolution that leads to a clear interference structure in the electron momentum distribution can be exploited for obtaining structural and/or dynamical information. As described in Section 6.2.1, the dominant structures are inter-, intracycle and holographic structures. It should be noted that there do exist experimental works that succeeded in reconstructing the phase of electron wavepackets[466,468], and also a theoretical proposal on how to use such data for reconstruction of the bound states from which they were emitted from[499]. But in these works the electron wavepackets were created by an entirely different process, namely by single-photon emission using XUV pulses, and thus these interferences do not contain information about the strong-field interaction process.

The first work that succeeded in retrieving the phase of EWPs from an electron momentum distribution created by the interaction of a strong field and an atom or molecule is, to best of the author's knowledge, the one performed by himself together with co-workers on **phase-retrieval from intracycle interferences**[226], see **Paper 8**. In that work not only the relative phase of the EWPs could be extracted from *measured* intracycle interference fringes, but even the sub-cycle phase-evolution of the bound state from which the EWPs originated could be reconstructed. This method will be discussed in detail below.

Structural and dynamical information can certainly also be extracted from holographic interference structures. However, so far, to the best of the author's knowledge, no experimental work exists that exploits this possibility. Theory work, e.g., the one by Zhou et al.[485], shows, however, that **phase-retrieval from holographic interference structures** created by near-forward rescattering EWPs can provide detailed access to the shape of the binding potential, see Fig. 6.4(b).

Phase-retrieval from intracycle interferences

The intracycle interference structures are due to the interference of two EWPs that each are emitted during one of two adjacent half-cycles of the laser field, as shown in Fig. 6.3(a). In Ref. [226] an $\omega/2\omega$ two-color field was used to measure interferences in the electron momentum distribution for helium and neon. Pronounced interferences are observed throughout the electron momentum distribution [Fig. 6.3(b)] for all relative phases $\Delta\varphi$. As shown in Fig. 6.3(b), the widest spacing of the intracycle structures and the highest momentum cut-off is observed for $\Delta\varphi = 0.5\pi$, where the laser field forms an attosecond double slit. Reconstruction is thus performed for this value of $\Delta\varphi$.

As described in detail in Ref. [226] and **Paper 8**, from the measured intracycle structures one can straightforwardly extract the interferogram $P(p_z) \propto \cos^2(\Delta\alpha(p_z)/2)$ with p_z the momentum component along the laser polarization direction, from which the interference phase $\Delta\alpha(p_z)$ can be extracted. By making use of the relation $p_z = -A(t_i)$ one can obtain from $\Delta\alpha(p_z)$ in the momentum space the evolution of the interference phase on sub-cycle times, $\Delta\alpha(\Delta t/2)$, where Δt is the time delay between the emission of the two wavepackets with time zero, $t = 0$, chosen to coincide with the zero of the laser field. Thus, from the intracycle interferences in the momentum space, the evolution of the relative phase of the two EWPs on attosecond times can be reconstructed. For the $\omega/2\omega$ pulse with $\Delta\varphi = \pi/2$ used in the experiment, delay times between 50 as $\lesssim \Delta t \lesssim$ 800 as can be probed with an estimated precision of better than 10 as at the longest delay times.

Before we discuss the information contained in $\Delta\alpha(\Delta t/2)$, we would like to strike out a key advantage of using the intracycle interferences for phase reconstruction. Because in the attosecond double slit the two EWPs are emitted during adjacent laser half-cycle such that the laser electric field $E(-\Delta t/2) = E(\Delta t/2)$, the phase of the EWPs obeys the symmetry $\alpha(-\Delta t/2) = \alpha(\Delta t/2)$ to a good degree of approximation, as has been confirmed by numerical simulations[226]. Consequently, the measured interference structure not only contains the relative phase of the two EWPs, but one can even obtain the phase of one of the two nearly identical EWPs, i.e., $\alpha(\Delta t/2) = \Delta\alpha(\Delta t/2)/2$. Thus, phase-reconstruction from the intracycle interferences is *self-referenced*. From a fundamental point of view this can be related to the well-known problem of achieving time-reversal in phase-reconstruction of, e.g., optical wavepackets: Referencing a wavepacket against itself in an auto-correlation arrangement cannot yield the phase of the wavepacket in the frequency space. This is due to the fundamental properties of the Fourier transformation which dictate that in frequency space only the difference of the two phases can be obtained. As a consequence the phase of two identical wavepackets cannot be measured straightforwardly in a self-referencing scheme. Obtaining the phase requires that the time is reversed for one of the wavepackets, which formally results in an auto-convolution rather than an auto-correlation. In this case the two phases add up and the phase can be obtained by simply dividing it by two. However, achieving time-reversal is in general not straightforward. The self-referencing quality of the intracycle EWP interferometry is thus a remarkable property and of uttermost practical importance.

Which information can now be obtained from the measured attosecond phase-evolution of the emitted EWP $\alpha(\Delta t/2)$? Because field-ionization is a coherent process, the emitted EWP inherits phase-information from the bound state that it is detached from[253]. This is the basis of HHG, where the radiation-emitting dipole oscillations are created by a coherent superposition of the recolliding EWP with the bound state. Subtracting all additional contributions to the phase that the EWP gains during the field-interaction in the continuum, yields the phase the EWP picks up from the bound state as it is detached from it, denoted as $\alpha_B(\Delta t/2)$. These additional contributions are due to the interaction of the free electron with the laser field, the corresponding phase is known as the Volkov phase $\alpha_V(\Delta t/2)$, and the phase due to the force of the Coulomb potential, which can be approximated as the Coulomb eikonal phase $\alpha_C(\Delta t/2)$[152]. The phase of the bound state is thus obtained as

$$\alpha_B(\Delta t/2) = \alpha(\Delta t/2) - \alpha_V(\Delta t/2) - \alpha_C(\Delta t/2). \tag{6.2}$$

From the measured $\alpha_B(\Delta t/2)$ detailed insight into the bound-state dynamics during its sub-cycle evolution can be gained. As shown in Ref. **[226]**, the slope of the measured $\alpha_B(\Delta t/2)$ varies over Δt and shows a small slope for small $\Delta t/2$ and a larger one for larger values of $\Delta t/2$. The temporal phase-evolution of a quantum state, $\phi(t) = E_n t$, depends linearly on the energy that this state evolves; its slope thus determines the "effective binding energy". The measured phase-evolution $\alpha_B(\Delta t/2)$ thus shows that the EWP is inititally, close to the zero crossing of the electric field at $\Delta t \approx 0$, split off from state(s) with small binding energies. Only at later times the slope approaches the binding energy I_p of the helium atom and the EWP is split off from the ground state. This deviation from an unperturbed linear evolution, which is assumed, for example, in the strong-field approximation for negligible groundstate depletion[500], reflects the dynamical polarization of the valence electron wavefunction or, equivalently, the transient population of excited states with lower binding energies. Because the transient population in this measurement is $< 1\%$[226], the clear visibility in the phase-evolution demonstrates the high sensitivity of this self-referenced method for wavefunction retrieval.

The temporal evolution of a quantum system with sub-10-attosecond precision and high sensitivity is, however, still not the only quantity that can be extract from the intracycle interferogram. By comparison to the wavefunction's phase extracted from a numerical simulation solution of the time-dependent Schrödinger equation (TDSE) at certain positions $\boldsymbol{r}_0$,

$$\alpha_B(\Delta t) \simeq \arg\left[\Psi(\boldsymbol{r}_0, \Delta t/2)\right], \tag{6.3}$$

can be used to measure the point where the EWPs probe the bound state's wavefunction. Moreover, the bound-state phase, α_B, contains also structural information on the state to be ionized.

Because the two interfering EWPs are released during different half-cycles with opposite sign of the laser electric field $E(t)$ *and* into opposite directions in configuration space, they also carry parity information about the bound state. It could be shown that for the even parity of the helium ground state (1s) the relative phase inherited by the two EWPs is zero, while the odd parity of the neon ground state (2p) introduces an offset of π on top of the dynamical phase evolution[226].

Intracycle EWP-interferometry can thus serve as a tool to extract structure and dynamics of the valence electron cloud in atoms and molecules on a sub-10-attosecond time scale, providing a complementary approach to higher-order harmonic spectroscopy[414,415,501] and single attosecond XUV pulse spectroscopy[502,503].

6.2.4 Laser-induced electron diffraction (LIED)

The previous Sections have shown that temporal and structural information is encoded in the interference structures contained in measured electron momentum distributions. While extraction of the attosecond temporal information is possible in an intuitive way, as described in detail in Section 6.2.3, extraction of the structural information from, e.g., holographic or intracycle interference structures is less straightforward. A very direct approach to extract structural information about the target from interferences in electron momentum distributions is electron diffraction. Conventional electron diffraction (CED)[504] uses energetic, multi-kilovolt, electron beams to record a diffraction pattern of the molecular gas sample and to obtain information about the molecular structure with pm spatial resolution. The temporal resolution of CED is, however, currently limited to hundreds of femtoseconds mainly due to Coulomb repulsion in the electron bunch used for diffraction[505]. As we will discuss in the following, the recollision process driven by strong laser fields opens up the possibility to realize the concept of laser-induced electron diffraction (LIED)[170,239,506,507]. In analogy to CED, the recolliding electrons scattering off the target molecule can be used to obtain structural information. While measurements using LIED necessitate some additional steps for retrieving the structural information about the target because of the strong laser field that drives the impinging electrons, an advantage of LIED over CED is that, in addition to pm spatial, few-femtosecond or even attosecond temporal resolution can be obtained.

Imaging with high-energy rescattering electrons The overall idea of LIED is that electrons returning to the target as a sub-cycle burst of energetic electrons with very high peak current density[416] can be used for sub-cycle imaging of the molecular structure. The spatial resolution obtained by diffraction is ultimately determined by the de Broglie wavelength of the scattering wave, which for recolliding electrons is given by $\lambda_e = 2\pi/\sqrt{2E_r}$, with $E_r = \boldsymbol{p}_r^2/2$ the recollision energy of the scattering electron. The recollision momentum $\boldsymbol{p}_r$, as derived in (2.7), is determined by the laser vector potential at the times of ionization and recollision according to

$$\boldsymbol{p}_r = \boldsymbol{p}(t_r, t_i) = \boldsymbol{A}(t_r) - \boldsymbol{A}(t_i), \tag{6.4}$$

and scales as $E_r \propto E_0^2 \lambda_o^2$ with E_0 the laser peak field strength and λ_o the laser wavelength, see Section 2.2.3. Recollision energies on the order of 100 eV are easily possible, corresponding to de Broglie wavelengths of about 1 Å. Based on these considerations the concept of diffraction imaging of molecules with recolliding electrons was first suggested in Ref. [508]. In that work diffraction patterns from forward scattering electrons were considered. However, later work pointed out that the elastically rescattering electrons that form the high-energy end of the ATI spectrum (HATI; see Section 2.2.4) in the range $2U_p < E_e < 10U_p$ are more suitable for realizing LIED[252], even though they are much less abundant. The two main reasons are[239,252–254,472,506,507], first, that the forward scattering electrons overlap with the direct electrons in the energy range $\leq 2U_p$, which due interference between these two groups of electrons makes the analysis of this portion of the momentum distribution very complicated. Second, for large scattering angles the electrons undergo a large momentum transfer $\boldsymbol{q} = \boldsymbol{p} - \boldsymbol{p}_r$, where $\boldsymbol{p}$ is the electron momentum after the scattering measured using, e.g., a REMI (Chapter 5), and $\boldsymbol{p}_r$ is the momentum of the recolliding electron at the time of scattering. As can be inferred from Fig. 6.5(a), the magnitude of the momentum transfer can be written as $|\boldsymbol{q}| = 2p_r|\sin(\theta/2)$ with θ the angle between the incidence direction of the recolliding electron and angle of detection. Thus, analysis of electrons scattered at large angles leads to a much higher momentum transfer. A 100 eV electron scattered at $\theta = 180°$ leads to a similar $\boldsymbol{q}$-value as a multi-kilovolt electron in a CED experiment scattered in the forward direction under typical small angles of $\theta \lesssim 5°$. By analysis of the HATI electrons it has been shown that LIED can indeed be used to obtain molecular structural information with a spatial resolution of a few pm using techniques originally developed for the established method of CED[254,255,509].

Extracting structure from electron momentum distributions The goal of CED experiments is to obtain the structure of a molecule, i.e., the positions of the atoms and their respective distances. The first step of reconstructing the atomic positions from CED experiments is to retrieve the so-called elastic scattering differential cross-sections (DCS)[504]. Fig. 6.5(b) shows an example of a measured DCS for N_2. If the electrons only scatter from the atomic cores, the independent atom model (IAM) can be applied to reconstruct the molecular contrast factor (MCF) from the DCS[254,507]. The MCF is the ratio of the molecular interference term in the DCS to the contributions representing the incoherent sum of scattering cross-sections from all the atoms in the molecule. Molecular structural information is only contained in the interference term. Examples of MCFs extracted from measured DCS are shown in Fig. 6.5(c) and (d). From the MCF the bond lengths can finally be extracted by fitting procedures. The underlying force that mediates the scattering of an electron off a molecule is the Coulomb repulsion between the impinging electron and the core and valence electrons. Application of the independent atom model requires that the electrons dominantly scatter from the atomic cores rather than from the bonding valence electrons which should look like transparent. Achieving core penetrating collisions in LIED requires high enough recollision energies, which signifies that mid-infrared laser wavelengths are used best for LIED. At the same time, long wavelengths lead to a better applicability of classical methods for enabling extraction of field-free diffraction data from the electron momentum spectra.

Time-resolving structural changes Experiments with mid-infrared wavelengths around 2 µm[254] and 3 µm[255,509,510] have succeeded in time-resolved measurements of bond lengths of various molecules with a precision of a few pm. In these experiments the opportunity to take snapshots of the molecular structure after a certain delay to the ionization step provided by the recollision process is exploited. The ionization step at t_i that detaches the electron used for imaging, triggers the dynamics, e.g., a molecular stretch motion[254,255,509]. The resulting change in molecular structure that takes place during the time $\tau = t_r - t_i$ is then probed at t_r by the rescattering event that creates a diffraction image from which the DCS and MCF are extracted. The ionization thus acts as the pump event, the recollision is the probe event. Because the ionization events take place around the peaks of the electric field oscillations and the recollisions happen about three quarter-oscillation cycles later, as explained by Fig. 2.4 and the text referring to it, the pump-probe delay τ depends on the wavelength of the laser field. Variation of the laser wavelength varies the pump-probe delay τ.

Quantitative rescattering theory Extraction of *field-free* electron-ion differential cross-sections (DCS) as a function of the scattering angle θ for a certain electron impact momentum p_r from the measured LIED momentum distributions is possible using the quantitative rescattering theory (QRS)[506,507,511–514]. The QRS states that field-free DCS $\sigma(p_r, \theta)$ can be extracted from measured HATI electron momentum distributions $D(\boldsymbol{p})$ using the relation

$$D(\boldsymbol{p}) = W(p_r)\sigma(p_r, \theta), \tag{6.5}$$

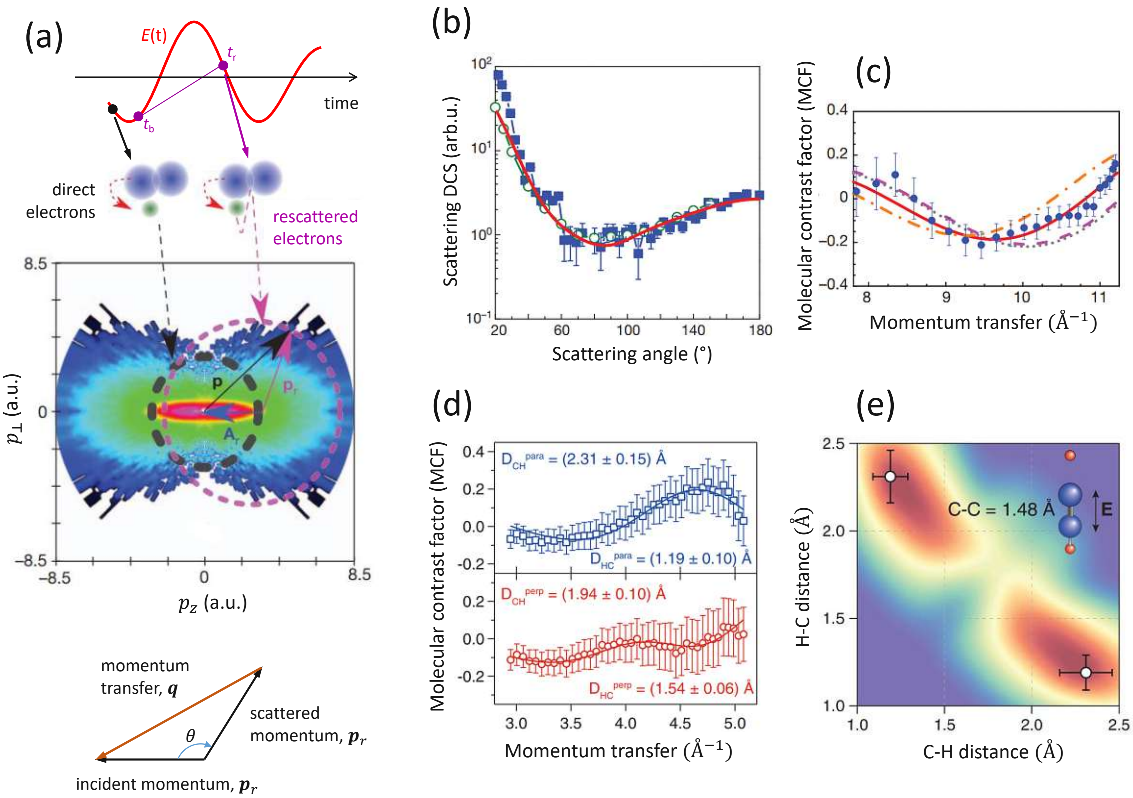

Figure 6.5: Laser-induced electron diffraction (LIED). (a) Imaging by LIED uses rescattering electrons in the energy range $2U_p < E_e < 10U_p$ (HATI electrons), shown in violet in the top panel. The direct electrons in the energy range $E_e < 2U_p$ (black) do not contain spatial information. The information about the molecular geometry recorded by the HATI electrons upon rescattering is contained in electron momentum distributions (center panel, adapted from Ref. [254]). Timing in these momentum distributions is encoded via the rescattering time t_r and momentum p_r on circles shifted along the laser polarization direction by the laser vector potential A_r at the rescattering instant. Decisive for the spatial resolution is the magnitude of the momentum transfer $|\boldsymbol{q}| = 2p_r|\sin(\theta/2)$ (bottom panel). (b) From the measured electron momentum distribution in (a) the field-free electron-ion differential cross-sections (DCS) can be extracted. The example (adapted from Ref. [254]) shows a DCS for N_2 measured with a laser pulse with a wavelength of 2 µm evaluated at $|\boldsymbol{p}_r| = 2.71$ a.u. (blue squares). The green circles are the results from a measurement using conventional electron diffraction (CED). The red line constitutes simulated data. (c) From the DCS in (b) the molecular contrast factor (MCF) is obtained. See text for details. The red line is the best fit to the measured data (with error bars) converted from (b). The orange and purple lines show results where the best-fit bond-length is varied by ±5 pm. The gray line is simulated data for the equilibrium bond length of N_2. (d) Molecular contrast factor (MCF) for aligned acetylene measured with a laser with a wavelength of 3.1 µm. The top panel shows parallel, the bottom panel perpendicular alignment of the acetylene molecules with respect to the laser polarization direction. Adapted from Ref. [255]. (e) Bond lengths extracted from the MCF in the top panel of (d) (shown with error bars) in comparison with numerical results (false color plot). The measured C-H distance of 2.31 Å shows that the C-H bond stretches considerably from its equilibrium value (1.07 Å) during the excursion time (9 fs) of the recolliding trajectory that is evaluated to obtain the MCF.

where $W(p_r)$ represents the flux of field-driven electrons that impinge on the molecule. It can be associated with the recolliding electron wavepacket integrated over the laser pulse duration and the laser focus volume. The momentum $\boldsymbol{p}$ in (6.5) denotes the momentum of the measured electrons, and p_r and θ are the magnitude of the recolliding electron at the time of scattering and the scattering angle, respectively, as defined above and sketched in Fig. 6.5(a). The key points of the QRS, which have been validated by comparison with 'exact' numerical data obtained by solving the time-dependent Schrödinger equation[506,507,511–514] and with experimental data on both atoms and molecules[254,255,509,510,515–519], are as follows: (i) the recolliding wavepacket $W(p_r)$ can be obtained using the SFA transition amplitude (2.37). $W(p_r)$ has been found to a good approximation independent of the direction perpendicular to the laser polarization direction ("plane wave-like") and therefore only depends on p_r. (ii) the influence of the laser field on the scattering electron and the sub-cycle probe-timing involved in the recollision can be described using classical relations as described in Section 2.2.2. (iii) the such obtained $\sigma(p_r, \theta)$ from (6.5) for a certain impact momentum p_r is *independent* of the laser parameters intensity, pulse duration and wavelength. The only role of the laser in LIED is to drive the returning electrons for scattering with momentum p_r.

Procedure to extract structural information In detail the procedure to obtain $\sigma(p_r, \theta)$ from the measured HATI electron momentum distribution $D(\boldsymbol{p})$ is as follows. One starts by selecting a certain electron impact energy E_r, e.g., 100 eV or 150 eV, at which $D(\boldsymbol{p})$ is evaluated. This defines the electron impact momentum $p_r = \sqrt{2E_r}$. Electrons impinging on the molecule with p_r are then elastically scattered under different angles θ. Immediately after rescattering, these electrons are thus found on a spherical surface (a circle in two-dimensions) with radius p_r and its centre at the origin in momentum space. After rescattering an electron is accelerated by the laser field. Therefore, in the final momentum distribution the sphere (circle) is displaced by $\boldsymbol{A}(t_r)$, as visualized in Fig. 6.5(a). Thus, to evaluate the $D(\boldsymbol{p})$ for a certain p_r along a given sphere (circle) defined by

$$\boldsymbol{p} = \boldsymbol{p}_r + \boldsymbol{A}(t_r), \tag{6.6}$$

the return time t_r must be chosen. Because of relation (6.4), for a certain p_r one should therefore also know the ionization time t_i, which requires the assumption of a certain recolliding trajectory class (either long or short). There is no unique recipe for this, but because of the higher ionization rate at earlier times after the field maxima, the choice of the long trajectories has been proposed[254]. However, since to some extent both trajectory classes contribute, a certain uncertainty is introduced for the pump-probe delay $\tau = t_r - t_i$ when performing time-resolved measurements using LIED[254,255,509]. It has been argued that for electrons that emerge with energies $> 4U_p$ a good choice for the recollision momentum is $p_r = \sqrt{2 \times 3.2U_p} = 1.26A_0$ with $A_0 = E_0/\omega_o$ the vector potential corresponding to the laser peak field strength E_0[506,507,513,517]. The reason is that scattered photoelectrons that exhibit the highest energies of $10U_p$ are those that have recollided with the molecule with roughly the highest energy of $3.2U_p$. If p_r is chosen as $p_r = 1.26A_0$, relation (6.6) leads to the simple relation $\boldsymbol{p} = \boldsymbol{p}_r \pm A_0\boldsymbol{e}_z = \boldsymbol{p}_r \pm (p_r/1.26)\boldsymbol{e}_z$, where we have assumed the laser polarization direction along z, and the $+$ and $-$ signs correspond to electrons that, before scattering, are moving toward the ion from the directions $z > 0$ and the $z < 0$, respectively. Whatever the choice for the shift of the sphere (circle) due to the vector potential at the time of rescattering, $\boldsymbol{A}_r$, the intensity of $D(\boldsymbol{p})$ is then evaluated along this sphere (circle) given by $\boldsymbol{p} = \boldsymbol{p}_r + \boldsymbol{A}_r$ as indicated in Fig. 6.5(a). Field-free DCS $\sigma(p_r, \theta)$ for certain p_r over θ within a momentum range corresponding to HATI rescattering electrons can then be obtained using (6.5). From these DCS the molecular contrast factor (MCF) is extracted and evaluated as described above.

Practical considerations for LIED experiments In practice, a number of points have to be considered when using LIED for time-resolved probing of molecular structure. For example, in a LIED experiment the returning electron scatters off its parent ion rather than off the neutral. As upon removal of an electron there are many possibilities for the intra-molecular ion electronic density distribution that meditates the scattering event, and additionally the electronic charge might also undergo very fast dynamics (e.g., charge density oscillations), this would greatly complicate the structural analysis. However, diffraction images taken with sufficiently high recollision energies as they can be obtained using long wavelength drive pulses, result in core penetrating hard collisions for which the exact shape of the valence electron density distribution is to a good approximation irrelevant. Thus, the structure of a molecule as given by the positions of its atoms can be reconstructed using the independent atom model (IAM). Further, in LIED the electron flux that scatters off the molecule and creates the diffraction pattern is taken from the molecule itself by ionization in the laser field. Thus, the flux of the returning electron wavepacket which is proportional to the tunneling ionization rates depends on the orientation of the molecules. Additionally, it has been shown that the continuum electron wavepacket carries spatial phase structure immediately following ionization[483], which might influence the diffraction pattern resulting from the scattering event. The orientation dependence of the ionization rate must therefore be considered in LIED experiments. Another point to be considered in the interpretation of LIED experiments are excitations that may occur during the scattering event. These inelastic scattering contributions might overlay the diffraction pattern created by elastic collisions and may introduce errors. Their contributions have, however, shown to be of little effect[254]. Also, one should not forget that in linearly polarized light consisting of several field oscillation cycles the electron returns to the parent multiple times. At each return the electron can scatter off the parent ion creating multiple contributions to the diffraction pattern. By choosing to work with the back-scattered high-energy HATI electrons, only the first, third, fifth, etc., returns contribute. The second, fourth, etc., returns are scattered into the other direction. Although at the third return the electron wavepacket has experienced already strong spreading and thus its intensity and therewith scattering contribution is small, a single recollision event would be preferred. To obtain such a single scattering event the use of OTC fields[326,327] or single-cycle laser pulses has been suggested.

Example implementations LIED, as described, has the potential to probe the structure of molecules with pm spatial and, in principle, attosecond temporal resolution. In practice, as pointed out above, the temporal resolution is somewhat limited by the problem of selecting a certain recollision trajectory, and also by the necessary electron statistics that requires the selection of a range of momenta around a certain circle corresponding to $\boldsymbol{p} = \boldsymbol{p}_r + \boldsymbol{A}(t_r)$. Recently, several stunning experiments succeeded in implementing LIED for the extraction of molecular structure from measured electron momentum distributions with a temporal resolution of around and better than one femtosecond[254,255,509]. In the work by Blaga et al.[254] the bond length of oxygen and nitrogen molecules is extracted from electron momentum distributions measured with three different mid-infrared wavelengths (1.7, 2.0 and 2.3 µm) with a spatial resolution of about ±5 pm. The wavelength variation corresponding to variation of the pump-probe delay permits to trace the stretch motion of the studied molecules initiated by the single ionization step over a time interval of about 2 fs around an instant of 5 fs after the ionization. Fig. 6.5(c) shows the molecular contrast factor (MCF) extracted from the measured DCS shown in Fig. 6.5(b), obtained with 2.0 µm pulses.

In the work by Wolter et al.[255] a laser with a wavelength of 3.1 µm is used to take a snapshot of the acetylene molecule with a similar spatial resolution as in the work by Blaga et al. while it undergoes fragmentation during the reaction $C_2H_2^{2+} \rightarrow C_2H^+ + H^+$ that is initiated by double ionization during the laser pulse. The long laser wavelength permits to probe the departure motion of the proton H^+ with a temporal resolution of better than 1 fs about 9 fs after the second ionization step that initiates the fragmentation. The molecules are probed for perpendicular and parallel alignment with respect to the laser polarization direction. The alignment is controlled by impulsive alignment with a preceding laser pulse that exhibits a wavelength of 1.7 µm. Fig. 6.5(d) shows the measured MCF for acetylene aligned parallel (top) and perpendicular (bottom) to the laser polarization direction. The alignment of the molecular axis with respect to the strong, ionizing

3.1 µm-pulse allows controlling the fragmentation process and therewith allows to resolve different bond dynamics for molecules aligned parallel and perpendicularly, respectively. Fig. 6.5(e) shows C-H and H-C distances for parallel alignment extracted from the MCF. Control of fragmentation reactions using molecular alignment will be discussed in greater detail in Section 8.3.

Finally, it should be noted that under certain conditions the procedure for extracting the DCS (and from this quantity the molecular bond lengths) from measured data can be simplified. Instead of analyzing the angular dependence of the diffraction pattern at a fixed p_r, one can fix the scattering direction and analyze the electron energy spectrum measured for aligned/oriented molecules[520]. This method was dubbed fixed-angle broadband laser-driven electron scattering (FABLES).

7

Optical attosecond mapping using tailored waveforms

The previous Chapter 6 discussed how attosecond and Ångström information can be extracted from electron momentum distributions generated by strong laser waveforms. We have established the mapping provided by the laser field as the key for extracting temporal resolution. High-harmonic generation (HHG), that is the generation of XUV/X-ray radiation with a strong laser field, builds on the very same field-driven recollision process that also underlies, e.g., the high-energy part of ATI photoelectron momentum spectra (see Section 2.2.4). Thus, it should not come as a surprise that very similar mapping methods can also be adopted for the extraction of attosecond and Ångström information from XUV/X-ray spectra generated by HHG. This Chapter discusses such mapping methods that build on optical (as opposed to electronic) carriers of information. Note, that in this Chapter we will not discuss methods for the production of XUV/X-ray pulses by HHG. This topic is discussed in Chapter 4.

Using the HHG process for extraction of dynamical and structural information about the field-driven target that generates the HH radiation (atom, molecule, solid) during the interaction with a strong laser field at the place of the interaction, i.e., *in situ*, has in fact grown into a large field of research during approximately the last two decades. There exists a whole plethora of works on *self-probing* of atoms, molecules, etc., with HHG, and techniques known as *high-harmonic spectroscopy* that allow tracing dynamics in the target over certain periods of time have been developed. It is therefore entirely beyond the scope of this Chapter to provide a comprehensive coverage of methods and works that have used HHG as an *in situ* probe technique. We are therefore forced to leave aside several important topics. For example, we will not discuss how to use HHG for obtaining insight into dynamics in solids[45,115,121,521], for the extraction of chiral properties of molecules[522], or mapping of dynamics into space using HHG with spatiotemporally coupled light fields (a technique known as *attosecond light houses*)[523–527]. In our discussion we will put our focus on *self-probing* of atoms and molecules. Special attention will be given to methods and works that build on the use of tailored waveforms, e.g., $\omega/2\omega$ or OTC pulses, for probing atoms and molecules using the HHG process. For a broader coverage of information extraction using HHG we refer to the numerous review papers, e.g., Refs. [21, 149, 238, 417, 528, 529], which mostly focus on atoms and molecules; Ref. [530] for a detailed insight into HHG in solids[530]; or Ref. [524] covering HHG using attosecond light houses.

7.1 Concepts of mapping with HHG

Because HHG is based on the interference of the rescattering electron wavepacket with the wavefunction remaining bound during ionization, as outlined in Section 2.2.4, the emitted photons during the 'recombination' step carry spatial and, via the mapping between the recollision and ionization times, $t_r = t_r(t_i)$ provided by the laser field (Section 2.2.3), also attosecond temporal information about the HHG process. In the following, as an overview over and introduction into the topic of *optical attosecond mapping*, we will describe the most frequently applied methods that make use of the opportunity to map spatial or/and temporal information contained in the HH radiation.

7.1.1 Mapping structure — orbital tomography

In HHG an electron wavepacket returning to the parent ion with an energy E_r generates high-harmonic radiation $\boldsymbol{\epsilon}(t)$ upon interference with the bound state wavefunction $|\psi_0(\boldsymbol{r})\rangle$, as described by (2.47). Owing to the the electron wavepacket's small de Broglie wavelength $\lambda_e(t) = 2\pi/\sqrt{2E_r}$ on the order of or even smaller than the bound state's dimensions, the emitted HH radiation contains information about the spatial structure of $|\psi_0(\boldsymbol{r})\rangle$. Thus, by recording the HH spectrum $\boldsymbol{\epsilon}(\omega) = \mathfrak{F}(\boldsymbol{\epsilon}(t))$ one might be able to measure the bound state's spatial structure, provided there is a way to extract this information from $\boldsymbol{\epsilon}(\omega)$. Under certain approximations this extraction is indeed possible, as we will sketch in the following. Methods that retrieve structure from high-harmonic radiation are usually summarized under the term *orbital tomography*. We note, because the spectrum is complex valued, measurement of $|\boldsymbol{\epsilon}(\omega)|^2$ is not sufficient in the general case. Methods for measuring the spectral phase will be discussed below. Using HH radiation for obtaining spatial information about the parent ion is somewhat complementary to the method of laser-induced electron diffraction (LIED, see Section 6.2.4) as it provides insight dominantly into the valence electron structure, while LIED seeks to probe the core atomic structure.

To get the essence of how the spatial structure of $|\psi_0(\boldsymbol{r})\rangle$ can be reconstructed from the measured HH spectrum, we start from expression (2.54), which describes that within the SFA $\boldsymbol{\epsilon}(\omega)$ can be obtained as a sum over quantum trajectories s,

$$\boldsymbol{\epsilon}(\omega) = -i\omega^2 \sum_s a(\boldsymbol{p}^s)\boldsymbol{d}^s_{\text{rec}}(\boldsymbol{p}^s, t^s_r). \tag{7.1}$$

In this expression $\boldsymbol{d}_{\text{rec}}(\boldsymbol{p}^s, t^s_r)$ is the recombination dipole matrix element, evaluated at the stationary momentum $\boldsymbol{p}^s$ and recombination time t^s_r, and $a(\boldsymbol{p}^s)$ is the complex amplitude of a continuum electron wavepacket that can be written as

$$a(\boldsymbol{p}^s) = -i\frac{1}{(t^s_r - t^s_i)^{3/2}}\left[\det(\tilde{S}'')\right]^{-1/2} \boldsymbol{d}_{\text{ion}}(\boldsymbol{p}, t^s_i)e^{iS(\boldsymbol{p},t^s_i,t^s_r)-i\omega t^s_r}, \tag{7.2}$$

with $\boldsymbol{d}_{\text{ion}}(\boldsymbol{p}, t_i)$ the ionization dipole matrix element defined in (2.49), $S(\boldsymbol{p}, t_i, t_r)$ the semi-classical action defined in (2.48), and $\tilde{S}''$ is the second derivative of $\tilde{S}$ with respect to ionization and recombination time, t_i and t_r, respectively, where $\tilde{S}(\boldsymbol{p}, t_i, t_r) = S(\boldsymbol{p}, t_i, t_r) - \omega t_r$.

The index s in (7.1) runs over all possible quantum trajectories that contribute to photon emission at the frequency ω as determined by the points of stationary-phase obtained by solving (2.53). As discussed in Section 2.2.5, for a sinusoidal, linearly polarized laser field one can find two classes of recolliding trajectories that lead to the same recollision energy, the short and the long trajectories. However, for comparison with experiments, in most cases only one of the two needs to be considered. This is because the HH spectrum observed in the far-field is the phase-coherent sum over all emitting dipoles in the focus of the laser beam that generate the HH radiation. By proper choice of the phase-matching conditions for the HH radiation it is possible to dominantly observe

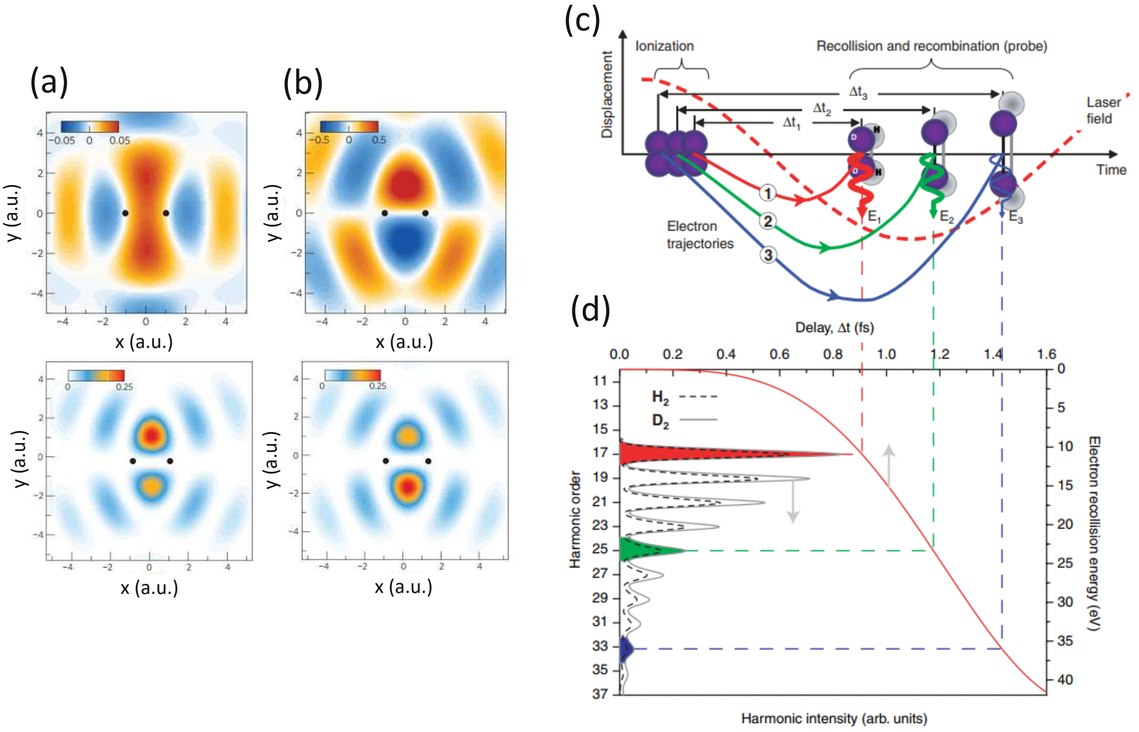

Figure 7.1: Mapping structure and dynamics with high-harmonic generation. (a),(b) Tomographic reconstructions of bound orbitals and holes in N_2 using the measured intensity and phase of high harmonic radiation; adapted from Ref. [415]. The top panels in (a) and (b) show the reconstructed HOMO and HOMO-1 orbitals of N_2, respectively. The bottom panels show the squared sum (a) and difference (b) of the wavefunctions in the respective top panels. These can be interpreted as the hole density in the ion at the instants of recollision and emission, respectively. See Section 7.1.1 for details about tomographic reconstruction of orbitals. (c),(d) Mapping sub-cycle dynamics with high-harmonic generation. (c) Trajectories with different recollision energies return at different times, cf. Fig. 2.4. Thus, sub-cycle time is mapped into the energy of high-harmonics (d). See Section 7.1.2 for further details. The examples in panels (c),(d), adapted from Ref. [241], show how this mapping can be exploited for measuring the few-femtosecond vibrational motion in H_2 and D_2.

the contributions of only one class of quantum trajectories, e.g., the short ones[160]. Also, it is mostly tolerable to only consider the first recollision instant and to neglect later ones. Still, even with these approximations, there exist two quantum trajectories within one laser cycle (one launched during each half-cycle) which lead to the same recollision energy and therewith the same photon energy. These two trajectories approach the parent ion from opposite sides. If we introduce the momentum of the recolliding electron at the time of recombination as $\boldsymbol{k} = \boldsymbol{p} + \boldsymbol{A}(t_r)$, these two trajectories thus exhibit recollision momenta $\boldsymbol{k}$ and $-\boldsymbol{k}$, respectively.

The relation between the electron momentum $\boldsymbol{k}$ and the photon energy ω is given by the stationary-phase equation (2.53) and reads $\omega = \boldsymbol{k}^2/2 + I_p$. This relation for the photon energy obtained from the SFA reflects the energy conservation at the recombination step. It states that the energy of the emitted photon is given by the kinetic energy of the recolliding electron plus the binding energy that the electron additionally gains during recombination to the bound state. It should be noted, though, that for better agreement with experimental results this relation needs to be heuristically modified to $\omega = \boldsymbol{k}^2/2$ (without I_p)[531]. The reason for this necessary modification is that in the SFA the influence of the long-range binding potential on the electron wave is neglected. However, in an attractive long-range potential the electron gains energy as it approaches the potential well. The energy that it gained at its center, i.e., at the position of the bound state where it recombines, is I_p. Thus, the electron kinetic energy should be modified as $E_k = \boldsymbol{k}^2/2 = \omega - I_p \rightarrow E_k = \omega - I_p + I_p = \omega$, i.e., $\omega = \boldsymbol{k}^2/2$[170,238,531,532].

With these considerations the HH spectrum (7.1) can be written as

$$\begin{aligned} \boldsymbol{\epsilon}(\omega) &\propto a(\boldsymbol{k})\boldsymbol{d}_{\text{rec}}(\boldsymbol{k}) + a(-\boldsymbol{k})\boldsymbol{d}_{\text{rec}}(-\boldsymbol{k}) \\ &\propto a(\boldsymbol{k})\langle \boldsymbol{k}|\hat{\boldsymbol{r}}|\psi_0(\boldsymbol{r})\rangle + a(-\boldsymbol{k})\langle -\boldsymbol{k}|\hat{\boldsymbol{r}}|\psi_0(\boldsymbol{r})\rangle, \end{aligned} \tag{7.3}$$

that is, as the product of the dipole recombination matrix element and $a(\boldsymbol{k})$. The two contributions to the HH spectrum obtained with linearly polarized light from the two recollision directions put constraints on the retrieval of the symmetry of the bound state and therefore need to be considered for a quantitative reconstruction. For obtaining a qualitative understanding we can, however, restrict us in the following to only one of the two contributions. If we for now ignore the exact composition of the complex amplitude $a(\boldsymbol{k})$ and assume that we can obtain it independently (suggestions for this procedure exist in the literature), we see that the HH spectrum written in the length gauge form can actually be comprehended as a Fourier transform of the bound state $|\psi_0(\boldsymbol{r})\rangle$ times $\boldsymbol{r}$,

$$\begin{aligned} \boldsymbol{\epsilon}(\omega) &\propto \langle \boldsymbol{k}|\boldsymbol{r}|\psi_0(\boldsymbol{r})\rangle \\ &\propto \langle e^{-i\boldsymbol{k}\cdot\boldsymbol{r}}|\boldsymbol{r}|\psi_0(\boldsymbol{r})\rangle \\ &\propto \int \boldsymbol{r}\cdot\psi_0(\boldsymbol{r})\, e^{i\boldsymbol{k}\cdot\boldsymbol{r}} \mathrm{d}\boldsymbol{r}. \end{aligned} \tag{7.4}$$

Thus, within the SFA and the approximation that the continuum electron wavepacket can be described by plane waves, the bound state $|\psi_0(\boldsymbol{r})\rangle$ can in principle be reconstructed from the measured harmonic spectrum. Before we proceed with this idea, we shall discuss three additional assumptions and simplifications that are necessary to perform such reconstruction in experiment.

The first assumption that the application of (7.4) requires is that both the amplitude and phase of the harmonic spectrum $\boldsymbol{\epsilon}(\omega)$ can be measured. In the first proof-of-principle demonstration of *orbital tomography* on N_2 by Itatani et al.[460] this was not the case. Instead, the known spectral phase was added in an *ad hoc* way during the reconstruction procedure. Later experiments on the same molecule by Haessler et al. were able to also measure the spectral phase of $\boldsymbol{\epsilon}(\omega)$[415]. Methods for measuring the phase of HH radiation will be discussed below in Section 7.1.3.

The second simplification concerns the description of the bound state. Thus far we were exclusively using the single electron picture. However, in the case of a molecule the bound state consists of multiple electrons. It has been shown that for a multi-electron system the relevant bound state wavefunction in the recombination dipole matrix element is the Dyson orbital[211,533]. The Dyson orbital, $\psi_D(\boldsymbol{r})$, is the scalar product of the multi-electron wavefunctions of the neutral and the ion that has lost one electron. Thus, the Dyson orbital is obtained by projecting out the difference between the neutral and the ion, which can be seen as a hole in the ion. For molecules our derivation stays valid if we make the replacement $|\psi_0(\boldsymbol{r})\rangle \rightarrow |\psi_D(\boldsymbol{r})\rangle$ in (7.4).

The third assumption is that the complex amplitude of the recolliding electron wavepacket, $a(\boldsymbol{k})$, can be obtained independently. This is equivalent with the idea that the main difference between the harmonic response of different gases arises from the recombination step of the three-step model rather than from the ionization or field-driven steps. The complex amplitude $a(\boldsymbol{k})$ in (7.2) is determined by the ionization matrix element $\boldsymbol{d}_{\text{ion}}(\boldsymbol{p}, t_i)$, the value of the ionization potential I_p and the laser field in the form of its vector potential $\boldsymbol{A}(t)$. Itatani et al. have suggested[460] to determine $a(\boldsymbol{k})$ using a reference measurement for the same laser field on a system that exhibits the same (or very similar) I_p and for which the recombination dipole matrix element can be calculated accurately, e.g., for rare gas atoms. By dividing the measured spectra of the reference system and the system under study, $a(\boldsymbol{k})$ can be obtained provided the ionization step (described by the ionization dipole matrix elements) and the continuum motion of the electron wavepacket take place the same for the two systems. This suggestion builds on the assumption that the continuum motion of the electron wavepacket is dominated by the strong laser field, and that the shape of the tunnel that is formed by the combined potential of the Coulomb potential and the laser field is to a good approximation independent of the precise structure of the ground state (*"all tunnels are alike"*). These assumptions have later been tested, and it has been found that under certain conditions and for certain molecular species $a(\boldsymbol{k})$ is indeed approximately independent of the target[534,535] and can thus be obtained by a separate reference measurement. It should be noted, though, that the generality of this approach has been questioned by a number of works. For example, it has been shown that the continuum electron wavepacket already carries a non-trivial spatial phase structure inherited from the bound state during the ionization step[483]. Also, it has been shown that the multi-electron response of molecules not only influences the ionization step but, even worse, also the recombination step[536]. This finding questions the applicability of the single active electron approximation used for the derivation of (7.4). Finally, the concept of the reconstruction of an orbital wavefunction, i.e., the measurement of a quantum object that is not an observable, is criticized for fundamental reasons[537].

In the following we will assume that (i) the amplitude of the continuum wavepacket can be obtained by a reference measurement, that (ii) it returns to the parent ion as a plane wave, that (iii) the single active electron approximation is valid, and also that (iv) the phase of the emitted dipole radiation can be measured. Then, based on the fact that the emitted radiation contains a Fourier transform of the Dyson orbital, as shown in (7.4) with $|\psi_0(\boldsymbol{r})\rangle \rightarrow |\psi_D(\boldsymbol{r})\rangle$, the spatial structure of $|\psi_D(\boldsymbol{r})\rangle$ can be reconstructed by a tomographic procedure. To see this, we assume that the laser field driving the HH process propagates along the y-direction. Then, as there is no component of the linearly polarized laser field pointing along y, the laser polarization lies in the xz-plane and drives the recolliding electron wavepackets along some direction $\theta = \mathrm{atan}(k_z/k_x)$. We further assume that the molecule under study is aligned along x (with some relevant axis). The alignment of a molecule along a certain direction in the lab-coordinate space can be achieved using laser impulsive alignment with a weak non-ionizing laser pulse preceding the pulse that generates the HH signal by a certain time Δt[538–542]. The time Δt is related to the dynamics of the rotational wavepacket that is created in the neutral molecule upon interaction with the alignment pulse. The strong pulse initiating the HH process then "catches" the molecule at a certain instant during the evolution of the rotational wavepacket where it is aligned along a certain direction. Molecular alignment will also be discussed in Section 8.3 in the context of controlling the breakage of a certain molecular bond.

The electron wavepacket recolliding with the molecule from a direction $\theta = \mathrm{atan}(k_z/k_x)$ may excite dipole oscillations in the molecule along x and z. In principle it could also excite oscillations along y, but the radiation emitted by these oscillations propagates along x and z and will therefore not reach the detector situated downstream the laser propagation direction along y. Thus, we only consider x and z-components of $\boldsymbol{d}_{\mathrm{rec}}(\boldsymbol{k})$ in the following. These components can be written as

$$d_{rec,\zeta}(\omega) \propto \int\int \left[\zeta \int \psi_D(x,y,z)\,\mathrm{d}y\right] e^{i(k_x x + k_z z)} \mathrm{d}x\,\mathrm{d}z, \tag{7.5}$$

for $\zeta = \{x,z\}$ and $\omega = \boldsymbol{k}^2/2$.* This shows that each component ζ of the HH dipole emission constitutes a Fourier transform of

$$\zeta\tilde{\psi}_D(x,z) = \zeta \int \psi_D(x,y,z)\,\mathrm{d}y. \tag{7.6}$$

---

*Here we made use of the heuristic relation $\omega = \boldsymbol{k}^2/2$ introduced above.

The measurement of $d_{rec,\zeta}(\omega)$ for a certain recollision angle θ thus yields data points in two-dimensional Fourier space of $\zeta\tilde{\psi}_D(k_x,k_z)$. Recording a whole HH spectrum for a certain recollision angle θ thus samples a polar line in the two-dimensional Fourier space spanned by k_x and k_z. This line is characterized by its radius $\omega = \boldsymbol{k}^2/2 = (k_x + k_y)^2/2$ and the angle θ. The whole Fourier space can be sampled by rotation of the laser polarization direction θ. The Dyson orbital projected onto the y-coordinate, $\tilde{\psi}_D(x,z)$, can then be reconstructed in real space by a two-dimensional inverse Fourier transform

$$\tilde{\psi}_D(x,z) = \frac{\mathfrak{F}_{\boldsymbol{k}\to\boldsymbol{r}} d_{rec,\zeta}(k_x,k_z)}{\zeta}. \tag{7.7}$$

In principle, both components ζ of the recombination dipole matrix element, $d_{rec,x}$ and $d_{rec,z}$, should contain the same information and one should be able to reconstruct the same orbital from each of them. In practice, due to the limited discrete sampling in Fourier space for only certain points of (ω,θ), the two matrix elements may not lead to the same reconstructed orbitals. It is thus usual[415,460] to use the average of the two reconstructed orbitals,

$$\tilde{\psi}_D(x,z) = \frac{1}{2}(\tilde{\psi}_{D,x}(x,z) + \tilde{\psi}_{D,z}(x,z)). \tag{7.8}$$

Orbital tomography was applied first in Ref. [460] for the reconstruction of the static HOMO of N_2. As mentioned, in this work the phase of the recombination dipole matrix element was not measured, but instead the spectral phase dependence known from the literature was added in an *ad hoc* way during the reconstruction procedure. Haessler et al.[415], also using N_2 as the example, performed the first tomographic measurement with phase-resolution, see Figs. 7.1(a) and (b). This allowed them to determine conditions where the contributions of the two highest orbitals are disentangled in the real and imaginary parts of the emission dipole moment, and enabled the tomographic reconstruction of both orbitals. Having the phase-information available in their measurements, the authors could also image the dynamic hole formed by the coherent superposition of the two orbitals. Thus, they could obtain images of the attosecond wavepacket created in the ionization process where electron density is removed from two orbitals. A different approach to obtaining the phase of the measured HH spectrum was demonstrated by Vozzi et al.[543]. By that they succeeded in an orbital reconstruction from a triatomic molecule, CO_2. In their experiment, instead of fixing the molecular alignment and varying the recollision direction, the authors measured the emitted HH intensity from CO_2 for a range of delays Δt between the alignment pulse and the pulse that generates the HH radiation. This yields a two-dimensional map that could be inverted by a phase-retrieval algorithm (and some additional calibrations) to yield the phase and intensity of the HH spectrum over the molecular alignment angle θ and thus could be inverted to yield the HOMO of CO_2 by a procedure similar to the one sketched above.

In Section 7.2.1 we will discuss how orbital tomography can benefit from the use of OTC pulses for generating the HH radiation. It will be shown that OTC pulses can be applied to solving problems with molecular symmetry, to performing tomography on atomic orbitals that cannot be rotated around the laser polarization direction, and to taking a snapshot of an orbital within a single laser pulse.

7.1.2 Mapping dynamics

In the previous Section we discussed how the process of HHG can be used to measure spatial properties of molecules. We will now discuss different methods that allow the retrieval of dynamical information from measured HH spectra. Let us consider the important case of tracing dynamics in a molecule. The dynamics may be induced either by the removal of an electron through ionization, or by electronic excitation of the molecule in a pump pulse, etc. Such a distortion of the molecular electronic configuration from its equilibrium may result in rearrangement dynamics of the electronic density, but at the same time also in rearrangement dynamics of the nuclei. These two types of dynamics typically take place on different time-scale. Because in molecules electronic valence levels are typically separated by up to several eV, the dynamics of the molecular electronic sub-system, e.g., rearrangements of a hole, may take place on the attosecond time-scale. In contrast, nuclear wavepackets typically span over only meV-ranges and thus take place on tens of fs to ps time-scales. Fortunately, HHG is, within limits, capable of tracing both types of dynamics.

Mapping fs- and ps-scale dynamics Suppose the molecular nuclear configuration changes in response to some pump event, e.g., a transition to an electronically excited state induced by the absorption of a resonant photon that induces dissociation of the molecule along a certain reaction coordinate. As the nuclei move, the multi-electron bound state $|\psi_b(\boldsymbol{r}, t)\rangle$ will also change from its initial configuration. As a consequence, the ionization and recombination dipole matrix elements, which are both determined by the shape of the bound state wavefunction at the ionization and recombination times, respectively, and therewith the emitted HH radiation may (in addition to any simultaneously occurring electronic dynamics) be modulated by the nuclear dynamics on tens of fs to ps time-scales. Recording the harmonic emission generated by a probe pulse for a range of delays τ to the pump event can thus provide insight into the molecular nuclear dynamics. The probe pulse should be short enough such that the nuclear configuration stays essentially frozen during the pulse. While this pump-probe approach with two pulses has been successfully demonstrated by a number of works, for example in Refs. [501, 544–547], it is often not straightforward to interpret the τ-dependent modulations of the recorded HH signal and to assign them to a certain dynamics. Another difficulty is to achieve a high enough sensitivity on those molecules that undergo the desired dynamics and to suppress the signal from the background. This is, in fact, a standard problem in pump-probe spectroscopy. A solution that overcomes this difficulty in HHG experiments is for example the inscription of a transient grating into the HHG medium[546,548]. Another possibility is to measure a certain polarization direction of the emitted HH signal[545]. Further details on this topic will be provided in this Section below.

Mapping sub-cycle time to photon energy Sensitivity of the HH signal to fast electronic dynamics occurring on the sub-femtosecond time-scale originates from the sub-cycle mapping of time to frequency inherent to the recollision process. As discussed in Section 2.2.3 and visualized in Fig. 2.4, the recollision energy sweeps from zero to its maximum value $3.17U_p$ and back to zero within a fraction of a laser-half-cycle. As the recollision energy $\boldsymbol{k}^2/2$, with $\boldsymbol{k} = \boldsymbol{k}(t_r(t_i))$, within the SFA directly translates to the photon energy as $\omega = \boldsymbol{k}^2/2 + I_p$, the recollision process maps the recollision time to the photon energy. If the macroscopic response of the HHG process is adjusted by phase-matching such that only one class of trajectories (either the short or the long ones) dominate the emission, emission time is uniquely mapped onto photon energy. Alternatively, one can record both classes of trajectories and use the fact that they are emitted with different divergences and thus can be spatially separated on the detector[266].

The sub-cycle mapping provided by the recollision process can immediately be exploited in experiments that study dynamics initiated by the ionization event. Note, that in this approach contrast-considerations mentioned above are not a problem, since all molecules that contribute to the HHG signal also undergo the ionization-induced dynamics. The ionization step at time t_i, thus, constitutes the pump event and the recombination step at t_r probes the dynamics taking place during $\tau = t_r - t_i$. The electron wavepacket propagation in the laser field thus constitutes the pump-probe delay. Since $t_r = t_r(t_i)$, each pump-probe delay $\tau = t_r(t_i) - t_i$ is uniquely mapped onto a certain harmonic energy as $\omega(\tau) = \boldsymbol{k}^2(\tau)/2 + I_p$. The HHG spectrum thus contains a sub-cycle movie of the ionization-induced dynamics, where time is encoded in the harmonic frequency ω, see Figs. 7.1(c) and (d) for a visualization. This movie spans over only a small range of delays τ (a fraction of a laser cycle), but time is very finely sampled by the recolliding trajectories. The temporal resolution of such experiments is, thus, very high and approaches the few-attosecond scale. Because the basis of this mapping is the energy-chirp of the recolliding electron wavepacket, $\boldsymbol{k}^2(\tau)/2$, i.e., the *attochirp*, this technique of achieving sub-cycle temporal resolution is also known as *chirp-encoded dynamics*. To change the pump-probe delay τ in this mapping technique, one can change the wavelength of the driving laser field. As τ is given by the electron propagation in the continuum and spans over a small window around roughly $0.7 \times T = 0.7 \times \lambda/c$, variation of λ moves the accessible range of τ. A more flexible way of varying τ is to use tailored fields where the recollision timing can be controlled by the field-shape, see Section 4.1 for more details on tailored fields used for HHG and adjustment of the recollision timing in this process. The concept of mapping ionization-induced dynamics into harmonic frequencies has been successfully demonstrated for attosecond electronic dynamics[414,415,461,549,550] and also for fast nuclear motion in H_2^+, D_2^+, and CH_4^+[241,551], cf. Figs. 7.1(c) and (d).

The underlying principle for the measurement of fast ionization-induced nuclear motion is the *nuclear autocorrelation function*, introduced in Ref. [240]. This function reads

$$C(\tau) = \int \chi_0(\boldsymbol{R})\chi(\boldsymbol{R},\tau)\mathrm{d}\boldsymbol{R} \tag{7.9}$$

and is the overlap integral of the nuclear part of the molecular wavefunction before ionization, $\chi_0(\boldsymbol{R})$, with the nuclear part of the wavefunction of the molecular ion after evolution during $\tau = t_r - t_i$. The coordinate $\boldsymbol{R}$ denotes the nuclear configuration. By adopting the Born-Oppenheimer (BO) approximation in the SFA derivation of the dipole (2.47) that determines the emitted HH radiation, the nuclear autocorrelation function (7.9) shows up as a modulating term. The appearance of the nuclear autocorrelation term in the SFA expression for the HH dipole emission has a very comprehensible reason: In HHG, radiation is emitted upon recombination of the recolliding electron to the initial state, as can for example be seen from (2.45). As the nuclei evolve, the probability to recombine to the initial state decreases, as described by the overlap of the initial and evolved nuclear wavefunctions in (7.9), which measures how different the states have become during evolution. The modulations of the HH signal described by (7.9) can therefore, in turn, be used for obtaining insight into nuclear motion, when it is fast enough such that it leads to a noticeable contribution to the HH signal via $C(\tau)$ during the sub-cycle interval τ between ionization and recombination. This is the case for C-H bonds studied in Refs. [241, 551]. The authors of these works have given the concept of using the nuclear autocorrelation function for studying nuclear motion the name PACER (probing attosecond dynamics by chirp-encoded recollision).

High-harmonic spectroscopy We have described above that HHG is a very valuable process for studying both electronic and nuclear dynamics in molecules. This opportunity that has been exploited in numerous works, for example in Refs. [241, 414, 415, 461, 501, 544, 546, 547, 549–553]. Using HHG for probing dynamics is usually referred to as *high-harmonic spectroscopy*. High-harmonic (HH) spectroscopy records and analyzes information about molecular structure and attosecond dynamics encoded in harmonic intensity, phase and polarizations of the emitted HH radiation. Measurement of phase and polarization of the HH radiation emitted from the molecular target is thus a crucial experimental ability and will be discussed later in this Section. To a large extent the attractiveness of HH spectroscopy for probing dynamics originates in its high sensitivity to even minute changes of the molecular (electronic and nuclear) structure that may result in noticeable changes of the harmonic emission due to phase-sensitivity of the HHG emission. This advantage is, however, often offset by the notorious problem of disentangling the dynamics from the measured HH radiation, as the dynamics can affect both the ionization and recombination steps. In order to understand the dynamics under study it is, thus, in most cases unavoidable to compare the experimental data to results of intricate simulations. Large efforts are thus undertaken to enhance the sensitivity of the measured HH signal to a certain process for enabling its assignment to a certain dynamics.

This can be achieved by obtaining control over the interaction of the laser field with the molecule. A parameter that crucially determines how the laser field interacts with the molecule is the alignment/orientation of the molecule in lab coordinate space, which can be controlled, if the molecule permits, using impulsive laser alignment/orientation[414,415,461,550]. In addition to achieving control over the interaction of the laser field with the molecules, one can also measure several complementary parameters of the emitted HH radiation. It has been shown by several works that the combined information obtained from these parameters often leads to enhanced insight. One parameter of the emitted HH radiation that can contain valuable information is its polarization state, $\boldsymbol{e}(\omega)$, as has been shown by polarization-resolved HHG experiments[396,461,545]. Probably the most crucial parameter of the emitted radiation, which is often decisive for the interpretation of the measured HH signal, is the phase $\varphi(\omega)$ of the emitted radiation[414,415,547,549,550]. Together with the polarization state, the phase allows to completely characterize the emitted HH radiation $\boldsymbol{\epsilon}(\omega) = |\boldsymbol{\epsilon}(\omega)|e^{i\varphi(\omega)}\boldsymbol{e}(\omega)$. Thus, phase and polarization in addition to the spectral intensity contain the complete information one can obtain from a HHG experiment. Still, even if the obtainable signal is completely characterized, it may be difficult to disentangle a certain dynamics from it. Thus, in order to further enhance the insight into the dynamics, multi-modal approaches that additionally use information from complementary experiments that measure electrons and/or ions, have been performed, see, e.g., Ref. [553].

A notoriously difficult problem is the disentanglement of so called *multi-channel contributions* to the HH radiation[414,415,461,547,549,550]. These correspond to HH emission that not only involves the ground state (X) of the ion but also excited states (A, B, ...) that are populated during the ionization step or by excitation during the laser interaction after the ionization event. The different possible states in which the ion can be prepared during the ionization step are called *channels*. Each of these different channels, which we can label by c, contribute to the HH emission during the recombination to the initial state of the neutral molecule, from which each of them originates. As the wavefunctions of these channels evolve on different energies, E_c, they accumulate different phases during ionization and recombination, $\varphi_c = E_c\tau$. Depending on the relative phase of the different channels the separate HH contributions associated with them will interfere and may modulate the harmonic spectrum. Interpretation of this *dynamic interferences* in the harmonic spectrum and associating them with a certain ionization dynamics at t_i and also laser-driven dynamics in the ion during ionization and recombination, is difficult and requires intricate modelling[414,461,549]. However, at the same time, these multi-channel contributions constitute a very interesting opportunity for studying attosecond electron wavepacket dynamics taking place in the molecular ion during ionization and recombination. Such wavepacket dynamics can, under certain conditions, be interpreted as the motion of a hole in the ion. As it are the relative phases of the different channels that contribute to the wavepacket dynamics (and to the HH emission), measurement of the phase of the emitted HH radiation is crucial for a correct interpretation of the attosecond wavepacket dynamics in the molecular ion, see Refs. [238, 414, 415, 549] for details.

7.1.3 Measurement of phase and polarization of HH radiation

Measurement of molecular structure and attosecond dynamics by high-harmonic spectroscopy strongly benefits from the experimental capability to measure the phase and polarization state of the emitted HH radiation (in addition to harmonic intensity), as was discussed above. In the following we will discuss methods for measuring the phase and polarization of HH radiation. As we will see, certain methods for measuring the phase can at the same time solve the notorious background problem in pump-probe experiments. That is, these methods can be used to enhance the relative contributions to the probe signal of the excited molecules and to suppress the signal-contributions from the unexcited molecules that constitute a background.

Transient grating spectroscopy uses two pulses, crossed at a small angle, to create a spatial interference pattern in the HHG gas sample that constitutes an intensity grating along the transversal direction with a periodicity that is determined by the crossing angle of the two beams and their wavelength[546,548]. This intensity modulation with typically some 10 μm spacing between neighbouring maxima, translates into a grating of excited molecules (at regions with high intensity) and unexcited molecules (at low-intensity regions). The excitation can for example be the alignment quality of molecules[546,548]. In high-intensity regions the molecules are aligned along a certain direction. In the low-intensity regions the alignment is poor or even random. Because the excitation (in this example the quality of the molecular alignment) modifies both the intensity and the phase of the emitted HH radiation, HHG from this molecular sample with a third pulse, will lead to diffraction peaks in the far field. From the measured diffraction efficiency in the HHG signal, it is possible to extract the phase (and amplitude) modulation of the grating, and thus the phase difference of the emission from excited (aligned) and unexcited (unaligned) molecules. Because the diffraction signal is created only from molecules that are excited, this method at the same time allows to suppress contributions from unexcited molecules.

Double-source interferometry HH radiation is generated in two spatially separated sample volumes with two drive pulses that are derived from the same laser pulse such that they are phase-locked with each other[414,554]. Due to the divergence of the two HH beams generated in the two volumes, they overlap in the far-field and create a spatial interference pattern similar to Youngs double slit. The fringe positions depend on the relative phase of both sources. Thus, by spectrally resolving the HH radiation, the relative phase over harmonic frequency can be retrieved from the spatial interference pattern. One of the two emitted HH waveforms provides the phase reference. In the second volume, some parameter is varied, e.g., the molecular alignment angle. From the spatial fringe shift one can then extract the dependence of the phase on this parameter. A major challenge in this scheme is to keep the relative phase of the two generating beams stable. Any phase-fluctuations between them, e.g., due to fluctuating delay, will translate into the far-field fringe pattern and will lead to errors in the retrieved relative phase.

Phase-retrieval by electron streaking The phase of the emitted HH radiation can certainly also be measured by converting the photons to electrons. This is a standard approach for characterizing attosecond pulses, usually called *attosecond streaking*[355,412,354]. From the modulations of photoelectron spectra generated by the HH radiation to be characterized induced by an additional laser field, the spectral phase of the HH radiation can be retrieved[555]. A variant of this approach for spectrally well separated harmonics is called RABITT (reconstruction of attosecond beating by interference of two-photon transitions)[556]. Thus, to measure the phase of the HH radiation emitted from the molecular sample under study, one needs to focus this radiation into a second gas jet, together with the reference laser field, and measure the kinetic energy of the emitted photoelectrons as a function of delay between the HH radiation and the laser field.

Phase-retrieval using mixed gases Finally, we only briefly mention that the phase of the HH radiation emitted from a molecular target can also be reconstructed from mixed gas samples with precisely known partial pressures[557]. One of the two gases is the molecular sample under study, the other one is a reference gas. The spectral interference of the two HH emissions encodes their relative phase. If the reference gas (e.g., consisting of atoms) is unaffected by the variation of some parameter (e.g., molecular alignment), the dependence of the phase of the HH radiation emitted from the molecules on this parameter can be extracted.

Measurement of HH polarization It was mentioned above that also the polarization state of the emitted HH radiation contains valuable information about molecular structure and dynamics taking place in molecules. This is understandable if one considers that a phase-shift and/or intensity difference between two components of the recombination dipole matrix element leads to elliptical HH emission with a certain angle of the polarization ellipse in the molecular frame of reference. Theoretical investigations have pointed out that such phase-shift or intensity variation can take place dynamically and thus the polarization state contains valuable information about the different contributing ionization channels and hole dynamics in a molecule[558]. This information about the attosecond dynamics taking place in a molecule contained in the polarization state could be retrieved from experimental data[461]. It has also been shown, based on the example of rotational dynamics, that polarization-sensitive detection of HH radiation with an anisotropy in its polarization state can be used to increase the contrast in the detection of the harmonic emission from excited molecules in pump-probe experiments[545]. Furthermore, the polarization of the HH radiation is a key parameter that gives access to both attosecond dynamics and structure when using two-dimensional tailored waveforms such as OTC pulses, see Section 7.2 for details. To measure the polarization state of HH radiation, some polarizing element for the XUV and soft X-ray wavelength range is needed. The simplest polarizer in this wavelength range is a plane metallic surface from which the HH beam reflects off under a certain angle. For not too small angles of the incident HH beam with the surface, metals typically exhibit a significantly higher reflectivity for s-polarized than for p-polarized light. This has been exploited in experiments that analyze HH radiation with photon energies well below 100 eV[375,396,461,545]. For higher photon energies this method becomes problematic as the reflectivity drastically decreases with increasing photon energy. Going to smaller reflection angle close to grazing incidence can partly compensate for this decrease in reflectivity, but the extinction ratio between s- and p-polarization also decreases. Metal surfaces are, thus, no longer practical for higher photon energies, but one can use custom designed metallic multi-layer mirrors[559] as polarizing elements.

7.2 Mapping structure and dynamics with tailored waveforms

The previous Section 7.1 has shown that it is in principle possible to extract both structural and dynamical information about the target from a measured HH spectrum. We have described the concept of *orbital tomography* for obtaining spatial information about the targets from the emitted HH radiation. Dynamical information can be measured using the toolbox of *high-harmonic spectroscopy*, which can achieve a temporal resolution down to a few attoseconds by exploiting the mapping of recollision time to photon energy. We have discussed that both concepts are subject to a number of limitations and necessitate certain approximations to extract the desired information from measured HH spectra. A problem of particular interest is the simultaneous extraction of spatial and dynamical properties. In this Section we will now show that several of these limitations that arise with single-colored, linearly polarized laser fields can be overcome if tailored waveforms are used. We will first discuss how OTC fields[**234**,**235**] can be used for the extraction of structural dynamics with attosecond resolution. Subsequently, we will discuss that tailored waveforms can not only be exploited for obtaining intricate insight into the photon-emission process, but even can be employed for gaining control over the HHG process by slightly modifying the recolliding electron trajectories.

7.2.1 Attosecond angular mapping

Orbital tomography, in its basic version using molecular alignment to rotate the bound state under study with respect to the polarization direction of the driving field, suffers from a series of shortcomings that all, eventually, originate in the use of linearly polarized light for recording the HH spectrum. As for linear polarization the direction of electron recollision and with it the wave vectors $\boldsymbol{k}$ remain restricted parallel to the polarization direction, it is unavoidable to perform a set of XUV spectral measurements in multi-shot mode for a range of alignment angles. Although the necessity for many measurements per reconstruction is inconvenient, there are still more fundamental disadvantages of the multi-shot method. The most important ones are probably these:

(i) Only snapshots temporally integrated over the whole drive pulse duration can be recorded. Thus, the temporal resolution that can be achieved is limited to the pulse duration and remains in the femtosecond range. As a consequence it is not straightforwardly possible to image attosecond electron dynamics, e.g., the evolution of a hole wavepacket[†].

(ii) Since it is necessary to align the molecule under study relative to the laser polarization direction, only molecules with a pronounced polarizability axis can be imaged.

(iii) Due to the angular dependence of the ionization rate the structures of the recolliding electron wavepacket changes, as the molecule is rotated. Thus, the amplitude of the continuum wavepacket $a(\boldsymbol{k})$ in (7.3) becomes dependent on the alignment angle. This compromises a central assumption of orbital tomography and complicates or may even prohibit the reconstruction procedure.

(iv) The problem of the angularly dependent ionization rate also concerns the phase-structure of $a(\boldsymbol{k})$. The continuum wavepacket emitted into a certain direction inherits the phase of the bound state from which it is detached. Therefore, the phase-structure and therewith the symmetry of the bound state cannot be obtained unambiguously when in linear light the wavepacket recollides from the same side[238,415].

These problems can be avoided by the use of OTC pulses for recording the HH spectrum. The use of OTC pulses for orbital tomography has been first discussed in Refs. [236, 237], see **Paper 2** and **Paper 3**. In these works, using the example of OTC fields synthesized by ω and its second harmonic 2ω (which we will also adopt for the discussion in this Section), it was shown that OTC fields enable imaging spatial restructuring of the bound state of atoms or molecules with attosecond resolution. That is, it becomes possible to map structural information about the bound state on laser sub-cycle time-scales. This also means that the whole bound state can be imaged by a single laser pulse without the necessity of multiple projections for different alignment angles. These opportunities are based on the unique property of OTC pulses to establish a mapping of recollision time to recollision angle and energy that we already described in detail above in the context of electron momentum mapping (see Section 6.1.2 for details). Applied to HHG, this two-dimensional subcycle dynamics of the recolliding electron trajectories translates into a sweep of the polarization of the emitted HH radiation on sub-cycle times. Together with the usual attochirp of the emitted HH bursts, which reflects a sub-cycle sweep of the emitted photon energy, this means that different photon energies are emitted with different polarizations and, most importantly, that both of these properties are synchronized on an attosecond time-scale, see Fig. 7.2(a).

The attosecond synchronization of photon energy and polarization can, after selections of a certain spectral region near the cut-off, be exploited for the production of isolated attosecond pulses, see Fig. 4.1(d) and corresponding text. In contrast, to image structural dynamics of a bound state one preferentially records and analyzes a broad range of photon energies[236,237]: This allows the reconstruction of the bound orbital within a single cycle of the fundamental driving field, and even allows tracing structural changes on attosecond times. A limit to the temporal resolution is only set by the desired spatial resolution. A detailed numerical investigation of the quality of the orbital reconstruction was performed in Ref. [237] by solving the time-dependent Schrödinger equation in single active electron approximation for a model potential, see Fig. 7.2(b). The feasibility of

---

[†] This limitation can be avoided if the multiple channels contributing to the HH emission, which are responsible for the formation of electron hole dynamics, can be disentangled in the measured harmonic spectra. This is, for example, possible when two contributing orbitals favorably differ in their symmetries such that their corresponding spectra are real and imaginary, respectively.[415]

single-shot and sub-cycle retrieval of the bound state was confirmed by calculating its coverage in momentum space by the recolliding electron wavepacket using a technique for numerically obtaining $a(\boldsymbol{k})$ from the numerically propagated wavefunctions[560]. Thus, the limitation in the temporal resolution that arises in orbital tomography with linearly polarized fields [problem (i) above] is circumvented with OTC fields.

Obtaining sub-cycle temporal resolution in orbital tomography is, however, not the only advantage of using OTC pulses for probing structural dynamics of bound states by HHG. In fact, also the other problems mentioned above, points (ii)-(iv), which deal with restrictions due to certain symmetry properties of the bound state, are removed by the use of OTC pulses. This is due to the property of OTC fields that they can drive electron wavepackets on two-dimensional trajectories and make them recollide with the parent ion from a direction different from their emission direction. Let us denote the emission angle of a certain trajectory during the ionization step, measured in the lab frame, by θ_i, and the angle under which this trajectory recollides with the parent ion, also measured in the lab frame, by θ_r, see the sketch in Fig. 7.2(c). The maximum angle between the emission and recollision directions $\Delta\theta = \theta_r - \theta_i$ can be substantial (exceeding 90°). In detail, $\Delta\theta$ depends on the intensities and wavelengths of the laser fields used for the generation of the OTC field and also varies with the relative phase $\Delta\varphi$ between the two colors. It is this difference angle $\Delta\theta$ and its huge sweep on laser sub-cycle intervals that is responsible for spatially sampling the bound state from different directions without the need to rotate the target. Thus, problem (ii) encountered with linearly polarized pulses is avoided with OTC fields. It is important to note, however, that it is dominantly the recollision angle θ_r that is responsible for the pronounced sub-cycle angular sweep of $\Delta\theta$[236,237]. In comparison, the angular sweep of the ionization angle θ_i is considerably smaller[151]. This is because, equivalent to the situation in linearly polarized light, the ionization time window is much smaller than the recollision time window since field-ionization takes place only within short fractions of a quarter cycle of the 2ω-field. Thus, during the short interval of the ionization the polarization of the OTC field only rotates by a relatively small angle, which translates into a correspondingly small sweep of θ_i.

As a consequence, due to the strong angular dependence of the ionization rate in molecules that is sensitive to the shape of the bound orbitals (in addition to their binding energy)[200,561], the ionization step in OTC fields works as a highly selective process for HHG: In a randomly oriented/aligned molecular gas sample only molecules whose orbitals are favorably oriented along θ_i will be ionized and therefore contribute to the HH radiation. Because θ_i stays largely fixed to a certain direction of an orbital, problem (iii), introduced by rotating θ_i over the whole orbital when using linear light, is strongly mitigated with OTC pulses. Because of the correlation between recollision angle and recollision energy, a certain energy range of the HH spectrum (or a certain harmonic in the case of a multi-cycle field) will be dominated by trajectories that ionize from a certain site (or lobe) of an orbital oriented along θ_i and recollide under $\theta_r = \theta_i + \Delta\theta$, i.e., along potentially yet another orbital lobe, see Fig. 7.2(d). Hence, OTC fields also help in solving problem (iv) that originates from imaging an orbital with a wavepacket that has inherited this orbital's phase. At the same time this spatial selectivity of the orbital contributions is advantageous for imaging targets that cannot be aligned, e.g., atoms.

In an experiment, the temporal and spatial information about the bound state is encoded in the energy spectrum and the polarization state of the HH radiation, respectively, cf. Fig. 7.2(a). The temporal information can be extracted analogously to the case of HHG with linearly polarized light, using the mapping of recollision time to photon energy. Extraction of the spatial information, however, requires that the polarization state of the HH spectrum, $\boldsymbol{\epsilon}(\omega) \propto \langle \boldsymbol{k}(\omega)|\boldsymbol{r}|\psi_0(\boldsymbol{r})\rangle$, is obtained. Because recollisions happen from different angles within the polarization plane of the OTC pulse, assumed in the xz plane, the HH radiation that is emitted perpendicularly to this plane, i.e., along y-direction, may exhibit polarization components in both x and z. HH emission within the plane xz will not be phase-matched nor detected; we can therefore disregard it. Thus, one needs to measure $\epsilon_x(\omega) \propto \langle \boldsymbol{k}(\omega)|x|\psi_0(\boldsymbol{r})\rangle$ and $\epsilon_z(\omega) \propto \langle \boldsymbol{k}(\omega)|z|\psi_0(\boldsymbol{r})\rangle$. From these quantities one

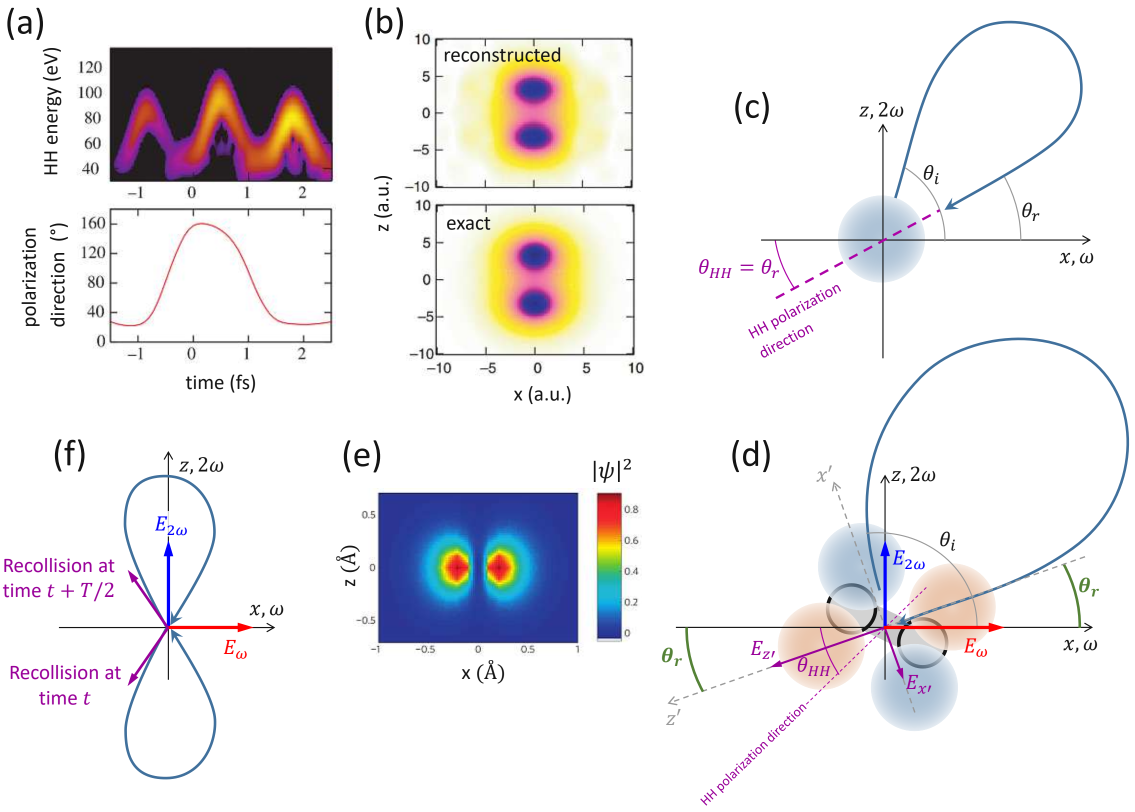

Figure 7.2: Optical attosecond angular mapping with OTC fields. (a) In an OTC field the recollision energy and angle vary on sub-cycle times synchronously with the field oscillations, cf. Fig. 6.2. This translates into a simultaneous sub-cycle variation of the generated high-harmonic energy (top panel) and, for a radially symmetric bound state, also of the polarization direction of the harmonics (bottom panel). (b) The sub-cycle variations of the harmonic energy and polarization direction can be employed for the implementation of single-shot orbital tomography. See text in Section 7.2.1 for details. Panels (a) and (b) are adapted from Ref. [237], see **Paper 3**. (c) Visualization of the correspondence between recollision angle θ_r and the polarization direction $\theta_{\mathrm{HH}} = \theta_r$ of the high-harmonic radiation for a radially symmetric bound state. θ_i denotes the ionization angle. (d) Correspondence between recollision angle θ_r and the polarization direction θ_{HH} of the high-harmonic radiation emitted by a non-symmetric bound state, e.g., a molecular orbital with π-symmetry. In the general case $\theta_{\mathrm{HH}} \neq \theta_r$ and the high-harmonic field exhibits components along both axes of the coordinate system (x'/z') aligned with the recollision direction. The rotation to the lab-frame (x/z) needs to be either calibrated using a measurement with a symmetric bound state [cf. (c)] or, for multi-cycle OTC fields, can be induced from the intensity ratio of the even and odd harmonics. The latter method is based on the symmetry breaking between two consecutive half-cycles along the $z, 2\omega$ axis, see (f) and text in Section 7.2.2 for details. (e) Reconstruction of the 2p state of neon from measured high-harmonics generated by an OTC field using the method described in (b). Adapted from Ref. [323]. (f) Visualization of recollision directions in an OTC field during two consecutive laser half-cycles at times t and $t + T/2$.

obtains the angle of the HH polarization, $\phi_{\mathrm{HH}} = \mathrm{atan}(\epsilon_z/\epsilon_x)$, in the lab frame, see Fig. 7.2(c) for a visualization. To measure ϕ_{HH} one can, for example, use a suitable polarizer (see Section 7.1.3). For multi-cycle OTC fields a simpler method can be adopted, as will be described below. To extract the spatial information contained in the recombination dipole matrix elements by means of a Fourier re-transformation of the form (7.7), the measured spectra $\epsilon_x(\omega)$ and $\epsilon_z(\omega)$ need to be transferred from the laboratory frame to the recolliding electron's frame, as sketched in Fig. 7.2(d). This rotation of the coordinate system can be done with the help of a calibration measurement using a spherically symmetric ground state, as in this case $\phi_{\mathrm{HH}} = \theta_r$, cf. Fig. 7.2(c).

Attosecond angular mapping of HHG with OTC pulses, as described in this Section, has been successfully implemented experimentally, e.g., in Refs. [323–325, 562]. In all of these works a multi-cycle OTC field has been used. As for a multi-cycle field the HH spectrum consists of well separated harmonic teeth, the angle $\phi_{\mathrm{HH}}(n\omega_o)$ at a certain harmonic n of the driving laser field with frequency ω_o can be obtained from the HH spectrum without the necessity of a polarizing element in the measurement. For a certain harmonic n (with n an odd number) it can be obtained simply by the relation

$$\phi_{\mathrm{HH}}(n\omega_o) = \arctan\left(\sqrt{\frac{I_n}{I_{n+1}}}\right), \tag{7.10}$$

where I_n is the intensity of the odd harmonic n and I_{n+1} the intensity of the adjacent even harmonic $n+1$[323]. Equ. (7.10) is based on the fact that the presence of the 2ω field breaks the symmetry between adjacent half-cycles of the OTC field, which results in the generation of even harmonics, while for a symmetric situation only odd harmonics are generated. This follows from general symmetry considerations[563,564]. A detailed description of the symmetry breaking by the 2ω field and how this can be exploited in measurements as well as a derivation of (7.10) will be given in Section 7.2.2; see discussion leading to (7.22).

In the remainder of this Section we want to outline three experiments that have made use of the opportunities that are opened up up by using OTC pulses for angularly mapping the HH radiation. Shafir et al. have used this concept for obtaining a tomographic image of the highest occupied orbital of neon, a 2p state[323,325], see Fig. 7.2(e). They calibrated ϕ_{HH} using HH emission from the symmetric ground state of helium. Although this experiment focused on a static object and did not exploit the sub-cycle timing contained in the HH spectrum, the measurement is a clear proof of the possibility to image bound states that cannot be aligned [point (ii) above]. Niikura et al. have extended this concept to molecules[324,562]. They were able to correctly retrieve the symmetry of the static π_g and σ_g orbitals of CO_2 and N_2, respectively[324]. This was possible by relying on the selection of a spatially fixed orbital due to the angular dependence of the ionization rate, and by exploiting the fact that OTC fields can circumvent the symmetry-blindness problems related to self-probing [points (iii) and (iv)] that we described above. Later they extended their experiment to the time-dependent case and demonstrated, using C_2H_6 as an example, the sensitivy of the angular mapping concept to the dynamics of an attosecond bound wavepacket prepared during ionization [point (i)][562]. Thus, together these experiments show that angular mapping of HHG using OTC fields can indeed be used to obtain information about the symmetry and structure of molecular bound-states and their evolution with attosecond resolution.

7.2.2 Gating techniques for HHG

Angular mapping with OTC fields discussed in Section 7.2.1 relies on large-scale steering of electron trajectories: Retrieval of structure demands that electron trajectories recollide from a large range of angles. This requires comparable field intensities along the two orthogonal directions. A large range of recollision angles is also advantageous for a sensitive mapping of sub-cycle times into the angular direction, which enables the simultaneous measurement of both the structure of bound-states and their evolution on attosecond time-scales, as described above. An alternative approach to the retrieval of attosecond bound-state dynamics, albeit with reduced sensitivity to structure, is possible by the concept of interferometry. We have shown in Section 6.2 that interferometry with electron wavepackets can give intricate insight into the dynamics of bound states and can, to some extent, also provide structural information. High-harmonic generation is, in fact, an interferometric process by its nature. On the one hand, this is because emission of HH radiation is induced by the interferometric superposition of the recolliding electron wavepacket with the parent ion's bound state, as reflected by the recombination dipole matrix element $\langle \boldsymbol{k}(\omega)|\hat{\boldsymbol{r}}|\psi_0(\boldsymbol{r})\rangle$. On the other hand, also the recollisions that take place from different sides during two adjacent laser half cycles, i.e., with electron wavevectors $\boldsymbol{k}$ and $-\boldsymbol{k}$, make an interferometer. These interferometric properties inherent to HHG can be exploited for measurements of attosecond dynamics and structure, as will be outlined in the following.

HHG as an interferometric process A mathematical formulation of the interferometric processes underlying HHG is given by (7.3), reproduced here for convenience,

$$\boldsymbol{\epsilon}(\omega) \propto a(\boldsymbol{k})\langle \boldsymbol{k}(\omega)|\hat{\boldsymbol{r}}|\psi_0(\boldsymbol{r})\rangle + a(-\boldsymbol{k})\langle -\boldsymbol{k}(\omega)|\hat{\boldsymbol{r}}|\psi_0(\boldsymbol{r})\rangle, \tag{7.11}$$

which we have obtained above from the more general formulation (7.1). We have discussed possibilities that are opened up by the existence of the interferometer represented by $\langle \boldsymbol{k}(\omega)|\hat{\boldsymbol{r}}|\psi_0(\boldsymbol{r})\rangle$ earlier in this Chapter, e.g., orbital tomography or high-harmonic spectroscopy, and also in Chapter 4 that discusses the generation of pulses using HHG. Here we will now focus on the additional opportunities provided by the interferometer that is based on the recollisions during adjacent half-cycles of a laser field. To this end, we will first discuss symmetry considerations in HHG. This will, in retrospect, justify the applicability of (7.10). Subsequently, we will show that both interferometers together can be used for *in situ* measurements of the process of HHG and allow to characterize and even to control the properties of the emitted HH radiation as it is produced.

We start our discussion from the general version of (7.11) derived in Section 2.2.5,

$$\boldsymbol{\epsilon}(\omega) \propto \sum_s \boldsymbol{d}_{\text{rec}}(\boldsymbol{p}^s, t_r^s)\,\boldsymbol{d}_{\text{ion}}(\boldsymbol{p}^s, t_i^s)\, e^{iS(\boldsymbol{p}^s, t_i^s, t_r^s) - i\omega t_r^s}, \tag{7.12}$$

with $\boldsymbol{d}_{\text{ion}}(\boldsymbol{p}^s, t_i^s) = \boldsymbol{E}(t_i^s)\langle \psi_0(\boldsymbol{r})|\hat{\boldsymbol{r}}|\boldsymbol{p}^s + \boldsymbol{A}(t_i^s)\rangle$ the dipole matrix element describing ionization at t_i^s and $\boldsymbol{d}_{\text{rec}}(\boldsymbol{p}^s, t_r^s) = \langle \boldsymbol{p}^s + \boldsymbol{A}(t_r^s)|\hat{\boldsymbol{r}}|\psi_0(\boldsymbol{r})\rangle$ the dipole matrix element describing recombination at t_r^s, and $S(\boldsymbol{p}^s, t_i^s, t_r^s)$ the semi-classical action, all evaluated at the stationary points $(\boldsymbol{p}^s, t_i^s, t_r^s)$ obtained by solution of the stationary-phase equations (2.53). The semi-classical action reads

$$S(\boldsymbol{p}^s, t_i, t_r) = \int_{t_i}^{t_r} \frac{1}{2}[\boldsymbol{p}^s + \boldsymbol{A}(t')]^2 \mathrm{d}t' + I_p(t_r - t_i). \tag{7.13}$$

For a periodic driving field with vector potential $\boldsymbol{A}(t)$ for which all cycles are identical, the HH spectrum $\boldsymbol{\epsilon}(\omega)$ is obtained by summing up all stationary points s from one *full* period T of the field, $0 < t < T$, i.e., for two adjacent half-cycles. If we restrict ourselves to one trajectory class, e.g., the short ones, we obtain one solution to the stationary-phase equations per half-cycle with stationary points $\boldsymbol{s}_1 = (\boldsymbol{p}^s, t_i^s, t_r^s)$ and $\boldsymbol{s}_2 = (-\boldsymbol{p}^s, t_i^s + T/2, t_r^s + T/2)$ for the first and second half-cycle, respectively. For a symmetric shape of the two adjacent half-cycles, e.g., for a sinusoidal continuous wave laser field, we find for the corresponding electron wave vectors at the recollision time $\boldsymbol{k}_1 = \boldsymbol{p}^s + \boldsymbol{A}(t_r^s)$ and $\boldsymbol{k}_2 = -\boldsymbol{p}^s + \boldsymbol{A}(t_r^s + T/2) = -\boldsymbol{p}^s - \boldsymbol{A}(t_r^s) = -\boldsymbol{k}_1$. We thus recover that the two recollisions occur from opposite sides, as expressed by (7.11). We can, without loosing generality, denote the two recollision directions by L (left) and R (right). Furthermore, we find for $\boldsymbol{D}(t_i^s, t_r^s) = \boldsymbol{d}_{\text{rec}}(\boldsymbol{p}^s, t_r^s)\boldsymbol{d}_{\text{ion}}(\boldsymbol{p}^s, t_i^s)$ the property $\boldsymbol{D}(t_i^s, t_r^s) = -\boldsymbol{D}(t_i^s + T/2, t_r^s + T/2)$, i.e., $\boldsymbol{D}_L = -\boldsymbol{D}_R$, where the minus sign comes from change of the sign of the electric field $\boldsymbol{E}(t)$, contained as a pre-factor in $\boldsymbol{d}_{\text{ion}}(\boldsymbol{p}^s, t_i^s)$, between the two adjacent half-cycles: $\boldsymbol{E}(t_i^s) = -\boldsymbol{E}(t_i^s + T/2)$. For the semi-classical action we find that $S_R = S_L$, such that we can rewrite (7.12) as

$$\begin{aligned} \boldsymbol{\epsilon}(\omega) &\propto \boldsymbol{D}_L e^{iS_L - i\omega t_r^s} + \boldsymbol{D}_R e^{iS_R - i\omega(t_r^s - T/2)} \\ &\propto \boldsymbol{D}_L e^{iS_L - i\omega t_r^s} - \boldsymbol{D}_L e^{iS_L - i\omega(t_r^s + T/2)} \\ &\propto \boldsymbol{D}_L e^{iS_L - i\omega t_r^s} \left[1 - e^{-i\omega T/2}\right]. \end{aligned} \tag{7.14}$$

Here, we have assumed the laser field to be a periodic function with periodicity $T = 2\pi/\omega_o$ and frequency ω_o. For the n-th harmonic of the fundamental frequency with $\omega = n\omega_o$ the expression $e^{-i\omega T/2} = e^{-i\pi\omega/\omega_o} = e^{-i\pi n}$ is 1 for even n, and -1 for odd n. It follows that $1 - e^{-i\omega T/2}$ is 0 for even n, and 2 for odd n. From (7.14) we thus recover the well-known fact that for a periodic function with equal positive and negative half-cycles the HH spectrum consists only of odd harmonics. A descriptive explanation for this result is that the HH emission is generated by two symmetric trajectories. The phase that the two corresponding electron wavepackets pick up during their continuum motion is identical, but because they recollide from opposite sides, their separate contributions to the overall dipole emission lead to destructive interference for the even Fourier components and constructive for the odd components. This is exactly the picture of the interferometer that we evoked above.

Detuning the HHG interferometer using two-color fields

In an interferometer the contributions from the two arms lead to interference at the output of the interferometer depending on their relative phase $\delta\phi$ at this point. In the case of HHG the two interfering objects are electron wavepackets. They are coherently split off from the bound state during tunnel ionization and then propagate in the continuum driven by the laser field. During their propagation they pick up phase determined by their semi-classical action. They are driven back to the position of the bound state where their relative phase $\delta\phi$ is evaluated during recombination. As in an optical interferometer it is irrelevant for the interference, how much phase the electron wavepackets have pick up during propagation. This can be a large value. What determines their interference is their relative phase $\delta\phi$. A slight detuning of the interferometer can therefore lead to a strong modification of the interference observed at the output.

How can we detune the electron wavepacket interferometer to influence the HH spectrum? Let us have a look at expression (7.14). This expression tells us that we need to introduce a small phase-shift $\delta\phi$ between the left (L) and right (R) contribution to the HH spectrum. This is equal to saying that we need to break the symmetry between the two adjacent half-cycles, i.e., we need to shape the field such that the two half-cycles become unequal. This was first demonstrated by Dudovich et al.[565], who have used a weak second harmonic field superposed with a certain phase delay $\Delta\varphi$ to unbalance the two half-cycles. It was shown that a 2ω field with a relative intensity of only about 10^{-3} of the ω field suffices to introduce a phase-shift $\delta\phi$ that is significant enough to modify the HH spectrum. This phase-shift unbalances the L and R contributions to the HH spectrum, such that the strict destructive interference for the even harmonics is no longer valid. Consequently, in the HH spectrum even harmonics appear for certain values of the $\omega/2\omega$-phase $\Delta\varphi$[565].

Symmetry-breaking using $\omega/2\omega$ fields To understand the breakage of the symmetry and the appearance of even harmonics in a linearly polarized $\omega/2\omega$ field of the form

$$\boldsymbol{E}(t) = \boldsymbol{E}_{\omega_o}(t) + \boldsymbol{E}_{2\omega_o}(t) = \boldsymbol{E}_{\omega_o}\cos(\omega_o t) + \boldsymbol{E}_{2\omega_o}\sin(2\omega_o t + \Delta\varphi), \tag{7.15}$$

we calculate how the additional second-harmonic field affects the electron's semi-classical trajectory and therewith the interference between recollisions from the left and right, respectively. During its excursion, the electron accumulates a phase ϕ. The additional field modifies the electron's trajectory and therewith changes the value of this phase by $\Delta\phi = \phi_2 - \phi_1$. Here, the subscript 1 denotes the phase accumulated when only the fundamental laser field is present, and 2 when both the fundamental and the second harmonic fields are used. As described above, to break the symmetry of the high-harmonic process and to obtain even harmonics, it is not necessary to impart a large additional phase to the electron. A small value of $\delta\phi \approx \pi$ between trajectories recolliding from the left and right, respectively, is sufficient to move from constructive to deconstructive interference. Thus, a very weak second harmonic field is sufficient. It shall only slightly perturb the electron's trajectory and shall not alter it so much that additional stationary solutions on top of the two trajectories that recollide from the left and right, respectively, become possible, as it is the case for a strong second harmonic field[477]. The phase ϕ that the electron accumulates during its field-driven motion in the continuum is, within the SFA, given by the semi-classical action integral (2.48) and reads

$$\phi = \int_{t_i}^{t_r} \frac{1}{2}[\boldsymbol{p} + \boldsymbol{A}(t')]^2 + I_p \, \mathrm{d}t', \tag{7.16}$$

where, for a given recollision energy and for a certain class of trajectories (e.g. the short ones), the times of recollision and ionization are uniquely connected such that $t_i = t_i(t_r)$. To calculate ϕ_2 we insert the second harmonic field into (7.16). This yields

$$\begin{aligned}
\phi_2 &= \int_{t_i(t_r)}^{t_r} \frac{1}{2}[\boldsymbol{p} + \boldsymbol{A}_{\omega_o}(t') + \boldsymbol{A}_{2\omega_o}(t')]^2 + I_p \, \mathrm{d}t' \\
&= \int_{t_i(t_r)}^{t_r} \frac{1}{2}[\boldsymbol{p}^2 + 2\boldsymbol{p}\boldsymbol{A}_{\omega_o}(t') + \boldsymbol{A}^2_{\omega_o}(t')] \, \mathrm{d}t' \\
&\quad + \frac{1}{2}\int_{t_i(t_r)}^{t_r} 2\boldsymbol{p}\boldsymbol{A}_{2\omega_o}(t') + 2\boldsymbol{A}_{\omega_o}(t')\boldsymbol{A}_{2\omega_o}(t') + \boldsymbol{A}^2_{2\omega_o}(t') \, \mathrm{d}t' \\
&\quad + I_p(t_r - t_i) \\
&\approx \phi_1 + \int_{t_i(t_r)}^{t_r} \boldsymbol{A}_{2\omega_o}[\boldsymbol{p} + \boldsymbol{A}_{\omega_o}(t')] \, \mathrm{d}t' = \phi_1 + \sigma(t_r, \Delta\varphi).
\end{aligned} \tag{7.17}$$

In the second to last step we have neglected the quadratically small term $\boldsymbol{A}^2_{2\omega_o}(t)$. The second term in the final expression of (7.17) is the additional phase that is caused by the second harmonic field. It is usually denoted by σ and, as it contains the second harmonic field, its value depends on the relative phase $\Delta\varphi$ between the fundamental and second harmonic. Within the SFA, the term $\boldsymbol{p} + \boldsymbol{A}_{\omega_o}(t)$ is the instantaneous momentum $\boldsymbol{p}_{\mathrm{SFA}}(t)$ of the electron that is caused by the fundamental field only. With that, $\sigma(t_r, \Delta\varphi)$ accumulated along a trajectory determined by the momentum $\boldsymbol{p}$ can be written as

$$\sigma(t_r, \Delta\varphi) = \int_{t_i(t_r)}^{t_r} \boldsymbol{p}_{\mathrm{SFA}}(t')\boldsymbol{A}_{2\omega_o}(t', \Delta\varphi) \, \mathrm{d}t'. \tag{7.18}$$

Now, let us see how $\sigma(t_r, \Delta\varphi)$ affects the interference during the recollision events and therewith the emission of the high-harmonics. As above, we compare trajectories that recollide during one half-cycle of the fundamental laser field (e.g. from the left), at time t_r, with trajectories that recollide one half-cycle later, at time $t_r + T/2$ (from the right). Obviously, $\boldsymbol{A}_{2\omega_o}(t_r + T/2) = \boldsymbol{A}_{2\omega_o} \sin(2\omega_o(t_r + T/2) + \Delta\varphi) = \boldsymbol{A}_{2\omega_o} \sin(2\omega_o t_r + \pi + \Delta\varphi) = -\boldsymbol{A}_{2\omega_o}(t_r)$. From that it follows that $\sigma(t_r + T/2, \Delta\varphi) = -\sigma(t_r, \Delta\varphi)$. This means that the phase difference of the two trajectories L and R, $\delta\phi = \sigma(t_r, \Delta\varphi) - \sigma(t_r + T/2, \Delta\varphi) = 2\sigma(t_r, \Delta\varphi)$, is no longer exactly zero or π as in the case of a single-frequency field discussed above. Instead, the phase difference can have, in principle, any value in between. As a result, by adding a second harmonic field to the fundamental, the strict destructive interference for even harmonics, described by (7.14) for a single-frequency field, is no longer valid and one also observes even harmonics.

Fig. 7.3(a) visualizes the different phases accumulated during the propagation of the L and R wavepacket, as well as the resulting changes to the HH spectrum and the appearance of the even harmonics. As we will show below, measurement of the intensity of the even harmonics for a very weak second harmonic field as a function of the $\omega/2\omega$-phase $\Delta\varphi$ allows obtaining intricate insight into the attosecond timing of the ionization and recombination processes.

Symmetry-breaking in an OTC field When an OTC pulse of the form (3.11) with field components of the fundamental frequency ω_o and second harmonic $2\omega_o$ along x and z, respectively,

$$\boldsymbol{E}(t) = E_{\omega_o}(t)\boldsymbol{e}_x + E_{2\omega_o}(t)\boldsymbol{e}_z, \tag{7.19}$$

is used for HHG, electron wavepackets are driven on two-dimensional trajectories. As described in Section 7.2.1, they recollide with the parent ion under a lab-frame angle θ_r, which depends on the relative strengths of the fundamental and second harmonic field and varies with the relative phase between the two colors, $\Delta\varphi$, see Fig. 7.2. The second harmonic field breaks the symmetry between adjacent half-cycles of the fundamental field. As described above, this breakage of the symmetry leads to the appearance of even harmonics. For a multi-cycle two-color field, when the changes in field strength due to the pulse's envelope can be neglected, the recollision scenario is the same for every field-cycle. It is thus sufficient to consider only one cycle of the two-color field. Fig. 7.2(f) shows that for a given value of $\Delta\varphi$, the recollision-direction along the polarization direction of the second harmonic field, z, is opposite for two adjacent half-cycles, while it is the same along the polarization direction of the fundamental field, x. The contribution to the n-th order of the harmonic spectrum at frequency $\omega = n\omega_o$ from the first half-cycle, denoted by the index 1, can be written as

$$\boldsymbol{\epsilon}(n\omega_o) \propto \epsilon_{x,1}(n\omega_o)\boldsymbol{e}_x + \epsilon_{z,1}(n\omega_o)\boldsymbol{e}_z, \tag{7.20}$$

where ϵ_x and ϵ_z denote the harmonic fields along x and z, respectively. The harmonic fields generated during the second half-cycle are identical to those generated during the first half-cycle, except for the symmetry-flip of the emission along z. Therefore, $\epsilon_{x,2}(t) = \epsilon_{x,1}(t + T/2)$ and $\epsilon_{z,2}(t) = -\epsilon_{z,1}(t + T/2)$, where the index 2 denotes the second half-cycle and $T = 2\pi/\omega_o$ is the period of the OTC field. In the frequency domain, the delay $T/2$ leads to a pre-factor $e^{-i\omega T/2} = e^{-i\pi\omega/\omega_o} = e^{-i\pi n}$, such that $\epsilon_{x,2}(n\omega_o) = \epsilon_{x,1}(n\omega_o) \cdot e^{-i\pi n}$ and $\epsilon_{z,2}(n\omega_o) = -\epsilon_{z,1}(n\omega_o) \cdot e^{-i\pi n}$. Thus, the total field generated at frequency $n\omega_o$ during one full cycle of the OTC field is given by

$$\begin{aligned}
\boldsymbol{\epsilon}(n\omega_o) &\propto (\epsilon_{x,1} + \epsilon_{x,2})\boldsymbol{e}_x + (\epsilon_{z,1} + \epsilon_{z,2})\boldsymbol{e}_z, \\
&\propto (\epsilon_{x,1} + \epsilon_{x,1}e^{-i\pi n})\boldsymbol{e}_x + (\epsilon_{z,1} - \epsilon_{z,1}e^{-i\pi n})\boldsymbol{e}_z, \\
&\propto \epsilon_x(1 + e^{-i\pi n})\boldsymbol{e}_x + \epsilon_z(1 - e^{-i\pi n})\boldsymbol{e}_z = \begin{cases} 2\epsilon_x(n\omega_o)\boldsymbol{e}_x & \text{for even n} \\ 2\epsilon_z(n\omega_o)\boldsymbol{e}_z & \text{for odd n} \end{cases},
\end{aligned} \tag{7.21}$$

where in the last line we have made use of the correspondence $|\epsilon_{x,z}| = |\epsilon_{x,z,1}| = |\epsilon_{x,z,2}|$ and have dropped the indices 1 and 2. Equ. (7.21) shows that odd and even harmonics are orthogonally polarized. Note, that for its derivation we did not use any properties of the bound state but only made use of the symmetry of the OTC field. It is thus valid for any symmetry of the bound state. Via the dipole matrix elements the symmetry of the bound state will, however, affect the emitted HH radiation $\epsilon_{x,z}(n\omega_o)$. For a spherically symmetric bound state, the induced HH polarizations along x and z and therewith the correspondingly emitted HH field components $\epsilon_{x,z}(n\omega_o)$ directly reflect the recollision angle $\theta_r(n\omega_o) = \arctan\left(\epsilon_z(n\omega_o)/\epsilon_x(n\omega_o)\right)$. Because (7.21) shows that $\epsilon_x(n\omega_o)$ and $\epsilon_z(n\omega_o)$ are proportional to the even and odd harmonics, respectively, measurement of their intensities, thus, amounts to measuring the recollision angle,

$$\theta_r(n\omega_o) = \arctan\left(\frac{\epsilon_z(n\omega_o)}{\epsilon_x(n\omega_o)}\right) = \arctan\left(\sqrt{\frac{I_{\text{odd}}(n\omega_o)}{I_{\text{even}}(n\omega_o)}}\right), \tag{7.22}$$

which is exactly (7.10).

In situ attosecond measurements using perturbative fields

The idea of understanding the HHG process as an interferometer that can be controlled by adding a second harmonic field, as described in the previous paragraphs, has proven a very fruitful concept for measurements of attosecond dynamics. Originally demonstrated in Ref. [565], this concept has been further developed and was successfully applied to the measurement and even control of the HHG process and the production of attosecond pulses *as they are produced*[452,453,565–568]. That is, the HH radiation is probed in the very same medium in which it is produced. Thus, these approaches are sometimes called *in situ*-methods to distinguish them from *ex situ*-methods that characterize the HH radiation by comparison to a reference pulse in a different medium. *In situ* methods are based on the idea that a weak field (e.g. a second harmonic field) is added to the strong driving field that generates the HH radiation. The weak field perturbs the interferometer inherent to the HHG process and alters the phase of the electron trajectories. This modification of the phase may manifest itself in a modification of the spatio-temporal properties of the emitted HH radiation. Measurement of these modifications allows obtaining insight into the attosecond dynamics underlying the HHG process.

To sketch this underlying principle of *in situ* methods we can build on the results derived above for the case where a weak second harmonic field is added to the strong field that drives the HHG process. We have seen that this weak additional field leads to an additional phase σ in the high-harmonic dipole moment given by (7.18). Equ. (7.18) for σ can be straightforwardly generalized to an arbitrary shape of the additional field, as long as its action is perturbative, which yields

$$\sigma(t_r,\tau) = -\int_{t_i(t_r)}^{t_r} \boldsymbol{p}_{\mathrm{SFA}}(t) \int_{t_i(t_r)}^{t} \boldsymbol{E}_p(t'+\tau)\,\mathrm{d}t'\,\mathrm{d}t. \tag{7.23}$$

Here, $\boldsymbol{E}_p(t'+\tau)$ is the perturbative field added with some adjustable delay τ to the strong field that drives the electron on a recolliding trajectory determined by $\boldsymbol{p}_{\mathrm{SFA}}(t)$. With $\boldsymbol{A}_p(t) = -\int_{-\infty}^{t} \boldsymbol{E}_p(t')\mathrm{d}t' = -[\int_{t_i}^{t} \boldsymbol{E}_p(t')\mathrm{d}t' + \int_{-\infty}^{t_i} \boldsymbol{E}_p(t')\mathrm{d}t']$ (7.23) resembles expression (7.18). Let's see how the additional, perturbative phase $\sigma(t_r,\tau)$ affects the high-harmonic emission process. From Section 2.2.5 we know that the harmonic dipole emission at time t_r, as given by the high-harmonic dipole moment $\boldsymbol{d}(t_r)$, is determined by the product of the ionization rate at the emission time of the electron, $t_i(t_r)$, and the recombination dipole matrix element describing the interference of the bound wavefunction $\psi_0(\boldsymbol{r})$ with the recolliding electron's wavefunction evaluated including the electron's phase S. Thus, the dipole emission at t_r can be written as[565]

$$\boldsymbol{d}(t_r) \propto \langle \psi_0(\boldsymbol{r}) | \hat{\boldsymbol{r}} | e^{-iS(t_r,t_i(t_r),\boldsymbol{r},\boldsymbol{p}^s)} \rangle. \tag{7.24}$$

In equ. (7.24) the phase S has been written with its explicit dependence on the coordinate $\boldsymbol{r}$, i.e., in a formulation that goes beyond the SFA and involves the influence of the ionic potential. If we now split the accumulated phase S into its contributions from the strong driving field, S_1, and the additional phase from the perturbative field σ, we obtain

$$\boldsymbol{d}(t_r) \propto \langle \psi_0(\boldsymbol{r}) | \hat{\boldsymbol{r}} | e^{-iS_1(t_r,t_i(t_r),\boldsymbol{r},\boldsymbol{p}^s) - i\sigma(t_r,t_i(t_r),\boldsymbol{r},\boldsymbol{p}^s)} \rangle. \tag{7.25}$$

It has been shown[565] that when (i) the phase accumulated due to the additional field is negligible as the electron moves across the ionic core and when (ii) the effect of the additional field on the electron trajectory near the core is negligible on the scale of the ground state, the influence the $\boldsymbol{r}$-dependent part of σ can be neglected and one can simplify (7.25) to

$$\boldsymbol{d}(t_r,\tau) \propto \langle \psi_0(\boldsymbol{r}) | \hat{\boldsymbol{r}} | e^{-iS_1(t_r,t_i(t_r),\boldsymbol{r},\boldsymbol{p}^s)} \rangle \; e^{-i\sigma(t_r,\tau)} = \boldsymbol{d}_1(t_r)\; e^{-i\sigma(t_r,\tau)}. \tag{7.26}$$

Thus, the dipole emission $\boldsymbol{d}_1(t_r)$ induced by the strong driving field is modulated by the phase σ due to the perturbative field. As a result, the dipole emission $\boldsymbol{d}(t,\tau)$ and therewith the generated

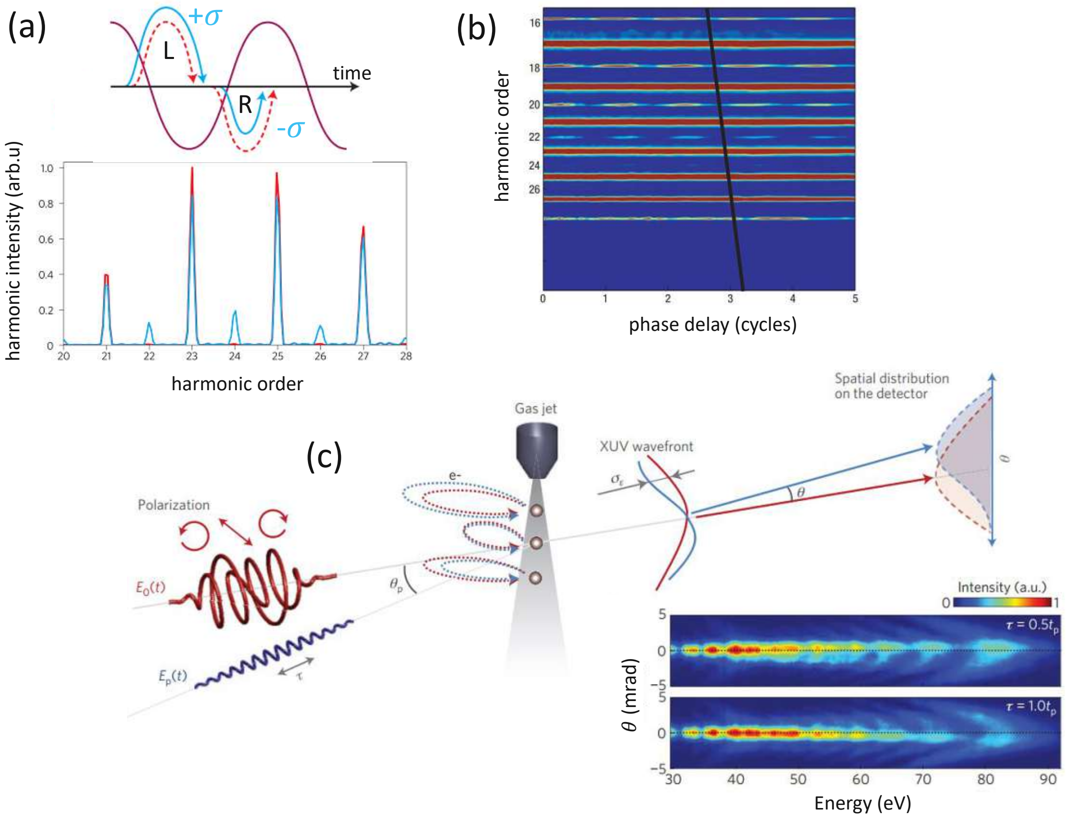

Figure 7.3: Gating techniques for high-harmonic generation using tailored waveforms. (a) The symmetry breaking between recollisions from the left (L) and right (R) induced by the addition of a weak 2ω field to a linearly polarized strong field with frequency ω, and the additional phase $\pm\sigma$ resulting from this weak perturbation of the recollision trajectories (top panel), leads to the appearance of even harmonics (bottom panel). Adapted from Ref. [568]. (b) Measured dependence of the even harmonics on the relative phase between the ω and 2ω fields. Adapted from Ref. [565]. (c) Illustration of the spatio-temporal measurement of an isolated attosecond pulse using a weak 2ω perturbation (blue) to a strong polarization-gating driving field (red). The non-collinearly added 2ω field perturbs the recollision trajectories in two spatial dimensions and weakly modifies the wavefront and therewith the propagation direction of the generated XUV harmonic radiation. Measurement of the propagation angle θ as a function of the harmonic energy (bottom right) allows for the spatio-temporal reconstruction of the generated attosecond XUV pulse. Adapted from Ref. [567].

harmonic field at the point of interaction in the gas-medium, $\boldsymbol{\epsilon}(t,\tau) \propto \frac{\mathrm{d}^2}{\mathrm{d}t^2}\boldsymbol{d}(t,\tau)$, depend on the delay τ between the strong driving field and the weak additional (perturbative) field $\boldsymbol{E}_p(t)$. In a more general formulation, the perturbative field leads to both amplitude- and phase-modulation of the generated harmonic field such that[567]

$$\boldsymbol{\epsilon}(t,\tau) \propto \boldsymbol{\epsilon}_1(t)[1+\alpha(t,\tau)]e^{-i\sigma(t,\tau)}. \tag{7.27}$$

Here, α denotes the amplitude modulation of the unperturbed harmonic field, $\boldsymbol{\epsilon}_1$, and σ is, as before, the phase modulation term. Together, the amplitude and phase modulation terms can be considered a gate function

$$G(t,\tau) = [1+\alpha(t,\tau)]e^{-i\sigma(t,\tau)}. \tag{7.28}$$

The key point is now to relate the action of the gate function to some observable that can be measured in an HHG experiment. Recording the variations of this observable as a function of the delay τ of the gate (or, equivalently, as a function of phase-delay $\Delta\varphi = \omega\tau$), allows reconstructing both the unperturbed harmonic field $\epsilon_1(t)$ and the gate $G(t,\tau)$. This opportunity has been exploited in a number of experiments. The pioneering work Ref. [565] used a weak second-harmonic field as the perturbative field $\boldsymbol{E}_p(t)$. This field was added collinearly and with parallel polarization direction to the strong field driving the HHG process. As explained above, this leads to a breakage of the symmetry between recollisions from the left and right and therewith to the appearance of even harmonics, see Fig. 7.3(a). The authors showed that the phase of the phase-modulation term, $\sigma(t, \Delta\varphi)$, depends linearly only on the emission time of the harmonics. Measuring the intensity modulation of the even harmonics as a function of the phase-delay $\Delta\varphi = \omega\tau$ between the strong fundamental and the weak second harmonic field, depicted in Fig. 7.3(b), thus, allowed the reconstruction of the emission, i.e., the recombination time t_r of individual harmonics.

Later, this work could be extended by the use of a collinear second harmonic field added with an orthogonal polarization direction[452]. The perturbations of the electron motion in the two polarization components act as two independent gates. The orthogonal component constitutes a 'displacement gate' that suppresses harmonics. At the same time the second-harmonic field breaks the symmetry between recollisions from left and right. The symmetry breaking is maximized when the lateral velocity of the recombining electron is a maximum, which constitutes a 'velocity gate'. These two independent gates allow to disentangle the emission times of the harmonics, t_r, from the ionization times, t_i, of the respective trajectories.

The *in situ* approach to attosecond probing of the HHG process could be further generalized by adding a weak second-harmonic gating field *non*-collinearly with a small angle θ_p to the strong driving field[567]. By this, a spatial modulation is added to the HHG process that can be read out from modulations of the spatial distribution of the harmonic beam along the transverse direction measured in the far field, see Fig. 7.3(c). The reason for the spatial modulations is that the time delay τ between the fundamental and second-harmonic beams varies depending on the transverse position y. Thus, also the phase σ that is added to the electron trajectories depends on y, $\sigma = \sigma(y)$. This y-dependence modifies the wavefront of the emitted harmonic field and therewith the spatial distribution observed in the far field. Measurement of the angular distribution of the harmonic intensity distribution for different photon energies as a function of τ thus allows to reconstruct the emitted harmonic field, see Fig. 7.3(c). An important advantage of the non-collinear approach over the collinear one is that it does not rely on symmetry-breaking between recollisions from the left and right taking place during consecutive laser half-cycles. Thus, the non-collinear is not limited to multiple HH emission bursts and can therefore be also used to reconstruct isolated attosecond pulses[567,568].

8

Controlling molecular processes with strong laser fields

Because of its tremendous practical importance, manipulation of physical or chemical processes and gaining control over their evolution, e.g., the breaking of a certain chemical bond in a polyatomic molecule, has been acknowledged as a crucial ability in both science and technology for decades. The nuclear motion involved in the breaking of a chemical bond in a molecule typically proceeds on time scales from several femtoseconds to picoseconds. These dynamics are driven by the derivatives of the potential formed by the intra-molecular electron distribution, which can restructure on much faster, attosecond, time scales. A suitable perturbation of the equilibrium bound electronic distribution, for example induced by ultrashort intense laser pulses, can therefore initiate nuclear motion towards a desired bond-breaking event. A relatively slow molecular fragmentation can thus be pre-determined on the much faster electronic time scale.

Strong, non-resonant laser fields are thus suitable tools to steer femtosecond to picosecond molecular bond breakage dynamics by controlled distortions of the electronic molecular system on sub-femtosecond time scales using field-sensitive processes such as strong-field ionization or electronic excitations. This possibility has been demonstrated by a huge number of works. For example, fragmentation reactions resulting in two moieties could be controlled using the carrier-envelope offset phase of few-cycle laser pulses as the control parameter[264,569,441,446,570–575]. Also, it was shown that selective removal of electrons from either inner or outer valence orbitals based on their different shapes[185] or their different sensitivity to laser intensity and/or pulse duration[576] can be a viable route to control molecular bond-breaking events.

In the following, the most important processes taking place during and after the interaction of a molecule with a strong and possibly tailored laser field will be discussed (Section 8.1). Subsequently, in Section 8.2, we will discuss principles for determining the outcome of molecular processes by carefully designing the interaction with the strong laser field. Sections 8.3 to 8.5 will then present examples where these principles were successfully applied. Finally, Section 8.6 will discuss methods for controlling molecular processes with the shape of the laser field.

8.1 Fundamentals of molecules in strong fields

Due to the incredibly rich dynamical and structural properties of molecules, the interaction of intense laser pulses with molecules may entail extremely complicated dynamics – in particular for the case of polyatomic molecules. This Section shall provide a short overview over the most important processes that may take place during and after the interaction of a strong laser field with most molecules. Because of the enormous complexity of large molecules (e.g., biologically relevant molecules) that complicates or makes it even impossible to understand the processes that are driven by the laser field, mostly ”small” molecules are studied in the field. Typically the molecules that have been studied so far consisted of only very few atoms. Often di- or triatomic molecules were investigated. Larger molecules with ten and more atoms were also studied, but are rather the exception. The short account of processes given below covers the most important processes that are observed for almost all molecules. Certainly, however, due to the large diversity of molecules with respect to their electronic and nuclear structure, the relevance of the different processes may vary strongly from molecule to molecule. It also needs to be mentioned that it is thoroughly beyond the scope of this work to provide an exhaustive coverage over all works and processes that have been investigated. Throughout this and the following Sections we will therefore restrict us to reviewing representative examples.

Alignment and orientation dependence of strong-field ionization Similar to atoms, the dominant process during the interaction of a strong laser field with molecules is single or multiple ionization. However, in contrast to atoms, for which this process is now relatively well understood, there are a number of characteristics and accompanying processes that render ionization of molecules much more complicated and make it an active field of research. One striking difference to atoms is that the ionization rate in molecules sensitively depends on the orientation of the molecule with respect to the laser polarization axis, as well as on the character of the molecular orbital from which an electron is removed[200,561,577–582]. These properties have a number of very important consequences. For example, it may lead to dominant ionization from lower-valence orbitals (see Paragraph below) which, in turn, itself has a number of fundamental implications for molecular fragmentation and/or restructuring processes. Furthermore, certain processes such as enhanced ionization (see Section 8.1.1 below) strongly depend on the molecular alignment and are completely inhibited for certain alignments. Because of this importance of the molecular alignment, methods for its control in an experiment have been developed[539–541,583,584]. Molecular alignment can be exploited for achieving selectivity in molecular bond-breaking processes as will be discussed in detail in Section 8.3.

Lower-valence shell ionization The electronic energy levels in molecules can be quite closely spaced such that, within a single particle picture, ionization may not only take place from the highest occupied molecular orbital (HOMO), but also from lower-lying valence orbitals (HOMO-1, HOMO-2, etc.) with a pronounced probability[404,585–589], especially when ionization from the highest lying states is suppressed due to a much smaller ionization rate caused by the shape of the orbital(s) that may feature negligible electron density (a node) along the laser polarization direction. Removal of an electron from lower-valence levels results in the preparation of the molecular ion in an electronically excited state. Thus, the shape of the orbital in combination with the molecular alignment with respect to the laser polarization direction can determine in which electronic state respectively on which potential energy surface (PES) the molecular ion is prepared. Thus, certain nuclear dynamics in the molecular ion associated with a certain PES can be suppressed or initiated during the ionization step. This can be exploited for, e.g., control of molecular bond-breaking dynamics as will be shown in Section 8.3.

Electronic excitation during and after ionization An intense laser field can also drive the transfer of population to electronically excited states[**226**,461,590–594] from which ionization can proceed more easily during the subsequent field cycles. Excitation of a molecule or molecular ion can also be induced by electron recollision in an analogous way as it is well-known for atoms[159,595,596]. Because excited states in a molecule or molecular ion can be dissociative, preparation of electronically excited states by the ionization process and/or by field-driven excitation occuring during the laser pulse may lead to fragmentation of the parent molecule[404,597]. For example, excitations due to removal of an electron from a lower-lying molecular orbital by electron recollision can be used to control fragmentation reactions of polyatomic molecules on the laser-sub-cycle time scale[264], as will be discussed in Section 8.6.1. Because electronically excited molecular ions can be created either during the ionization process by ionization from lower-valence levels (see corresponding Paragraph above), or by field-induced excitation after the ionization process, an important question is how these processes can be disentangled. Observing the dependence of these two contributions on the laser field parameters separately may open up possibilities for determining molecular fragmentation and dissociation processes, as will be discussed in detail in Section 8.4.

Interplay between nuclear motion and ionization The laser field may also trigger nuclear dynamics and chemical bond rearrangement processes. Depending on the shape of the involved potential energy surfaces (PESs) on which the nuclear dynamics proceeds, the binding energy may vary. Thus, the ionization probability becomes modulated by the nuclear motion. Temporally resolving the modulations of the ionization yield using pump-probe measurements with two delayed ultrashort intense pulses can thus provide insight into the nuclear motion set in pace by the first of the two pulses, as has been shown in recent measurements for vibrational dynamics in CO_2[598,599]. Likewise, the induced vibrational motion can be visualized using a technique called *time-resolved Coulomb explosion imaging*. In this technique the second pulse (multiply) ionizes the molecule upon which it undergoes fragmentation due to the repulsive Coulomb forces between the nuclei. Assuming purely Coulomb-shaped PESs the geometry prior to the application of the second pulse can be reconstructed as has been shown, e.g., for the simplest molecules, H_2 and D_2,[443,444,600–602], for more complicated diatomic molecules such as N_2, O_2 and CO[603], or for triatomic molecules[604]. A very important and ubiquitous manifestation of the influence of nuclear motion in the ionization behaviour is the process of enhanced ionization (EI)[605,606] originally described for the H_2 molecule. In this process the ionization rate is strongly enhanced at a critical internuclear distance, R_c, as compared to the ionization rate at the equilibrium internuclear distance or that at an internuclear distance much larger than R_c. Although enhanced ionization has been acknowledged as a very general process and as such has been observed for a range of different di- and tri-atomic molecules, a recent series of experiments and simulations have shown that EI takes place largely differently for polyatomic molecules, in particular for the important class of hydrocarbons. A detailed account of EI will be given below in Section 8.1.1. The influence of the nuclear motion during the laser pulse does, of course, not only show up in the EI process. In fact, any kind of nuclear motion, in particular geometrical restructuring during laser interaction will affect the ionization and therewith potentially also the subsequent fragmentation or dissociation behaviour. This will be explained in detail in Section 8.5.

Fragmentation/dissociation processes Probably the most striking difference of the interaction of a strong laser pulse with a molecule as compared to that with an atom is the capability of molecules to fragment or dissociate[‡]. These processes are of fundamental importance in nature. For example, chemistry can be loosely defined as bond-breaking and bond-making. Breakage of a molecular bond, i.e., the fragmentation or dissociation of a molecule, can thus be perceived as one of the elementary building blocks of chemistry, but is also of uttermost importance in the physical and biological sciences. Molecular fragmentation and dissociation processes taking place after irradiation with an intense laser pulse have been studied by literally countless works. The dynamics of bond-breaking processes crucially depends on the mass of the involved fragments and the shapes of the potential energy curves/surfaces on which the processes take place. Typical time scales

---

[‡] The terms dissociation and fragmentation are often used synonymously. Here, we use the term dissociation to indicate a process where a molecule breaks into a number of neutral moieties, or into a set of a mixed neutral and ionic moieties, whereas fragmentation is used to indicate the breakage into only ionic moieties.

range from about ten femtoseconds for fragmentations involving the light protons, to the picosecond time-scale for heavy moieties. The bond-breaking dynamics after laser-interaction crucially depends on which state(s) the molecule is left after the laser pulse has faded. While the dissociation or fragmentation can proceed promptly after the application of the laser pulse, in particular if the molecule is prepared in an ionic state, it may also happen that bond-breaking processes take place with a considerable delay to the laser-interaction. The author and co-workers have reported that the process where a light proton is split off (deprotonation), can exhibit a very long retardation of hundreds of nanoseconds[607]. The observed **slow deprotonation** coexists with its almost prompt counter-part. The physics underlying this slow deprotonation is the population of high-lying vibrational states in electronically excited states during laser-interaction. Molecules prepared in such states exhibit a very long survival time as these states decay only with a very small rate.

An important point in molecular fragmentation is that usually there exist several *pathways* towards a certain set of fragments, called a *channel*. While it is simple to fragment a molecule with an intense laser pulse, it is challenging to unequivocally identify and characterize the moieties of a certain channel, and even more difficult to securely identify the pathway that has been taken. One often applied technique for such studies is coincidence momentum imaging, see, e.g., Refs. [185, 569, 576, 598, 607–613] and the examples in Sections 8.2 to 8.6.

Likewise, while it is simple to break *some* bond in a molecule, it is challenging to break a *specific* bond in a molecule. This problem has for decades been the subject of the field called *quantum coherent control* that applies weak (temporally shaped) femtosecond laser pulses to *resonantly* excite vibrational dynamics[614–617]. Stunning achievements have been made in this field. However, with the availability of strong and also tailored laser fields a new paradigm for non-resonantly controlling molecular bond-breaking processes by directly steering the electrons has become available. This possibility will be discussed in detail in Sections 8.2 to 8.6.

Geometrical restructuring dynamics Prior to fragmentation/dissociation the molecule might restructure. Here, we understand restructuring as a large-scale change in geometry that may lead to the production of new species during a subsequent fragmentation process. One example would be the generation of O_2^+ from CO_2^{2+} that has been observed recently by the author and co-workers[613]. A prominent and highly studied example for a complex restructuring process is ultrafast hydrogen or proton migration that has been observed in many molecules, e.g., in methanol[618,619] and, as it has been identified by experiments that this process takes place during the laser-interaction with very short pulses, it is claimed that this process can take place on extremely fast time-scales. Later, proton migration has been studied also in a range of other molecules and has been observed for, e.g., two-[609] and three-body[608,610] fragmentation processes of 1,3-butadiene, in acetylene[185,620] and in allene[621]. Laser-driven geometrical restructuring of polyatomic molecules can even result in the migration of several moieties within one molecule which might form new bonds and will be ejected as new species, e.g., H_2^+ from ethylene[264] or H_3^+ from methanol[622], and it has also been observed that several different protons and deuterons migrate within a molecule leading to many different possible combinations of final fragmentation products[623]. Sections 8.2 to 8.6 will discuss geometrical restructuring processes during and after laser-interaction in greater detail.

Bond formation Until now, strong laser fields have almost exclusively been used to induce and also control the breakage of molecular bonds. Successful examples for this type of research will be discussed during Sections 8.2 to 8.6. However, thus far only few works have considered the investigation of bond-formation using strong fields. This might seem surprising since the formation of a chemical bond is probably the essential process in nature and ultimately determines the foundations of life. One reason for this neglect is that interactions between intense laser pulses and molecules are usually studied in single-molecule environments in the gas phase which impedes the observation of a potentially occurring bond-forming reaction a priori. Also, it is not easily possible to provide a bath in the gas phase that absorbs the excessive energy set free during the creation of a chemical bond. Successful observations of laser-induced bond-formation processes have therefore used clouds of ultracold atoms in magneto-optical traps[624] or have used metal surfaces as the mediating bath[625]. Another approach is to exploit the selectivity of a multi-photon transition for the creation of a bond between accidentially suitably spaced atoms in a randomly distributed gas sample, as has been demonstrated for creation of bonds in excited magnesium dimers Mg_2[626]. Recent experiments indicate, though, that inside laser-driven plasma channels, so-called filaments, bond-forming reactions do take place, i.e., a strong laser pulse can indeed induce the formation of a chemical bond (in addition to a simple bond-breaking reaction); examples are $N^+ + O_2 \rightarrow NO^+ + O^*$[627], $N^{2+} + N^2 \rightarrow N^{4+}$[628], or the formation of several stable neutral species such as CO_2, C_2H_2 and H_2O in a dense gas mixture of CO and H_2[629]. Unfortunately, it is difficult to study the molecular dynamics that underlie bond-formation reactions in the dense multi-particle plasma environment of a filament. The most widely used indirect technique is to detect the fluorescence signal emitted from the molecules and molecular moieties in the filament. This signal is, however, a cumulative signal over a huge number of molecular emitters and also affected by macroscopic propagation effects. Also, it does not permit statements (or only in a very limited way) about the ultrafast dynamics of the underlying molecular processes. Furthermore, the dense plasma environment prevents obtaining more specific information, e.g., about the role of neighbouring molecules involved in the observed reactions, let alone very profound questions such as how the moieties share their electrons to form a bond. As a consequence the understanding of the underlying dynamics that lead to the observed bond-formations is currently very rudimentary. More detailed investigations necessitate a well-defined reaction environment and more specific ultrafast methods that are able to capture the underlying nuclear and electronic processes. Nevertheless, it is foreseeable that the investigation of strong-field-induced bond-forming reactions and gaining control over this process will become an important research field within the next decade.

8.1.1 Enhanced ionization

An important discovery in the ionization behaviour of molecules is that of the process of enhanced ionization (EI) that was already shortly discussed above. EI has been investigated in numerous experimental and theoretical works for different molecular species, e.g., H_2/D_2[605,606,630–636], I_2[637–640], N_2[641–643], and Cl_2[644]. It was found that in many cases the ionization rate is strongly enhanced around a critical internuclear distance, R_c. This enhancement can be explained by a mechanism where at R_c electrons can tunnel directly into the continuum through the field-suppressed intramolecular potential barrier from the potential well that is uplifted in energy by the laser field, when at the same time the electronic density localizes on the upper potential well. This charge localization on the upper potential well is due to a strong coupling between charge-resonance states, which is why this mechanism has been dubbed **charge-resonance enhanced ionization (CREI)**[605,606,642]. Although this simple picture needs to be modified for certain situations such as for π or δ molecular states[633] or for non-symmetric molecules[645,646], and in detail is affected by laser-sub-cycle electron dynamics[635,636], the underlying mechanisms leading to efficient single- or few-electron laser-ionization in small molecules can in many cases be explained by (variants of) the CREI mechanism.

Experiments by the author and co-workers[184,647,648] on strong-field multiple ionization of polyatomic molecules such as CH_4, C_2H_2, C_2H_4, and C_4H_6 have revealed surprisingly high charge states up to +14 for relatively moderate laser intensities. The detailed analysis of the experimental results showed that there exists some multiple-bond version of EI, in which EI takes place at several bonds in parallel. See **Paper 16** and **Paper 17** for details. Theoretical works using time-dependent Hartree-Fock (TDHF)[649–651] and time-dependent density functional theory (TDDFT)[184,186] have confirmed the high charge states measured in these experiments as well as the experimentally found involvement of multiple bonds in the ionization mechanism. However, the mechanism that leads to the strong enhancement of ionization from both the most weakly and also the more strongly bound inner-valence orbitals was still unclear.

By multi-particle coincidence momentum imaging experiments together with the complementary insight obtained through quantum chemical simulations based on the time-dependent density functional theory (TDDFT) and using the acetylene molecule as a model system the author and co-workers finally succeeded in establishing an intuitive explanation of the intensely debated mechanism behind the efficient laser-ionization of polyatomic molecules[188], see **Paper 18** for details. The measurements and simulations revealed that the strong enhancement of the ionization for molecules aligned parallel to the laser polarization direction is due to the combination of (i) a strong increase in the coupling between lower-valence σ orbitals (also to weakly bound and even unbound orbitals from the LUMO complex) and (ii) the geometrically induced energy upshift of the orbitals as the C-H internuclear distance increases beyond a certain value (about 2.5 Å for acetylene, roughly 2-2.5 times the internuclear distance). The reason for the increased coupling is the increase of the dipole transition matrix elements and the closeness of the energy levels. To express the two mentioned key-ingredients in this identified mechanism, it was named **EIC-MOUSE** (**E**nhanced **I**onization from laser-**C**oupled **M**ultiple **O**rbitals that are **U**p-**S**hifted in **E**nergy). For molecules aligned perpendicularly to the laser polarization direction this mechanism is inhibited, since at the equilibrium C-H internuclear distance dominantly π electrons are ejected which does not result in a stretch of the C-H bonds that is necessary for entering the regime of enhanced ionization.

The EIC-MOUSE mechanism shows a number of features that render it different from the CREI mechanism[605,606,642]: The first important feature of EIC-MOUSE is that it builds on the strong energy upshift at field-free conditions of multiple orbitals for stretched molecular configuration which, secondly, leads to enhanced ionization for molecules stretched *beyond* a certain critical internuclear distance rather than only *around* the critical internuclear distance. In the enhanced ionization regime, thirdly, the laser-field-induced coupling between *multiple* orbitals becomes crucial, whereas for CREI only *two* charge-resonant states are coupled. Fourth, in EIC-MOUSE not only the coupling between bound orbitals but also coupling with high-lying and potentially unbound orbitals contributes to the enhanced ionization. Fifth, while for CREI the laser-driven coupling of the two (charge-resonant) orbitals results in an oscillatory charge-localization at two different locations inside the molecule, which is a necessary condition for efficient ionization from the energy-upshifted potential well at the critical internuclear distance, the coupling of the multiple orbitals in EIC-MOUSE does, in contrast, not necessarily lead to oscillatory charge localization, and is also not required. It is thought that, although the EIC-MOUSE mechanism was developed for the example of acetylene, it can also explain the high charge states measured in many experiments on various hydrocarbon molecules such as those described in Refs. [**184**, **647**, **648**] and [643, 652, 653].

8.2 Principles of strong-field control of molecular bond-breaking

Fragmentation or dissociation processes of molecules, potentially preceded by isomerization processes such as a proton migration[609], are of fundamental importance in nature and are studied in the physical, chemical, and also biological sciences. As has been mentioned in Section 8.1, controlling such processes with light pulses has been a research goal of quantum coherent control for decades. More recently, with the availability of ultrashort intense laser pulses, possibly with a tailored field evolution and in different wavelength ranges, an alternative approach to determining the breakage of molecular bonds has been investigated. In this approach, one exploits the strong laser electric field as a driving force that can act directly onto the intra-molecular valence electron cloud that actually forms a chemical bond. This is a fundamentally different approach to controlling molecular dynamics than the one used in quantum coherent control, where weak (shaped) light pulses and pulse sequences are used to steer a system from an initial quantum state to the desired one by excitation of nuclear vibrational motion taking place on tens of femtoseconds to picoseconds[614–617,654].

In contrast, in the strong-field approach, an ultrashort, intense laser pulse is used to precisely and selectively distort the valence electron cloud by driving sub-cycle processes such as field-ionization and by that, in turn, induces dynamics of the nuclei. That is, a strong laser field that may last for only a few oscillation periods is harnessed for controlling much slower molecular restructuring and bond-breaking processes that involve nuclear motion proceeding on time-scales from tens of femtoseconds to possibly microseconds. These nuclear processes, however, are preceded and ultimately determined by much faster processes — intra-molecular dynamics of the valence electrons that form the chemical bonds, which, due to their (multi-)eV-scale bandwidth of energy levels, exhibit characteristic restructuring time-scales that reach into the sub-femtoseconds. Therefore, even though the strong laser field only couples to the valence electrons in the molecule and induces distortions on sub-cycle times, by using different parameters of the laser pulses as control knobs, e.g., peak intensity, duration, oscillation period (wavelength) or the sub-femtosecond evolution of the laser electric field, the motion of the nuclei can be controlled, or rather *pre-determined*, on time-scales that can be much longer than the duration of the laser pulses.

Thus, two very different time-scales may be involved in the control of bond-breaking processes using strong laser fields. A fast one, on which the laser field interacts with the electrons in the molecule (e.g. the ionization process, or field-driven population of excited states), and a potentially much longer one, on which the molecular restructuring takes place. Because the laser field interacts with the molecule only during the short duration of the laser pulse, for heavy and slow nuclei it can, thus, never guide the molecular restructuring dynamics along a desired fragmentation pathway during times when the laser pulse is long over. It is only possible to determine the outcome of the fragmentation reaction during the short laser interaction time, i.e., on a pre-restructuring time-scale. To stress this context, one may refer to this type of defining the bond-breaking dynamics as pre-determination.

For very light nuclei and associated very fast nuclear dynamics, e.g., for hydrogen bonds, the nuclei might move significantly during the interaction with the strong laser field, even for very short pulses. In that special case the nuclear motion can be influenced during its motion by modulating the concomitant electron dynamics with the laser field. This case will be discussed in Sections 8.5 and 8.6. As in this case both the nuclear and the electronic configuration change on the time-scale of the laser field oscillations, tailoring the field-evolution becomes sensible, cf. Section 8.6.

In general, pre-determining or controlling fragmentation and accompanying isomerization processes is possible by preparing the molecule or molecular ion in specific dissociative states from which the reaction proceeds through a desired fragmentation *pathway* on (multi-dimensional) potential energy surfaces/curves towards a certain set of final fragment products, which we call a *channel*. In particular for multi-body fragmentation reactions of polyatomic molecules there often exist a number of different pathways that lead to the same set of fragments[**576**,**610**]. Preparation in suitable dissociative states can be achieved either during the ionization process by removing electrons from specific orbitals, but also by subsequent excitation and state-coupling processes during the interaction with the laser field. In practice, a mixture of these excitation mechanisms may be at work and their relative importance may strongly depend on the laser pulse parameters, in particular on intensity and pulse duration[**610**,**611**].

Preparation of a molecular ion in a certain dissociative excited state by ionization is possible by removing specific inner-valence shell electrons[**264**,404,405]. As excited electronic states in a molecular ion are often dissociative, the removal of an inner-valence shell electron during ionization, and therewith the preparation of the molecular ion in an excited state, may initiate the fragmentation of the molecular ion. It has been shown that this type of preparation can even be used to predetermine molecular fragmentation on a laser-sub-cycle time-scale[264]. Excitation to higher ionic energy levels during the laser pulse, on the other hand, can be achieved by field-induced transitions[461,591,592,594] or also by electron recollision[159,595,596].

In the following Sections 8.3-8.6, in order to illustrate the different control strategies outlined above, we will discuss in detail examples of works that have successfully implemented these strategies. The discussion will be structured along the method that is exploited. We will discuss strong-field control . . .

(i) **. . . by selective ionization from specific (inner-valence) orbitals.**
Based on the different shapes of the orbitals, e.g., Refs. [**185**, **576**], see Section 8.3.

(ii) **. . . by a combination of selective ionization and field-induced excitations.**
Based on the different sensitivity of ionization to orbital shape, laser intensity, and pulse duration, e.g., Refs. [**576**, **610**–**612**], see Section 8.4.

(iii) **. . . by control over the delay between multiple ionization steps timed to the nuclear motion.**
Based on timing ionization steps to concomitant nuclear motion, e.g., Refs. [**598**, **612**], see Section 8.5.

(iv) **. . . by controlling ionization and/or field-induced excitations using tailored laser waveforms.**
Based on asymmetry of tailored waveform, e.g., Refs. [**264**] and [34, 446, 575], see Section 8.6.

8.3 Selective bond-breaking by controlled lower-valence ionization

In this Section we will discuss how molecular bond-breaking processes can be determined by selective ionization from specific inner valence orbitals. We will see that selectivity in the ionization process allows for the controlled population of specific electronic surfaces in the ion connected with certain reaction pathways. As a result, it becomes possible to determine the relative probability of individual reaction pathways starting from the same parent molecular ion, as has been demonstrated first by the author and co-workers using the acetylene molecule as the example, see Ref. [**185**] and **Paper 12** for details.

The control strategy adopted in this work can be explained as follows (see Fig. 8.1 for reference): If two π-electrons are removed from acetylene, the stable electronic ground state of the dication is reached and dissociation is inhibited. The removal of one π- and one σ-electron, however, puts the dication into an excited electronic state. Different electronic states feature, in general, different characteristic potential energy surfaces. The dissociation or isomerization processes that follow the ionization event may therefore, in turn, proceed along different specific nuclear degrees of freedom and as a result will end up in different fragmentation channels. Controlling the population of a specific excited electronic surface in the dication by determining the ratio of ionization from different orbitals (e.g. σ vs. π), allows, thus, to control the yield of a certain fragmentation channel associated with this electronic surface.

To determine from which molecular valence orbital electrons are removed, one can exploit the different angular-dependent ionization rates of inner and outer valence electrons. Depending on the symmetry of the orbital and its relative orientation to the direction of the laser electric field, ionization rates may differ substantially[187,585]. While, qualitatively, in acetylene σ-type orbitals are in general preferentially field-ionized when the laser polarization direction is parallel to the molecular axis, π-type orbitals are preferentially ionized for perpendicular alignment. Quantitatively, however, ionization rates depend on the shapes, symmetries, ionization potentials and multi-electron nature of the molecular orbitals, as well as on the parameters of the ionizing laser pulse[187].

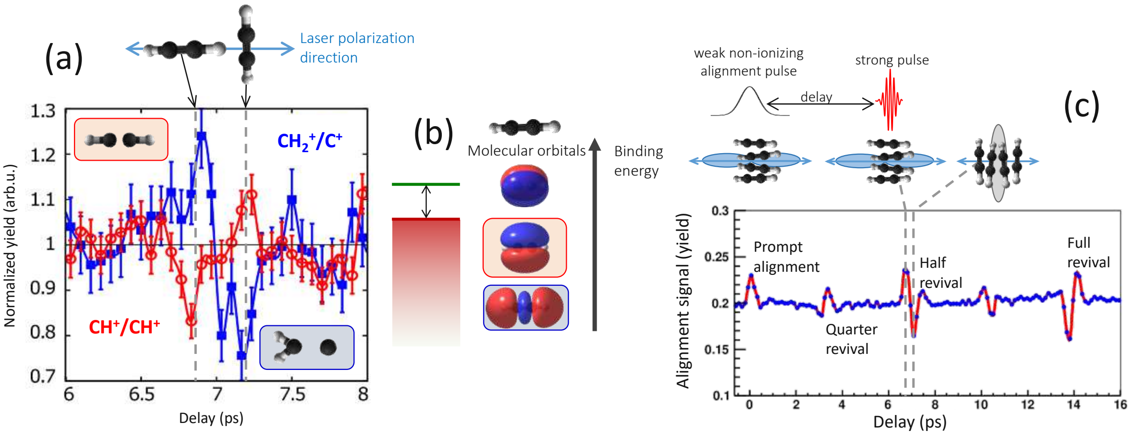

Figure 8.1: Control over molecular fragmentation reactions using selective ionization from specific orbitals. (a) Measured normalized yields of two fragmentation channels of acetylene (indicated in the figure) over pump-probe delay between the weak alignment pulse and the strong ionizing pulse around the half revival of the rotational wavepacket induced by the alignment pulse, whose signature is depicted in (c) by the measured proton yield. For parallel alignment the yield of the fragmentation channel involving proton migration (blue) in (a) is strongly enhanced over the channel where the center bond breaks (red); for perpendicular alignment the situation is reversed. This can be explained by the sensitivity of the underlying ionization processes to the shapes of the molecular orbitals associated with a certain fragmentation reaction, see panel (b). Adapted from Ref. [185]. See text and **Paper 12** for details.

To obtain orbital-selectivity in the ionization process, the angle of alignment of the molecular axis with respect to the laser polarization direction can be controlled. The alignment angle can be manipulated using laser impulsive alignment with a weak non-ionizing laser pulse[538–541]. Upon interaction with the alignment pulse, a rotational wavepacket is created in the neutral C_2H_2 molecule. A second, strong laser pulse, delayed by Δt, ionizes the transiently aligned molecules and induces fragmentations. From the fragments a signature of the rotational wavepacket can be calculated, shown in Fig. 8.1(c) as a function of Δt. Around the half-revival time of the rotational wavepacket the molecular alignment is parallel to the laser polarization direction and changes to perpendicular shortly later.

As could be demonstrated, this strategy of controlling the ionization process by the molecular alignment applied to acetylene is capable of determining not only the yields of specific bond-breaking channels but also the *relative* probability of individual reaction pathways[185]. This is shown in Fig. 8.1(a) for the two fragmentation channels $C_2H_2^{2+} \rightarrow CH_2^+ + C^+$ and $C_2H_2^{2+} \rightarrow CH^+ + CH^+$. The two important features of the measured fragmentation yields over Δt around the half-revival are that (i) they both show a pronounced dependence on the transient alignment, and (ii) even more importantly, their delay-dependence differs. While the yield of the fragmentation channel $C_2H_2^{2+} \rightarrow CH_2^+ + C^+$ peaks at parallel alignment, the yield of the channel $C_2H_2^{2+} \rightarrow CH^+ + CH^+$ peaks at perpendicular alignment. By adjustment of Δt it is thus possible to relatively enhance the yield of one channel with respect to the other (in this example, Ref. [185], by about 150%). This demonstrates the potential of molecular alignment to selectively enhance or suppress individual fragmentation channels of the same parent ion of polyatomic molecules on a very short time scale.

8.4 Role of electronic excitation processes in bond-breaking control

In Section 8.3 it was shown that bond-breaking reactions in polyatomic molecules can be determined by controlling the population of specific dissociative excited state in the molecular ion via selective ionization from certain valence orbitals. In general, however, the population of dissociative states may not only be determined during the ionization step by ionization from lower-valence orbitals, but *also* by field-driven excitations taking place after or in the course of the ionization dynamics. Both processes, ionization and excitation, are driven by the laser field oscillations and thus may take place on very fast time-scales long before nuclear motion sets in. However, they may exhibit a different sensitivity to the parameters of the laser field. Thus, for a refined view on light-field control of molecular bond-breaking processes, in particular in polyatomic molecules where excitation processes might be relatively more important than in small di- or triatomic molecules due to the more closely spaced electronic level structure of larger quantum systems, and for which due to their higher complexity a variety of different dissociation pathways coexist, the different influence of both processes and their potentially different dependence on laser pulse parameters must be considered.

To visualize this, we consider the bond-breaking processes $C_2H_4^{2+} \rightarrow CH_2^+ + CH_2^+$ and $C_2H_4^{2+} \rightarrow C_2H_3^+ + H^+$ of the ethylene molecule as examples. Fig. 8.2(a) shows potential energy curves, calculated using quantum chemical methods, for a variation of the bond-length of the center C-C bond[576]. It can be seen that the fragmentation *channel*, in which the center C-C bond is broken, can be reached by (at least) three different *pathways*, marked by arrows in Fig. 8.2(a). Two of the three indicated pathways are directly reached by removal of electrons from lower-valence orbitals. If at least one of the two electrons that are removed during the double ionization process is taken from the HOMO-2, a dissociative excited state is populated and the molecule disintegrates by breakage of the center C-C bond. The third pathway that results in the breakage of this bond cannot be reached simply be ionization from lower-valence orbitals, but necessitates field-driven population transfer. In detail, in this pathway the molecule is prepared in the ground ionic state during the double ionization process by removal of two electrons from the HOMO. Subsequently an additional field-driven excitation to a higher excited state occurs, from which the molecule fragments via breakage of the center C-C bond.

By the analysis of measured kinetic energy release (KER) and angular distributions of fragment ions measured by coincidence momentum imaging in an experiment performed by the author and co-workers[576] it was possible to disentangle the different contributions of (i) ionization from lower-valence orbitals and (ii) field-induced population transfer to the overall yields of the two above-introduced fragmentation channels that consist in the breakage of the center C-C and terminal C-H bonds, respectively; see **Paper 14** for details. Disentangling the different pathway-contributions allows to separately investigate their dependence on the laser pulse parameters, e.g., on peak intensity and pulse duration. It turns out that for the channel resulting in C-C breakage the relative importance of the pathway that involves field-driven excitations to higher electronic energy levels increases with laser peak intensity[576]. In contrast, the channel involving C-H breakage is reached by ionization dominantly from HOMO and HOMO-1 and thus does not necessitate the removal of electrons from low-lying valence orbitals (and therewith no high intensities), nor is it possible to influence its slow dissociation dynamics via field-induced population transfer during the short laser pulse.

Thus, the experiment demonstrates that the relative importance of the different molecular pathways along different dissociative electronically excited states, by which a particular set of final fragmentation products can be reached, may strongly depend on the parameters of the laser pulse. In turn, by properly choosing the pulse parameters it becomes in many cases possible to steer the molecular dynamics along a desired pathway in the phase-space spanned by the nuclear coordinates and momenta towards a certain set of final fragment ions. Indeed, this was demonstrated

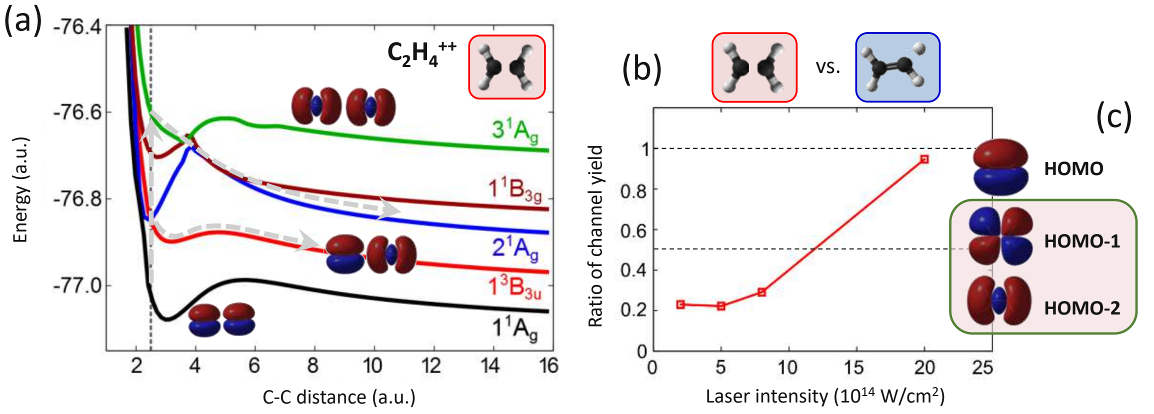

Figure 8.2: Pre-determination of molecular fragmentation by selective ionization and field-induced excitations. Adapted from Ref. [576]. (a) Different pathways (indicated by gray dashed arrows) on various potential energy curves (in color) towards breakage of the center C-C bond of the ethylene dication. The three indicated pathways can be associated with selective ionization from certain (inner-valence) orbitals [indicated by cartoons of their shapes, cf. (c)], and field-induced (vertical) population transfer to higher potential energies *after* ionization [arrow to 3^1A_g potential energy curve in green]. A detailed investigation (see text for details) shows that these pathways become more likely with increasing laser intensity, while the fragmentation pathways towards C-H bond breakage, in contrast, are not enhanced. This behaviour can be used to relatively enhance C-C bond-breakage over C-H bond-breakage [see (b)] using the laser intensity as a control parameter. See the feature article discussing this result in **Physics**[655] and **Paper 14** for further details.

in Ref. [576]: The strongly different dependence on pulse intensity of C-C and C-H bond-breakage could be exploited for enhancing the relative yield of the former channel as compared to the latter by about 400%, see Fig. 8.2(b). Selective population of excited ionic states by controlling intramolecular electronic processes (in particular electron removal from lower-valence orbitals and non-adiabatic population transfer) with strong non-resonant laser fields is, thus, an efficient and general method for selectively enhancing or suppressing individual fragmentation channels.

8.5 Role of coupling between electron and nuclear motion

So far, in Sections 8.3 and 8.4, pre-determination of bond-breakage with a strong laser field could be described by neglecting nuclear motion during the laser interaction. This is, in general, possible when the nuclear motion is slow as compared to the duration of the ionizing laser pulse[406,656] — a prerequisite that is often not fulfilled for light nuclei, in particular for hydrogen bonds as in H_2[657], or in hydrocarbons as strikingly exemplified by the process of enhanced ionization[188,648] discussed in Section 8.1.1. Here we will discuss how the motion of the nuclei that may take place during the laser interaction can modify the outcome of a bond-breaking reaction. The decisive moments during the laser interaction are those, when the dynamics of the bound electrons is non-adiabatically influenced by the laser field, e.g., at the instants when an electron is emitted or when an excitation takes place. Thus, the timing of the electron removal relative to the nuclear motion is a crucial parameter that can determine the outcome of a bond-breaking reaction.

Single pulse-control over electron dynamics relative to nuclear motion An experiment by the author and co-workers has shown that the delay between successive ionization steps is indeed crucial for the fragmentation behaviour[612], see **Paper 13** for details. In that work the interplay between the electronic and nuclear dynamics during a laser-induced fragmentation reaction of a polyatomic molecule, ethylene, into three moieties that involve the breakage of two chemical bonds is studied. As compared to a fragmentation reaction where only one bond is broken, there exist a number of processes that are only present when the molecule breaks into three moieties. For example, a three-body fragmentation, which can only occur in a polyatomic molecules, takes place along (at least) two nuclear coordinates. Thus, the fragmentation dynamics must be necessarily described by molecular potential energy surfaces (PESs) rather than only one-dimensional potential energy curves. Furthermore, if a polyatomic molecule fragments into three moieties, the sequence and timing of the two involved fragmentation steps become important[610]: The two fragmentation steps can occur concertedly (simultaneous breaking of two bonds) or sequentially (one after another). For a sequential fragmentation dynamics it becomes additionally important which one of the two involved bonds breaks first.

The experiment, supported by quantum simulations, shows that the outcome of fragmentation reactions of the ethylene trication that involve the breakage of more than one chemical bond sensitively depends on the duration of the intense, non-resonant, ultrashort drive laser pulse. Specifically it is shown that the ratio of yields for fragmentation into three vs. two fragment ions can be determined by using the duration of the laser pulses as a parameter. The relative probability to fragment into two vs. three ionic fragments is enhanced by roughly an order of magnitude if the laser pulse duration is increased from 4.5 fs to 25 fs, see Fig. 8.3(b) for measured data. The underlying mechanism is the relative timing of successive electron release events and the concomitant nuclear motion: The longer period during which molecular bonds can stretch when interacting with long laser pulses, and the resulting lower potential energy available to the fragmentation, leads to a strong relative enhancement of the two-body fragmentation reaction, see Figs. 8.3(a) and 8.3(c) for a plot of the calculated potential energy surfaces of the di- and trication and for a visualization of the crucial influence of the delay between the two ionization events. In contrast, for short pulses, for which the molecular bonds have almost no time to stretch in the dication between the second and third ionization step, the molecular ion is prepared at higher potential energy and breakage of two bonds, i.e., fragmentation into three moieties, becomes more probable. A decisive dynamical parameter in this mechanism is the C-H vibrational period of about 11 fs for both the neutral[658] and dication[659].

Thus, from this discussion and the data in Fig. 8.3(b), it follows that the precise timing of laser-induced distortions of the electronic system (e.g. by ionization) with respect to concomitant nuclear motion can selectively determine the outcome of molecular bond-breaking processes. As long as the nuclear motion that is responsible for the decisive modification of the molecular geometry and therewith for the effectiveness of the control is fast enough such it can take place during an ultrashort intense laser pulse (e.g., the stretch motion of a C-H bond), the duration of this laser pulse can be used as a control parameter for determining the outcome of the fragmentation reaction. However, for slower nuclear motion such as a C-C stretch, in order to achieve matching between the nuclear dynamics and the decisive electronic excitation (i.e., the third ionization step in our example), the pulses should be much longer than 30 fs[612]. For still slower nuclear motion, heavily stretched pulses needed to be used, which renders the single-pulse approach impractical[406,611]. In this case, double-pulse schemes can be used instead, as will be described in the following.

Control over the ionization timing with double-pulse schemes Precise timing of laser-induced modifications of the molecular electronic system (e.g., by removal of an electron) with respect to the concomitant nuclear motion can be an effective method to determine the breakage of a molecular bond, as discussed above. This strategy can be summarized as follows: In a multiple ionization process, the final molecular ionic state may be reached via different pathways along intermediately populated ionic potential energy surfaces (see also Section 8.4). Between each ion-

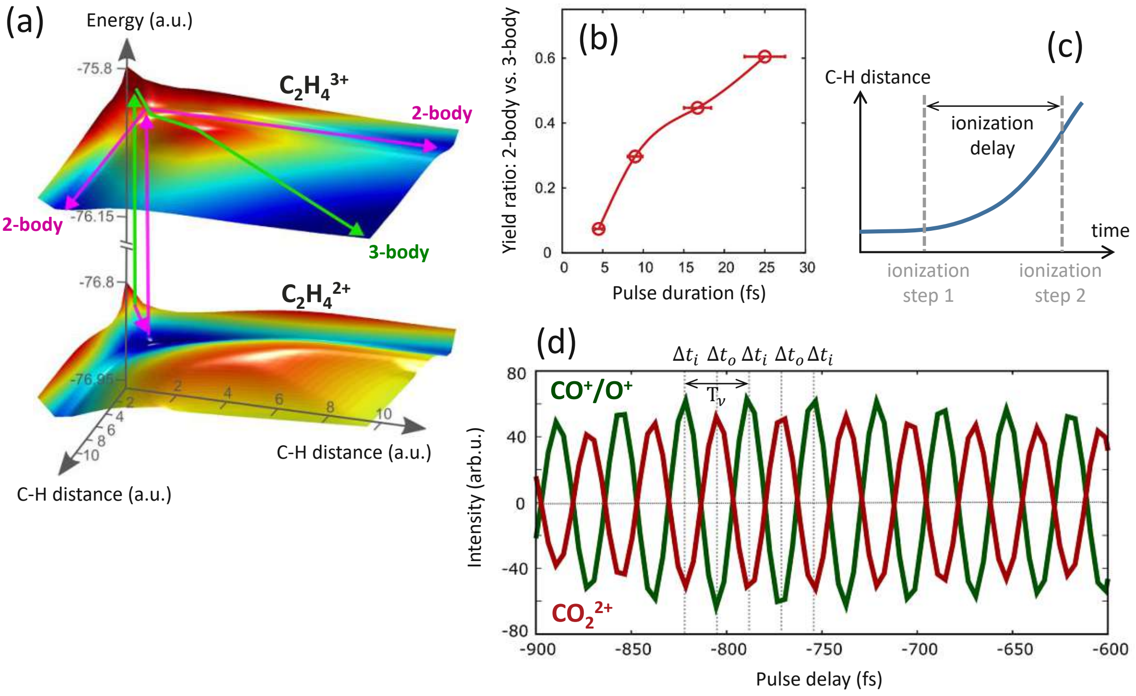

Figure 8.3: Role of coupling between electron and nuclear motion. (a) Potential energy surfaces of $C_2H_4^{2+}$ and $C_2H_4^{3+}$ as a function of two C-H distances. Depending on the stretch motion in the dication, two or three protons are ejected during fragmentation via C-H bond-breakage on the tricationic surface (see purple and green arrows). If the delay between the second and third ionization steps is large, the C-H bonds can stretch for a longer time on the dicationic surface, see (c). Population of the tricationic surface at larger C-H distances (possible for longer pulses) leads to dominantly two-body fragmentation, whereas shorter C-H distances (achieved for short pulses) result in dominantly three-body fragmentation (a). The pulse duration can thus be used as a control parameter to distinguish between two- and three-body fragmentation (b). Adapted from Ref. [612], see **Paper 13** or text for details. Fragmentation control via the delay between two ionization steps can be extended to slower dynamics and longer delays using two-pulse sequences. This is demonstrated for CO_2 in (d). The delay between the two pulses/ionization events determines whether CO_2^{2+} is prepared in a stable configuration, or whether it fragments into CO^+/O^+. For delays Δt_o at the outer turning points of the vibrational dynamics in the cation, fragmentation is preferred. At the inner turning points, reached at delays Δt_i, the dication is more likely produced. T_ν indicates the vibrational period. Adapted from Ref. [598]. See **Paper 15** or text for details.

ization step nuclear restructuring may take place on the ionic potential energy surface(s) populated during the previous ionization event. The further fate of the molecule and therewith the outcome of a molecular fragmentation reaction depends on the history of all electron removal processes and on the delay between successive ionization steps. However, as we have seen, for slow nuclear dynamics this approach becomes impractical when implemented with a single laser pulse. A way out is to generalize this concept to arbitrary delays between two ionization events using a double-pulse scheme with two precisely timed ultrashort pulses.

In an experiment performed by the author and co-workers this scheme has been implemented using double ionization of CO_2 and breakage into the two fragments CO^+/O^+ as an example, see Ref. [598] and **Paper 15** for details. In this experiment it is shown that the relative timing of the two independent ionization events, each of which taking place during one of the two delayed pulses, determine the pathway towards the final state in the doubly charged molecular ion. After the first pulse different electronic and vibrational dynamics are triggered on the different intermediately populated states in CO_2^+. By scanning the delay, Δt, between the two pulses these dynamics are mapped into the modulations of the CO_2^{2+} and CO^+/O^+ ion yields at times $t = \Delta t$ and can be retrieved by a spectral analysis of these modulations[598,599].

By filtering the different spectral peaks and performing phase-preserving inverse Fourier transforms for each of them, insight into the nuclear dynamics underlying the branching of the molecular pathway into CO_2^{2+} or CO^+/O^+ can be gained. Fig. 8.3(d) shows that the yield of CO^+/O^+ is high when that of CO_2^{2+} is low and vice versa, and that both yields peak only once per C-O vibrational period. These anti-cyclic yield modulations show that only one population event of CO_2^{2+} per vibrational period leads to dissociation respectively production of stable CO_2^{2+}. A detailed analysis reveals that the population event that leads to dissociation takes place at the inner turning point of the vibrational motion, i.e., when the C-O internuclear distance minimizes, and stable CO_2^{2+} is prepared more likely at the outer turning point. Thus, the fact that the probabilities for creating CO^+/O^+ respectively CO_2^{2+} peak at distinctively different pulse delay Δt demonstrates that a double-pulse scheme provides selectivity for determining not only the pathways across intermediate molecular states (here: in CO_2^+) but also for controlling the fragmentation behaviour of polyatomic molecules, therewith enhancing the flexibility of single-pulse control schemes discussed in Sections 8.3 and 8.4.

8.6 Waveform control of molecular processes

In the previous Sections 8.3-8.5 it was shown that by gaining control over the field-driven processes of ionization and excitation and by additionally suitably adapting the field-driven electronic dynamics to match the nuclear dynamics of the molecule that takes place concomitantly with the electronic dynamics, the breakage of specific molecular bonds and even the pathway towards a certain bond-breaking processes can be controlled. As these processes take place on laser-sub-cycle time-scales, it should not come as a surprise to us that determining molecular bond-breakage processes is also possible by controlling the field-interaction with the electronic system by tailoring the sub-cycle evolution of the laser field. An asymmetry of the field-shape that is possible to create with tailored waveforms such as those discussed in Chapter 3, can induce an asymmetry in the electronic dynamics and thereby determine the directionality of charge-localization and/or bond-breaking processes. Using tailored waveforms is, thus, a viable way of determining the breakage of a molecular bond, as we will discuss in the following. Our discussion will cover all currently used tailored fields, i.e., few-cycle pulses with a known CEP (Section 8.6.1) as well as linearly polarized tailored two- and multi-color field shapes and two-dimensional tailored waveforms such as OTC, CRTC and EPTC pulses (Section 8.6.2). We will discuss key achievements made with these pulse shapes and will outline the basic mechanisms underlying the observations. However, as the mechanisms depend strongly on the shape of the laser field applied in the experiments and also on the specific properties of the molecule under study, it is certainly entirely beyond the scope of this discussion to provide an exhaustive coverage of all works in this field and to give detailed explanations of the control mechanism for each and every combination of laser field shape and molecule. For details we refer to the cited papers. Further information can also be obtained from the recent review papers Refs. [446, 660] and also from the more general overview papers Refs. [32, 34, 352].

8.6.1 Control of bond-breaking using the CEP of few-cycle pulses

Since the first demonstration of control over the charge-localization during the laser-induced dissociation of the D_2 molecule by Kling et al. in 2006[441], a large number of works have investigated control over the fragmentation dynamics in various molecules by exploiting the asymmetry in the sub-cycle field-evolution of few-cycle pulses for specific values of the CEP that serves as the control parameter in these works. Successful demonstrations comprise control over the charge-localization during fragmentation of H_2 (and variants such as D_2, HD, and the molecular ions H_2^+/D_2^+)[441,443–445,572,574,661–663], of CO[571,594], and of DCl[570,664]; control over the fragmentation probability in polyatomic molecules such as C_4H_6[264] and CS_2[573]; selective CEP-control over the breakage of a specific bond in small polyatomic molecules such as HDO[665], C_2H_2/C_2D_2[569,575] or N_2O[666], and even in relatively large molecules such as toluene[667]; control over proton-migration reactions in C_2H_2 and C_3H_4[668]. In the following, we will discuss key aspects of CEP-control of molecular bond-breakage. In our discussion we will not explicitly distinguish whether the experiments have been performed using laser pulse trains with actively stabilized CEP, or whether the data have been accumulated in CEP-tagging mode (see Section 3.1.3 for a description of these two approaches). Although, conceptually, by recording data in CEP-tagging mode one does, strictly speaking, not control the dynamics but merely observes the outcome of the experiments with the CEP as an accessible experimental parameter, CEP-dependent data acquired with either method are equivalent.

Control of charge-localization during bond-breakage The first process that was tried to control with the asymmetric field-shape of a CEP-controlled few-cycle laser pulse was the localization of the remaining electron during the dissociation taking place upon single ionization of H_2 (or, equivalently, D_2), i.e., $H_2 \xrightarrow{\text{ionization}} H_2^+ \xrightarrow{\text{dissociation}} H^+ + H$. Dissociation of this simplest of all molecules in its singly ionized state can be understood by considering merely two potential energy curves, the binding $1s\sigma_g$ and the dissociative $2p\sigma_u$, see Fig. 8.4(a). Preparation of the molecule in the $2p\sigma_u$ energy state results in its very fast dissociation on the time-scale of a few femtoseconds. The energy released during this process is transferred as kinetic energy to the nuclei. Because of the monotonic decrease of the $2p\sigma_u$ potential energy curve with the internuclear distance R, the value of R at which this dissociative level is populated is mapped into the energy of the fragments. Dissociation of the molecule thus provides a molecular clock on the few-femtosecond range that can be read out be measurement of the fragments' kinetic energy. This clock has been used in numerous experiments, e.g., in Refs. [416, 418].

During the dissociation process of the singly charged ion the remaining electron needs to localize on one of the two nuclei, either the one emitted to the left or that emitted to the right. This localization process can be described in terms of the superposition of the atomic electronic wavefunctions that are localized on either of the two hydrogen atoms, the one on the left and the one on the right, $\phi_{\text{left}}(R)$ and $\phi_{\text{right}}(R)$, respectively. With these, within the Born-Oppenheimer approximation with R as a parameter, the gerade (g) and ungerade (u) molecular electronic wavefunctions associated with the binding $1s\sigma_g$ and anti-binding $2p\sigma_u$ electronic energy levels can be defined as $\phi_g(R) = 1/\sqrt{2}(\phi_{\text{left}}(R) + \phi_{\text{right}}(R))$ and $\phi_u(R) = 1/\sqrt{2}(\phi_{\text{left}}(R) - \phi_{\text{right}}(R))$, respectively. Coherent superposition of the gerade and ungerade energy levels with symmetric respectively antisymmetric wavefunctions leads to wavefunctions where the electron is localized either on the left, $\Psi_{\text{left}}(R) = 1/\sqrt{2}(\phi_{\text{g}}(R) + \phi_{\text{u}}(R))$, or on the right, $\Psi_{\text{right}}(R) = 1/\sqrt{2}(\phi_{\text{g}}(R) - \phi_{\text{u}}(R))$, nucleus. Coupling of the two energy levels $1s\sigma_g$ and $2p\sigma_u$ and transfer of population between them in the course of the laser interaction can thus lead to an asymmetry in the electron localization, depending on how the laser interaction takes place. Measurement of the fragment ions' energies to the left and to the right, or measurement of the fragment ions' momenta, provides detailed insight into the dissociation and charge-localization process, and reveals a possible asymmetry in the electron localization. There exist a number of pathways that result in population of the anti-binding energy level and therewith in the dissociation of the molecule, see Fig. 8.4(a) for a visualization. If the laser-interaction is such that both phase-possibilities for superposition of the two energy levels are equal, as it is the case for laser pulses with symmetric field-shapes, e.g., laser pulses consisting of many oscillation periods, the probabilities that the electron localizes on the right or left nucleus will be equal and no asymmetry will be measured. However, using asymmetric laser field shapes, such as CEP-controlled few-cycle laser pulses, it is possible to control the charge-localization and to induce an asymmetry in the number of charged fragments emitted to the left or to the right, respectively.

Experimentally obtained asymmetries of D^+ ions created during dissociative single ionization of D_2 by few-cycle laser pulses as a function of the CEP, φ_{CE}, of the pulses, taken from Ref. [441], are depicted in Fig. 8.4(b). For certain values of the CEP, the D^+ ions are emitted with a higher probability to the right, for $\varphi_{\mathrm{CE}} \rightarrow \varphi_{\mathrm{CE}} + \pi$, i.e., for a mirrored pulse shape, the D^+ are more likely emitted to the left. The asymmetry is highest in the energy range 3-8 eV. Qualtiatively similar asymmetries have been reported also in other works on the dissociation of H_2/D_2[443,444,572,574,661,663]. It should be noted, though, that those works investigated different aspects of the field-controlled dissociation process and therefore the observed asymmetries differ in details and, e.g., appear in different energy ranges. We will come back to that point below. The **mechanism behind the CEP-dependent asymmetries in charge-localization in H_2/D_2** shown in Fig. 8.4(b) has been explained by the interplay of the timing of the ionization step, an excitation step due to electron recollision and the nuclear motion taking place concomitantly with the laser interaction[441,446,669,670]. The different steps leading to the charge-localization are indicated by the numbers in Fig. 8.4(a). Upon field-ionization of the molecule, the $1s\sigma_g$ energy level is populated and vibrational motion is started (❶). About 1.7 fs later, at the time of the first recollision, the emitted electron recollides and excites the molecule, thereby leading to population of the dissociative $2p\sigma_u$ level (❷). The fragment energy range of 3-8 eV in which the highest asymmetry is observed, matches the timing of vibrational motion and the resulting internuclear distance at which the recollision-excitation occurs. During the dissociation process, as the nuclei move apart and R increases, the $1s\sigma_g$ and $2p\sigma_u$ energy levels come closer and the energy difference between them decreases. At this stage of the dissociation process the laser field couples the two levels and leads to oscillatory population transfer between them and, thus, to oscillations of the electron localization on the left and right nucleus, respectively, according to $\Psi_{\mathrm{left,right}}(R) = 1/\sqrt{2}(\phi_{\mathrm{g}}(R) \pm \phi_{\mathrm{u}}(R))$. The frequency of the oscillatory electron localization between left and right nucleus is proportional to the energy difference between the two levels and is thus highest in the beginning, and slow towards the end of the dissociation process, where the levels are almost degenerate. The coupling between the two levels is weak in the beginning, as the energy difference is much larger than the photon energy. In this phase of the dissociation process, the electronic motion is dominantly adiabatic and almost no population transfer takes place. For a certain range of R, the energy difference approximately matches the photon energy and the coupling between the two levels is strongest. During this phase of the dissociation process, rapid oscillatory population transfer and localization dynamics takes place. For still larger R the photon energy becomes larger than the energy difference between the two levels, the coupling and localization dynamics becomes weaker and slower and finally completely ceases, leading to the final localization of the electron on one of the two nuclei. A flip of the CEP by π changes the sign of the laser electric field and therefore leads to a change in the sign of the prepared electronic wavepacket. Thus, since the nuclear motion takes place exactly the same, the evolution and final value of the localization becomes mirrored. Scanning the CEP between 0 and 2π leads to a sinusoidal behaviour of the final asymmetry, with no asymmetry measured for certain intermediate values of the CEP, cf. the measured data in Fig. 8.4(b).

The key point in the described mechanism that is responsible for the observation of an asymmetry in the charge-localization is the field-driven coherent superposition of electronic states of opposite parity. In the work by Kling et al.[441] this coherent superposition was provided by population

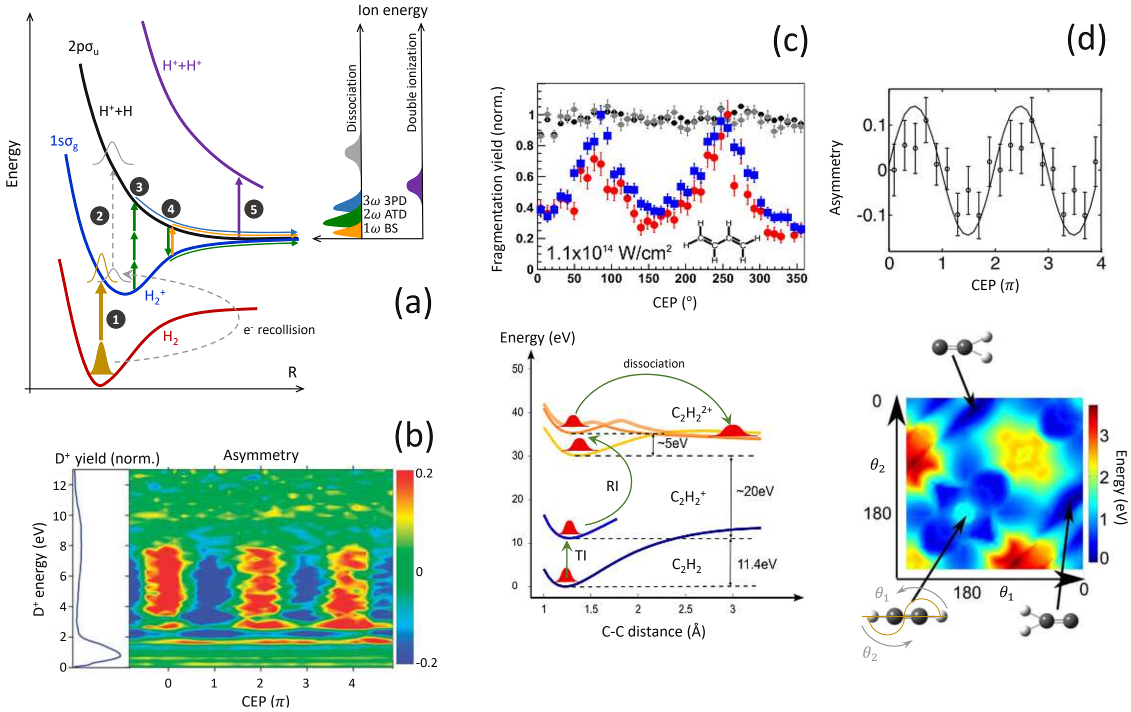

Figure 8.4: CEP-control of molecular bond-breaking. (a) Pathways for dissociation and fragmentation of H_2. Tunnel ionization (❶) prepares a vibrational wavepacket on the $1s\sigma_g$ potential energy curve of H_2^+. Electron recollision (❷) may populate the dissociative $2p\sigma_u$ curve at a short internuclear distance R leading to high proton energies (axis on the right). Absorption of three photons (❸) results in dissociation along the 3ω pathway (three-photon dissociation, 3PD). Emission of one photon at ❹ (green arrow) leads to dissociation on the $1s\sigma_g$ curve via the 2ω pathway (above-threshold dissociation, ATD). Absorption of one photon (orange arrow at ❹) results in dissociation on the $2p\sigma_u$ curve via the 1ω pathway (bond-softening, BS). At a large internuclear distance (❺) a second ionization event may take place via the CREI mechanism (see Section 8.1.1). (b) The localization of the remaining charge during dissociation via the pathway ❶ and ❷ shows a strong dependence on the CEP of a few-cycle laser pulse. Adapted from Ref. [441]. See text for details. (c) CEP-control of the fragmentation of polyatomic molecules. Adapted from Ref. **[264]**. The top panel shows the example of 1,3-butadiene. Blue and red data points depict measured yields (normalized to one) of the fragmentation reactions leading to $CH_3^+/C_3H_3^+$ and $C_2H_3^+/C_2H_3^+$, respectively. For comparison, the ionization yields of the singly and doubly charged molecular ions are denoted by black dots and gray squares, respectively. The bottom panel depicts for the example of C_2H_2 the mechanism underlying the pronounced CEP-dependence of the fragmentation yield measured for the breakage of the center C-C bond. TI indicates tunnel ionization, and RI recollision ionization. See the feature article in **Physics**[671] discussing this result and **Paper 11** for further details. (d) Strong-field steering of hydrogen migration. The top panel shows the CEP-dependent asymmetry parameter of H_3^+ ions emitted from $C_3H_4^{2+}$ after hydrogen migration. A similar result is obtained for acetylene. The bottom panel depicts for acetylene the potential energy surface (encoded in color, see color scale) of the state on which the hydrogen migration reaction occurs. The reaction coordinates (angles θ_1 and θ_2) are indicated. Adapted from Ref. [668]. See text for details.

of the 2pσ_u state by electron recollision and subsequent field-driven coupling of the 1sσ_g and 2pσ_u states. However, the electron recollision-step is not essential. In principle, it is sufficient that the field imprints some asymmetry in the population of the two opposite-parity states. This has been expressed by the *general theory of CEP effects*[672] in the form of interferences of different pathways that can be taken during the dissociation. A detailed analysis of this **pathway-interference picture of charge-localization** shows that the asymmetry results from the interference of two dissociation pathways which differ by one in the number of absorbed photons. This is proven by experiments that employ a significantly higher laser peak intensity, where electron recollision is not the dominant mechanism by which the dissociative 2pσ_u is populated[663]. In these experiments, in accord with the interference picture, the asymmetry is induced by radiative excitation pathways corresponding to the absorption of odd numbers of photons, see Fig. 8.4(a) for a visualization of the possible interfering pathways. The pathways associated with the absorption of one, net two, and three photons are commonly known as *bond softening* (BS)[673], *above-threshold dissociation* (ATD)[674], and *three-photon dissociation* (3PD)[675], respectively. 3PD and BS both populate the 2pσ_u state, see transitions indicated by green arrows at ❸ and an orange arrow at ❹, respectively, in the schematics in Fig. 8.4(a). ATD is a net-two-photon process, where absorption of three photons is followed by emission of one photon resulting in the dissociation on the ground 1sσ_g state, indicated by the green arrows at ❸ and ❹, respectively, in Fig. 8.4(a). The interference of these three basic field-driven dissociation pathways of H_2^+ leads to a dependence of the asymmetry on the CEP in specific proton energy ranges. In fact, based on this mechanism an asymmetry in the charge-localization – and even a stronger one than demonstrated using the CEP – can also be induced using two- and multi-color tailored waveforms as will be discussed below.

H_2 and D_2 have been serving as a test-bed for the study of the interaction of strong fields with molecules for decades and a whole plethora of works using these molecules as examples exists. This research on H_2/D_2 has lead to the discovery of many important processes that in the same or at least in a similar form can also be found in more complicated molecules. However, while the unique properties of H_2/D_2, namely (i) the extremely simple energy level structure with special symmetry properties that (ii) enables very efficient charge-localization upon superposition of these levels, and (iii) the outstandingly fast nuclear motion that proceeds on a similar time-scale as laser-oscillations in the visible and near-infrared, were important for obtaining a basic understanding of molecular processes in strong laser fields and were exploited for mapping dynamics[416,418,676], these special properties of H_2/D_2 also put a limit on the usage of them as test-molecules with general validity. This limitation should certainly also arise for the charge-localization process described above that strongly builds on the properties (i)-(iii). Therefore, after an initial phase of experiments that demonstrated successful control over charge-localization in H_2/D_2 using the CEP, a subsequent series of experiments were investigating the generality of the approach by **extending CEP-control to more complicated molecules**. One series of experiments investigated extension of charge-localization control with the CEP to multi-electron systems such as CO[571,594] or DCl[570,664]. While in all these experiments it was possible to control the charge-localization with the CEP, the underlying dynamics were found to deviate, in some cases quite strongly, from those established for H_2/D_2. For example, the theoretical analysis of the experiments on DCl showed[570,664] that the charge-localization in this case is mainly determined by the asymmetric ionization step due to the interplay of the pronounced dependence of the ionization rate on the molecular orientation with respect to the laser polarization direction and on the field-asymmetry given by the CEP. The decisive influence of the ionization step has been outlined in detail in Sections 8.3 and 8.4. In CO the asymmetry can, in principle, also arise from the orientation dependence of the ionization rate, but additionally also from recollision-excitation and laser-induced population transfer between excited electronic states of CO^+ during the dissociation, similar to H_2/D_2. Theoretical analysis[446,594] has shown that indeed all these effects play a role for the experimentally observed CEP-dependent charge-localization, but it is difficult to unequivocally disentangle their separate influences.

Section 8.5 discussed that the dynamics of the nuclei and that of the field-interaction with the electronic system must match, such that the decisive excitation/coupling that determines the further fate of the molecule and potentially induces an asymmetry occurs at the optimum nuclear distance. The mechanism that underlies control of charge-localization in H_2/D_2 crucially depends on exactly this **interplay between the nuclear motion and coupling**. This is because the relative timing of the ionization and recollision-excitation steps on the one hand, and the decisive strong coupling between the $1s\sigma_g$ and $2p\sigma_u$ energy levels must be adequately timed to each other for a strong asymmetry. And it is the nuclear motion that links the two processes: As indicated in Fig. 8.4(a), the delay from the recollision-excitation step and until the instant where the internuclear distance is reached at which strongest coupling occurs, should ideally be such that at this instant the laser pulse has not yet faded and the intensity is still high enough to drive a strong coupling. Obviously, this delay crucially depends on the mass of the involved nuclei. Consequently, experiments have shown a strong difference in the observed asymmetry between H_2 and D_2[574]. To ideally match the delay between the excitation step and the internuclear distance of strongest coupling, one would need to adapt the pulse duration to the nuclear motion, cf. Ref. **[612]** and descriptions in Section 8.5. However, the asymmetry of the field-shape of a few-cycle pulse strongly decreases with the number of cycles. Indeed, experiments have shown that the influence of the CEP on the asymmetry of the charge-localization decreases exponentially with the laser pulse's number of cycles[661]. Therefore, simply increasing the pulse duration is not an option. Instead, to extend CEP-control of charge-localization to molecules with slower nuclear motion, the wavelength of the driving laser pulse needs to be increased[572]. This way a small number of cycles and therewith a strong asymmetry in the field-shape can be preserved, while at the same time the pulse duration increases due to the longer cycle duration for longer wavelengths.

CEP-control of bond-breakage in polyatomic molecules An important step was to extend waveform control of molecular bond-breaking with the CEP of few-cycle laser pulses to polyatomic molecules. The first experiment that succeeded in demonstrating such type of control was performed by the author and co-workers, see Ref. **[264]** and **Paper 11**. In that work the CEP-dependence of the fragmentation of different polyatomic molecules (C_2H_2, C_2H_4, and C_4H_6) was investigated using the CEP-tagging method (see Section 3.1.3). The top panel of Fig. 8.4(c) shows exemplarily for C_4H_6 that the yield of different fragmentation channels features a strong dependence on the CEP. A similar dependence of the fragmentation yield on the CEP was observed for all investigated molecules. This behaviour was explained using the example of the fragmentation reaction $C_2H_2^{2+} \rightarrow CH^+ + CH^+$, for which potential energy curves over the the C-C bond distance calculated by quantum chemical methods are shown in the bottom panel of Fig. 8.4(c). Based on the experimentally observed dependence of the yield-modulations over CEP on the laser intensity, it could be concluded that recollision-ionization is the main mechanism that leads to double-ionization. According to the potential energy curves, the doubly charged molecular ion can be prepared in the stable ground state or in one of the dissociative lower excited states, which are associated with removing an electron during electron-recollision from either the HOMO or from the lower-valence orbitals (HOMO-1, HOMO-2). Removal of an electron from the lower-valence orbitals requires about 5 eV more energy (see potential energy levels). This additional energy needs to be imparted to the ion by the recolliding electron. Thus, control over its recollision energy opens up the possibility to selectively remove a second electron from either the HOMO or from lower-valence orbitals, and by that to populate either the binding ground or the dissociative excited states, respectively. As for a given pulse peak intensity the recollision energy in a few-cycle laser pulse depends on the CEP, the ionization from lower-valence states and therewith the fragmentation can be very selectively turned on or off using the CEP as a parameter. For certain values of the CEP, φ_{CE}, the recolliding electron has enough energy to overcome the ionization barrier to the excited states, while for $\varphi_{CE} \rightarrow \varphi_{CE} + \pi/2$ the recollision energy is insufficient to remove an electron from the lower valence orbitals. In between these CEP-values the recollision energy and therewith the lower-valence ionization probability decreases monotonically, which explains the experimentally observed strong π-periodic CEP-modulation of the fragmentation yield. In fact, this control mechanism is equivalent to that described in Sections 8.3 and 8.4, where the ionization from lower-valence orbitals, and therewith the population of dissociative excited states, was controlled by the molecular alignment respectively larger ionization probabilities for increasing pulse intensity. The only difference is that, here the ionization probability from lower-valence orbitals is controlled by the CEP-dependence of the recollision energy.

While the energy level structure of acetylene in Fig. 8.4(c) is shown as a function of the C-C bond length, associated with breakage of the center bond, the experiments described in Ref. [264] also reported an equally strong CEP-modulation of the dependence of the deprotonation reactions in acetylene and ethylene, $C_2H_2^{2+} \to C_2H^+ + H^+$ and $C_2H_4^{2+} \to C_2H_3^+ + H^+$, respectively. Breakage of hydrogen bonds is, in general, a very important reaction in chemistry and biology, and is of practical relevance for a variety of technologically important processes such as combustion and catalysis. Laser-induced deprotonation has thus been the subject of numerous studies, e.g., Refs. [150, 184, 186, 188, 607, 647]. CEP-control of the deprotonation process for $C_2H_2^{2+}/C_2D_2^{2+}$ has, for example, also been reported in Refs. [569] and [575], respectively. However, in these works not only control over the yield of the fragmentation reaction was achieved, but also the directionality of the reaction, i.e., whether the left or the right C-H bond was broken, could be controlled. Bond-selectivity is an important quality in any control scheme. Therefore, in the following, using the examples of Refs. [569] and [575], we will discuss how this can be achieved using the CEP as the control parameter.

Bond-selectivity and control of restructuring processes Selective CEP-control over the breakage of a specific bond in polyatomic molecules has been reported for example for C_2D_2[569] and C_2H_2[575], for N_2O[666] and also for HDO[665]. Interestingly, in the two works Refs. [569] and [575] two different responsible mechanisms have been identified for the directional breakage of a specific C-D/C-H bond. Below we will describe both mechanisms. A variant of the mechanism described in Ref. [575] has also been made responsible for the observation of CEP-control of restructuring reactions in C_2H_2 and C_3H_4 prior to the breakage of a bond[668] and is also thought to be responsible for CEP-control of restructuring reactions in toluene[667].

We start by discussing the results and explanations of Miura et al.[569]. They show that the asymmetry

$$A(\varphi_{\mathrm{CE}}, p_\parallel) = \frac{N_{\mathrm{left}}(\varphi_{\mathrm{CE}}, p_\parallel) - N_{\mathrm{right}}(\varphi_{\mathrm{CE}}, p_\parallel)}{N_{\mathrm{left}}(\varphi_{\mathrm{CE}}, p_\parallel) + N_{\mathrm{right}}(\varphi_{\mathrm{CE}}, p_\parallel)}, \tag{8.1}$$

of D^+ ions ejected from $C_2D_2^{2+}$ parallel to the laser polarization direction shows a significant dependence on the CEP φ_{CE}. $N_{\mathrm{left,right}}$ in (8.1) denotes the number of D^+ ions to the left and right, respectively, and $p_\parallel$ denotes the momentum of the ejected ion parallel to the laser polarization direction. For $\varphi_{\mathrm{CE}} = \pi/2$ the left C-D bond is broken more likely, while for $\varphi_{\mathrm{CE}} \to \varphi_{\mathrm{CE}} + \pi$, i.e., for $\varphi_{\mathrm{CE}} = 3\pi/2$, the right bond is broken more likely[‡]. To explain the observed asymmetry $A(\varphi_{\mathrm{CE}})$, Miura et al. argue that the sub-cycle timing of the second ionization step relative to the peaks of the driving laser field is decisive. For the laser parameters used in the experiment, the second ionization step takes place via impact ionization, as can be inferred from the CEP-dependence of the momenta of the molecular ions. Therefore, due to the strict sub-cycle timing of recolliding electrons with respect to the laser field, the instants when $C_2D_2^{2+}$ is prepared within the laser cycle is precisely defined. Upon preparation of $C_2D_2^{2+}$ by recollision-ionization, for $\varphi_{\mathrm{CE}} = \pi/2$ ($\varphi_{\mathrm{CE}} = 3\pi/2$) the molecular dication subsequently experiences a considerable fraction of the positive (negative) half-cycle of the laser electric field. During this period the C-D internuclear distance may be stretched to a certain extent and the C-D chemical bond on the positive (negative) side of the electric field is weakened because the electron density at this C-D chemical bond is lowered

---

[‡] These data have been obtained using the CEP-tagging technique (see Section 3.1.3). Therefore the CEP-values given here might have a constant offset from those of the laser pulses impinging on the molecules.

by the strong field. This **CEP-dependent laser field-assisted chemical bond weakening** induces a larger separation of the C-D internuclear distance on the positive (negative) electric field side for $\varphi_{CE} = \pi/2$ ($\varphi_{CE} = 3\pi/2$). The increased displacement may enhance the charge separation between D^+ and C_2D^+ on the right (left) side, resulting in the emission of D^+ to the right (left) direction and therewith in $A(\varphi_{CE} = \pi/2) > 0$ ($A(\varphi_{CE} = 3\pi/2) < 0$). Thus, for $\varphi_{CE} = \pi/2$ ($\varphi_{CE} = 3\pi/2$) the directionality of the laser electric field right after the one dominant recollision event during the few-cycle laser pulse breaks the symmetry and causes asymmetric emission of D^+. For $\varphi_{CE} = 0$, in contrast, there exist two almost equally strong recollision events that can cause double ionization, and therefore the bond-weakening processes induced by the subsequent evolution of the laser field at the left and right bonds cancel, leading to $A(\varphi_{CE} = 0) \approx 0$, as observed in the experiment.

A very similar periodic modulation of the asymmetry of bond-breakage with the CEP is observed by Alnaser et al.[575]. In that work, the asymmetry of the ejection of a proton from acetylene is studied. The experimentally obtained $A(\varphi_{CE}, p_{\|})$ as defined by (8.1) shows a 2π-periodic dependence on CEP. By means of quantum dynamical calculations it is shown that the demonstrated directional control does, however, not originate from electronic motion effects. Instead, the mechanism is based on the manipulation of the phases of individual components of the multi-mode vibrational wavepacket by the laser field in the neutral molecule and cation. In this type of **control of bond-breaking by superposition of vibrational modes**, the superposition is formed through a non-resonant process and is controlled on a sub-cycle time-scale. Quantum chemical simulations show that the decisive preparation of the vibrational wavepacket formed by a superposition of the symmetric and anti-symmetric C-H stretch mode takes place in the neutral and cation, and is transferred to the dication during the second ionization step that takes place via electron recollision. While the symmetric mode contributions to the vibrational wavepacket occur solely due to the ionization step, the time-dependent population of the anti-symmetric mode follows the electric field evolution of the few-cycle pulse, and the CEP of the laser pulse imprints a certain phase $e^{i\varphi_{CE}t}$ onto the anti-symmetric mode. Thus, the sign in the superposition of the symmetric and anti-symmetric modes can be varied with the CEP. This is demonstrated by means of simulations that show that vibrational wavepackets composed of a superposition of the two modes with a phase of 0 and π lead to a change in the direction of the proton emission[575]. As a result, the asymmetry $A(\varphi_{CE}, p_{\|})$ of ejecting the proton either to the left or to the right oscillates with a periodicity of 2π in the CEP.

An interesting application of this mechanism is the control of restructuring reactions taking place prior to bond-breakage. An intensely studied restructuring reaction is proton migration that we have repeatedly mentioned above. As such restructuring reactions can often be decomposed into elementary superpositions of different vibrational modes, they should also be amenable to CEP-control by this mechanism. Indeed, this has been shown by Kübel et al. for proton migration reactions in C_2H_2 and C_3H_4[668], see the measured CEP-dependent asymmetry of H_3^+ ions emitted from $C_3H_4^{2+}$ following the migration of one hydrogen atom to the opposite molecular terminal site in the top panel of Fig. 8.4(d). The mechanism underlying the asymmetric emission was explained by quantum chemical simulations for acetylene, for which an almost identical CEP-dependence of bond-breakage after hydrogen migration was observed. The lower panel of Fig. 8.4(d) shows the potential energy surface of the state of the acetylene dication on which isomerization occurs. The binding energy, encoded in color, is plotted as a function of the two reactive coordinates θ_1 and θ_2 indicated in the figure. The initial form of the molecule and the two isomerized configurations are indicated by arrows. The simulations show that the CEP determines the sign in the superposition of the vibrational modes and thereby influences whether the left proton moves to the right or the right proton to the left.

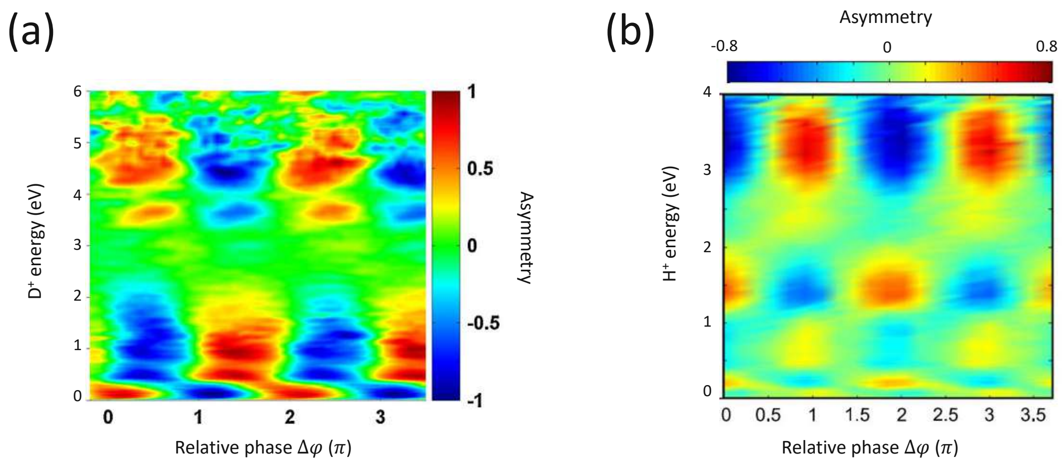

Figure 8.5: Control of bond-breaking with $\omega/2\omega$ pulses. Measured asymmetries of D^+ (a) and H^+ (b) emission during dissociation of D_2 (a) and H_2 (b) with $\omega/2\omega$ pulses as a function of the relative phase, $\Delta\varphi$, between the two colors. The result in (a) has been obtained with wavelengths 800/400 nm (adapted from Ref. [442]), the one in (b) was measured with 1800/900 nm pulses (adapted from Ref. [679]). See text for details.

8.6.2 Control of bond-breaking with tailored two- and multi-color pulses

In this Section we will discuss control over molecular bond-breaking processes using intense pulses that have been tailored by coherent waveform synthesis of two or more pulses of different colors, as discussed in Sections 3.2 and 3.3 above. Both, control with linearly polarized and two-dimensional waveforms will be discussed.

Linearly polarized tailored waveforms Bond-breaking control in molecules with linearly polarized tailored waveforms has been considered for more than twenty years. The first process that was successfully controlled was – as with CEP-control – the charge-localization during dissociation of the hydrogen molecule (and its deuterated versions)[282,677,678]. In these experiments control was achieved using the relative phase of linearly polarized $\omega/2\omega$ pulses as the control parameter. More recent works have studied **charge-localization during hydrogen-dissociation with two-color pulses** in greater detail using momentum resolution of the generated fragments and with different wavelength combinations of the tailored drive pulses[442,679,680,681]. Compared with CEP-stabilized few-cycle pulses discussed in the previous Section, control with longer two-color pulses is experimentally easier to implement (in particular for the $\omega/2\omega$ case). From a more fundamental point of view, by the combination of two colors (and also for more sophisticated types of waveform synthesis) the laser waveform can be tailored on a cycle-scale rather than on an envelope-scale. That is, the asymmetry of the field is imprinted on every single cycle, while for a few-cycle pulse the asymmetry quickly vanishes with the number of its cycles. Therefore, two-color pulses and other tailored waveforms allow to generate much longer asymmetric pulses, which is a crucial advantage that allows to impart asymmetry to the electronic system during a much longer time-scale of nuclear motion. As we have discussed in Sections 8.5 and 8.6.1, matching the time-scales of the interaction with the electrons to the concomitant nuclear dynamics is a prerequisite for efficient control over bond-breaking and/or charge-localization processes.

Fig. 8.5 shows examples of measured asymmetries of H^+/D^+ emission during dissociation of

H_2/D_2 with $\omega/2\omega$ pulses as a function of the relative phase, $\Delta\varphi$, between the two colors. A clear left-right asymmetry in certain H^+/D^+ energy ranges, each with a periodicity of π in $\Delta\varphi$, can be observed. That is, the localization of the remaining electron on the two nuclei can be switched by a parity flip of the two-color field. Although the data have been obtained with $\omega/2\omega$ pulses of different color-combinations (see caption of Fig. 8.5 for details), the phase-dependences of the asymmetries look qualitatively similar but, however, are observed in different energy ranges. This can be readily explained by the pathway-interference picture[442,679,681] that has been described above in connection with CEP-control of H_2/D_2 dissociation, see Section 8.6.1. According to this picture, the interference of dissociation pathways that differ by one in the number of absorbed photons leads to the observed $\Delta\varphi$-dependent charge localization. The dependence of the asymmetries on $\Delta\varphi$ and the energy ranges in which they are observed can be ascribed to pathways associated with the absorption of one, two, and three photons, i.e., to the processes of *bond softening* (BS), *above-threshold dissociation* (ATD), and *three-photon dissociation* (3PD), respectively. Contributions from recollision-excitation are also observed[442,679]. Because a two-color field can induce the dissociation of H^+/D^+ by the absorption of various combinations of absorbed photons with different energies, and because the photon energies determine in which H^+/D^+ energy ranges the asymmetries are observed, the energy ranges can be modified by the combination of colors. This can be seen by comparison of results obtained with $\omega/2\omega$ pulses in the visible/near-infrared (800/400 nm)[442] and near/mid-infrared (1800/900 nm)[679], shown in Figs. 8.5(a) and (b), respectively, and also has been demonstrated by applying $\omega/3\omega$ pulses (1800/600 nm)[680]. Moreover, due the long duration of the two-color field, the implications of which we have discussed in the previous paragraph, significantly stronger asymmetries in comparison with those observed with CEP-controlled few-cycle pulses can be induced[442,679]. The maximum achieved asymmetry can still be further enhanced by optimization of the waveform: Theoretical works have investigated the use of synthesized waveforms for enhancing the quality of the control over the charge-localization during H_2/D_2 dissociation using, e.g., two-color combinations[682] with non-integer frequency ratios, or the combination of a mid-infrared pulse with a far-infrared pulse that essentially resembles the action of a strong DC field[683].

A key research goal is the **extension of waveform control of molecular bond-breaking to polyatomic molecules**. Despite the complexity of polyatomic molecules a number of works have demonstrated successful control over different aspects of bond-breaking processes in such molecules using the relative phase, $\Delta\varphi$, between the two colors in $\omega/2\omega$ pulses as the control parameter. So far, almost exclusively 800/400 nm $\omega/2\omega$ pulses generated with Titanium-Sapphire laser systems have been used. In the following we will discuss the key points that were established by these works. To our knowledge the first works that have succeeded in directional control of bond-breaking in a molecule more complicated than $H_2/D_2/HD$ were the ones by Ohmura et al.[684,685]. In those works a pronounced $\Delta\varphi$-dependent asymmetry in the emission of different moieties split off during dissociative ionization of molecules that exhibit a pronounced permanent dipole and head-to-tail asymmetry (IBr, CH_3I, and C_3H_5I) was observed. Follow-up works[686–688] have shown similar $\Delta\varphi$-dependent asymmetries also for other, even larger, molecules. These asymmetries and their variation with $\Delta\varphi$ was explained by the orientation-dependence of the ionization and fragmentation process due to the head-to-tail asymmetry of the intra-molecular electronic density. Similar bond-breaking control based on the asymmetry of the ionization and fragmentation process in the asymmetric $\omega/2\omega$ field has also been demonstrated for the toluene and methanol molecules in Refs. [689–691]. In a recent work this approach was extended to synthesized waveforms that consist of four colors $\omega + 2\omega + 3\omega + 4\omega$ generated by nonlinear frequency conversion from the fundamental wavelength 1064 nm[692].

Current efforts, using smaller molecules such as CO[693], CO_2[694] or acetylene[695] as the objects of study, are dedicated to understanding the $\Delta\varphi$-dependent directionality of the bond-breaking process in $\omega/2\omega$ pulses in a more thorough way by trying to establish a correspondence with the pathway-interference picture available for H_2 (described above)[695] or by considering the influence of nuclear motion[694]. An important step towards such a more thorough understanding is the ability to distinguish experimentally the influence of laser-induced state coupling and selective ionization on the observed asymmetries. This was demonstrated using a two-pulse scheme consisting of a circularly polarized pulse followed by a delayed $\omega/2\omega$ pulse[693]. In that scheme, the different origins of the fragments' asymmetries can be extracted from different regions of the momentum plane using electron-ion coincidence methods.

Two-dimensional tailored waveforms The previous paragraphs have described that linearly polarized tailored waveforms can be used to selectively control bond-breaking processes in molecules. The underlying mechanisms are based on the combined actions of the asymmetry in the ionization and fragmentation processes[687] and phase-sensitive field-driven excitation and population processes[693]. Two-dimensional tailored waveforms introduced in Section 3.2, i.e., orthogonal two-color (OTC) fields, counter- and co-rotating two-color (CRTC/CoRTC) fields, and elliptically polarized two-color (EPTC) fields, offer a still higher flexibility for adapting the field-interaction to the structure of the molecule and additionally allow to control electron recollision processes simultaneously in time and space. A series of experiments was testing the use of such fields for molecular bond-breaking control[331,333,336,696], see Fig. 8.6 for selected results.

Using **OTC pulses** two-dimensional directional proton emission in the dissociation reaction $H_2^+ \rightarrow H^+ + H$ was observed[696]. This bench-mark experiment exemplifies key differences between waveform control in one and two spatial dimensions. The localization of the electron is determined, just as in the interaction with linearly polarized tailored waveforms, by quantum interference of nuclear wavepackets of opposite parities. Control of the charge localization in two dimensions with two-dimensional fields requires that the conditions for pathway interferences are not only met in energy but also in space. Thus, asymmetric directional emission of H^+ requires the interference of opposite parity nuclear wavepackets with the same kinetic energies and, additionally, they must be emitted into the same direction. However, the laser-coupling between the two opposite parity electronic states associated with the nuclear wavepackets, the $1s\sigma_g$ and $2p\sigma_u$ states, peaks sharply along the laser polarization direction, such that the two orthogonal field-components of an OTC field cause dissociation dominantly along their respective laser polarization direction. H^+ fragments are therefore dominantly observed along the direction of the ω-field, and at high momenta due to the action of the 2ω-field. A considerable fraction of H^+ fragments is, however, also observed in between these dominant contributions, see Fig. 8.6(a). These fragments represent nuclear wavepackets that are steered in two spatial dimensions. By variation of the relative phase of the two colors, $\Delta\varphi$, their asymmetry and therewith the localization of the remaining electron can be controlled[696]. Two-dimensional control of charge localization during H_2 dissociation is thus possible using OTC pulses. Later, this scheme was extended to the multi-electron case. Using CO as an example the possibility of controlling directional bond-breaking in the reaction $CO^{2+} \rightarrow C^+ + O^+$ was studied[331]. In that experiment $\Delta\varphi$-dependent directional bond-breaking as a function of both kinetic energy and emission directions of the nuclear fragments was observed in different fragment momentum regions. These momentum distributions demonstrate that the directionality of C^+ emission reverses when $\Delta\varphi$ flips its sign, thus, demonstrating control over the fragmentation process. The directional emission was attributed to the contributions of both sequential and non-sequential double ionization pathways, whose relative strengths and directionality strongly vary with $\Delta\varphi$.

Motivated by the success of two-dimensional charge-localization control with OTC pulses, the bench-mark experiment on H_2 was repeated using **CRTC and CoRTC pulses**[333]. It was found that, similar to the case of OTC pulses, the asymmetry of H^+-ejection can be controlled in two-dimensional space with $\Delta\varphi$, see Figs. 8.6(b) and (c). The underlying mechanism is identical to that found for OTC pulses, namely parity-sensitive pathway-interferences in certain energy ranges and along specific H^+ emission directions. As can be seen in Fig. 8.6, the directional dependence of the observed asymmetries strongly resembles the shapes of the laser fields and exhibit trefoil

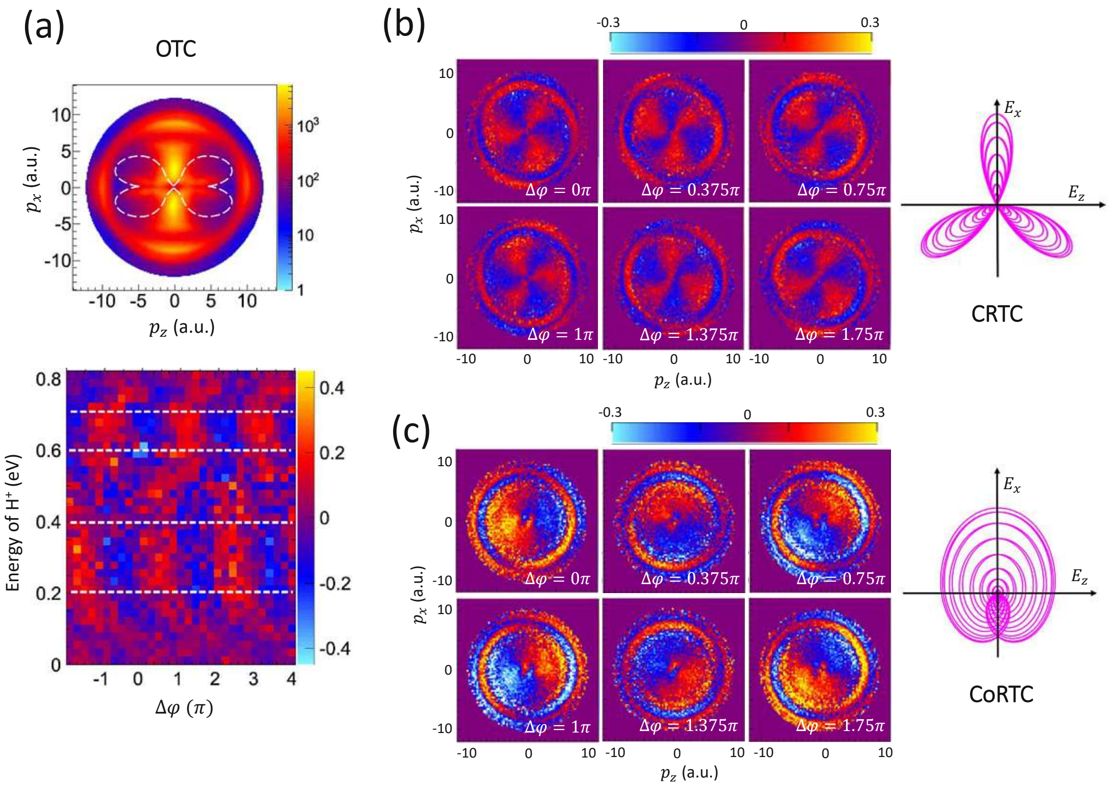

Figure 8.6: Control of bond-breaking with two-dimensional tailored waveforms. (a) Two-dimensional directional proton emission in dissociative ionization of H_2 with an $\omega/2\omega$ OTC field composed of an 800 nm pulse and its second harmonic. Adapted from Ref. [696]. The top panel shows the momentum distribution of protons in the OTC field's polarization plane for a relative phase $\Delta\varphi = 0$ of the two colors. The butterfly structure indicates proton emission in between the polarization directions of the ω and 2ω pulses along a certain polar angle θ. The bottom panel shows the asymmetry (indicated by the color code) of proton emission into the polar angle range $45^\circ < \theta < 65^\circ$ as a function of $\Delta\varphi$, showing that the proton emission/charge-localization can be controlled by the field's shape in two dimensions. (b) Measured two-dimensional asymmetry patterns of the directional emission of protons from H_2^+ for certain relative phases $\Delta\varphi$ (indicated in the panels) of a CRTC pulse (field shape shown on the right). Adapted from Ref. [333]. (c) Same as (b), but for a CoRTC pulse (adapted from the same reference). The field shape of the respective pulses is reflected in the proton emission patterns. Variation of $\Delta\varphi$ merely rotates the peaks of the fields but does not change their sub-cycle evolutions.

shapes for the CRTC pulses and semi-lunar ones for CoRTC pulses. As for these pulses the field-shape within the laser polarization plane is independent of $\Delta\varphi$ and merely rotates about its center if $\Delta\varphi$ is varied (see also Section 3.3), the shapes of the observed two-dimensional asymmetries obviously reflect the field-shapes. This can, again similar to OTC pulses, be explained by the strong directionality of the dipole coupling between the $1s\sigma_g$ and $2p\sigma_u$ states, which leads to highest coupling and therewith strongest dissociation for largest field-strengths, hence, along the vectorial peaks of the two-dimensional fields. Thus, the number of peaks of the two-dimensional laser field is reflected in the observed asymmetry of H^+ emission.

While for OTC and CRTC pulses electron recollision is possible, recollisions can be suppressed using **EPTC pulses**, similar to CoRTC pulses. As a result, EPTC pulses allow investigating the $\Delta\varphi$-

dependent asymmetries induced solely by field-driven electronic processes such as the coupling between opposite parity states and the ionization dynamics in the asymmetric field. Asymmetries induced by the ionization step are for example due to a higher ionization probability along a certain molecular axis caused by the shape of molecular orbitals (as was discussed above in connection with control using linearly polarized tailored waveforms) or can also be due to an ionization process that is sensitive to charge-localization such as enhanced ionization (see Section 8.1.1). Wu et al. investigated the dissociative ionization with EPTC pulses for a range of molecules and molecular-like systems (H_2, N_2, Ar_2, and CO) and compared their $\Delta\varphi$-sensitivity[336]. They found strong $\Delta\varphi$-dependent asymmetries of the yield for all investigated species and fragmentation channels.

Bibliography

---

[1] Wikipedia, *Photonics*, (2018) https://en.wikipedia.org/wiki/Photonics (visited on 01/17/2018) (cited on page 1).

[2] Wikipedia, *Biophotonics*, (2018) https://en.wikipedia.org/wiki/Biophotonics (visited on 01/17/2018) (cited on page 1).

[3] Wikipedia, *Nanophotonics*, (2018) https://en.wikipedia.org/wiki/Nanophotonics (visited on 01/17/2018) (cited on page 1).

[4] Wikipedia, *Quantum Optics*, (2018) https://en.wikipedia.org/wiki/Quantum_optics (visited on 01/17/2018) (cited on page 1).

[5] Optical Society of America (OSA), *Ultrafast Photonics*, (2018) http://www.osa.org/en-us/100/osa100/items/ultrafast_photonics/ (visited on 01/15/2018) (cited on page 1).

[6] Nature Publishing Group, *Ultrafast Photonics*, (2018) https://www.nature.com/subjects/ultrafast-photonics (visited on 01/19/2018) (cited on page 1).

[7] A. H. Zewail, *Femtochemistry. Past, present, and future*, Pure Appl. Chem. **72**, 2219–2231 (2000) (cited on page 2).

[8] F. Krausz, *The birth of attosecond physics and its coming of age*, Phys. Scr. **91**, 063011 (2016) (cited on pages 2, 9, 43).

[9] M. Kitzler and S. Gräfe, eds., *Ultrafast Dynamics Driven by Intense Light Pulses*, Vol. 86, Springer Series on Atomic, Optical, and Plasma Physics (Springer International Publishing, Cham, 2016) (cited on page 2).

[10] S. L. Chin, G. Farkas, and F. Yergeau, *Observation of Kr and Xe ions created by intense nanosecond CO2 laser pulses*, J. Phys. B At. Mol. Phys. **16**, L223–L226 (1983) (cited on page 2).

[11] S. L. Chin, F. Yergeau, and P. Lavigne, *Tunnel ionisation of Xe in an ultra-intense CO2 laser field with multiple charge creation*, J. Phys. B At. Mol. Phys. **18**, L213–L215 (1985) (cited on page 2).

[12] S. Augst, D. Strickland, . . ., J. H. Eberly, *Tunneling ionization of noble gases in a high-intensity laser field*, Phys. Rev. Lett. **63**, 2212–2215 (1989) (cited on page 2).

[13] S. Augst, D. D. Meyerhofer, . . ., S. L. Chin, *Laser ionization of noble gases by Coulomb-barrier suppression*, J. Opt. Soc. Am. B **8**, 858 (1991) (cited on pages 2, 12).

[14] J. Krause, K. Schafer, and K. Kulander, *High-order harmonic generation from atoms and ions in the high intensity regime*, Phys. Rev. Lett. **68**, 3535–3538 (1992) (cited on pages 2, 8).

[15] K. J. Schafer, B. Yang, . . ., K. C. Kulander, *Above threshold ionization beyond the high harmonic cutoff*, Phys. Rev. Lett. **70**, 1599–1602 (1993) (cited on pages 2, 8, 13, 24).

[16] P. Corkum, *Plasma perspective on strong field multiphoton ionization*, Phys. Rev. Lett. **71**, 1994–1997 (1993) (cited on pages 2, 8, 13, 24).

[17] G. G. Paulus, W. Becker, . . ., H. Walther, *Rescattering effects in above-threshold ionization: a classical model*, J. Phys. B At. Mol. Opt. Phys. **27**, L703–L708 (1994) (cited on pages 2, 8, 13, 16, 24, 34).

[18] A. McPherson, G. Gibson, . . ., C. K. Rhodes, *Studies of multiphoton production of vacuum-ultraviolet radiation in the rare gases*, J. Opt. Soc. Am. B **4**, 595 (1987) (cited on pages 2, 9, 21).

[19] M. Ferray, A. L'Huillier, . . ., C. Manus, *Multiple-harmonic conversion of 1064 nm radiation in rare gases*, J. Phys. B At. Mol. Opt. Phys. **21**, L31–L35 (1988) (cited on pages 2, 9, 21).

[20] T. Popmintchev, M.-C. Chen, . . ., H. C. Kapteyn, *Bright Coherent Ultrahigh Harmonics in the keV X-ray Regime from Mid-Infrared Femtosecond Lasers*, Science **336**, 1287–1291 (2012) (cited on page 2).

[21] F. Krausz and M. Ivanov, *Attosecond physics*, Rev. Mod. Phys. **81**, 163–234 (2009) (cited on pages 2, 4, 9, 29, 87).

[22] C. D. Lin, A.-T. Le, . . ., H. Wei, *Attosecond and Strong-Field Physics* (Cambridge University Press, 04/2018) (cited on pages 2, 4).

[23] A. Baltuska, M. Uiberacker, . . ., T. Hänsch, *Phase-controlled amplification of few-cycle laser pulses*, IEEE J. Sel. Top. Quantum Electron. **9**, 972–989 (2003) (cited on pages 2, 32, 33, 37).

[24] A. Baltuška, T. Fuji, and T. Kobayashi, *Controlling the Carrier-Envelope Phase of Ultrashort Light Pulses with Optical Parametric Amplifiers*, Phys. Rev. Lett. **88**, 133901 (2002) (cited on pages 2, 33, 37).

[25] A. Baltuska, T. Udem, . . ., F. Krausz, *Attosecond control of electronic processes by intense light fields.* Nature **421**, 611–5 (2003) (cited on pages 2, 32, 33).

[26] S. Haessler, T. Balčiunas, . . ., L. E. Chipperfield, *Optimization of Quantum Trajectories Driven by Strong-Field Waveforms*, Phys. Rev. X **4**, 021028 (2014) (cited on pages 2, 37, 38, 46).

[27] A. Wirth, M. T. Hassan, . . ., E. Goulielmakis, *Synthesized Light Transients*, Science **334**, 195–200 (2011) (cited on pages 2, 37, 46, 47).

[28] S.-W. Huang, G. Cirmi, . . ., F. X. Kärtner, *High-energy pulse synthesis with sub-cycle waveform control for strong-field physics*, Nat. Photonics **5**, 475–479 (2011) (cited on pages 2, 37).

[29] O. D. Mücke, S. Fang, . . ., F. X. Kärtner, *Toward Waveform Nonlinear Optics Using Multimillijoule Sub-Cycle Waveform Synthesizers*, IEEE J. Sel. Top. Quantum Electron. **21**, 1–12 (2015) (cited on pages 2, 37, 46).

[30] F. Calegari, G. Sansone, . . ., M. Nisoli, *Advances in attosecond science*, J. Phys. B At. Mol. Opt. Phys. **49**, 062001 (2016) (cited on pages 4, 9, 43).

[31] S. R. Leone and D. M. Neumark, *Attosecond science in atomic, molecular, and condensed matter physics*, Faraday Discuss. **194**, 15–39 (2016) (cited on pages 4, 9, 43).

[32] M. J. J. Vrakking, *Attosecond imaging*, Phys. Chem. Chem. Phys. **16**, 2775 (2014) (cited on pages 4, 43, 122).

[33] L. Gallmann, C. Cirelli, and U. Keller, *Attosecond Science: Recent Highlights and Future Trends*, Annu. Rev. Phys. Chem. **63**, 447–469 (2012) (cited on pages 4, 43).

[34] M. F. Kling and M. J. J. Vrakking, *Attosecond electron dynamics.* Annu. Rev. Phys. Chem. **59**, 463–92 (2008) (cited on pages 4, 116, 122).

[35] S. R. Leone, C. W. McCurdy, . . ., M. J. J. Vrakking, *What will it take to observe processes in 'real time'?*, Nat. Photonics **8**, 162–166 (2014) (cited on pages 5, 43).

[36] T. Fennel, K. H. Meiwes-Broer, . . ., E. Suraud, *Laser-driven nonlinear cluster dynamics*, Rev. Mod. Phys. **82**, 1793–1842 (2010) (cited on page 5).

[37] S. L. Chin, T. .-.-J. Wang, . . ., Z. Z. Xu, *Advances in intense femtosecond laser filamentation in air*, Laser Phys. **22**, 1–53 (2012) (cited on pages 5, 6).

[38] P. Hommelhoff and M. Kling, eds., *Attosecond Nanophysics: From Basic Science to Applications* (Wiley-VCH, 2015) (cited on pages 5, 6).

[39] U. Teubner and P. Gibbon, *High-order harmonics from laser-irradiated plasma surfaces*, Rev. Mod. Phys. **81**, 445–479 (2009) (cited on pages 5, 7, 9).

[40] M. Durach, A. Rusina, . . ., M. I. Stockman, *Metallization of Nanofilms in Strong Adiabatic Electric Fields*, Phys. Rev. Lett. **105**, 086803 (2010) (cited on pages 5, 7, 8).

[41] B. Zaks, R. B. Liu, and M. S. Sherwin, *Experimental observation of electron–hole recollisions*, Nature **483**, 580–583 (2012) (cited on pages 5, 7).

[42] A. Schiffrin, T. Paasch-Colberg, . . ., F. Krausz, *Optical-field-induced current in dielectrics.* Nature **493**, 70–4 (2013) (cited on pages 5, 7, 8).

[43] M. Schultze, E. M. Bothschafter, . . ., F. Krausz, *Controlling dielectrics with the electric field of light*, Nature **493**, 75–78 (2012) (cited on pages 5, 7, 8).

[44] T. Higuchi, M. I. Stockman, and P. Hommelhoff, *Strong-Field Perspective on High-Harmonic Radiation from Bulk Solids*, Phys. Rev. Lett. **113**, 213901 (2014) (cited on page 5).

[45] G. Vampa, T. J. Hammond, . . ., P. B. Corkum, *Linking high harmonics from gases and solids*, Nature **522**, 462–464 (2015) (cited on pages 5, 7, 9, 87).

[46] T. T. Luu, M. Garg, . . ., E. Goulielmakis, *Extreme ultraviolet high-harmonic spectroscopy of solids*, Nature **521**, 498–502 (2015) (cited on pages 5, 7, 47).

[47] H. Mashiko, K. Oguri, . . ., H. Gotoh, *Petahertz optical drive with wide-bandgap semiconductor*, Nat. Phys. **12**, 741–745 (2016) (cited on pages 5, 7).

[48] M. Lucchini, S. A. Sato, . . ., U. Keller, *Attosecond dynamical Franz-Keldysh effect in polycrystalline diamond*, Science **353**, 916–919 (2016) (cited on pages 5, 7).

[49] B. Ulrich, A. Vredenborg, . . ., R. Dörner, *Double-ionization mechanisms of the argon dimer in intense laser fields*, Phys. Rev. A - At. Mol. Opt. Phys. **82**, 013412 (2010) (cited on pages 5, 21).

[50] B. Manschwetus, H. Rottke, . . ., W. Sandner, *Mechanisms underlying strong-field double ionization of argon dimers*, Phys. Rev. A **82**, 013413 (2010) (cited on pages 5, 9, 21).

[51] J. Wu, A. Vredenborg, . . ., R. Dörner, *Multiple Recapture of Electrons in Multiple Ionization of the Argon Dimer by a Strong Laser Field*, Phys. Rev. Lett. **107**, 043003 (2011) (cited on pages 5, 21).

[52] B. Ulrich, A. Vredenborg, . . ., R. Dörner, *Imaging of the Structure of the Argon and Neon Dimer, Trimer, and Tetramer*, J. Phys. Chem. A **115**, 6936–6941 (2011) (cited on page 5).

[53] J. Wu, X. Gong, . . ., R. Dörner, *Strong Field Multiple Ionization as a Route to Electron Dynamics in a van der Waals Cluster*, Phys. Rev. Lett. **111**, 083003 (2013) (cited on pages 5, 67).

[54] A. von Veltheim, B. Manschwetus, . . ., W. Sandner, *Frustrated Tunnel Ionization of Noble Gas Dimers with Rydberg-Electron Shakeoff by Electron Charge Oscillation*, Phys. Rev. Lett. **110**, 023001 (2013) (cited on pages 5, 9).

[55] A. V. Veltheim, "Noble Gas Dimers in Strong Laser Fields", Dissertation (Technische Universität Berlin, 2015) (cited on page 5).

[56] I. Georgescu, U. Saalmann, and J. Rost, *Attosecond Resolved Charging of Ions in a Rare-Gas Cluster*, Phys. Rev. Lett. **99**, 183002 (2007) (cited on page 5).

[57] M. Lezius, S. Dobosz, . . ., M. Schmidt, *Explosion Dynamics of Rare Gas Clusters in Strong Laser Fields*, Phys. Rev. Lett. **80**, 261–264 (1998) (cited on page 5).

[58] E. Skopalová, Y. C. El-Taha, . . ., J. P. Marangos, *Pulse-Length Dependence of the Anisotropy of Laser-Driven Cluster Explosions: Transition to the Impulsive Regime for Pulses Approaching the Few-Cycle Limit*, Phys. Rev. Lett. **104**, 203401 (2010) (cited on page 5).

[59] M. Smits, C. de Lange, . . ., D. Rayner, *Dynamic Polarization in the Strong-Field Ionization of Small Metal Clusters*, Phys. Rev. Lett. **93**, 203402 (2004) (cited on page 5).

[60] C. Siedschlag and J.-M. Rost, *Enhanced ionization in small rare gas-clusters*, Phys. Rev. A **67**, 013404 (2003) (cited on page 5).

[61] C. Siedschlag and J. Rost, *Electron Release of Rare-Gas Atomic Clusters under an Intense Laser Pulse*, Phys. Rev. Lett. **89**, 173401 (2002) (cited on page 5).

[62] M. Krishnamurthy, J. Jha, . . ., T. Brabec, *Ion charge state distribution in the laser-induced Coulomb explosion of argon clusters*, J. Phys. B At. Mol. Opt. Phys. **39**, 625–632 (2006) (cited on page 5).

[63] C. Jungreuthmayer, M. Geissler, . . ., T. Brabec, *Microscopic Analysis of Large-Cluster Explosion in Intense Laser Fields*, Phys. Rev. Lett. **92**, 133401 (2004) (cited on page 5).

[64] T. Ditmire, J. W. G. Tisch, . . ., M. H. R. Hutchinson, *High-energy ions produced in explosions of superheated atomic clusters*, Nature **386**, 54–56 (1997) (cited on page 5).

[65] L. Poisson, K. D. Raffael, . . ., A. Maquet, *Low Field Laser Ionization of Argon Clusters: The Remarkable Fragmentation Dynamics of Doubly Ionized Clusters*, Phys. Rev. Lett. **99**, 103401 (2007) (cited on page 5).

[66] L. Cederbaum, J. Zobeley, and F. Tarantelli, *Giant Intermolecular Decay and Fragmentation of Clusters*, Phys. Rev. Lett. **79**, 4778–4781 (1997) (cited on page 5).

[67] W. Bang, G. Dyer, . . ., T. Ditmire, *Optimization of the neutron yield in fusion plasmas produced by Coulomb explosions of deuterium clusters irradiated by a petawatt laser*, Phys. Rev. E **87**, 023106 (2013) (cited on page 6).

[68] V. Strelkov, U. Saalmann, . . ., J. Rost, *Monitoring Atomic Cluster Expansion by High-Harmonic Generation*, Phys. Rev. Lett. **107**, 113901 (2011) (cited on page 6).

[69] C. Vozzi, M. Nisoli, . . ., G. Tondello, *Cluster effects in high-order harmonics generated by ultrashort light pulses*, Appl. Phys. Lett. **86**, 111121 (2005) (cited on page 6).

[70] J. W. G. Tisch, T. Ditmire, . . ., M. H. R. Hutchinson, *Investigation of high-harmonic generation from xenon atom clusters*, J. Phys. B At. Mol. Opt. Phys. **30**, L709–L714 (1997) (cited on page 6).

[71] D. F. Zaretsky, P. Korneev, and W. Becker, *High-order harmonic generation in clusters irradiated by an infrared laser field of moderate intensity*, J. Phys. B At. Mol. Opt. Phys. **43**, 105402 (2010) (cited on page 6).

[72] V. Véniard, R. Taïeb, and A. Maquet, *Simple model for harmonic generation from atomic clusters*, Phys. Rev. A **60**, 3952–3959 (1999) (cited on page 6).

[73] S. L. Chin, *Femtosecond Laser Filamentation*, Vol. 55, Springer Series on Atomic, Optical, and Plasma Physics (Springer New York, New York, NY, 2010) (cited on page 6).

[74] H. L. Xu and S. L. Chin, *Femtosecond laser filamentation for atmospheric sensing*, Sensors **11**, 32–53 (2011) (cited on page 6).

[75] H.-L. Li, X.-Y. Wei, . . ., H.-B. Sun, *Femtosecond laser filamentation for sensing combustion intermediates: A comparative study*, Sensors Actuators B Chem. **203**, 887–890 (2014) (cited on page 6).

[76] H. L. Xu, J. F. Daigle, . . ., S. L. Chin, *Femtosecond laser-induced nonlinear spectroscopy for remote sensing of methane*, Appl. Phys. B Lasers Opt. **82**, 655–658 (2006) (cited on page 6).

[77] H. Xu, Y. Cheng, . . ., H.-B. Sun, *Femtosecond laser ionization and fragmentation of molecules for environmental sensing*, Laser \& Photonics Rev. **9**, 275–293 (2015) (cited on page 6).

[78] S. Yuan, T. Wang, . . ., H. Zeng, *Humidity measurement in air using filament-induced nitrogen monohydride fluorescence spectroscopy*, Appl. Phys. Lett. **104**, 091113 (2014) (cited on page 6).

[79] J. Kasparian and J.-P. Wolf, *Ultrafast laser spectroscopy and control of atmospheric aerosols.* Phys. Chem. Chem. Phys. **14**, 9291–300 (2012) (cited on page 6).

[80] W. Kruer, *The Physics Of Laser Plasma Interactions (Frontiers in Physics)* (Westview Press, 2003) (cited on page 6).

[81] D. A. Jaroszynski, R. Bingham, and R. Cairns, *Laser-Plasma Interactions* (CRC Press, 2009) (cited on page 6).

[82] S. Corde, K. Ta Phuoc, . . ., E. Lefebvre, *Femtosecond x rays from laser-plasma accelerators*, Rev. Mod. Phys. **85**, 1–48 (2013) (cited on page 6).

[83] E. Esarey, C. B. Schroeder, and W. P. Leemans, *Physics of laser-driven plasma-based electron accelerators*, Rev. Mod. Phys. **81**, 1229–1285 (2009) (cited on page 6).

[84] F. Krausz and M. I. Stockman, *Attosecond metrology: from electron capture to future signal processing*, Nat. Photonics **8**, 205–213 (2014) (cited on pages 6, 7).

[85] M. I. Stockman, *Nanoplasmonics: past, present, and glimpse into future*, Opt. Express **19**, 22029–22106 (2011) (cited on page 6).

[86] P. Vasa, C. Ropers, . . ., C. Lienau, *Ultra-fast nano-optics*, Laser \& Photonics Rev. **3**, 483–507 (2009) (cited on pages 6, 7).

[87] J. P. Toennies and A. F. Vilesov, *Superfluid Helium Droplets: A Uniquely Cold Nanomatrix for Molecules and Molecular Complexes*, Angew. Chemie Int. Ed. **43**, 2622–2648 (2004) (cited on page 6).

[88] H. Thomas, A. Helal, . . ., T. Ditmire, *Explosions of Xenon Clusters in Ultraintense Femtosecond X-Ray Pulses from the LCLS Free Electron Laser*, Phys. Rev. Lett. **108**, 133401 (2012) (cited on page 6).

[89] F. Süßmann, L. Seiffert, . . ., T. Fennel, *Field propagation-induced directionality of carrier-envelope phase-controlled photoemission from nanospheres*, Nat. Commun. **6**, 7944 (2015) (cited on page 6).

[90] S. Zherebtsov, T. Fennel, . . ., M. F. Kling, *Controlled near-field enhanced electron acceleration from dielectric nanospheres with intense few-cycle laser fields*, Nat. Phys. **7**, 656–662 (2011) (cited on page 6).

[91] K. F. MacDonald, Z. L. Sámson, . . ., N. I. Zheludev, *Ultrafast active plasmonics*, Nat. Photonics **3**, 55–58 (2008) (cited on page 6).

[92] L. Wimmer, G. Herink, . . ., C. Ropers, *Terahertz control of nanotip photoemission*, Nat. Phys. **10**, 432–436 (2014) (cited on page 6).

[93] P. Dombi, A. Hörl, . . ., U. Hohenester, *Ultrafast Strong-Field Photoemission from Plasmonic Nanoparticles*, Nano Lett. **13**, 674–678 (2013) (cited on page 6).

[94] B. Piglosiewicz, S. Schmidt, . . ., C. Lienau, *Carrier-envelope phase effects on the strong-field photoemission of electrons from metallic nanostructures*, Nat. Photonics **8**, 37–42 (2013) (cited on page 6).

[95] G. Herink, D. R. Solli, . . ., C. Ropers, *Field-driven photoemission from nanostructures quenches the quiver motion*, Nature **483**, 190–193 (2012) (cited on page 6).

[96] M. Krüger, M. Schenk, and P. Hommelhoff, *Attosecond control of electrons emitted from a nanoscale metal tip*, Nature **475**, 78–81 (2011) (cited on page 6).

[97] F. Süßmann and M. Kling, *Attosecond nanoplasmonic streaking of localized fields near metal nanospheres*, Phys. Rev. B **84**, 121406 (2011) (cited on page 6).

[98] Y.-Y. Yang, E. Csapó, . . ., M. F. Kling, *Optimization of the Field Enhancement and Spectral Bandwidth of Single and Coupled Bimetal Core–Shell Nanoparticles for Few-Cycle Laser Applications*, Plasmonics **7**, 99–106 (2011) (cited on page 6).

[99] M. Sivis, M. Duwe, . . ., C. Ropers, *Extreme-ultraviolet light generation in plasmonic nanostructures*, Nat. Phys. **9**, 304–309 (2013) (cited on page 6).

[100] Y.-y. Yang, A. Scrinzi, . . ., M. F. Kling, *High-harmonic and single attosecond pulse generation using plasmonic field enhancement in ordered arrays of gold nanoparticles with chirped laser pulses*, Opt. Express **21**, 2195–2205 (2013) (cited on page 6).

[101] M. Sivis, M. Duwe, . . ., C. Ropers, *Nanostructure-enhanced atomic line emission.* Nature **485**, E1–2, discussion E2–3 (2012) (cited on page 6).

[102] S. L. Stebbings, F. Süßmann, . . ., M. F. Kling, *Generation of isolated attosecond extreme ultraviolet pulses employing nanoplasmonic field enhancement: optimization of coupled ellipsoids*, New J. Phys. **13**, 073010 (2011) (cited on page 6).

[103] I.-Y. Park, S. Kim, . . ., S.-W. Kim, *Plasmonic generation of ultrashort extreme-ultraviolet light pulses*, Nat. Photonics **5**, 677–681 (2011) (cited on page 6).

[104] S. F. Becker, M. Esmann, . . ., C. Lienau, *Gap-Plasmon-Enhanced Nanofocusing Near-Field Microscopy*, ACS Photonics **3**, 223–232 (2016) (cited on page 7).

[105] M. Stockman, M. Kling, . . ., F. Krausz, *Attosecond nanoplasmonic-field microscope*, Nat. Photonics **1**, 539–547 (2007) (cited on page 7).

[106] S. H. Chew, F. Süßmann, . . ., U. Kleineberg, *Time-of-flight-photoelectron emission microscopy on plasmonic structures using attosecond extreme ultraviolet pulses*, Appl. Phys. Lett. **100**, 051904 (2012) (cited on page 7).

[107] M. Durach, A. Rusina, . . ., M. Stockman, *Predicted Ultrafast Dynamic Metallization of Dielectric Nanofilms by Strong Single-Cycle Optical Fields*, Phys. Rev. Lett. **107**, 086602 (2011) (cited on pages 7, 8).

[108] A. V. Mitrofanov, A. J. Verhoef, . . ., A. Baltuška, *Optical Detection of Attosecond Ionization Induced by a Few-Cycle Laser Field in a Transparent Dielectric Material*, Phys. Rev. Lett. **106**, 147401 (2011) (cited on pages 7, 8).

[109] P. Földi, M. G. Benedict, and V. S. Yakovlev, *The effect of dynamical Bloch oscillations on optical-field-induced current in a wide-gap dielectric*, New J. Phys. **15**, 063019 (2013) (cited on page 7).

[110] G. Wachter, C. Lemell, . . ., K. Yabana, *Ab Initio Simulation of Electrical Currents Induced by Ultrafast Laser Excitation of Dielectric Materials*, Phys. Rev. Lett. **113**, 087401 (2014) (cited on pages 7, 8).

[111] O. Kwon, T. Paasch-Colberg, . . ., D. Kim, *Semimetallization of dielectrics in strong optical fields.* Sci. Rep. **6**, 21272 (2016) (cited on pages 7, 8).

[112] A. Sommer, E. M. Bothschafter, . . ., F. Krausz, *Attosecond real time observation of the nonlinear polarization and energy transfer in dielectrics*, Nature **i**, 86–90 (2016) (cited on page 7).

[113] M. Schultze, K. Ramasesha, . . ., S. R. Leone, *Attosecond band-gap dynamics in silicon*, Science **346**, 1348–1352 (2014) (cited on page 7).

[114] M. Wu, D. A. Browne, . . ., M. B. Gaarde, *Multilevel perspective on high-order harmonic generation in solids*, Phys. Rev. A **94**, 063403 (2016) (cited on page 7).

[115] G. Ndabashimiye, S. Ghimire, . . ., D. A. Reis, *Solid-state harmonics beyond the atomic limit*, Nature **534**, 520–523 (2016) (cited on pages 7, 87).

[116] M. Wu, S. Ghimire, . . ., M. B. Gaarde, *High-harmonic generation from Bloch electrons in solids*, Phys. Rev. A **91**, 043839 (2015) (cited on page 7).

[117] P. G. Hawkins, M. Y. Ivanov, and V. S. Yakovlev, *Effect of multiple conduction bands on high-harmonic emission from dielectrics*, Phys. Rev. A **91**, 013405 (2015) (cited on page 7).

[118] M. Hohenleutner, F. Langer, . . ., R. Huber, *Real-time observation of interfering crystal electrons in high-harmonic generation*, Nature **523**, 572–575 (2015) (cited on page 7).

[119] G. Vampa, C. R. McDonald, . . ., T. Brabec, *Theoretical Analysis of High-Harmonic Generation in Solids*, Phys. Rev. Lett. **113**, 073901 (2014) (cited on pages 7, 9).

[120] S. Ghimire, A. D. DiChiara, . . ., D. A. Reis, *Generation and propagation of high-order harmonics in crystals*, Phys. Rev. A **85**, 043836 (2012) (cited on page 7).

[121] S. Ghimire, A. D. DiChiara, . . ., D. A. Reis, *Observation of high-order harmonic generation in a bulk crystal*, Nat. Phys. **7**, 138–141 (2011) (cited on pages 7, 9, 87).

[122] E. Magerl, S. Neppl, . . ., P. Feulner, *A flexible apparatus for attosecond photoelectron spectroscopy of solids and surfaces*, Rev. Sci. Instrum. **82**, 063104 (2011) (cited on page 7).

[123] M. Meyer, P. Radcliffe, . . ., N. M. Kabachnik, *Angle-Resolved Electron Spectroscopy of Laser-Assisted Auger Decay Induced by a Few-Femtosecond X-Ray Pulse*, Phys. Rev. Lett. **108**, 063007 (2012) (cited on page 7).

[124] S. Neppl, R. Ernstorfer, . . ., P. Feulner, *Attosecond Time-Resolved Photoemission from Core and Valence States of Magnesium*, Phys. Rev. Lett. **109**, 087401 (2012) (cited on page 7).

[125] A. Guggenmos, A. Akil, . . ., U. Kleineberg, *Attosecond photoelectron streaking with enhanced energy resolution for small-bandgap materials*, Opt. Lett. **41**, 3714 (2016) (cited on page 7).

[126] S. Neppl, R. Ernstorfer, . . ., R. Kienberger, *Direct observation of electron propagation and dielectric screening on the atomic length scale*, Nature **517**, 342–346 (2015) (cited on page 7).

[127] A. L. Cavalieri, N. Müller, . . ., U. Heinzmann, *Attosecond spectroscopy in condensed matter*, Nature **449**, 1029–32 (2007) (cited on page 7).

[128] M. Lucchini, L. Castiglioni, . . ., U. Keller, *Light-Matter Interaction at Surfaces in the Spatiotemporal Limit of Macroscopic Models*, Phys. Rev. Lett. **115**, 137401 (2015) (cited on page 7).

[129] R. Locher, L. Castiglioni, . . ., U. Keller, *Energy-dependent photoemission delays from noble metal surfaces by attosecond interferometry*, Optica **2**, 405 (2015) (cited on page 7).

[130] Z. Tao, C. Chen, . . ., M. Murnane, *Direct time-domain observation of attosecond final-state lifetimes in photoemission from solids*, Science **353**, 62–67 (2016) (cited on page 7).

[131] L. Miaja-Avila, J. Yin, . . ., H. Kapteyn, *Ultrafast studies of electronic processes at surfaces using the laser-assisted photoelectric effect with long-wavelength dressing light*, Phys. Rev. A **79**, 030901 (2009) (cited on page 7).

[132] L. Miaja-Avila, G. Saathoff, . . ., H. C. Kapteyn, *Direct Measurement of Core-Level Relaxation Dynamics on a Surface-Adsorbate System*, Phys. Rev. Lett. **101**, 046101 (2008) (cited on page 7).

[133] F. Quéré, *Ultrafast science: Attosecond plasma optics*, Nat. Phys. **5**, 93–94 (2009) (cited on page 7).

[134] H. Vincenti, S. Monchocé, . . ., F. Quéré, *Optical properties of relativistic plasma mirrors*, Nat. Commun. **5**, 3403 (2014) (cited on page 7).

[135] A. Borot, A. Malvache, . . ., R. Lopez-Martens, *Attosecond control of collective electron motion in plasmas*, Nat. Phys. **8**, 416–421 (2012) (cited on page 7).

[136] J. Fuchs, A. A. Gonoskov, . . ., X. Q. Yan, *Plasma devices for focusing extreme light pulses*, Eur. Phys. J. Spec. Top. **223**, 1169–1173 (2014) (cited on page 7).

[137] M. Thévenet, A. Leblanc, . . ., J. Faure, *Vacuum laser acceleration of relativistic electrons using plasma mirror injectors*, Nat. Phys. **12**, 355–360 (2015) (cited on page 7).

[138] S. Monchocé, S. Kahaly, . . ., F. Quéré, *Optically Controlled Solid-Density Transient Plasma Gratings*, Phys. Rev. Lett. **112**, 145008 (2014) (cited on page 7).

[139] A. Borot, A. Malvache, . . ., R. Lopez-Martens, *High-harmonic generation from plasma mirrors at kilohertz repetition rate.* Opt. Lett. **36**, 1461–1463 (2011) (cited on page 7).

[140] G. D. Tsakiris, K. Eidmann, . . ., F. Krausz, *Route to intense single attosecond pulses*, New J. Phys. **8**, 19 (2006) (cited on page 7).

[141] P. Heissler, R. Hörlein, . . ., G. D. Tsakiris, *Few-Cycle Driven Relativistically Oscillating Plasma Mirrors: A Source of Intense Isolated Attosecond Pulses*, Phys. Rev. Lett. **108**, 235003 (2012) (cited on page 7).

[142] G. Yudin and M. Ivanov, *Nonadiabatic tunnel ionization: Looking inside a laser cycle*, Phys. Rev. A **64**, 013409 (2001) (cited on pages 8, 12).

[143] G. Yudin and M. Ivanov, *Physics of correlated double ionization of atoms in intense laser fields: Quasistatic tunneling limit*, Phys. Rev. A **63**, 033404 (2001) (cited on page 8).

[144] M. Y. Ivanov, M. Spanner, and O. Smirnova, *Anatomy of strong field ionization*, J. Mod. Opt. **52**, 165–184 (2005) (cited on pages 8, 9, 12).

[145] A. A. Jauho and K. Johnsen, *Dynamical Franz-Keldysh effect*, Phys. Rev. Lett. **76**, 4576–4579 (1996) (cited on page 8).

[146] P. B. Corkum and F. Krausz, *Attosecond science*, Nat. Phys. **3**, 381–387 (2007) (cited on pages 8, 9, 19).

[147] H. Niikura and P. Corkum, *Attosecond and Angstrom science*, Adv. At. Mol. Opt. Phys. **54**, 511 (2007) (cited on pages 8, 19, 64).

[148] P. B. Corkum, *Recollision physics*, Phys. Today **64**, 36 (2011) (cited on pages 8, 19).

[149] M. Y. Ivanov, R. Kienberger, . . ., D. M. Villeneuve, *Attosecond physics*, J. Phys. B At. Mol. Opt. Phys. **39**, R1–R37 (2006) (cited on pages 8, 9, 19, 29, 87).

[150] X. Xie, S. Roither, . . ., M. Kitzler, *Probing the influence of the Coulomb field on atomic ionization by sculpted two-color laser fields*, New J. Phys. 15, 043050 (2013) (cited on pages 8, 13, 70, 128).

[151] L. Zhang, X. Xie, . . ., M. Kitzler, *Laser-sub-cycle two-dimensional electron-momentum mapping using orthogonal two-color fields*, Phys. Rev. A 90, 061401 (2014) (cited on pages 8, 13, 38, 39, 69, 70, 99).

[152] D. G. Arbó, K. Ishikawa, . . ., J. Burgdörfer, *Diffraction at a time grating in above-threshold ionization: The influence of the Coulomb potential*, Phys. Rev. A **82**, 043426 (2010) (cited on pages 8, 73, 79).

[153] P. Agostini, F. Fabre, . . ., N. Rahman, *Free-Free Transitions Following Six-Photon Ionization of Xenon Atoms*, Phys. Rev. Lett. **42**, 1127–1130 (1979) (cited on pages 9, 16).

[154] G. Paulus, F. Grasbon, . . ., W. Becker, *Above-threshold ionization by an elliptically polarized field: interplay between electronic quantum trajectories*, Phys. Rev. Lett. **84**, 3791 (2000) (cited on pages 9, 72, 77).

[155] F. Grasbon, G. Paulus, . . ., S. De Silvestri, *Above-Threshold Ionization at the Few-Cycle Limit*, Phys. Rev. Lett. **91**, 173003 (2003) (cited on pages 9, 16, 20, 34).

[156] P. Colosimo, G. Doumy, . . ., L. F. DiMauro, *Scaling strong-field interactions towards the classical limit*, Nat. Phys. **4**, 386–389 (2008) (cited on pages 9, 12).

[157] B. Walker, B. Sheehy, . . ., K. Kulander, *Precision Measurement of Strong Field Double Ionization of Helium*, Phys. Rev. Lett. **73**, 1227–1230 (1994) (cited on pages 9, 13, 20).

[158] B. Feuerstein, R. Moshammer, . . ., W. Sandner, *Separation of Recollision Mechanisms in Nonsequential Strong Field Double Ionization of Ar: The Role of Excitation Tunneling*, Phys. Rev. Lett. **87**, 043003 (2001) (cited on pages 9, 13, 20).

[159] A. Rudenko, K. Zrost, . . ., J. Ullrich, *Correlated Multielectron Dynamics in Ultrafast Laser Pulse Interactions with Atoms*, Phys. Rev. Lett. **93**, 253001 (2004) (cited on pages 9, 13, 20, 110, 116).

[160] T. Popmintchev, M.-C. Chen, . . ., H. C. Kapteyn, *The attosecond nonlinear optics of bright coherent X-ray generation*, Nat. Photonics **4**, 822–832 (2010) (cited on pages 9, 21, 89).

[161] M. de Boer, J. Hoogenraad, . . ., H. Muller, *Adiabatic stabilization against photoionization: An experimental study*, Phys. Rev. A **50**, 4085–4098 (1994) (cited on pages 9, 21).

[162] B. Manschwetus, T. Nubbemeyer, . . ., W. Sandner, *Strong Laser Field Fragmentation of H2: Coulomb Explosion without Double Ionization*, Phys. Rev. Lett. **102**, 113002 (2009) (cited on pages 9, 21).

[163] S. Larimian, C. Lemell, . . ., X. Xie, *Localizing high-lying Rydberg wave packets with two-color laser fields*, Phys. Rev. A 96, 021403 (2017) (cited on pages 9, 21, 56).

[164] S. Larimian, S. Erattupuzha, . . ., X. Xie, *Coincidence spectroscopy of high-lying Rydberg states produced in strong laser fields*, Phys. Rev. A 94, 033401 (2016) (cited on pages 9, 21).

[165] S. Erattupuzha, V. Hanus, . . ., M. Kitzler, "Laser-sub-cycle Fragmentation Dynamics of Argon Dimers", in INT. CONF. ON ULTRAF. PHENOM. (2016), UTu4A.17 (cited on pages 9, 21, 22).

[166] J. Weisshaupt, V. Juvé, . . ., A. Baltuska, *High-brightness table-top hard X-ray source driven by sub-100-femtosecond mid-infrared pulses*, Nat. Photonics **8**, 927–930 (2014) (cited on page 9).

[167] J. Itatani, H. Niikura, and P. B. Corkum, *Attosecond Science*, Phys. Scr. **110**, 112 (2004) (cited on page 9).

[168] M. Hentschel, R. Kienberger, . . ., F. Krausz, *Attosecond metrology*, Nature **414**, 509–513 (2001) (cited on pages 9, 44).

[169] M. Chini, K. Zhao, and Z. Chang, *The generation, characterization and applications of broadband isolated attosecond pulses*, Nat. Photonics **8**, 178–186 (2014) (cited on page 9).

[170] M. Lein, *Molecular imaging using recolliding electrons*, J. Phys. B At. Mol. Opt. Phys. **40**, R135–R173 (2007) (cited on pages 9, 19, 64, 80, 90).

[171] W. Becker, F. Grasbon, . . ., H. Walther, *Above-threshold ionization: From classical features to quantum effects*, Adv. At. Mol. Opt. Phys., Advances In Atomic, Molecular, and Optical Physics **48**, edited by B. Bederson and H. Walther, 35–98 (2002) (cited on pages 9, 16, 19, 22–24, 34).

[172] D. B. Milošević and F. Ehlotzky, *Scattering and Reaction Processes in Powerful Laser Fields*, Adv. At. Mol. Opt. Phys. **49**, 373–532 (2003) (cited on pages 9, 19).

[173] A. Becker and F. H. M. Faisal, *Intense-field many-body S-matrix theory*, J. Phys. B At. Mol. Opt. Phys. **38**, R1–R56 (2005) (cited on pages 9, 12, 28).

[174] W. Becker, X. Liu, . . ., J. H. Eberly, *Theories of photoelectron correlation in laser-driven multiple atomic ionization*, Rev. Mod. Phys. **84**, 1011–1043 (2012) (cited on page 9).

[175] C. F. de Morisson Faria and X. Liu, *Electron–electron correlation in strong laser fields*, J. Mod. Opt. **58**, 1076–1131 (2011) (cited on pages 9, 21, 25, 71).

[176] L. Torlina and O. Smirnova, *Time-dependent analytical R-matrix approach for strong-field dynamics. I. One-electron systems*, Phys. Rev. A **86**, 043408 (2012) (cited on page 9).

[177] L. Torlina, M. Ivanov, . . ., O. Smirnova, *Time-dependent analytical R-matrix approach for strong-field dynamics. II. Many-electron systems*, Phys. Rev. A **86**, 043409 (2012) (cited on pages 9, 12, 28).

[178] S. V. Popruzhenko, *Keldysh theory of strong field ionization: history, applications, difficulties and perspectives*, J. Phys. B At. Mol. Opt. Phys. **47**, 204001 (2014) (cited on page 9).

[179] O. Smirnova, M. Spanner, and M. Ivanov, *Analytical solutions for strong field-driven atomic and molecular one- and two-electron continua and applications to strong-field problems*, Phys. Rev. A **77**, 033407 (2008) (cited on pages 9, 12, 13, 28).

[180] J. Zanghellini, M. Kitzler, . . ., A. Scrinzi, *An MCTDHF Approach to Multielectron Dynamics in Laser Fields*, Laser Phys. 13, 1064–1068 (2003) (cited on page 9).

[181] M. Kitzler, J. Zanghellini, . . ., T. Brabec, *Ionization dynamics of extended multielectron systems*, Phys. Rev. A 70, 041401 (2004) (cited on page 9).

[182] J. Zanghellini, M. Kitzler, . . ., A. Scrinzi, *Testing the multi-configuration time-dependent Hartree–Fock method*, J. Phys. B At. Mol. Opt. Phys. 37, 763–773 (2004) (cited on page 9).

[183] J. Caillat, J. Zanghellini, . . ., A. Scrinzi, *Correlated multielectron systems in strong laser fields: A multiconfiguration time-dependent Hartree-Fock approach*, Phys. Rev. A 71, 012712 (2005) (cited on page 9).

[184] S. Bubin, M. Atkinson, . . ., M. Kitzler, *Strong laser-pulse-driven ionization and Coulomb explosion of hydrocarbon molecules*, Phys. Rev. A 86, 043407 (2012) (cited on pages 9, 11, 12, 113, 114, 128).

[185] X. Xie, K. Doblhoff-Dier, . . ., M. Kitzler, *Selective Control over Fragmentation Reactions in Polyatomic Molecules Using Impulsive Laser Alignment*, Phys. Rev. Lett. 112, 163003 (2014) (cited on pages 9, 109, 112, 116, 117).

[186] A. Russakoff, S. Bubin, . . ., K. Varga, *Time-dependent density-functional study of the alignment-dependent ionization of acetylene and ethylene by strong laser pulses*, Phys. Rev. A 91, 023422 (2015) (cited on pages 9, 11, 12, 113, 128).

[187] K. Doblhoff-Dier, M. Kitzler, and S. Gräfe, *Theoretical investigation of alignment-dependent intense-field fragmentation of acetylene*, Phys. Rev. A 94, 013405 (2016) (cited on pages 9, 11, 116).

[188] S. Erattupuzha, C. L. Covington, . . ., M. Kitzler, *Enhanced ionisation of polyatomic molecules in intense laser pulses is due to energy upshift and field coupling of multiple orbitals*, J. Phys. B At. Mol. Opt. Phys. 50, 125601 (2017) (cited on pages 9, 114, 119, 128).

[189] L. Zhang, X. Xie, . . ., M. Kitzler, *Subcycle Control of Electron-Electron Correlation in Double Ionization*, Phys. Rev. Lett. 112, 193002 (2014) (cited on pages 9, 21, 38, 71).

[190] M. S. Schöffler, X. Xie, . . ., M. Kitzler, *Laser-subcycle control of sequential double-ionization dynamics of helium*, Phys. Rev. A 93, 063421 (2016) (cited on pages 9, 13, 15, 34, 58, 59, 66–68).

[191] P. Wustelt, M. Möller, . . ., M. Kitzler, *Numerical investigation of the sequential-double-ionization dynamics of helium in different few-cycle-laser-field shapes*, Phys. Rev. A 95, 023411 (2017) (cited on pages 9, 66).

[192] P. Ho, R. Panfili, . . ., J. Eberly, *Nonsequential Double Ionization as a Completely Classical Photoelectric Effect*, Phys. Rev. Lett. **94**, 093002 (2005) (cited on page 9).

[193] Y. Zhou, C. Huang, . . ., P. Lu, *Classical Simulations Including Electron Correlations for Sequential Double Ionization*, Phys. Rev. Lett. **109**, 053004 (2012) (cited on pages 9, 67).

[194] Wikipedia, *Atomic Units*, (2018) https://en.wikipedia.org/wiki/Atomic_units (visited on 02/02/2017) (cited on pages 10, 167).

[195] A. Scrinzi, M. Geissler, and T. Brabec, *Ionization Above the Coulomb Barrier*, Phys. Rev. Lett. **83**, 706–709 (1999) (cited on page 11).

[196] L. Keldysh, *Ionization in the field of a strong electromagnetic wave*, Zh. Eksp. Teor. Fiz. **47**, 1945–1957 (1964) (cited on pages 11, 13, 23).

[197] A. M. Perelomov, V. S. Popov, and M. V. Terent'ev, *Ionization of Atoms in an Alternating Electric Field*, Sov. Phys. JETP **23**, 924–934 (1966) (cited on page 11).

[198] M. V. Ammosov, N. Delone, and V. P. Krainov, *Tunnel ionization of complex atoms and of atomic ions in an alternating electromagnetic field*, Sov. Phys. JETP **64**, 1191 (1986) (cited on page 11).

[199] X. M. Tong and C. D. Lin, *Empirical formula for static field ionization rates of atoms and molecules by lasers in the barrier-suppression regime*, J. Phys. B At. Mol. Opt. Phys. **38**, 2593–2600 (2005) (cited on page 11).

[200] X. Tong, Z. Zhao, and C. Lin, *Theory of molecular tunneling ionization*, Phys. Rev. A **66**, 033402 (2002) (cited on pages 11, 99, 110).

[201] M. Spanner and S. Patchkovskii, *One-electron ionization of multielectron systems in strong nonresonant laser fields*, Phys. Rev. A **80**, 063411 (2009) (cited on page 11).

[202] R. Murray, M. Spanner, . . ., M. Y. Ivanov, *Tunnel Ionization of Molecules and Orbital Imaging*, Phys. Rev. Lett. **106**, 173001 (2011) (cited on page 11).

[203] S.-F. Zhao, J. Xu, . . ., C. D. Lin, *Effect of orbital symmetry on the orientation dependence of strong field tunnelling ionization of nonlinear polyatomic molecules*, J. Phys. B At. Mol. Opt. Phys. **44**, 035601 (2011) (cited on page 11).

[204] H. R. Reiss, *Limits on Tunneling Theories of Strong-Field Ionization*, Phys. Rev. Lett. **101**, 043002 (2008) (cited on page 11).

[205] H. R. Reiss, *Unsuitability of the Keldysh parameter for laser fields*, Phys. Rev. A **82**, 023418 (2010) (cited on page 11).

[206] G. Andriukaitis, T. Balčiūnas, . . ., H. C. Kapteyn, *90 GW peak power few-cycle mid-infrared pulses from an optical parametric amplifier*, Opt. Lett. **36**, 2755 (2011) (cited on page 12).

[207] P. N. Malevich, G. Andriukaitis, . . ., P. B. Phua, *High energy and average power femtosecond laser for driving mid-infrared optical parametric amplifiers.* Opt. Lett. **38**, 2746–9 (2013) (cited on page 12).

[208] A. Talebpour, S. Larochelle, and S. L. Chin, *Suppressed tunnelling ionization of the D2 molecule in an intense Ti:sapphire laser pulse*, J. Phys. B At. Mol. Opt. Phys. **31**, L49–L58 (1998) (cited on page 12).

[209] S. Larochelle, A. Talebpour, and S. L. Chin, *Non-sequential multiple ionization of rare gas atoms in a Ti:Sapphire laser field*, J. Phys. B At. Mol. Opt. Phys. **31**, 1201–1214 (1998) (cited on pages 12, 13, 20).

[210] A. D. Shiner, B. E. Schmidt, . . ., D. M. Villeneuve, *Probing collective multi-electron dynamics in xenon with high-harmonic spectroscopy*, Nat. Phys. **7**, 464–467 (2011) (cited on page 12).

[211] S. Patchkovskii, Z. Zhao, . . ., D. Villeneuve, *High Harmonic Generation and Molecular Orbital Tomography in Multielectron Systems: Beyond the Single Active Electron Approximation*, Phys. Rev. Lett. **97**, 1–4 (2006) (cited on pages 12, 90).

[212] Z. B. Walters and O. Smirnova, *Attosecond correlation dynamics during electron tunnelling from molecules*, J. Phys. B At. Mol. Opt. Phys. **43**, 161002 (2010) (cited on page 12).

[213] F. Ferrari, F. Calegari, . . ., M. Nisoli, *High-energy isolated attosecond pulses generated by above-saturation few-cycle fields*, Nat. Photonics **4**, 875–879 (2010) (cited on page 13).

[214] D. Fittinghoff, P. Bolton, . . ., K. Kulander, *Observation of nonsequential double ionization of helium with optical tunneling*, Phys. Rev. Lett. **69**, 2642–2645 (1992) (cited on pages 13, 20).

[215] T. Weber, H. Giessen, . . ., R. Dörner, *Correlated electron emission in multiphoton double ionization*, Nature **405**, 658–61 (2000) (cited on pages 13, 20).

[216] S. Popruzhenko and D. Bauer, *Strong field approximation for systems with Coulomb interaction*, J. Mod. Opt. **55**, 2573–2589 (2008) (cited on pages 13, 28).

[217] T.-M. Yan, S. V. Popruzhenko, . . ., D. Bauer, *Low-Energy Structures in Strong Field Ionization Revealed by Quantum Orbits*, Phys. Rev. Lett. **105**, 253002 (2010) (cited on pages 13, 28).

[218] T.-M. Yan and D. Bauer, *Sub-barrier Coulomb effects on the interference pattern in tunneling-ionization photoelectron spectra*, Phys. Rev. A **86**, 053403 (2012) (cited on pages 13, 28).

[219] L. Torlina, J. Kaushal, and O. Smirnova, *Time-resolving electron-core dynamics during strong-field ionization in circularly polarized fields*, Phys. Rev. A **88**, 053403 (2013) (cited on pages 13, 28).

[220] F. Faisal, *Multiple absorption of laser photons by atoms*, J. Phys. B At. Mol. **6**, L89 (1973) (cited on pages 13, 23).

[221] H. Reiss, *Effect of an intense electromagnetic field on a weakly bound system*, Phys. Rev. A **22**, 1786–1813 (1980) (cited on pages 13, 23).

[222] H. Van Linden van den Heuvell and H. Muller, "Limiting cases of excess-photon ionization", in PROC. 4TH INT. CONF. MULTIPHOT. PROCESS. JILA, BOULDER, COLOR. JULY 13-17, 1987, edited by S. J. Smith and P. L. Knight (1988), pp. 25–34 (cited on pages 13, 24).

[223] N. B. Delone and V. P. Krainov, *Energy and angular electron spectra for the tunnel ionization of atoms by strong low-frequency radiation*, J. Opt. Soc. Am. B **8**, 1207 (1991) (cited on pages 13, 16).

[224] G. Paulus, W. Nicklich, . . ., H. Walther, *Plateau in above threshold ionization spectra*, Phys. Rev. Lett. **72**, 2851–2854 (1994) (cited on pages 16, 19, 34).

[225] G. Paulus, W. Nicklich, . . ., H. Walther, *High-order above-threshold ionization of atomic hydrogen using intense, ultrashort laser pulses*, J. Phys. B At. Mol. Opt. Phys. **29**, L249–L256 (1996) (cited on pages 16, 34).

[226] X. Xie, S. Roither, . . ., M. Kitzler, *Attosecond Probe of Valence-Electron Wave Packets by Subcycle Sculpted Laser Fields*, Phys. Rev. Lett. 108, 193004 (2012) (cited on pages 16, 20, 38, 69, 72–76, 78–80, 110).

[227] D. G. Arbó, S. Yoshida, . . ., J. Burgdörfer, *Interference Oscillations in the Angular Distribution of Laser-Ionized Electrons near Ionization Threshold*, Phys. Rev. Lett. **96**, 143003 (2006) (cited on pages 16, 20, 69).

[228] D. G. Arbó, K. L. Ishikawa, . . ., J. Burgdörfer, *Intracycle and intercycle interferences in above-threshold ionization: The time grating*, Phys. Rev. A **81**, 021403 (2010) (cited on pages 16, 20, 69, 73).

[229] D. G. Arbó, E. Persson, and J. Burgdörfer, *Time double-slit interferences in strong-field tunneling ionization*, Phys. Rev. A **74**, 063407 (2006) (cited on pages 16, 73).

[230] A. Alnaser, X. Tong, . . ., C. Cocke, *Laser-peak-intensity calibration using recoil-ion momentum imaging*, Phys. Rev. A **70**, 23413 (2004) (cited on page 16).

[231] P. Dietrich, N. Burnett, . . ., P. Corkum, *High-harmonic generation and correlated two-electron multiphoton ionization with elliptically polarized light*, Phys. Rev. A **50**, R3585–R3588 (1994) (cited on pages 17, 38).

[232] H. Eichmann, A. Egbert, . . ., J. K. McIver, *Polarization-dependent high-order two-color mixing*, Phys. Rev. A **51**, R3414–R3417 (1995) (cited on pages 17, 29, 41, 48).

[233] D. B. Milošević, W. Becker, and R. Kopold, *Generation of circularly polarized high-order harmonics by two-color coplanar field mixing*, Phys. Rev. A **61**, 063403 (2000) (cited on pages 17, 41, 48).

[234] M. Kitzler and M. Lezius, *Spatial Control of Recollision Wave Packets with Attosecond Precision*, Phys. Rev. Lett. 95, 253001 (2005) (cited on pages 17, 38, 40, 70, 97).

[235] M. Kitzler, K. O'Keeffe, and M. Lezius, *Attosecond control of electronic motion using light wave synthesis*, J. Mod. Opt. 53, 57–66 (2006) (cited on pages 17, 38, 70, 97).

[236] M. Kitzler, X. Xie, . . ., A. Baltuska, *Optical attosecond mapping by polarization selective detection*, Phys. Rev. A 76, 011801 (2007) (cited on pages 17, 38, 40, 47, 70, 98, 99).

[237] M. Kitzler, X. Xie, . . ., A. Baltuska, *Angular encoding in attosecond recollision*, New J. Phys. 10, 025029 (2008) (cited on pages 17, 38, 40, 45, 47, 69, 70, 98–100).

[238] S. Haessler, J. Caillat, and P. Salières, *Self-probing of molecules with high harmonic generation*, J. Phys. B At. Mol. Opt. Phys. **44**, 203001 (2011) (cited on pages 19, 64, 87, 90, 95, 98).

[239] J. Xu, C. I. Blaga, . . ., L. F. DiMauro, *Time-resolved molecular imaging*, J. Phys. B At. Mol. Opt. Phys. **49**, 112001 (2016) (cited on pages 19, 80).

[240] M. Lein, *Attosecond Probing of Vibrational Dynamics with High-Harmonic Generation*, Phys. Rev. Lett. **94**, 053004 (2005) (cited on pages 19, 94).

[241] S. Baker, J. S. Robinson, . . ., J. P. Marangos, *Probing proton dynamics in molecules on an attosecond time scale.* Science **312**, 424–7 (2006) (cited on pages 19, 64, 89, 94).

[242] B. Yang, K. J. Schafer, . . ., L. F. DiMauro, *Intensity-dependent scattering rings in high order above-threshold ionization*, Phys. Rev. Lett. **71**, 3770–3773 (1993) (cited on page 19).

[243] G. G. Paulus, F. Grasbon, . . ., S. De Silvestri, *Absolute-phase phenomena in photoionization with few-cycle laser pulses.* Nature **414**, 182–4 (2001) (cited on pages 20, 34).

[244] D. Milošević, G. Paulus, and W. Becker, *Phase-Dependent Effects of a Few-Cycle Laser Pulse*, Phys. Rev. Lett. **89**, 153001 (2002) (cited on pages 20, 77).

[245] G. Paulus, F. Lindner, . . ., F. Krausz, *Measurement of the Phase of Few-Cycle Laser Pulses*, Phys. Rev. Lett. **91**, 253004 (2003) (cited on pages 20, 34).

[246] F. Lindner, G. Paulus, . . ., F. Krausz, *Gouy Phase Shift for Few-Cycle Laser Pulses*, Phys. Rev. Lett. **92**, 113001 (2004) (cited on page 20).

[247] T. Wittmann, B. Horvath, . . ., R. Kienberger, *Single-shot carrier–envelope phase measurement of few-cycle laser pulses*, Nat. Phys. **5**, 357–362 (2009) (cited on pages 20, 30, 34).

[248] A. M. Sayler, T. Rathje, . . ., G. G. Paulus, *Real-time pulse length measurement of few-cycle laser pulses using above-threshold ionization*, Opt. Express **19**, 4464 (2011) (cited on pages 20, 30, 34).

[249] A. M. Sayler, T. Rathje, . . ., G. G. Paulus, *Precise, real-time, every-single-shot, carrier-envelope phase measurement of ultrashort laser pulses*, Opt. Lett. **36**, 1 (2011) (cited on pages 20, 30, 34).

[250] T. Rathje, N. G. Johnson, . . ., A. M. Sayler, *Review of attosecond resolved measurement and control via carrier–envelope phase tagging with above-threshold ionization*, J. Phys. B At. Mol. Opt. Phys. **45**, 074003 (2012) (cited on pages 20, 30, 34, 58).

[251] Y. Huismans, A. Rouzée, . . ., M. J. J. Vrakking, *Time-resolved holography with photoelectrons.* Science **331**, 61–4 (2011) (cited on pages 20, 73–75).

[252] M. Spanner, O. Smirnova, . . ., M. Y. Ivanov, *Reading diffraction images in strong field ionization of diatomic molecules*, J. Phys. B At. Mol. Opt. Phys. **37**, L243–L250 (2004) (cited on pages 20, 38, 73, 74, 80).

[253] M. Meckel, D. Comtois, . . ., P. B. Corkum, *Laser-induced electron tunneling and diffraction.* Science **320**, 1478–82 (2008) (cited on pages 20, 79, 80).

[254] C. I. Blaga, J. Xu, . . ., C. D. Lin, *Imaging ultrafast molecular dynamics with laser-induced electron diffraction*, Nature **483**, 194–197 (2012) (cited on pages 20, 80–84).

[255] B. Wolter, M. G. Pullen, . . ., J. Biegert, *Ultrafast electron diffraction imaging of bond breaking in di-ionized acetylene*, Science **354**, 308–312 (2016) (cited on pages 20, 38, 81–84).

[256] C. Figueira de Morisson Faria, H. Schomerus, . . ., W. Becker, *Electron-electron dynamics in laser-induced nonsequential double ionization*, Phys. Rev. A **69**, 043405 (2004) (cited on pages 21, 25).

[257] C. Figueira de Morisson Faria, X. Liu, . . ., M. Lewenstein, *Classical and quantum-mechanical treatments of nonsequential double ionization with few-cycle laser pulses*, Phys. Rev. A **70**, 043406 (2004) (cited on pages 21, 25).

[258] X. Liu, C. F. D. M. Faria, . . ., P. B. Corkum, *Attosecond electron thermalization by laser-driven electron recollision in atoms*, J. Phys. B At. Mol. Opt. Phys. **39**, L305–L311 (2006) (cited on page 21).

[259] R. Kopold, W. Becker, . . ., W. Sandner, *Routes to Nonsequential Double Ionization*, Phys. Rev. Lett. **85**, 3781–3784 (2000) (cited on pages 21, 25).

[260] M. Weckenbrock, A. Becker, . . ., R. Dörner, *Electron-Electron Momentum Exchange in Strong Field Double Ionization*, Phys. Rev. Lett. **91**, 123004 (2003) (cited on page 21).

[261] A. Staudte, C. Ruiz, . . ., R. Dörner, *Binary and Recoil Collisions in Strong Field Double Ionization of Helium*, Phys. Rev. Lett. **99**, 263002 (2007) (cited on pages 21, 59).

[262] X. Liu and C. Figueira de Morisson Faria, *Nonsequential Double Ionization with Few-Cycle Laser Pulses*, Phys. Rev. Lett. **92**, 133006 (2004) (cited on page 21).

[263] X. Liu, H. Rottke, . . ., H. Walther, *Nonsequential Double Ionization at the Single-Optical-Cycle Limit*, Phys. Rev. Lett. **93**, 263001 (2004) (cited on page 21).

[264] X. Xie, K. Doblhoff-Dier, . . ., M. Kitzler, *Attosecond-Recollision-Controlled Selective Fragmentation of Polyatomic Molecules*, Phys. Rev. Lett. 109, 243001 (2012) (cited on pages 21, 34, 58, 109, 111, 112, 115, 116, 123, 125, 127, 128).

[265] M. Lewenstein, P. Balcou, . . ., P. Corkum, *Theory of high-harmonic generation by low-frequency laser fields*, Phys. Rev. A **49**, 2117–2132 (1994) (cited on pages 21, 26).

[266] P. Balcou, P. Salières, . . ., M. Lewenstein, *Generalized phase-matching conditions for high harmonics: The role of field-gradient forces*, Phys. Rev. A **55**, 3204–3210 (1997) (cited on pages 21, 93).

[267] A. Rundquist, C. G. D. III, . . ., H. C. Kapteyn, *Phase-Matched Generation of Coherent Soft X-rays*, Science **280**, 1412–1415 (1998) (cited on page 21).

[268] T. Popmintchev, M.-C. Chen, . . ., H. C. Kapteyn, *Phase matching of high harmonic generation in the soft and hard X-ray regions of the spectrum.* Proc. Natl. Acad. Sci. U. S. A. **106**, 10516–21 (2009) (cited on page 21).

[269] M. V. Fedorov and A. M. Movsesian, *Field-induced effects of narrowing of photoelectron spectra and stabilisation of Rydberg atoms*, J. Phys. B At. Mol. Opt. Phys. **21**, L155–L158 (1988) (cited on page 21).

[270] M. P. de Boer and H. G. Muller, *Observation of large populations in excited states after short-pulse multiphoton ionization*, Phys. Rev. Lett. **68**, 2747–2750 (1992) (cited on page 21).

[271] R. R. Jones, D. W. Schumacher, and P. H. Bucksbaum, *Population trapping in Kr and Xe in intense laser fields*, Phys. Rev. A **47**, R49–R52 (1993) (cited on page 21).

[272] M. P. Hertlein, P. H. Bucksbaum, and H. G. Muller, *Evidence for resonant effects in high-order ATI spectra*, J. Phys. B At. Mol. Opt. Phys. **30**, L197–L205 (1997) (cited on page 21).

[273] H. G. Muller, *Tunneling Excitation to Resonant States in Helium as Main Source of Superponderomotive Photoelectrons in the Tunneling Regime*, Phys. Rev. Lett. **83**, 3158–3161 (1999) (cited on page 21).

[274] E. Wells, I. Ben-Itzhak, and R. R. Jones, *Ionization of Atoms by the Spatial Gradient of the Pondermotive Potential in a Focused Laser Beam*, Phys. Rev. Lett. **93**, 023001 (2004) (cited on page 21).

[275] T. Nubbemeyer, K. Gorling, . . ., W. Sandner, *Strong-Field Tunneling without Ionization*, Phys. Rev. Lett. **101**, 233001 (2008) (cited on page 21).

[276] U. Eichmann, T. Nubbemeyer, . . ., W. Sandner, *Acceleration of neutral atoms in strong short-pulse laser fields.* Nature **461**, 1261–4 (2009) (cited on page 21).

[277] D. B. Milošević, G. G. Paulus, . . ., W. Becker, *Above-threshold ionization by few-cycle pulses*, J. Phys. B At. Mol. Opt. Phys. **39**, R203–R262 (2006) (cited on pages 22–24).

[278] Wikipedia, *Stationary-phase method*, (2018) https://en.wikipedia.org/wiki/Method_of_steepest_descent (visited on 06/06/2018) (cited on page 24).

[279] H. G. Muller, P. H. Bucksbaum, . . ., A. Zavriyev, *Above-threshold ionisation with a two-colour laser field*, J. Phys. B At. Mol. Opt. Phys. **23**, 2761–2769 (1990) (cited on pages 29, 35, 69).

[280] K. Schafer and K. Kulander, *Phase-dependent effects in multiphoton ionization induced by a laser field and its second harmonic*, Phys. Rev. A **45**, 8026–8033 (1992) (cited on pages 29, 35, 69).

[281] D. W. Schumacher, F. Weihe, . . ., P. H. Bucksbaum, *Phase Dependence of Intense Field Ionization: A Study Using Two Colors*, Phys. Rev. Lett. **73**, 1344–1347 (1994) (cited on pages 29, 35, 69).

[282] B. Sheehy, B. Walker, and L. DiMauro, *Phase Control in the Two-Color Photodissociation of HD+*, Phys. Rev. Lett. **74**, 4799–4802 (1995) (cited on pages 29, 130).

[283] T. Brabec and F. Krausz, *Intense few-cycle laser fields: Frontiers of nonlinear optics*, Rev. Mod. Phys. **72**, 545–591 (2000) (cited on page 29).

[284] L.-Y. Peng, W.-C. Jiang, . . ., Q. Gong, *Tracing and controlling electronic dynamics in atoms and molecules by attosecond pulses*, Phys. Rep. **575**, 1–71 (2015) (cited on pages 29, 43).

[285] Z. Chang, P. B. Corkum, and S. R. Leone, *Attosecond optics and technology: progress to date and future prospects*, J. Opt. Soc. Am. B **33**, 1081 (2016) (cited on pages 29, 43).

[286] M. Kübel, K. J. Betsch, . . ., B. Bergues, *Carrier-envelope-phase tagging in measurements with long acquisition times*, New J. Phys. **14**, 093027 (2012) (cited on pages 30, 34).

[287] S. Fukahori, T. Ando, . . ., G. G. Paulus, *Determination of the absolute carrier-envelope phase by angle-resolved photoelectron spectra of Ar by intense circularly polarized few-cycle pulses*, Phys. Rev. A **95**, 053410 (2017) (cited on pages 30, 34).

[288] T. Udem, R. Holzwarth, and T. Hänsch, *Optical frequency metrology*, Nature **416**, 233–237 (2002) (cited on page 32).

[289] T. Udem, “Die Messung der Frequenz von Licht mit modengekoppelten Lasern”, Habilitationsschrift (Ludwig–Maximilians–Universität München, 2002) (cited on page 32).

[290] H. Telle, G. Steinmeyer, . . ., U. Keller, *Carrier-envelope offset phase control: A novel concept for absolute optical frequency measurement and ultrashort pulse generation*, Appl. Phys. B **69**, 327–332 (1999) (cited on page 32).

[291] A. Apolonski, A. Poppe, . . ., F. Krausz, *Controlling the phase evolution of few-cycle light pulses*, Phys. Rev. Lett. **85**, 740–743 (2000) (cited on page 32).

[292] D. Jones, S. Diddams, . . ., S. Cundiff, *Carrier-envelope phase control of femtosecond mode-locked lasers and direct optical frequency synthesis*, Science **288**, 635–40 (2000) (cited on page 32).

[293] R. Holzwarth, T. Udem, . . ., P. S. J. Russell, *Optical Frequency Synthesizer for Precision Spectroscopy*, Phys. Rev. Lett. **85**, 2264–2267 (2000) (cited on page 32).

[294] L. Xu, T. W. Hänsch, . . ., F. Krausz, *Route to phase control of ultrashort light pulses*, Opt. Lett. **21**, 2008 (1996) (cited on page 32).

[295] T. Fuji, A. Apolonski, and F. Krausz, *Self-stabilization of carrier-envelope offset phase by use of difference-frequency generation*, Opt. Lett. **29**, 632–634 (2004) (cited on pages 32, 33).

[296] T. Fuji, J. Rauschenberger, . . ., F. Krausz, *Monolithic carrier-envelope phase-stabilization scheme*, Opt. Lett. **30**, 332 (2005) (cited on pages 32, 33).

[297] T. Fuji, J. Rauschenberger, . . ., F. Krausz, *Attosecond control of optical waveforms*, New J. Phys. **7**, 116–116 (2005) (cited on pages 32, 33).

[298] S. Koke, C. Grebing, . . ., G. Steinmeyer, *Direct frequency comb synthesis with arbitrary offset and shot-noise-limited phase noise*, Nat. Photonics **4**, 462–465 (2010) (cited on page 33).

[299] F. Lücking, A. Assion, . . ., G. Steinmeyer, *Long-term carrier-envelope-phase-stable few-cycle pulses by use of the feed-forward method*, Opt. Lett. **37**, 2076 (2012) (cited on page 33).

[300] B. Borchers, F. Lücking, and G. Steinmeyer, *Acoustic frequency combs for carrier-envelope phase stabilization.* Opt. Lett. **39**, 544–7 (2014) (cited on page 33).

[301] B. Borchers, S. Koke, . . ., G. Steinmeyer, *Carrier-envelope phase stabilization with sub-10 as residual timing jitter.* Opt. Lett. **36**, 4146–8 (2011) (cited on page 33).

[302] G. Cerullo, A. Baltuška, . . ., C. Vozzi, *Few-optical-cycle light pulses with passive carrier-envelope phase stabilization*, Laser \& Photonics Rev. **5**, 323–351 (2011) (cited on pages 33, 36).

[303] H. Geiseler, N. Ishii, . . ., J. Itatani, *Long-term passive stabilization of the carrier-envelope phase of an intense infrared few-cycle pulse source*, Appl. Phys. B Lasers Opt. **117**, 941–946 (2014) (cited on page 33).

[304] R. Dörner, V. Mergel, . . ., H. Schmidt-Böcking, *Cold Target Recoil Ion Momentum Spectroscopy: a 'momentum microscope' to view atomic collision dynamics*, Phys. Rep. **330**, 95–192 (2000) (cited on pages 34, 55).

[305] J. Ullrich, R. Moshammer, . . ., H. Schmidt-B cking, *Recoil-ion and electron momentum spectroscopy: reaction-microscopes*, Reports Prog. Phys. **66**, 1463–1545 (2003) (cited on page 34).

[306] J. Mikosch and S. Patchkovskii, *Coincidence and covariance data acquisition in photoelectron and -ion spectroscopy. I. Formal theory*, J. Mod. Opt. **60**, 1426–1438 (2013) (cited on pages 34, 57).

[307] J. Mikosch and S. Patchkovskii, *Coincidence and covariance data acquisition in photoelectron and -ion spectroscopy. II. Analysis and applications*, J. Mod. Opt. **60**, 1439–1451 (2013) (cited on pages 34, 57).

[308] N. Johnson, O. Herrwerth, . . ., G. Paulus, *Single-shot carrier-envelope-phase-tagged ion-momentum imaging of nonsequential double ionization of argon in intense 4-fs laser fields*, Phys. Rev. A **83**, 013412 (2011) (cited on pages 34, 58).

[309] F. Ehlotzky, *Atomic phenomena in bichromatic laser fields*, Phys. Rep. **345**, 175–264 (2001) (cited on page 35).

[310] I. Babushkin, C. Brée, . . ., A. Husakou, *Terahertz and higher-order Brunel harmonics: from tunnel to multiphoton ionization regime in tailored fields*, J. Mod. Opt. **64**, 1078–1087 (2017) (cited on page 36).

[311] Wikipedia, *Commensurability*, (2018) https://en.wikipedia.org/wiki/Commensurability_(mathematics) (visited on 02/10/2018) (cited on page 36).

[312] E. J. Takahashi, P. Lan, . . ., K. Midorikawa, *Attosecond nonlinear optics using gigawatt-scale isolated attosecond pulses*, Nat. Commun. **4**, 2691 (2013) (cited on pages 37, 44, 46).

[313] E. J. Takahashi, P. Lan, . . ., K. Midorikawa, *Infrared Two-Color Multicycle Laser Field Synthesis for Generating an Intense Attosecond Pulse*, Phys. Rev. Lett. **104**, 233901 (2010) (cited on pages 37, 44–46).

[314] S. Haessler, T. Balčiūnas, . . ., A. Baltuška, *Enhanced multi-colour gating for the generation of high-power isolated attosecond pulses*, Sci. Rep. **5**, 10084 (2015) (cited on pages 37, 38, 45, 46).

[315] T. Balciunas, A. J. Verhoef, . . ., A. Baltuska, *Optical and THz signatures of sub-cycle tunneling dynamics*, Chem. Phys. **414**, 92–99 (2013) (cited on pages 37, 50, 51).

[316] T. Balčiūnas, D. Lorenc, . . ., S. Haessler, *CEP-stable tunable THz-emission originating from laser-waveform-controlled sub-cycle plasma-electron bursts*, Opt. Express **23**, 15278 (2015) (cited on pages 37, 49–51, 53).

[317] C. Manzoni, O. D. Mücke, . . ., F. X. Kärtner, *Coherent pulse synthesis: towards sub-cycle optical waveforms*, Laser Photon. Rev. **9**, 129–171 (2015) (cited on pages 37, 46).

[318] L. Chipperfield, J. Robinson, . . ., J. Marangos, *Ideal Waveform to Generate the Maximum Possible Electron Recollision Energy for Any Given Oscillation Period*, Phys. Rev. Lett. **102**, 063003 (2009) (cited on pages 37, 46).

[319] C. Manzoni, S.-W. Huang, . . ., G. Cerullo, *Coherent synthesis of ultra-broadband optical parametric amplifiers*, Opt. Lett. **37**, 1880 (2012) (cited on page 37).

[320] E. Goulielmakis and F. Krausz, *Making optical waves, tracing electrons in real-time: The onset of the attosecond realm*, Prog. Electromagn. Res. **147**, 127–140 (2014) (cited on pages 37, 46).

[321] I. Kim, C. Kim, . . ., C. Nam, *Highly Efficient High-Harmonic Generation in an Orthogonally Polarized Two-Color Laser Field*, Phys. Rev. Lett. **94**, 243901 (2005) (cited on pages 38, 47).

[322] C. Ruiz, D. J. Hoffmann, . . ., J. P. Marangos, *Control of the polarization of attosecond pulses using a two-color field*, New J. Phys. **11**, 113045 (2009) (cited on pages 38, 48).

[323] D. Shafir, Y. Mairesse, . . ., N. Dudovich, *Atomic wavefunctions probed through strong-field light–matter interaction*, Nat. Phys. **5**, 412–416 (2009) (cited on pages 38, 100, 101).

[324] H. Niikura, N. Dudovich, . . ., P. Corkum, *Mapping Molecular Orbital Symmetry on High-Order Harmonic Generation Spectrum Using Two-Color Laser Fields*, Phys. Rev. Lett. **105**, 053003 (2010) (cited on pages 38, 101).

[325] D. Shafir, Y. Mairesse, . . ., N. Dudovich, *Probing the symmetry of atomic wavefunctions from the point of view of strong field-driven electrons*, New J. Phys. **12**, 073032 (2010) (cited on pages 38, 101).

[326] R. Murray and M. Ivanov, *Two-color control of laser induced electron diffraction*, J. Mod. Opt. **55**, 2513–2525 (2008) (cited on pages 38, 84).

[327] R. Murray, C. Ruiz, . . ., M. Y. Ivanov, *Control of diffraction of electron wave packets on diatomic molecules using two-colour fields*, J. Phys. B At. Mol. Opt. Phys. **43**, 135601 (2010) (cited on pages 38, 84).

[328] Y. Zhou, C. Huang, . . ., P. Lu, *Correlated electron dynamics in nonsequential double ionization by orthogonal two-color laser pulses*, Opt. Express **19**, 2301 (2011) (cited on pages 38, 71).

[329] M. Richter, M. Kunitski, . . ., R. Dörner, *Streaking Temporal Double-Slit Interference by an Orthogonal Two-Color Laser Field*, Phys. Rev. Lett. **114**, 143001 (2015) (cited on page 38).

[330] Z. Yuan, D. Ye, . . ., L. Fu, *Intensity-dependent two-electron emission dynamics with orthogonally polarized two-color laser fields*, Phys. Rev. A **91**, 063417 (2015) (cited on pages 38, 71).

[331] Q. Song, P. Lu, . . ., J. Wu, *Dissociative double ionization of CO in orthogonal two-color laser fields*, Phys. Rev. A **95**, 013406 (2017) (cited on pages 38, 132).

[332] C. A. Mancuso, K. M. Dorney, . . ., M. M. Murnane, *Controlling Nonsequential Double Ionization in Two-Color Circularly Polarized Femtosecond Laser Fields*, Phys. Rev. Lett. **117**, 133201 (2016) (cited on pages 40, 71).

[333] K. Lin, X. Gong, . . ., J. Wu, *Directional bond breaking by polarization-gated two-color ultrashort laser pulses*, J. Phys. B At. Mol. Opt. Phys. **49**, 025603 (2016) (cited on pages 40, 132, 133).

[334] S. Eckart, M. Richter, . . ., R. Dörner, *Nonsequential Double Ionization by Counterrotating Circularly Polarized Two-Color Laser Fields*, Phys. Rev. Lett. **117**, 133202 (2016) (cited on pages 40, 69, 71).

[335] J. Wu, M. Meckel, . . ., R. Dörner, *Coulomb Asymmetry in Strong Field Multielectron Ionization of Diatomic Molecules*, Phys. Rev. Lett. **108**, 043002 (2012) (cited on pages 40, 71).

[336] J. Wu, A. Vredenborg, . . ., R. Dörner, *Comparison of dissociative ionization of H2, N2, Ar2, and CO by elliptically polarized two-color pulses*, Phys. Rev. A **87**, 023406 (2013) (cited on pages 40, 132, 134).

[337] X. Gong, M. Kunitski, . . ., J. Wu, *Simultaneous probing of geometry and electronic orbital of ArCO by Coulomb-explosion imaging and angle-dependent tunneling rates*, Phys. Rev. A **88**, 013422 (2013) (cited on page 40).

[338] O. Kfir, P. Grychtol, . . ., O. Cohen, *Helicity-selective phase-matching and quasi-phase matching of circularly polarized high-order harmonics: towards chiral attosecond pulses*, J. Phys. B At. Mol. Opt. Phys. **49**, 123501 (2016) (cited on pages 40, 41, 48, 49, 71).

[339] A. Fleischer, O. Kfir, . . ., O. Cohen, *Spin angular momentum and tunable polarization in high-harmonic generation*, Nat. Photonics **8**, 543–549 (2014) (cited on pages 41, 48, 54).

[340] O. Kfir, P. Grychtol, . . ., O. Cohen, *Generation of bright phase-matched circularly-polarized extreme ultraviolet high harmonics*, Nat. Photonics **9**, 99–105 (2014) (cited on pages 41, 48).

[341] T. Fan, P. Grychtol, . . ., H. C. Kapteyn, *Bright circularly polarized soft X-ray high harmonics for X-ray magnetic circular dichroism*, Proc. Natl. Acad. Sci. **112**, 14206–14211 (2015) (cited on pages 41, 48, 49).

[342] D. B. Milošević and W. Becker, *Attosecond pulse trains with unusual nonlinear polarization*, Phys. Rev. A **62**, 011403 (2000) (cited on pages 41, 48).

[343] K.-J. Yuan and A. D. Bandrauk, *High-order elliptically polarized harmonic generation in extended molecules with ultrashort intense bichromatic circularly polarized laser pulses*, Phys. Rev. A **81**, 063412 (2010) (cited on pages 41, 48).

[344] K.-J. Yuan and A. D. Bandrauk, *Circularly polarized attosecond pulses from molecular high-order harmonic generation by ultrashort intense bichromatic circularly and linearly polarized laser pulses*, J. Phys. B At. Mol. Opt. Phys. **45**, 074001 (2012) (cited on pages 41, 48).

[345] D. B. Milošević, *Generation of elliptically polarized attosecond pulse trains*, Opt. Lett. **40**, 2381 (2015) (cited on pages 41, 48).

[346] L. Medišauskas, J. Wragg, . . ., M. Y. Ivanov, *Generating Isolated Elliptically Polarized Attosecond Pulses Using Bichromatic Counterrotating Circularly Polarized Laser Fields*, Phys. Rev. Lett. **115**, 153001 (2015) (cited on pages 41, 48).

[347] F. Mauger, A. D. Bandrauk, and T. Uzer, *Circularly polarized molecular high harmonic generation using a bicircular laser*, J. Phys. B At. Mol. Opt. Phys. **49**, 10LT01 (2016) (cited on pages 41, 48, 49).

[348] X. Xie, A. Scrinzi, . . ., M. Kitzler, *Internal Momentum State Mapping Using High Harmonic Radiation*, Phys. Rev. Lett. 101, 033901 (2008) (cited on pages 41, 48–50).

[349] M. Schultze, A. Wirth, . . ., F. Krausz, *State-of-the-art attosecond metrology*, J. Electron Spectros. Relat. Phenomena **184**, 68–77 (2011) (cited on page 43).

[350] F. Frank, C. Arrell, . . ., J. W. G. Tisch, *Invited Review Article: Technology for Attosecond Science*, Rev. Sci. Instrum. **83**, 071101 (2012) (cited on page 43).

[351] G. Cerullo, S. De Silvestri, and M. Nisoli, *Light at the extremes: From femto- to atto-science for real-time studies of atomic and electronic motions*, EPL (Europhys. Lett.) **112**, 24001 (2015) (cited on page 43).

[352] F. Lépine, G. Sansone, and M. J. Vrakking, *Molecular applications of attosecond laser pulses*, Chem. Phys. Lett. **578**, 1–14 (2013) (cited on pages 43, 122).

[353] M. Drescher, M. Hentschel, . . ., F. Krausz, *X-ray pulses approaching the attosecond frontier.* Science **291**, 1923–7 (2001) (cited on page 44).

[354] R. Kienberger, E. Goulielmakis, . . ., F. Krausz, *Atomic transient recorder.* Nature **427**, 817 (2004) (cited on pages 44, 96).

[355] R. Kienberger, M. Hentschel, . . ., F. Krausz, *Steering attosecond electron wave packets with light.* Science 297, 1144–8 (2002) (cited on pages 44, 96).

[356] P. B. Corkum, N. H. Burnett, and M. Y. Ivanov, *Subfemtosecond pulses*, Opt. Lett. **19**, 1870 (1994) (cited on page 44).

[357] G. Sansone, E. Benedetti, . . ., M. Nisoli, *Isolated single-cycle attosecond pulses.* Science **314**, 443–6 (2006) (cited on page 44).

[358] I. J. Sola, E. Mével, . . ., M. Nisoli, *Controlling attosecond electron dynamics by phase-stabilized polarization gating*, Nat. Phys. **2**, 319–322 (2006) (cited on page 44).

[359] J. Mauritsson, P. Johnsson, . . ., M. Gaarde, *Attosecond Pulse Trains Generated Using Two Color Laser Fields*, Phys. Rev. Lett. **97**, 013001 (2006) (cited on page 44).

[360] S. Gilbertson, Y. Wu, . . ., Z. Chang, *Isolated attosecond pulse generation using multicycle pulses directly from a laser amplifier*, Phys. Rev. A **81**, 043810 (2010) (cited on page 44).

[361] X. Feng, S. Gilbertson, . . ., Z. Chang, *Generation of Isolated Attosecond Pulses with 20 to 28 Femtosecond Lasers*, Phys. Rev. Lett. **103**, 183901 (2009) (cited on page 44).

[362] H. Merdji, T. Auguste, . . ., S. R. Leone, *Isolated attosecond pulses using a detuned second-harmonic field*, Opt. Lett. **32**, 3134 (2007) (cited on page 44).

[363] B. Kim, J. An, . . ., D. E. Kim, *Optimization of multi-cycle two-color laser fields for the generation of an isolated attosecond pulse*, Opt. Express **16**, 10331 (2008) (cited on page 44).

[364] V. Tosa, C. Altucci, . . ., M. D. Lazar, *Single attosecond pulse generation by two laser fields*, IEEE J. Sel. Top. Quantum Electron. **102**, 102–105 (2012) (cited on page 44).

[365] J. Mestayer, W. Zhao, . . ., J. Burgdörfer, *Transporting Rydberg Electron Wave Packets with Chirped Trains of Pulses*, Phys. Rev. Lett. **99**, 183003 (2007) (cited on page 46).

[366] M. T. Hassan, T. T. Luu, . . ., E. Goulielmakis, *Optical attosecond pulses and tracking the nonlinear response of bound electrons*, Nature **530**, 66–70 (2016) (cited on page 47).

[367] C. Kim, I. Kim, and C. Nam, *Generation of a strong attosecond pulse train with an orthogonally polarized two-color laser field*, Phys. Rev. A **72**, 33817 (2005) (cited on page 47).

[368] C.-Z. Xu, Y. Liu, . . ., T.-C. Chiang, *Photoemission Circular Dichroism and Spin Polarization of the Topological Surface States in Ultrathin Bi2Te3 Films*, Phys. Rev. Lett. **115**, 016801 (2015) (cited on page 47).

[369] C. Boeglin, E. Beaurepaire, . . ., J.-Y. Bigot, *Distinguishing the ultrafast dynamics of spin and orbital moments in solids.* Nature **465**, 458–61 (2010) (cited on page 47).

[370] K. L. Reid, *Photoelectron angular distributions: developments in applications to isolated molecular systems*, Mol. Phys. **110**, 131–147 (2012) (cited on page 47).

[371] C. Chen, Z. Tao, . . ., M. Murnane, *Tomographic reconstruction of circularly polarized high-harmonic fields: 3D attosecond metrology.* Sci. Adv. **2**, e1501333 (2016) (cited on page 48).

[372] D. D. Hickstein, F. J. Dollar, . . ., C. G. Durfee, *Non-collinear generation of angularly isolated circularly polarized high harmonics*, Nat. Photonics **9**, 743–750 (2015) (cited on pages 48, 49).

[373] G. Lambert, B. Vodungbo, . . ., M. Fajardo, *Towards enabling femtosecond helicity-dependent spectroscopy with high-harmonic sources*, Nat. Commun. **6**, 6167 (2015) (cited on page 48).

[374] A. Ferré, C. Handschin, . . ., Y. Mairesse, *A table-top ultrashort light source in the extreme ultraviolet for circular dichroism experiments*, Nat. Photonics **9**, 93–98 (2014) (cited on page 48).

[375] X. Zhou, R. Lock, . . ., M. Murnane, *Elliptically Polarized High-Order Harmonic Emission from Molecules in Linearly Polarized Laser Fields*, Phys. Rev. Lett. **102**, 073902 (2009) (cited on pages 48, 54, 97).

[376] C. Hernández-García, C. G. Durfee, . . ., A. Becker, *Schemes for generation of isolated attosecond pulses of pure circular polarization*, Phys. Rev. A **93**, 043855 (2016) (cited on page 48).

[377] K.-J. Yuan and A. D. Bandrauk, *Single Circularly Polarized Attosecond Pulse Generation by Intense Few Cycle Elliptically Polarized Laser Pulses and Terahertz Fields from Molecular Media*, Phys. Rev. Lett. **110**, 023003 (2013) (cited on page 48).

[378] K.-J. Yuan and A. D. Bandrauk, *Generation of circularly polarized attosecond pulses by intense ultrashort laser pulses from extended asymmetric molecular ions*, Phys. Rev. A **84**, 023410 (2011) (cited on page 48).

[379] S. Long, W. Becker, and J. K. McIver, *Model calculations of polarization-dependent two-color high-harmonic generation*, Phys. Rev. A **52**, 2262–2278 (1995) (cited on page 48).

[380] I. Barth and J. Manz, *Electric ring currents in atomic orbitals and magnetic fields induced by short intense circularly polarized π laser pulses*, Phys. Rev. A **75**, 012510 (2007) (cited on page 49).

[381] M. Tonouchi, *Cutting-edge terahertz technology*, Nat. Photonics **1**, 97–105 (2007) (cited on page 50).

[382] X. Yang, X. Zhao, . . ., Y. Luo, *Biomedical Applications of Terahertz Spectroscopy and Imaging*, Trends Biotechnol. **34**, 810–824 (2016) (cited on page 50).

[383] A. Y. Pawar, D. D. Sonawane, . . ., D. V. Derle, *Terahertz technology and its applications*, Drug Invent. Today **5**, 157–163 (2013) (cited on page 50).

[384] D. Saeedkia, *Handbook of terahertz technology for imaging, sensing and communications* (Woodhead Publishing Limited, 2013) (cited on page 50).

[385] D. J. Cook and R. M. Hochstrasser, *Intense terahertz pulses by four-wave rectification in air*, Opt. Lett. **25**, 1210 (2000) (cited on page 50).

[386] K.-Y. Kim, J. H. Glownia, . . ., G. Rodriguez, *Terahertz emission from ultrafast ionizing air in symmetry-broken laser fields.* Opt. Express **15**, 4577–4584 (2007) (cited on page 50).

[387] K. Y. Kim, A. J. Taylor, . . ., G. Rodriguez, *Coherent control of terahertz supercontinuum generation in ultrafast laser–gas interactions*, Nat. Photonics **2**, 605–609 (2008) (cited on page 50).

[388] A. Houard, Y. Liu, . . ., A. Mysyrowicz, *Polarization analysis of terahertz radiation generated by four-wave mixing in air*, Opt. Lett. **33**, 1195 (2008) (cited on page 50).

[389] N. Karpowicz and X.-C. Zhang, *Coherent Terahertz Echo of Tunnel Ionization in Gases*, Phys. Rev. Lett. **102**, 093001 (2009) (cited on page 50).

[390] M. Kress, T. Löffler, . . ., H. G. Roskos, *Terahertz-pulse generation by photoionization of air with laser pulses composed of both fundamental and second-harmonic waves*, Opt. Lett. **29**, 1120 (2004) (cited on page 50).

[391] I. Babushkin, S. Skupin, . . ., J. Herrmann, *Tailoring terahertz radiation by controlling tunnel photoionization events in gases*, New J. Phys. **13**, 123029 (2011) (cited on page 50).

[392] I. Babushkin, W. Kuehn, . . ., T. Elsaesser, *Ultrafast Spatiotemporal Dynamics of Terahertz Generation by Ionizing Two-Color Femtosecond Pulses in Gases*, Phys. Rev. Lett. **105**, 053903 (2010) (cited on page 50).

[393] M. Kreß, T. Löffler, . . ., H. G. Roskos, *Determination of the carrier-envelope phase of few-cycle laser pulses with terahertz-emission spectroscopy*, Nat. Phys. **2**, 327–331 (2006) (cited on page 50).

[394] F. Brunel, *Harmonic generation due to plasma effects in a gas undergoing multiphoton ionization in the high-intensity limit*, J. Opt. Soc. Am. B **7**, 521 (1990) (cited on page 50).

[395] E. Cabrera-Granado, Y. Chen, . . ., S. Skupin, *Spectral self-action of THz emission from ionizing two-color laser pulses in gases*, New J. Phys. **17**, 023060 (2015) (cited on page 51).

[396] J. Levesque, Y. Mairesse, . . ., D. Villeneuve, *Polarization State of High-Order Harmonic Emission from Aligned Molecules*, Phys. Rev. Lett. **99**, 243001 (2007) (cited on pages 54, 95, 97).

[397] T. Harada and T. Kita, *Mechanically ruled aberration-corrected concave gratings*, Appl. Opt. **19**, 3987 (1980) (cited on page 54).

[398] N. Nakano, H. Kuroda, . . ., T. Harada, *Development of a flat-field grazing-incidence XUV spectrometer and its application in picosecond XUV spectroscopy*, Appl. Opt. **23**, 2386 (1984) (cited on page 54).

[399] N. Dudovich, J. Tate, . . ., M. Gaarde, *Subcycle spatial mapping of recollision dynamics*, Phys. Rev. A **80,** 011806 (2009) (cited on page 54).

[400] U. Bergmann, M. Ivanovic, . . ., S. Cramer, “High-resolution x-ray imaging using Rowland-circle Bragg optics”, in 2001 IEEE NUCL. SCI. SYMP. CONF. REC. Vol. 3 (2001), pp. 1481–1483 (cited on page 54).

[401] J. Ullrich, R. Moshammer, . . ., L. Spielberger, *Recoil-ion momentum spectroscopy*, J. Phys. B At. Mol. Opt. Phys. **30,** 2917–2974 (1997) (cited on pages 55, 72).

[402] V. de Jesus, A. Rudenko, . . ., J. Ullrich, *Reaction microscopes applied to study atomic and molecular fragmentation in intense laser fields: non-sequential double ionization of helium*, J. Electron Spectros. Relat. Phenomena **141,** 127–142 (2004) (cited on page 55).

[403] S. Roither, “Investigation of Strong Laser Field-Induced Fragmentation Dynamics of Hydrocarbon Molecules using Coincidence Momentum Imaging”, Dissertation (Technische Universität Wien, 2011) (cited on pages 55, 57).

[404] A. E. Boguslavskiy, J. Mikosch, . . ., A. Stolow, *The multielectron ionization dynamics underlying attosecond strong-field spectroscopies.* Science **335,** 1336–40 (2012) (cited on pages 57, 72, 110, 111, 115).

[405] K. Hosaka, A. Yokoyama, . . ., R. Itakura, *Correlation between a photoelectron and a fragment ion in dissociative ionization of ethanol in intense near-infrared laser fields.* J. Chem. Phys. **138,** 204301 (2013) (cited on pages 57, 115).

[406] M. Koch, P. Heim, . . ., W. E. Ernst, *Direct observation of a photochemical activation energy: a case study of acetone photodissociation*, J. Phys. B At. Mol. Opt. Phys. 50, 125102 (2017) (cited on pages 57, 119, 120).

[407] A. Rudenko, V. de Jesus, . . ., J. Ullrich, *Correlated Two-Electron Momentum Spectra for Strong-Field Nonsequential Double Ionization of He at 800 nm*, Phys. Rev. Lett. **99,** 263003 (2007) (cited on page 59).

[408] B. Baguenard, J. B. Wills, . . ., C. Bordas, *Velocity-map imaging electron spectrometer with time resolution*, Rev. Sci. Instrum. **75,** 324–328 (2004) (cited on page 61).

[409] F. Süßmann, S. Zherebtsov, . . ., M. F. Kling, *Single-shot velocity-map imaging of attosecond light-field control at kilohertz rate*, Rev. Sci. Instrum. **82,** 093109 (2011) (cited on page 61).

[410] M. J. J. Vrakking, *An iterative procedure for the inversion of two-dimensional ion/photoelectron imaging experiments*, Rev. Sci. Instrum. **72,** 4084 (2001) (cited on page 61).

[411] A. Takahashi, M. Nishizawa, . . ., K. Kinoshita, “New femtosecond streak camera with temporal resolution of 180 fs”, in PROC. SPIE 2116, GENER., AMPL., MEAS. OF ULTRASH. LASER PULSES, edited by R. P. Trebino and I. A. Walmsley (05/1994), pp. 275–284 (cited on page 64).

[412] M. Kitzler, N. Milosevic, . . ., T. Brabec, *Quantum Theory of Attosecond XUV Pulse Measurement by Laser Dressed Photoionization*, Phys. Rev. Lett. 88, 88–91 (2002) (cited on pages 64, 96).

[413] J. Itatani, F. Quéré, . . ., P. Corkum, *Attosecond streak camera*, Phys. Rev. Lett. **88,** 173903 (2002) (cited on page 64).

[414] O. Smirnova, Y. Mairesse, . . ., M. Y. Ivanov, *High harmonic interferometry of multi-electron dynamics in molecules*, Nature **460,** 972–7 (2009) (cited on pages 64, 72, 80, 94–96).

[415] S. Haessler, J. Caillat, . . ., P. Salières, *Attosecond imaging of molecular electronic wavepackets*, Nat. Phys. **6,** 200–206 (2010) (cited on pages 64, 72, 80, 89, 90, 92, 94, 95, 98).

[416] H. Niikura, F. Légaré, . . ., P. B. Corkum, *Sub-laser-cycle electron pulses for probing molecular dynamics.* Nature **417,** 917–22 (2002) (cited on pages 64, 80, 123, 126).

[417] J. P. Marangos, S. Baker, . . ., R. Torres, *Dynamic imaging of molecules using high order harmonic generation.* Phys. Chem. Chem. Phys. **10,** 35–48 (2008) (cited on pages 64, 87).

[418] H. Niikura, F. Légaré, . . ., P. B. Corkum, *Probing molecular dynamics with attosecond resolution using correlated wave packet pairs.* Nature **421,** 826 (2003) (cited on pages 64, 123, 126).

[419] C. Maharjan, A. Alnaser, . . ., C. Cocke, *Momentum imaging of doubly charged ions of Ne and Ar in the sequential ionization region*, Phys. Rev. A **72,** 041403 (2005) (cited on pages 65–68).

[420] P. Eckle, A. N. Pfeiffer, . . ., U. Keller, *Attosecond ionization and tunneling delay time measurements in helium.* Science **322,** 1525–9 (2008) (cited on page 66).

[421] P. Eckle, M. Smolarski, . . ., U. Keller, *Attosecond angular streaking*, Nat. Phys. **4,** 565–570 (2008) (cited on page 66).

[422] A. N. Pfeiffer, C. Cirelli, . . ., U. Keller, *Attoclock reveals natural coordinates of the laser-induced tunnelling current flow in atoms*, Nat. Phys. **8,** 76–80 (2011) (cited on page 66).

[423] A. N. Pfeiffer, C. Cirelli, . . ., U. Keller, *Probing the Longitudinal Momentum Spread of the Electron Wave Packet at the Tunnel Exit*, Phys. Rev. Lett. **109**, 083002 (2012) (cited on page 66).

[424] A. N. Pfeiffer, C. Cirelli, . . ., U. Keller, *Recent attoclock measurements of strong field ionization*, Chem. Phys. **414**, 84–91 (2013) (cited on page 66).

[425] A. N. Pfeiffer, C. Cirelli, . . ., U. Keller, *Breakdown of the independent electron approximation in sequential double ionization*, New J. Phys. **13**, 093008 (2011) (cited on pages 66, 67).

[426] A. N. Pfeiffer, C. Cirelli, . . ., U. Keller, *Timing the release in sequential double ionization*, Nat. Phys. **7**, 428–433 (2011) (cited on pages 66, 67).

[427] P. Wustelt, M. Möller, . . ., G. G. Paulus, *Momentum-resolved study of the saturation intensity in multiple ionization*, Phys. Rev. A **91**, 031401 (2015) (cited on page 66).

[428] J. Wu, L. Schmidt, . . ., R. Dörner, *Multiorbital Tunneling Ionization of the CO Molecule*, Phys. Rev. Lett. **108**, 183001 (2012) (cited on pages 66, 67).

[429] J. Wu, M. Meckel, . . ., R. Dörner, *Probing the tunnelling site of electrons in strong field enhanced ionization of molecules*, Nat. Commun. **3**, 1113 (2012) (cited on pages 66, 67).

[430] J. Wu, M. Magrakvelidze, . . ., R. Dörner, *Understanding the role of phase in chemical bond breaking with coincidence angular streaking.* Nat. Commun. **4**, 2177 (2013) (cited on pages 66, 67).

[431] X. Gong, Q. Song, . . ., H. Zeng, *Strong-Field Dissociative Double Ionization of Acetylene*, Phys. Rev. Lett. **112**, 243001 (2014) (cited on pages 66, 67).

[432] X. Gong, M. Kunitski, . . ., J. Wu, *Multielectron effects in strong-field dissociative ionization of molecules*, Phys. Rev. A **89**, 043429 (2014) (cited on pages 66, 67).

[433] T. Ai-Hong, F. Guo-Qiang, and L. Dan, *Electron dynamics of molecular double ionization by elliptically polarized few-cycle laser pulses*, Opt. Commun. **338**, 484–491 (2015) (cited on page 66).

[434] J. Wu and R. Dörner, "Angular Streaking for Strong Field Ionization of Molecules—Attosecond Physics Without Attosecond Pulses", in *Ultrafast dyn. driven by intense light pulses from atoms to solids, from lasers to intense x-rays*, edited by M. Kitzler and S. Grafe (Springer Series on Atomic, Optical, and Plasma Physics, 2016), pp. 49–61 (cited on pages 66, 67).

[435] A. S. Landsman, M. Weger, . . ., U. Keller, *Ultrafast resolution of tunneling delay time*, Optica **1**, 343 (2014) (cited on pages 66, 67).

[436] A. S. Landsman and U. Keller, *Attosecond science and the tunnelling time problem*, Phys. Rep. **547**, 1–24 (2015) (cited on pages 66, 67).

[437] M. Klaiber, K. Z. Hatsagortsyan, and C. H. Keitel, *Tunneling Dynamics in Multiphoton Ionization and Attoclock Calibration*, Phys. Rev. Lett. **114**, 083001 (2015) (cited on page 67).

[438] L. Torlina, F. Morales, . . ., O. Smirnova, *Interpreting attoclock measurements of tunnelling times*, Nat. Phys. **11**, 503–508 (2015) (cited on page 67).

[439] N. Camus, E. Yakaboylu, . . ., R. Moshammer, *Experimental Evidence for Quantum Tunneling Time*, Phys. Rev. Lett. **119**, 023201 (2017) (cited on page 67).

[440] C. R. McDonald, G. Orlando, . . ., T. Brabec, *Tunnel Ionization Dynamics of Bound Systems in Laser Fields: How Long Does It Take for a Bound Electron to Tunnel?*, Phys. Rev. Lett. **111**, 090405 (2013) (cited on page 67).

[441] M. F. Kling, C. Siedschlag, . . ., M. J. J. Vrakking, *Control of electron localization in molecular dissociation.* Science **312**, 246–8 (2006) (cited on pages 67, 109, 123–125).

[442] D. Ray, F. He, . . ., C. Cocke, *Ion-Energy Dependence of Asymmetric Dissociation of D2 by a Two-Color Laser Field*, Phys. Rev. Lett. **103**, 223201 (2009) (cited on pages 67, 130, 131).

[443] M. Kremer, B. Fischer, . . ., J. Ullrich, *Electron Localization in Molecular Fragmentation of H2 by Carrier-Envelope Phase Stabilized Laser Pulses*, Phys. Rev. Lett. **103**, 213003 (2009) (cited on pages 67, 111, 123, 124).

[444] B. Fischer, M. Kremer, . . ., J. Ullrich, *Steering the Electron in H2+ by Nuclear Wave Packet Dynamics*, Phys. Rev. Lett. **105**, 223001 (2010) (cited on pages 67, 111, 123, 124).

[445] N. G. Kling, K. J. Betsch, . . ., I. Ben-Itzhak, *Carrier-Envelope Phase Control over Pathway Interference in Strong-Field Dissociation of H2+*, Phys. Rev. Lett. **111**, 163004 (2013) (cited on pages 67, 123).

[446] M. F. Kling, P. von den Hoff, . . ., R. de Vivie-Riedle, *(Sub-)femtosecond control of molecular reactions via tailoring the electric field of light.* Phys. Chem. Chem. Phys. **15**, 9448–67 (2013) (cited on pages 67, 109, 116, 122, 124, 126).

[447] P. Lan, Y. Zhou, . . ., K. Midorikawa, *Revealing the role of electron correlation in sequential double ionization*, Phys. Rev. A **89**, 033424 (2014) (cited on page 67).

[448] A. Tong, Y. Zhou, and P. Lu, *Resolving subcycle electron emission in strong-field sequential double ionization*, Opt. Express **23**, 15774 (2015) (cited on pages 67, 68).

[449] S. Skruszewicz, J. Tiggesbäumker, . . ., D. Bauer, *Two-Color Strong-Field Photoelectron Spectroscopy and the Phase of the Phase*, Phys. Rev. Lett. **115**, 043001 (2015) (cited on pages 69, 70).

[450] S. Yu, Y. Wang, . . ., X. Liu, *Coulomb effect on photoelectron momentum distributions in orthogonal two-color laser fields*, Phys. Rev. A **94**, 033418 (2016) (cited on page 71).

[451] M. Richter, M. Kunitski, . . ., R. Dörner, *Ionization in orthogonal two-color laser fields: Origin and phase dependences of trajectory-resolved Coulomb effects*, Phys. Rev. A **94**, 033416 (2016) (cited on pages 71, 77).

[452] D. Shafir, H. Soifer, . . ., N. Dudovich, *Resolving the time when an electron exits a tunnelling barrier*, Nature **485**, 343–346 (2012) (cited on pages 71, 106, 108).

[453] O. Pedatzur, G. Orenstein, . . ., N. Dudovich, *Attosecond tunnelling interferometry*, Nat. Phys. **11**, 815–819 (2015) (cited on pages 71, 106).

[454] J. Henkel and M. Lein, *Analysis of electron trajectories with two-color strong-field ionization*, Phys. Rev. A **92**, 013422 (2015) (cited on page 71).

[455] J. L. Chaloupka and D. D. Hickstein, *Dynamics of Strong-Field Double Ionization in Two-Color Counterrotating Fields*, Phys. Rev. Lett. **116**, 143005 (2016) (cited on page 71).

[456] E. Hasović, W. Becker, and D. B. Milošević, *Electron rescattering in a bicircular laser field*, Opt. Express **24**, 6413 (2016) (cited on page 71).

[457] I. Barth and O. Smirnova, *Spin-polarized electrons produced by strong-field ionization*, Phys. Rev. A **88**, 013401 (2013) (cited on page 71).

[458] A. Hartung, F. Morales, . . ., R. Dörner, *Electron spin polarization in strong-field ionization of xenon atoms*, Nat. Photonics **10**, 526–528 (2016) (cited on page 71).

[459] Y. Hasegawa, R. Loidl, . . ., H. Rauch, *Violation of a Bell-like inequality in single-neutron interferometry*, Nature **425**, 45–48 (2003) (cited on page 72).

[460] J. Itatani, J. Levesque, . . ., D. M. Villeneuve, *Tomographic imaging of molecular orbitals.* Nature **432**, 867–71 (2004) (cited on pages 72, 90, 92).

[461] Y. Mairesse, J. Higuet, . . ., O. Smirnova, *High Harmonic Spectroscopy of Multichannel Dynamics in Strong-Field Ionization*, Phys. Rev. Lett. **104**, 213601 (2010) (cited on pages 72, 94, 95, 97, 110, 116).

[462] R. Dörner, V. Mergel, . . ., H. Schmidt-Böcking, *Kinematically complete experiments using cold target recoil ion momentum spectroscopy*, Nucl. Instruments Methods Phys. Res. Sect. B Beam Interact. with Mater. Atoms **124**, 225–231 (1997) (cited on page 72).

[463] T. Weinacht, J. Ahn, and P. Bucksbaum, *Measurement of the Amplitude and Phase of a Sculpted Rydberg Wave Packet*, Phys. Rev. Lett. **80**, 5508–5511 (1998) (cited on page 72).

[464] M. Wollenhaupt, A. Assion, . . ., G. Gerber, *Interferences of Ultrashort Free Electron Wave Packets*, Phys. Rev. Lett. **89**, 173001 (2002) (cited on page 72).

[465] F. Quéré, J. Itatani, . . ., P. Corkum, *Attosecond Spectral Shearing Interferometry*, Phys. Rev. Lett. **90**, 073902 (2003) (cited on page 72).

[466] T. Remetter, P. Johnsson, . . ., A. L'Huillier, *Attosecond electron wave packet interferometry*, Nat. Phys. **2**, 323–326 (2006) (cited on pages 72, 78).

[467] P. Johnsson, J. Mauritsson, . . ., K. J. Schafer, *Attosecond Control of Ionization by Wave-Packet Interference*, Phys. Rev. Lett. **99**, 233001 (2007) (cited on page 72).

[468] J. Mauritsson, T. Remetter, . . ., M. Nisoli, *Attosecond Electron Spectroscopy Using a Novel Interferometric Pump-Probe Technique*, Phys. Rev. Lett. **105**, 053001 (2010) (cited on pages 72, 78).

[469] G. G. Paulus, F. Zacher, . . ., M. Kleber, *Above-Threshold Ionization by an Elliptically Polarized Field: Quantum Tunneling Interferences and Classical Dodging*, Phys. Rev. Lett. **80**, 484–487 (1998) (cited on pages 72, 77).

[470] A. Rudenko, K. Zrost, . . ., J. Ullrich, *Resonant structures in the low-energy electron continuum for single ionization of atoms in the tunnelling regime*, J. Phys. B At. Mol. Opt. Phys. **37**, L407–L413 (2004) (cited on pages 72, 74).

[471] C. M. Maharjan, A. S. Alnaser, . . ., C. L. Cocke, *Wavelength dependence of momentum-space images of low-energy electrons generated by short intense laser pulses at high intensities*, J. Phys. B At. Mol. Opt. Phys. **39**, 1955–1964 (2006) (cited on pages 72, 74).

[472] S. Yurchenko, S. Patchkovskii, . . ., G. Yudin, *Laser-Induced Interference, Focusing, and Diffraction of Rescattering Molecular Photoelectrons*, Phys. Rev. Lett. **93**, 223003 (2004) (cited on pages 73, 80).

[473] M. Busuladžić, A. Gazibegović-Busuladžić, . . ., W. Becker, *Angle-Resolved High-Order Above-Threshold Ionization of a Molecule: Sensitive Tool for Molecular Characterization*, Phys. Rev. Lett. **100**, 203003 (2008) (cited on page 73).

[474] F. Lindner, M. Schätzel, . . ., G. Paulus, *Attosecond Double-Slit Experiment*, Phys. Rev. Lett. **95**, 040401 (2005) (cited on page 73).

[475] D. G. Arbó, K. L. Ishikawa, . . ., J. Burgdörfer, *Doubly differential diffraction at a time grating in above-threshold ionization: Intracycle and intercycle interferences*, Nucl. Instruments Methods Phys. Res. Sect. B Beam Interact. with Mater. Atoms **279**, 24–30 (2012) (cited on page 73).

[476] R. Gopal, K. Simeonidis, . . ., M. Kling, *Three-Dimensional Momentum Imaging of Electron Wave Packet Interference in Few-Cycle Laser Pulses*, Phys. Rev. Lett. **103**, 053001 (2009) (cited on page 73).

[477] D. G. Arbó, S. Nagele, . . ., J. Burgdörfer, *Interference of electron wave packets in atomic ionization by subcycle sculpted laser pulses*, Phys. Rev. A 89, 043414 (2014) (cited on pages 73, 104).

[478] D. G. Arbó, *The effect of the Coulomb potential on subcycle interference of electron wave packets in atomic ionization by two-colour laser pulses*, J. Phys. B At. Mol. Opt. Phys. **47**, 204008 (2014) (cited on page 73).

[479] T. Marchenko, Y. Huismans, . . ., M. J. J. Vrakking, *Criteria for the observation of strong-field photoelectron holography*, Phys. Rev. A **84**, 053427 (2011) (cited on pages 74, 75).

[480] X.-B. Bian, Y. Huismans, . . ., A. D. Bandrauk, *Subcycle interference dynamics of time-resolved photoelectron holography with midinfrared laser pulses*, Phys. Rev. A **84**, 043420 (2011) (cited on pages 74, 75).

[481] D. Hickstein, P. Ranitovic, . . ., H. Kapteyn, *Direct Visualization of Laser-Driven Electron Multiple Scattering and Tunneling Distance in Strong-Field Ionization*, Phys. Rev. Lett. **109**, 073004 (2012) (cited on pages 74, 75).

[482] Y. Huismans, A. Gijsbertsen, . . ., M. J. J. Vrakking, *Scaling Laws for Photoelectron Holography in the Midinfrared Wavelength Regime*, Phys. Rev. Lett. **109**, 013002 (2012) (cited on pages 74, 75).

[483] M. Meckel, A. Staudte, . . ., M. Spanner, *Signatures of the continuum electron phase in molecular strong-field photoelectron holography*, Nat. Phys. **10**, 594–600 (2014) (cited on pages 74, 75, 84, 91).

[484] X. Song, C. Lin, . . ., J. Chen, *Unraveling nonadiabatic ionization and Coulomb potential effect in strong-field photoelectron holography*, Sci. Rep. **6**, 28392 (2016) (cited on pages 74, 75).

[485] Y. Zhou, O. I. Tolstikhin, and T. Morishita, *Near-Forward Rescattering Photoelectron Holography in Strong-Field Ionization: Extraction of the Phase of the Scattering Amplitude*, Phys. Rev. Lett. **116**, 173001 (2016) (cited on pages 74–76, 78).

[486] X.-B. Bian and A. D. Bandrauk, *Attosecond Time-Resolved Imaging of Molecular Structure by Photoelectron Holography*, Phys. Rev. Lett. **108**, 263003 (2012) (cited on pages 74, 75).

[487] M. Haertelt, X.-B. Bian, . . ., P. B. Corkum, *Probing Molecular Dynamics by Laser-Induced Backscattering Holography*, Phys. Rev. Lett. **116**, 133001 (2016) (cited on pages 74, 75).

[488] W. Yang, Z. Sheng, . . ., X. Song, *Molecular photoelectron holography with circularly polarized laser pulses*, Opt. Express **22**, 2519 (2014) (cited on pages 74, 77).

[489] Y. Li, Y. Zhou, . . ., P. Lu, *Identifying backward-rescattering photoelectron hologram with orthogonal two-color laser fields*, Opt. Express **24**, 23697 (2016) (cited on pages 74, 77).

[490] D. Gabor, *A New Microscopic Principle*, Nature **161**, 777–778 (1948) (cited on page 74).

[491] L. J. Zipp, A. Natan, . . ., P. H. Bucksbaum, *Probing electron delays in above-threshold ionization*, Optica **1**, 361 (2014) (cited on page 75).

[492] M. Lein, *Simpolator*, (2017) https://lein.itp.uni-hannover.de/simpolatorframe.html (visited on 04/01/2017) (cited on page 75).

[493] R. Freeman, P. Bucksbaum, . . ., M. Geusic, *Above-threshold ionization with subpicosecond laser pulses*, Phys. Rev. Lett. **59**, 1092–1095 (1987) (cited on page 76).

[494] X. Xie, S. Roither, . . ., M. Kitzler, *Channel-resolved subcycle interferences of electron wave packets emitted from H2 in two-color laser fields*, High Power Laser Sci. Eng. 4, e40 (2016) (cited on page 76).

[495] X. Xie, T. Wang, . . ., M. Kitzler, *Disentangling Intracycle Interferences in Photoelectron Momentum Distributions Using Orthogonal Two-Color Laser Fields*, Phys. Rev. Lett. 119, 243201 (2017) (cited on pages 76, 77).

[496] J.-W. Geng, W.-H. Xiong, . . ., Q. Gong, *Nonadiabatic Electron Dynamics in Orthogonal Two-Color Laser Fields with Comparable Intensities*, Phys. Rev. Lett. **115**, 193001 (2015) (cited on page 77).

[497] X. Xie, *Two-Dimensional Attosecond Electron Wave-Packet Interferometry*, Phys. Rev. Lett. **114**, 173003 (2015) (cited on page 77).

[498] X. Gong, C. Lin, . . ., J. Wu, *Energy-Resolved Ultrashort Delays of Photoelectron Emission Clocked by Orthogonal Two-Color Laser Fields*, Phys. Rev. Lett. **118**, 143203 (2017) (cited on page 77).

[499] K. Klünder, P. Johnsson, . . ., J. Mauritsson, *Reconstruction of attosecond electron wave packets using quantum state holography*, Phys. Rev. A **88**, 033404 (2013) (cited on page 78).

[500] M. Lewenstein, K. Kulander, . . ., P. Bucksbaum, *Rings in above-threshold ionization: A quasiclassical analysis*, Phys. Rev. A **51**, 1495–1507 (1995) (cited on page 79).

[501] W. Li, X. Zhou, . . ., M. M. Murnane, *Time-resolved dynamics in N2O4 probed using high harmonic generation.* Science **322**, 1207–11 (2008) (cited on pages 80, 93, 94).

[502] E. Goulielmakis, Z.-H. Loh, . . ., F. Krausz, *Real-time observation of valence electron motion.* Nature **466**, 739–743 (2010) (cited on page 80).

[503] M. Uiberacker, T. Uphues, . . ., F. Krausz, *Attosecond real-time observation of electron tunnelling in atoms.* Nature **446**, 627–32 (2007) (cited on page 80).

[504] I. Hargittai and M. Hargittai, *Stereochemical Applications of Gas-Phase Electron Diffraction* (Wiley, 1998) (cited on pages 80, 81).

[505] A. H. Zewail, *Four-Dimensional Electron Microscopy*, Science **328**, 187–193 (2010) (cited on page 80).

[506] C. D. Lin, A.-T. Le, . . ., R. Lucchese, *Strong-field rescattering physics—self-imaging of a molecule by its own electrons*, J. Phys. B At. Mol. Opt. Phys. **43**, 122001 (2010) (cited on pages 80, 81, 83).

[507] J. Xu, Z. Chen, . . ., C. D. Lin, *Self-imaging of molecules from diffraction spectra by laser-induced rescattering electrons*, Phys. Rev. A **82**, 033403 (2010) (cited on pages 80, 81, 83).

[508] T. Zuo, A. Bandrauk, and P. Corkum, *Laser-induced electron diffraction: a new tool for probing ultrafast molecular dynamics*, Chem. Phys. Lett. **259**, 313–320 (1996) (cited on page 80).

[509] M. G. Pullen, B. Wolter, . . ., J. Biegert, *Imaging an aligned polyatomic molecule with laser-induced electron diffraction*, Nat. Commun. **6**, 7262 (2015) (cited on pages 81, 83, 84).

[510] B. Wolter, M. G. Pullen, . . ., J. Biegert, *Strong-Field Physics with Mid-IR Fields*, Phys. Rev. X **5**, 021034 (2015) (cited on pages 81, 83).

[511] T. Morishita, A.-T. Le, . . ., C. D. Lin, *Potential for ultrafast dynamic chemical imaging with few-cycle infrared lasers*, New J. Phys. **10**, 025011 (2008) (cited on pages 81, 83).

[512] T. Morishita, A.-T. Le, . . ., C. D. Lin, *Accurate Retrieval of Structural Information from Laser-Induced Photoelectron and High-Order Harmonic Spectra by Few-Cycle Laser Pulses*, Phys. Rev. Lett. **100**, 013903 (2008) (cited on pages 81, 83).

[513] Z. Chen, A.-T. Le, . . ., C. D. Lin, *Origin of species dependence of high-energy plateau photoelectron spectra*, J. Phys. B At. Mol. Opt. Phys. **42**, 061001 (2009) (cited on pages 81, 83).

[514] Z. Chen, A.-T. Le, . . ., C. Lin, *Quantitative rescattering theory for laser-induced high-energy plateau photoelectron spectra*, Phys. Rev. A **79**, 033409 (2009) (cited on pages 81, 83).

[515] D. Ray, B. Ulrich, . . ., C. Cocke, *Large-Angle Electron Diffraction Structure in Laser-Induced Rescattering from Rare Gases*, Phys. Rev. Lett. **100**, 143002 (2008) (cited on page 83).

[516] M. Okunishi, T. Morishita, . . ., K. Ueda, *Experimental Retrieval of Target Structure Information from Laser-Induced Rescattered Photoelectron Momentum Distributions*, Phys. Rev. Lett. **100**, 143001 (2008) (cited on page 83).

[517] M. Okunishi, H. Niikura, . . ., K. Ueda, *Extracting Electron-Ion Differential Scattering Cross Sections for Partially Aligned Molecules by Laser-Induced Rescattering Photoelectron Spectroscopy*, Phys. Rev. Lett. **106**, 063001 (2011) (cited on page 83).

[518] C. Wang, M. Okunishi, . . ., K. Ueda, *Extraction of electron–ion differential scattering cross sections for C 2 H 4 by laser-induced rescattering photoelectron spectroscopy*, J. Phys. B At. Mol. Opt. Phys. **45**, 131001 (2012) (cited on page 83).

[519] J. Xu, C. I. Blaga, . . ., L. F. DiMauro, *Laser-Induced Electron Diffraction for Probing Rare Gas Atoms*, Phys. Rev. Lett. **109**, 233002 (2012) (cited on page 83).

[520] J. Xu, C. I. Blaga, . . ., L. F. DiMauro, *Diffraction using laser-driven broadband electron wave packets*, Nat. Commun. **5**, 1–6 (2014) (cited on page 85).

[521] H. Liu, Y. Li, . . ., D. A. Reis, *High-harmonic generation from an atomically thin semiconductor*, Nat. Phys. **13**, 262–265 (2016) (cited on page 87).

[522] R. Cireasa, A. E. Boguslavskiy, . . ., V. R. Bhardwaj, *Probing molecular chirality on a sub-femtosecond timescale*, Nat. Phys. **11**, 654–658 (2015) (cited on page 87).

[523] H. Vincenti and F. Quéré, *Attosecond Lighthouses: How To Use Spatiotemporally Coupled Light Fields To Generate Isolated Attosecond Pulses*, Phys. Rev. Lett. **108**, 113904 (2012) (cited on page 87).

[524] F. Quéré, H. Vincenti, . . ., R. Lopez-Martens, *Applications of ultrafast wavefront rotation in highly nonlinear optics*, J. Phys. B At. Mol. Opt. Phys. **47**, 124004 (2014) (cited on page 87).

[525] J. A. Wheeler, A. Borot, . . ., F. Quéré, *Attosecond lighthouses from plasma mirrors*, Nat. Photonics **6**, 829–833 (2012) (cited on page 87).

[526] T. J. Hammond, G. G. Brown, . . ., P. B. Corkum, *Attosecond pulses measured from the attosecond lighthouse*, Nat. Photonics **10**, 171–175 (2016) (cited on page 87).

[527] K. T. Kim, C. Zhang, . . ., F. Quéré, *Photonic streaking of attosecond pulse trains*, Nat. Photonics **7**, 651–656 (2013) (cited on page 87).

[528] C. Altucci, R. Velotta, and J. Marangos, *Ultra-fast dynamic imaging: an overview of current techniques, their capabilities and future prospects*, J. Mod. Opt. **57**, 916–952 (2010) (cited on page 87).

[529] J. P. Marangos, *Development of high harmonic generation spectroscopy of organic molecules and biomolecules*, J. Phys. B At. Mol. Opt. Phys. **49**, 132001 (2016) (cited on page 87).

[530] S. Ghimire, G. Ndabashimiye, . . ., D. A. Reis, *Strong-field and attosecond physics in solids*, J. Phys. B At. Mol. Opt. Phys. **47**, 204030 (2014) (cited on page 87).

[531] M. Lein, N. Hay, . . ., P. Knight, *Interference effects in high-order harmonic generation with molecules*, Phys. Rev. A **66**, 023805 (2002) (cited on page 90).

[532] P. Salières, A. Maquet, . . ., R. Taïeb, *Imaging orbitals with attosecond and Ångström resolutions: toward attochemistry?*, Reports Prog. Phys. **75**, 062401 (2012) (cited on page 90).

[533] R. Santra and A. Gordon, *Three-Step Model for High-Harmonic Generation in Many-Electron Systems*, Phys. Rev. Lett. **96**, 1–4 (2006) (cited on page 90).

[534] J. Levesque, D. Zeidler, . . ., D. Villeneuve, *High Harmonic Generation and the Role of Atomic Orbital Wave Functions*, Phys. Rev. Lett. **98**, 183903 (2007) (cited on page 91).

[535] A.-T. Le, T. Morishita, and C. D. Lin, *Extraction of the species-dependent dipole amplitude and phase from high-order harmonic spectra in rare-gas atoms*, Phys. Rev. A **78**, 023814 (2008) (cited on page 91).

[536] G. Jordan and A. Scrinzi, *Core-polarization effects in molecular high harmonic generation*, New J. Phys. **10**, 025035 (2008) (cited on page 91).

[537] W. H. E. Schwarz, *Measuring orbitals: provocation or reality?*, Angew. Chem. Int. Ed. **45**, 1508–17 (2006) (cited on page 91).

[538] B. Friedrich and D. Herschbach, *Alignment and Trapping of Molecules in Intense Laser Fields*, Phys. Rev. Lett. **74**, 4623–4626 (1995) (cited on pages 91, 117).

[539] J. Ortigoso, M. Rodríguez, . . ., B. Friedrich, *Time evolution of pendular states created by the interaction of molecular polarizability with a pulsed nonresonant laser field*, J. Chem. Phys. **110**, 3870 (1999) (cited on pages 91, 110, 117).

[540] F. Rosca-Pruna and M. Vrakking, *Experimental Observation of Revival Structures in Picosecond Laser-Induced Alignment of I2*, Phys. Rev. Lett. **87**, 153902 (2001) (cited on pages 91, 110, 117).

[541] H. Stapelfeldt and T. Seideman, *Colloquium: Aligning molecules with strong laser pulses*, Rev. Mod. Phys. **75**, 543–557 (2003) (cited on pages 91, 110, 117).

[542] V. Kumarappan, S. S. Viftrup, . . ., H. Stapelfeldt, *Aligning molecules with long or short laser pulses*, Phys. Scr. **76**, C63–C68 (2007) (cited on page 91).

[543] C. Vozzi, M. Negro, . . ., S. Stagira, *Generalized molecular orbital tomography*, Nat. Phys. **7**, 822–826 (2011) (cited on page 92).

[544] N. L. Wagner, A. Wuest, . . ., H. C. Kapteyn, *Monitoring molecular dynamics using coherent electrons from high harmonic generation*, Proc. Natl. Acad. Sci. U. S. A. **103**, 13279–13285 (2006) (cited on pages 93, 94).

[545] Y. Mairesse, S. Haessler, . . ., P. Salières, *Polarization-resolved pump–probe spectroscopy with high harmonics*, New J. Phys. **10**, 025028 (2008) (cited on pages 93, 95, 97).

[546] H. J. Wörner, J. B. Bertrand, . . ., D. M. Villeneuve, *Following a chemical reaction using high-harmonic interferometry*, Nature **466**, 604–607 (2010) (cited on pages 93, 94, 96).

[547] H. J. Wörner, J. B. Bertrand, . . ., D. M. Villeneuve, *Conical intersection dynamics in NO2 probed by homodyne high-harmonic spectroscopy.* Science **334**, 208–12 (2011) (cited on pages 93–95).

[548] Y. Mairesse, D. Zeidler, . . ., P. B. Corkum, *High-order harmonic transient grating spectroscopy in a molecular jet*, Phys. Rev. Lett. **100**, 143903 (2008) (cited on pages 93, 96).

[549] O. Smirnova, S. Patchkovskii, . . ., M. Y. Ivanov, *Strong-field control and spectroscopy of attosecond electron-hole dynamics in molecules.* Proc. Natl. Acad. Sci. U. S. A. **106**, 16556–61 (2009) (cited on pages 94, 95).

[550] P. M. Kraus, B. Mignolet, . . ., H. J. Wörner, *Measurement and laser control of attosecond charge migration in ionized iodoacetylene*, Science **350**, 790–795 (2015) (cited on pages 94, 95).

[551] S. Baker, J. Robinson, . . ., J. Marangos, *Dynamic Two-Center Interference in High-Order Harmonic Generation from Molecules with Attosecond Nuclear Motion*, Phys. Rev. Lett. **101**, 053901 (2008) (cited on page 94).

[552] H. Wörner, J. Bertrand, . . ., D. Villeneuve, *High-Harmonic Homodyne Detection of the Ultrafast Dissociation of Br2 Molecules*, Phys. Rev. Lett. **105**, 103002 (2010) (cited on page 94).

[553] A. Ferré, A. E. Boguslavskiy, . . ., Y. Mairesse, *Multi-channel electronic and vibrational dynamics in polyatomic resonant high-order harmonic generation*, Nat. Commun. **6**, 5952 (2015) (cited on pages 94, 95).

[554] X. Zhou, R. Lock, . . ., H. Kapteyn, *Molecular Recollision Interferometry in High Harmonic Generation*, Phys. Rev. Lett. **100**, 073902 (2008) (cited on page 96).

[555] Y. Mairesse and F. Quéré, *Frequency-resolved optical gating for complete reconstruction of attosecond bursts*, Phys. Rev. A **71**, 011401(R) (2005) (cited on page 96).

[556] Y. Mairesse, A. de Bohan, . . ., P. Salières, *Attosecond synchronization of high-harmonic soft x-rays.* Science **302**, 1540–3 (2003) (cited on page 96).

[557] T. Kanai, E. Takahashi, . . ., K. Midorikawa, *Destructive Interference during High Harmonic Generation in Mixed Gases*, Phys. Rev. Lett. **98**, 153904 (2007) (cited on page 96).

[558] O. Smirnova, S. Patchkovskii, . . ., M. Y. Ivanov, *Attosecond Circular Dichroism Spectroscopy of Polyatomic Molecules*, Phys. Rev. Lett. **102**, 063601 (2009) (cited on page 97).

[559] T. Imazono, K. Sano, . . ., M. Koike, *Development and performance test of a soft x-ray polarimeter and ellipsometer for complete polarization analysis*, Rev. Sci. Instrum. **80**, 085109 (2009) (cited on page 97).

[560] X. Xie, G. Jordan, . . ., A. Scrinzi, *Time and momentum distributions of rescattering electrons*, J. Mod. Opt. **54**, 999–1010 (2007) (cited on page 99).

[561] D. Pavičić, K. Lee, . . ., D. Villeneuve, *Direct Measurement of the Angular Dependence of Ionization for N2, O2, and CO2 in Intense Laser Fields*, Phys. Rev. Lett. **98**, 243001 (2007) (cited on pages 99, 110).

[562] H. Niikura, H. Wörner, . . ., P. Corkum, *Probing the Spatial Structure of a Molecular Attosecond Electron Wave Packet Using Shaped Recollision Trajectories*, Phys. Rev. Lett. **107**, 093004 (2011) (cited on page 101).

[563] O. E. Alon, V. Averbukh, and N. Moiseyev, *Selection Rules for the High Harmonic Generation Spectra*, Phys. Rev. Lett. **80**, 3743–3746 (1998) (cited on page 101).

[564] F. Ceccherini, D. Bauer, and F. Cornolti, *Dynamical symmetries and harmonic generation*, J. Phys. B At. Mol. Opt. Phys. **34**, 5017–5029 (2001) (cited on page 101).

[565] N. Dudovich, O. Smirnova, . . ., P. B. Corkum, *Measuring and controlling the birth of attosecond XUV pulses*, Nat. Phys. **2**, 781–786 (2006) (cited on pages 103, 106–108).

[566] K. T. Kim, C. Zhang, . . ., P. B. Corkum, *Petahertz optical oscilloscope*, Nat. Photonics **7**, 958–962 (2013) (cited on page 106).

[567] K. T. Kim, C. Zhang, . . ., P. B. Corkum, *Manipulation of quantum paths for space–time characterization of attosecond pulses*, Nat. Phys. **9**, 159–163 (2013) (cited on pages 106–108).

[568] K. T. Kim, D. M. Villeneuve, and P. B. Corkum, *Manipulating quantum paths for novel attosecond measurement methods*, Nat. Photonics **8**, 187–194 (2014) (cited on pages 106–108).

[569] S. Miura, T. Ando, . . ., M. Nisoli, *Carrier-envelope-phase dependence of asymmetric CD bond breaking in C2D2 in an intense few-cycle laser field*, Chem. Phys. Lett. 595-596, 61–66 (2014) (cited on pages 109, 112, 123, 128).

[570] I. Znakovskaya, P. von den Hoff, . . ., M. F. Kling, *Waveform control of orientation-dependent ionization of DCl in few-cycle laser fields.* Phys. Chem. Chem. Phys. **13**, 8653–8 (2011) (cited on pages 109, 123, 126).

[571] Y. Liu, X. Liu, . . ., Q. Gong, *Selective Steering of Molecular Multiple Dissociative Channels with Strong Few-Cycle Laser Pulses*, Phys. Rev. Lett. **106**, 073004 (2011) (cited on pages 109, 123, 126).

[572] I. Znakovskaya, P. von den Hoff, . . ., M. Kling, *Subcycle Controlled Charge-Directed Reactivity with Few-Cycle Midinfrared Pulses*, Phys. Rev. Lett. **108**, 063002 (2012) (cited on pages 109, 123, 124, 127).

[573] D. Mathur, K. Dota, . . ., J. a. Dharmadhikari, *Carrier-Envelope-Phase Effects in Ultrafast Strong-Field Ionization Dynamics of Multielectron Systems: Xe and CS2*, Phys. Rev. Lett. **110**, 083602 (2013) (cited on pages 109, 123).

[574] H. Xu, T.-Y. Xu, . . ., I. V. Litvinyuk, *Effect of nuclear mass on carrier-envelope-phase-controlled electron localization in dissociating molecules*, Phys. Rev. A **89**, 041403 (2014) (cited on pages 109, 123, 124, 127).

[575] A. Alnaser, M. Kübel, . . ., M. Kling, *Subfemtosecond steering of hydrocarbon deprotonation through superposition of vibrational modes*, Nat. Commun. **5**, 3800 (2014) (cited on pages 109, 116, 123, 128, 129).

[576] X. Xie, S. Roither, . . ., M. Kitzler, *Electronic Predetermination of Ethylene Fragmentation Dynamics*, Phys. Rev. X 4, 021005 (2014) (cited on pages 109, 112, 115, 116, 118, 119).

[577] C. Guo, M. Li, . . ., G. Gibson, *Single and double ionization of diatomic molecules in strong laser fields*, Phys. Rev. A **58**, R4271–R4274 (1998) (cited on page 110).

[578] J. Muth-Böhm, A. Becker, and F. Faisal, *Suppressed Molecular Ionization for a Class of Diatomics in Intense Femtosecond Laser Fields*, Phys. Rev. Lett. **85**, 2280–2283 (2000) (cited on page 110).

[579] A. Alnaser, S. Voss, . . ., C. Cocke, *Effects Of Molecular Structure on Ion Disintegration Patterns In Ionization of O2 and N2 by Short Laser Pulses*, Phys. Rev. Lett. **93**, 113003 (2004) (cited on page 110).

[580] D. Mathur, A. Dharmadhikari, . . ., J. Dharmadhikari, *Molecular symmetry effects in the ionization of CS2 by intense few-cycle laser pulses*, Phys. Rev. A **78**, 013405 (2008) (cited on page 110).

[581] L. Holmegaard, J. L. Hansen, . . ., L. Bojer Madsen, *Photoelectron angular distributions from strong-field ionization of oriented molecules*, Nat. Phys. **6**, 428–432 (2010) (cited on page 110).

[582] J. L. Hansen, L. Holmegaard, . . ., L. B. Madsen, *Orientation-dependent ionization yields from strong-field ionization of fixed-in-space linear and asymmetric top molecules*, J. Phys. B At. Mol. Opt. Phys. **45**, 015101 (2012) (cited on page 110).

[583] T. Seideman and E. Hamilton, *Nonadiabatic alignment by intense pulses. Concepts, theory, and directions*, Adv. At. Mol. Opt. Phys. **52**, 289–329 (2005) (cited on page 110).

[584] A. Goban, S. Minemoto, and H. Sakai, *Laser-Field-Free Molecular Orientation*, Phys. Rev. Lett. **101**, 13001 (2008) (cited on page 110).

[585] A. Talebpour, A. Bandrauk, . . ., S. Chin, *Multiphoton ionization of inner-valence electrons and fragmentation of ethylene in an intense Ti:sapphire laser pulse*, Chem. Phys. Lett. **313**, 789–794 (1999) (cited on pages 110, 116).

[586] B. K. McFarland, J. P. Farrell, . . ., M. Gühr, *High harmonic generation from multiple orbitals in N2.* Science **322**, 1232–5 (2008) (cited on page 110).

[587] P. von den Hoff, I. Znakovskaya, . . ., R. de Vivie-Riedle, *Effects of multi orbital contributions in the angular-dependent ionization of molecules in intense few-cycle laser pulses*, Appl. Phys. B **98**, 659–666 (2009) (cited on page 110).

[588] H. Akagi, T. Otobe, . . ., P. B. Corkum, *Laser tunnel ionization from multiple orbitals in HCl*, Science **325**, 1364–7 (2009) (cited on page 110).

[589] C. Wu, H. Zhang, . . ., H. Su, *Tunneling ionization of carbon dioxide from lower-lying orbitals*, Phys. Rev. A **83**, 033410 (2011) (cited on page 110).

[590] M. Lezius, V. Blanchet, . . ., M. Ivanov, *Nonadiabatic Multielectron Dynamics in Strong Field Molecular Ionization*, Phys. Rev. Lett. **86**, 51–54 (2001) (cited on page 110).

[591] M. Lezius, V. Blanchet, . . ., A. Stolow, *Polyatomic molecules in strong laser fields: Nonadiabatic multielectron dynamics*, J. Chem. Phys. **117**, 1575 (2002) (cited on pages 110, 116).

[592] A. Markevitch, S. Smith, . . ., R. Levis, *Nonadiabatic dynamics of polyatomic molecules and ions in strong laser fields*, Phys. Rev. A **68**, 011402(R) (2003) (cited on pages 110, 116).

[593] I. Litvinyuk, F. Légaré, . . ., T. Brabec, *Shakeup Excitation during Optical Tunnel Ionization*, Phys. Rev. Lett. **94**, 033003 (2005) (cited on page 110).

[594] I. Znakovskaya, P. von Den Hoff, . . ., M. Kling, *Attosecond Control of Electron Dynamics in Carbon Monoxide*, Phys. Rev. Lett. **103**, 103002 (2009) (cited on pages 110, 116, 123, 126).

[595] H. W. van der Hart, *Sequential versus non-sequential double ionization in strong laser fields*, J. Phys. B At. Mol. Opt. Phys. **33**, L699–L705 (2000) (cited on pages 110, 116).

[596] V. L. B. de Jesus, B. Feuerstein, . . ., J. Ullrich, *Atomic structure dependence of nonsequential double ionization of He, Ne and Ar in strong laser pulses*, J. Phys. B At. Mol. Opt. Phys. **37**, L161–L167 (2004) (cited on pages 110, 116).

[597] T. Ikuta, K. Hosaka, . . ., R. Itakura, *Separation of ionization and subsequent electronic excitation for formation of electronically excited ethanol cation in intense laser fields*, J. Phys. B At. Mol. Opt. Phys. **44**, 191002 (2011) (cited on page 111).

[598] S. Erattupuzha, S. Larimian, . . ., M. Kitzler, *Two-pulse control over double ionization pathways in CO2*, J. Chem. Phys. 144, 024306 (2016) (cited on pages 111, 112, 116, 121, 122).

[599] A. Rudenko, V. Makhija, . . ., V. Kumarappan, *Strong-field-induced wave packet dynamics in carbon dioxide molecule*, Faraday Discuss. **194**, 463–478 (2016) (cited on pages 111, 122).

[600] T. Ergler, A. Rudenko, . . ., J. Ullrich, *Spatiotemporal Imaging of Ultrafast Molecular Motion: Collapse and Revival of the D2+ Nuclear Wave Packet*, Phys. Rev. Lett. **97**, 193001 (2006) (cited on page 111).

[601] B. Feuerstein, T. Ergler, . . ., J. Ullrich, *Complete Characterization of Molecular Dynamics in Ultrashort Laser Fields*, Phys. Rev. Lett. **99**, 153002 (2007) (cited on page 111).

[602] T. Ergler, B. Feuerstein, . . ., J. Ullrich, *Quantum-Phase Resolved Mapping of Ground-State Vibrational D2 Wave Packets via Selective Depletion in Intense Laser Pulses*, Phys. Rev. Lett. **97**, 103004 (2006) (cited on page 111).

[603] S. De, M. Magrakvelidze, . . ., C. Cocke, *Following dynamic nuclear wave packets in N2, O2, and CO with few-cycle infrared pulses*, Phys. Rev. A **84**, 043410 (2011) (cited on page 111).

[604] F. Légaré, K. Lee, . . ., P. Corkum, *Laser Coulomb-explosion imaging of small molecules*, Phys. Rev. A **71**, 013415 (2005) (cited on page 111).

[605] T. Seideman, M. Ivanov, and P. Corkum, *Role of Electron Localization in Intense-Field Molecular Ionization*, Phys. Rev. Lett. **75**, 2819–2822 (1995) (cited on pages 111, 113, 114).

[606] T. Zuo and A. D. Bandrauk, *Charge-resonance-enhanced ionization of diatomic molecular ions by intense lasers*, Phys. Rev. A **52**, R2511–R2514 (1995) (cited on pages 111, 113, 114).

[607] S. Larimian, S. Erattupuzha, . . ., X. Xie, *Fragmentation of long-lived hydrocarbons after strong field ionization*, Phys. Rev. A 93, 053405 (2016) (cited on pages 112, 128).

[608] H. Xu, T. Okino, . . ., M. Kitzler, *Two-proton migration in 1,3-butadiene in intense laser fields.* Phys. Chem. Chem. Phys. 12, 12939–12942 (2010) (cited on page 112).

[609] H. Xu, T. Okino, . . ., M. Kitzler, *Hydrogen migration and C–C bond breaking in 1,3-butadiene in intense laser fields studied by coincidence momentum imaging*, Chem. Phys. Lett. 484, 119–123 (2010) (cited on pages 112, 114).

[610] L. Zhang, S. Roither, . . ., M. Kitzler, *Path-selective investigation of intense laser-pulse-induced fragmentation dynamics in triply charged 1,3-butadiene*, J. Phys. B At. Mol. Opt. Phys. 45, 085603 (2012) (cited on pages 112, 115, 116, 120).

[611] H. Xu, T. Okino, . . ., S.-L. Chin, *Effect of laser parameters on ultrafast hydrogen migration in methanol studied by coincidence momentum imaging.* J. Phys. Chem. A 116, 2686–90 (2012) (cited on pages 112, 115, 116, 120).

[612] X. Xie, E. Lötstedt, . . ., M. Kitzler, *Duration of an intense laser pulse can determine the breakage of multiple chemical bonds*, Sci. Rep. 5, 12877 (2015) (cited on pages 112, 116, 120, 121, 127).

[613] S. Larimian, S. Erattupuzha, . . ., X. Xie, *Molecular oxygen observed by direct photoproduction from carbon dioxide*, Phys. Rev. A 95, 011404 (2017) (cited on page 112).

[614] R. Judson and H. Rabitz, *Teaching lasers to control molecules*, Phys. Rev. Lett. **68**, 1500–1503 (1992) (cited on pages 112, 115).

[615] A. Assion, T. Baumert, . . ., G. Gerber, *Control of Chemical Reactions by Feedback-Optimized Phase-Shaped Femtosecond Laser Pulses*, Science **282**, 919–922 (1998) (cited on pages 112, 115).

[616] H. Rabitz, R. de Vivie-Riedle, . . ., K. Kompa, *Whither the Future of Controlling Quantum Phenomena?*, Science **288**, 824–828 (2000) (cited on pages 112, 115).

[617] R. J. Levis, G. M. Menkir, and H. Rabitz, *Selective bond dissociation and rearrangement with optimally tailored, strong-field laser pulses.* Science **292**, 709–13 (2001) (cited on pages 112, 115).

[618] T. Okino, Y. Furukawa, . . ., H. Nakano, *Coincidence momentum imaging of ultrafast hydrogen migration in methanol and its isotopomers in intense laser fields*, Chem. Phys. Lett. **423**, 220–224 (2006) (cited on page 112).

[619] R. Itakura, P. Liu, . . ., H. Nakano, *Two-body Coulomb explosion and hydrogen migration in methanol induced by intense 7 and 21 fs laser pulses.* J. Chem. Phys. **127**, 104306 (2007) (cited on page 112).

[620] H. Ibrahim, B. Wales, . . ., F. Légaré, *Tabletop imaging of structural evolutions in chemical reactions demonstrated for the acetylene cation*, Nat. Commun. **5**, 4422 (2014) (cited on page 112).

[621] H. Xu, T. Okino, and K. Yamanouchi, *Ultrafast delocalization of hydrogen atoms in allene in intense laser fields*, Appl. Phys. A **104**, 941–945 (2011) (cited on page 112).

[622] Y. Furukawa, K. Hoshina, . . ., H. Nakano, *Ejection of triatomic hydrogen molecular ion from methanol in intense laser fields*, Chem. Phys. Lett. **414**, 117–121 (2005) (cited on page 112).

[623] R. Kanya, T. Kudou, . . ., K. Yamanouchi, *Hydrogen scrambling in ethane induced by intense laser fields: statistical analysis of coincidence events.* J. Chem. Phys. **136**, 204309 (2012) (cited on page 112).

[624] W. Salzmann, T. Mullins, . . ., A. Lindinger, *Coherent Transients in the Femtosecond Photoassociation of Ultracold Molecules*, Phys. Rev. Lett. **100**, 233003 (2008) (cited on page 113).

[625] P. Nuernberger, D. Wolpert, . . ., G. Gerber, *Femtosecond quantum control of molecular bond formation*, Proc. Natl. Acad. Sci. **107**, 10366–10370 (2010) (cited on page 113).

[626] L. Levin, W. Skomorowski, . . ., Z. Amitay, *Coherent Control of Bond Making*, Phys. Rev. Lett. **114**, 233003 (2015) (cited on page 113).

[627] Y. Petit, S. Henin, . . ., J. P. Wolf, *Production of ozone and nitrogen oxides by laser filamentation*, Appl. Phys. Lett. **97**, 9–12 (2010) (cited on page 113).

[628] H. L. Xu, A. Azarm, . . ., S. L. Chin, *The mechanism of nitrogen fluorescence inside a femtosecond laser filament in air*, Chem. Phys. **360**, 171–175 (2009) (cited on page 113).

[629] A. du Plessis, C. a. Strydom, . . ., L. R. Botha, *Laser induced and controlled chemical reaction of carbon monoxide and hydrogen.* J. Chem. Phys. **135**, 204303 (2011) (cited on page 113).

[630] A. D. Bandrauk and J. Ruel, *Charge-resonance-enhanced ionization of molecular ions in intense laser pulses: Geometric and orientation effects*, Phys. Rev. A **59**, 2153–2162 (1999) (cited on page 113).

[631] D. Pavičić, A. Kiess, . . ., H. Figger, *Intense-laser-field ionization of the hydrogen molecular ions H2+ and D2+ at critical internuclear distances*, Phys. Rev. Lett. **94**, 163002 (2005) (cited on page 113).

[632] T. K. Kjeldsen, L. B. Madsen, and J. P. Hansen, *Ab initio studies of strong-field ionization of arbitrarily oriented H 2 + molecules*, Phys. Rev. A **74**, 035402 (2006) (cited on page 113).

[633] G. Lagmago Kamta and A. Bandrauk, *Effects of molecular symmetry on enhanced ionization by intense laser pulses*, Phys. Rev. A **75**, 041401 (2007) (cited on page 113).

[634] N. Suzuki, I. Kawata, and K. Yamashita, *Comparison of the mechanisms of enhanced ionization of H2 and in intense laser fields*, Chem. Phys. **338**, 348–353 (2007) (cited on page 113).

[635] N. Takemoto and A. Becker, *Multiple Ionization Bursts in Laser-Driven Hydrogen Molecular Ion*, Phys. Rev. Lett. **105**, 203004 (2010) (cited on page 113).

[636] N. Takemoto and A. Becker, *Time-resolved view on charge-resonance-enhanced ionization*, Phys. Rev. A **84**, 023401 (2011) (cited on page 113).

[637] D. Strickland, Y. Beaudoin, . . ., P. Corkum, *Optical studies of inertially confined molecular iodine ions*, Phys. Rev. Lett. **68**, 2755–2758 (1992) (cited on page 113).

[638] E. Constant, H. Stapelfeldt, and P. B. Corkum, *Observation of Enhanced Ionization of Molecular Ions in Intense Laser Fields*, Phys. Rev. Lett. **76**, 4140–4143 (1996) (cited on page 113).

[639] H. Chen, L. Fang, . . ., G. N. Gibson, *Angle-resolved and internuclear-separation-resolved measurements of the ionization rate of the B state of I2 by strong laser fields*, Phys. Rev. A - At. Mol. Opt. Phys. **84**, 043427 (2011) (cited on page 113).

[640] H. Chen, V. Tagliamonti, and G. N. Gibson, *Enhanced ionization of an inner orbital of I2 by strong laser fields*, Phys. Rev. A **86**, 051403 (2012) (cited on page 113).

[641] L. Frasinski, K. Codling, . . ., W. Toner, *Femtosecond dynamics of multielectron dissociative ionization by use of a picosecond laser*, Phys. Rev. Lett. **58**, 2424–2427 (1987) (cited on page 113).

[642] K. Codling, L. J. Frasinski, and P. A. Hatherly, *On the field ionisation of diatomic molecules by intense laser fields*, J. Phys. B At. Mol. Opt. Phys. **22**, L321–L327 (1989) (cited on pages 113, 114).

[643] C. Cornaggia, D. Normand, and J. Morellec, *Role of the molecular electronic configuration in the Coulomb fragmentation of N2 , C2H2 and C2H4 in an intense laser field*, J. Phys. B At. Mol. Opt. Phys. **25**, L415–L422 (1992) (cited on pages 113, 114).

[644] M. Schmidt, D. Normand, and C. Cornaggia, *Laser-induced trapping of chlorine molecules with pico- and femtosecond pulses*, Phys. Rev. A **50**, 5037–5045 (1994) (cited on page 113).

[645] E. Dehghanian, A. D. Bandrauk, and G. Lagmago Kamta, *Enhanced ionization of the non-symmetric HeH+ molecule driven by intense ultrashort laser pulses*, J. Chem. Phys. **139**, 084315 (2013) (cited on page 113).

[646] G. Lagmago Kamta and A. D. Bandrauk, *Nonsymmetric molecules driven by intense few-cycle laser pulses: Phase and orientation dependence of enhanced ionization*, Phys. Rev. A - At. Mol. Opt. Phys. **76**, 053409 (2007) (cited on page 113).

[647] S. Roither, X. Xie, . . ., M. Kitzler, *High Energy Proton Ejection from Hydrocarbon Molecules Driven by Highly Efficient Field Ionization*, Phys. Rev. Lett. 106, 163001 (2011) (cited on pages 113, 114, 128).

[648] X. Xie, S. Roither, . . ., M. Kitzler, *Role of proton dynamics in efficient photoionization of hydrocarbon molecules*, Phys. Rev. A 89, 023429 (2014) (cited on pages 113, 114, 119).

[649] E. Lötstedt, T. Kato, and K. Yamanouchi, *Enhanced ionization of acetylene in intense laser fields*, Phys. Rev. A **85**, 041402 (2012) (cited on page 113).

[650] E. Lötstedt, T. Kato, and K. Yamanouchi, *Efficient ionization of one-dimensional acetylene investigated by time-dependent Hartree-Fock calculations*, Phys. Rev. A **86**, 023401 (2012) (cited on page 113).

[651] E. Lötstedt, T. Kato, and K. Yamanouchi, *Intramolecular electron dynamics in the ionization of acetylene by an intense laser pulse.* J. Chem. Phys. **138**, 104304 (2013) (cited on page 113).

[652] C. Cornaggia, M. Schmidt, and D. Normand, *Laser-induced nuclear motions in the Coulomb explosion of C2H2+ ions*, Phys. Rev. A **51**, 1431–1437 (1995) (cited on page 114).

[653] C. Cornaggia, *Electronic dynamics of charge resonance enhanced ionization probed by laser-induced alignment in C 2 H 2*, J. Phys. B At. Mol. Opt. Phys. **49**, 19LT01 (2016) (cited on page 114).

[654] M. Shapiro and P. Brumer, *Quantum Control of Molecular Processes*, 2nd ed. (Wiley-VCH Verlag GmbH & Co. KGaA, Weinheim, Germany, 12/2012) (cited on page 115).

[655] J. Wu, *Controlling a Molecule's Fate*, Physics **7**, 36 (2014) (cited on page 119).

[656] P. Sándor, V. Tagliamonti, . . ., T. Weinacht, *Strong Field Molecular Ionization in the Impulsive Limit: Freezing Vibrations with Short Pulses*, Phys. Rev. Lett. **116**, 063002 (2016) (cited on page 119).

[657] A. Alnaser, X. Tong, . . ., C. Cocke, *Routes to Control of H2 Coulomb Explosion in Few-Cycle Laser Pulses*, Phys. Rev. Lett. **93**, 183202 (2004) (cited on page 119).

[658] T. Shimanouchi, *Tables of molecular vibrational frequencies. Consolidated volume II*, J. Phys. Chem. Ref. Data **6**, 993 (1977) (cited on page 120).

[659] K. Lammertsma, M. Barzaghi, . . ., P. v. R. Schleyer, *The ethylene dication: a theoretical study of the ethylene dication (C2H42+) potential-energy surface*, J. Am. Chem. Soc. **105**, 5252–5257 (1983) (cited on page 120).

[660] A. S. Alnaser and I. V. Litvinyuk, *Subfemtosecond directional control of chemical processes in molecules*, J. Phys. B At. Mol. Opt. Phys. **50**, 032002 (2017) (cited on page 122).

[661] M. Kling, C. Siedschlag, . . ., M. Vrakking, *Strong-field control of electron localisation during molecular dissociation*, Mol. Phys. **106**, 455–465 (2008) (cited on pages 123, 124, 127).

[662] T. Rathje, A. M. Sayler, . . ., G. G. Paulus, *Coherent Control at Its Most Fundamental: Carrier-Envelope-Phase-Dependent Electron Localization in Photodissociation of a H2+ Molecular Ion Beam Target*, Phys. Rev. Lett. **111**, 093002 (2013) (cited on page 123).

[663] H. Xu, J. P. MacLean, . . ., I. V. Litvinyuk, *Carrier-envelope-phase-dependent dissociation of hydrogen*, New J. Phys. **15**, 023034 (2013) (cited on pages 123, 124, 126).

[664] H. Li, X. M. Tong, . . ., M. F. Kling, *Intensity dependence of the dissociative ionization of DCl in few-cycle laser fields*, J. Phys. B **49**, 015601 (2016) (cited on pages 123, 126).

[665] D. Mathur, K. Dota, . . ., P. Vasa, *Selective breaking of bonds in water with intense, 2-cycle, infrared laser pulses*, J. Chem. Phys. **143**, 244310 (2015) (cited on pages 123, 128).

[666] M. Kübel, A. S. Alnaser, . . ., M. F. Kling, *Strong-field control of the dissociative ionization of N2O with near-single-cycle pulses*, New J. Phys. **16**, 065017 (2014) (cited on pages 123, 128).

[667] H. Li, N. G. Kling, . . ., S. Kaziannis, *Carrier-envelope phase dependence of the directional fragmentation and hydrogen migration in toluene in few-cycle laser fields*, Struct. Dyn. **3**, 043206 (2016) (cited on pages 123, 128).

[668] M. Kübel, R. Siemering, . . ., M. F. Kling, *Steering Proton Migration in Hydrocarbons Using Intense Few-Cycle Laser Fields*, Phys. Rev. Lett. **116**, 193001 (2016) (cited on pages 123, 125, 128, 129).

[669] S. Gräfe and M. Y. Ivanov, *Effective Fields in Laser-Driven Electron Recollision and Charge Localization*, Phys. Rev. Lett. **99**, 163603 (2007) (cited on page 124).

[670] F. Kelkensberg, G. Sansone, . . ., M. Vrakking, *A semi-classical model of attosecond electron localization in dissociative ionization of hydrogen*, Phys. Chem. Chem. Phys. **13**, 8647–8652 (2011) (cited on page 124).

[671] G. Cerullo and C. Vozzi, *Coherent Control of Chemical Reactions on the Attosecond Time Scale*, Physics **5**, 138 (2012) (cited on page 125).

[672] V. Roudnev and B. D. Esry, *General Theory of Carrier-Envelope Phase Effects*, Phys. Rev. Lett. **99**, 220406 (2007) (cited on page 126).

[673] P. H. Bucksbaum, A. Zavriyev, . . ., D. W. Schumacher, *Softening of the H2+ molecular bond in intense laser fields*, Phys. Rev. Lett. **64**, 1883–1886 (1990) (cited on page 126).

[674] A. Zavriyev, P. H. Bucksbaum, . . ., D. W. Schumacher, *Ionization and dissociation of H2 in intense laser fields at 1.064 µm, 532 nm, and 355 nm*, Phys. Rev. A **42**, 5500–5513 (1990) (cited on page 126).

[675] I. V. Litvinyuk, A. S. Alnaser, . . ., D. M. Villeneuve, *Wavelength-dependent study of strong-field Coulomb explosion of hydrogen*, New J. Phys. **10**, 083011 (2008) (cited on page 126).

[676] H. Niikura, D. M. Villeneuve, and P. B. Corkum, *Mapping Attosecond Electron Wave Packet Motion*, Phys. Rev. Lett. **94**, 083003 (2005) (cited on page 126).

[677] M. R. Thompson, M. K. Thomas, . . ., K. Codling, *One and two-colour studies of the dissociative ionization and Coulomb explosion of with intense Ti:sapphire laser pulses*, J. Phys. B At. Mol. Opt. Phys. **30**, 5755–5772 (1997) (cited on page 130).

[678] B. Sheehy, *Chemical processes in intense optical fields*, Annu. Reports Sect. "C" (Phys. Chem.) **97**, 383–410 (2001) (cited on page 130).

[679] V. Wanie, H. Ibrahim, . . ., F. Légaré, *Coherent control of D2/H2 dissociative ionization by a mid-infrared two-color laser field*, J. Phys. B At. Mol. Opt. Phys. **49**, 025601 (2016) (cited on pages 130, 131).

[680] H. Xu, H. Hu, . . ., I. V. Litvinyuk, *Coherent control of the dissociation probability of H2+ in ω-3ω two-color fields*, Phys. Rev. A **93**, 063416 (2016) (cited on pages 130, 131).

[681] X. Xie, S. Roither, . . ., M. Kitzler, "Stimulated Raman Scattering Induced Molecular Dissociation", in 6TH INT. CONF. ON ATTOSECOND PHYS. (2017), Technical Digest, Paper Nr. 92 (cited on pages 130, 131).

[682] P. Lan, E. J. Takahashi, and K. Midorikawa, *Efficient control of electron localization by subcycle waveform synthesis*, Phys. Rev. A **86**, 013418 (2012) (cited on page 131).

[683] Z. Wang, K. Liu, . . ., P. Lu, *Steering the electron in dissociating H2+ via manipulating two-state population dynamics by a weak low-frequency field*, Phys. Rev. A **91**, 043419 (2015) (cited on page 131).

[684] H. Ohmura, T. Nakanaga, and M. Tachiya, *Coherent Control of Photofragment Separation in the Dissociative Ionization of IBr*, Phys. Rev. Lett. **92**, 113002 (2004) (cited on page 131).

[685] H. Ohmura and T. Nakanaga, *Quantum control of molecular orientation by two-color laser fields*, J. Chem. Phys. **120**, 5176 (2004) (cited on page 131).

[686] H. Ohmura, N. Saito, and M. Tachiya, *Selective Ionization of Oriented Nonpolar Molecules with Asymmetric Structure by Phase-Controlled Two-Color Laser Fields*, Phys. Rev. Lett. **96**, 173001 (2006) (cited on page 131).

[687] H. Ohmura, N. Saito, . . ., S. Ichimura, *Dissociative ionization of a large molecule studied by intense phase-controlled laser fields*, Phys. Rev. A **77**, 053405 (2008) (cited on pages 131, 132).

[688] H. Ohmura, N. Saito, and T. Morishita, *Quantum control of molecular tunneling ionization in the spatiotemporal domain*, Phys. Rev. A **83**, 063407 (2011) (cited on page 131).

[689] S. Kaziannis, N. Kotsina, and C. Kosmidis, *Interaction of toluene with two-color asymmetric laser fields: Controlling the directional emission of molecular hydrogen fragments*, J. Chem. Phys. **141**, 104319 (2014) (cited on page 131).

[690] N. Kotsina, S. Kaziannis, and C. Kosmidis, *Hydrogen migration in methanol studied under asymmetric fs laser irradiation*, Chem. Phys. Lett. **604**, 27–32 (2014) (cited on page 131).

[691] N. Kotsina, S. Kaziannis, and C. Kosmidis, *Phase dependence of OD+, HOD+, and H3+ ions released from the deuterated dication of methanol under ω/2ω laser field irradiation*, Int. J. Mass Spectrom. **380**, 34–39 (2015) (cited on page 131).

[692] H. Ohmura and N. Saito, *Quantum control of a molecular ionization process by using Fourier-synthesized laser fields*, Phys. Rev. A **92**, 053408 (2015) (cited on page 131).

[693] Q. Song, Z. Li, . . ., J. Wu, *Disentangling the role of laser coupling in directional breaking of molecules*, Phys. Rev. A **94**, 053419 (2016) (cited on pages 131, 132).

[694] T. Endo, H. Fujise, . . ., A. Hishikawa, *Coincidence momentum imaging of asymmetric Coulomb explosion of CO2 in phase-locked two-color intense laser fields*, J. Electron Spectros. Relat. Phenomena **207**, 50–54 (2016) (cited on pages 131, 132).

[695] Q. Song, X. Gong, . . ., J. Wu, *Directional deprotonation ionization of acetylene in asymmetric two-color laser fields*, J. Phys. B At. Mol. Opt. Phys. **48**, 094007 (2015) (cited on page 131).

[696] X. Gong, P. He, . . ., J. Wu, *Two-Dimensional Directional Proton Emission in Dissociative Ionization of H2*, Phys. Rev. Lett. **113**, 203001 (2014) (cited on pages 132, 133).

Acronyms and abbreviations

ABI	above barrier ionization
ADK	tunneling theory named after Ammosov, Delone and Krainov
AOM	acousto optical modulator
ATD	above threshold dissociation
ATI	above threshold ionization
BO	Born-Oppenheimer
BS	bond-softening
CCD	charge-coupled device
CED	conventional electron diffraction
CE(P)	carrier-envelope (phase)
COLTRIMS	cold target recoil ion momentum spectroscopy
(CR)EI	(charge-resonance) enhanced ionization
CTMC	classical trajectory Monte Carlo
CRTC/CoRTC	counter-rotating two-color/co-rotating two-color
DCS	differential cross-section
DFG	difference frequency generation
EIC-MOUSE	enhanced ionization from laser-coupled multiple orbitals that are up-shifted in energy
EPTC	elliptically polarized two-color
EWP	electron wavepacket
FFI	frustrated field ionization
FWHM	full width at half maximum
HATI	high-energy/high-order ATI
HH(G)	high harmonic (generation)
(HO)MO	(highest occupied) molecular orbital
KER	kinetic energy release
KFR	tunneling theory named after Keldysh, Faisal and Reiss
LIED	laser-induced electron diffraction
MCF	molecular contrast factor
MCP	micro-channel plate
MCTDHF	multi-configuration time-dependent Hartree-Fock
NSDI/NSMI	non-sequential double/multiple ionization
OTC	orthogonally polarized two-color
OPA	optical parametric amplification
PEMD	photoelectron momentum distribution
PEPICO/PIPICO	photoelectron-photoion coincidence/photoion-photoion coincidence
PES/PEC	potential energy surface/curve
QRS	quantitative rescattering theory
REMI	reaction microscope/microscopy

RESI	recollision-induced excitation and subsequent field ionization
SAE	single active electron
SAM	spin angular momentum
SDI	sequential double ionization
SFA	strong-field approximation
SHG	second-harmonic generation
SMM	simple man's model
(TD)DFT	(time-dependent) density functional theory
(TD)HF	(time-dependent) Hartree-Fock
TDSE	time-dependent Schrödinger equation
THz	Terahertz
VMI	velocity map imaging
WLG	white light generation
XUV	extreme ultraviolet
3PD	three-photon dissociation

c	speed of light
I_p	ionization potential
U_p	ponderomotive potential
$\omega/2\omega, \omega/3\omega, \omega/n\omega, \ldots$	two-color tailored waveforms consisting of two fields with a frequency ratio of 2, 3, $n, \ldots$
ω_o	(fundamental) laser oscillation frequency
ω_r	pulse repetition frequency/rate
$T = \frac{2\pi}{\omega_o}$	laser oscillation period
$T_r = \frac{2\pi}{\omega_r}$	time between pulses in a pulse train, cavity round trip time
$\Delta\varphi$	relative phase between two laser fields
φ_{CE}	carrier-envelope offset phase
ω_{CE}	carrier-envelope offset frequency
$\boldsymbol{E}(t)$	laser electric field
$\boldsymbol{A}(t)$	laser vector potential
$\boldsymbol{\epsilon}(t), \boldsymbol{\epsilon}(\omega)$	harmonic field in time/frequency domain

Atomic Units

Atomic units are used for convenience in quantum physics, as by setting the fundamental constants *electron rest mass*, m_e, *elementary charge*, e, *reduced Planck's constant*, $\hbar$, and *Coulomb's constant*, $1/4\pi\varepsilon_0$, to unity,

$$m_{\mathrm{e}} = e = \hbar = \frac{1}{4\pi\varepsilon_0} = 1,$$

numbers become handy and equations become simplified substantially (see Ref. [194] for further details). With that settings one obtains from the value of the fine-structure constant

$$\alpha = \frac{e^2}{(4\pi\epsilon_0)\hbar c} \approx 1/137,$$

which, being a dimensionless quantity, has the same numerical value in all system of units, the value of the speed of light in atomic units as

$$c = 1/\alpha \approx 137.$$

The value of 1 atomic unit for other important quantities transfers to SI units as follows:

quantity	SI	
charge	$1.602 \times 10^{-19}\,\mathrm{C}$	charge of the electron, e
mass	$9.109 \times 10^{-31}\,\mathrm{kg}$	mass of the electron, m_e
length	$5.2917 \times 10^{-11}\,\mathrm{m}$	radius of the first Bohr orbit, a_0
velocity	$2.1877 \times 10^{6}\,\mathrm{m/s}$	electron velocity in the first Bohr orbit, v_B
momentum	$1.9926 \times 10^{-24}\,\mathrm{kg\ m/s}$	electron momentum in first Bohr orbit, $m_e v_B$
time	$24.189 \times 10^{-18}\,\mathrm{s}$	$\tau_0 = \frac{a_0}{v_B}$, roughly 24.2 as
frequency	$4.1341 \times 10^{16}\,\mathrm{s}^{-1}$	$\frac{1}{\tau_0}$
energy	$4.359 \times 10^{-18}\,\mathrm{J} \approx 21.21\,\mathrm{eV}$	twice the ionization potential of hydrogen
electric field	$5.142 \times 10^{11}\,\mathrm{V/m}$	$E_0 = \frac{e}{4\pi\varepsilon_0 a_0^2}$
intensity	$3.5094452 \times 10^{16}\,\mathrm{W/cm^2}$	$I_0 = \frac{1}{2}\varepsilon_0 c E_0^2$

Acknowledgments

The scientific work that led to the publications attached in the following has been a collaborative effort of many people and I am immensely grateful to all of them for their contributions. Particular thanks go those people who have obtained their PhD degree at Photonics Institute during this work and who I was allowed to guide in their efforts. These were Stefan Roither, whose brave pioneering labor in building the Cleveland Steamer is legendary; Li Zhang, who was courageously taming two-color experiments and C++ codes; Sonia Erattupuzha, who was putting lots of effort in harvesting large potatoes and finally became queen of COLTRIMS; and Sina Larimian, who eventually outgrew the role of the crown prince and obtained an impressive amount of results. Many thanks guys, it was fun working with you!

The work of the PhD students would, however, not have been so successful if I couldn't have counted also on the help of several Post-Docs: I am very grateful to Daniil Kartashov, whose commitment in our efforts of obtaining colorful laser light in our labs was crucial for our great success. Spasibo bol'shoe, Daniil! It is my pleasure to thank Markus Schöffler. His help and advice in building and constantly improving the REMI and his passion for dancing were key for literally all our experiments described in this thesis. Danke vielmals, Markus! Ich hoffe du kommst bald wieder einmal zum Tanzen nach Wien. Special thanks go to Xinhua Xie, whose brilliance in data analysis and intuition in physics was (and still is) in many cases a decisive factor in the interpretation of our data measured with the REMI. Xièxiè nǐ bāngzhù wǒ, Xinhua!

I am also very grateful that we could always count on the help and support of the whole Ultrafast Laser Group at Photonics Institute. Exemplarily for the whole group I want to acknowledge the help of Audrius Pugzlys and the support from Andrius Baltuska, the leader of the group. Many thanks, Andrius, for all the scientific freedom that I have been enjoying for so many years now!

Finally, I want to thank all the persons, who I am currently working together with, for their strong commitment. These are Václav Hanus and Sarayoo Kangaparambil, and also Xinhua Xie as senior member, the current team working with the REMI; and Martin Kirchner and Paolo Carpeggiani, who are working on expanding our activities to dynamics probed with XUV attosecond pulses. You are doing great work, guys!

One of the most important and also joyful aspects of successful science is and always has been collaboration with other scientists. I am very grateful that for working on the publications in this thesis I could count on the help and input from many national and international collaborators. And I take it as a good sign that I need to apologize that I cannot mention all of them here but need to restrict myself to a few exemplary acknowledgments.

One of the most long-standing collaboration exists with the group of Prof. Kaoru Yamanouchi, The University of Tokyo. I am grateful to Prof. Yamanouchi for support through many years and for numerous invitations during which I was allowed to get to know Japanese culture and enjoy Japanese food. Domo arigatou gozaimasu, Prof. Yamanouchi! I am very happy that this collaboration was not only scientifically very influential but also initiated a number of dear personal relations, in particular with Erik Lötstedt, Huailiang Xu (now at Jilin University, China), Atsushi Iwasaki, Reika Kanya, Kana Yamada and many more. Arigatou gozaimasu, friends!

I am also extremely grateful about the collaboration with the group of Prof. Xiaojun Liu, which is situated a little bit further to the west of Japan, in Wuhan, China, more precisely at the Wuhan Institute of Physics and Mathematics of the Chinese Academy of Sciences. The simulations performed by Xiaojun's group were crucial for the interpretation of several experiments in this thesis. Xièxiè nǐ bāngzhù wǒ, Xiaojun!

Still further to the west we arrive in Europe. As the proverb says, why seek far when the good is close. This proverb is perfectly applicable to the theory group of Prof. Joachim Burgörfer at TU Wien, with which we have been successfully collaborating for many years. Herzlichen Dank, Joachim!

The collaboration with the Burgörfer-group has, in fact, already spawned and has created additional roots to the north, at the University of Jena, Germany, where a very helpful collaborator and dear friend, Prof. Stefanie Gräfe, has moved to. Vielen Dank für alles, Steffi!

The University of Jena seems to attract people that are successful and helpful likewise. Quite a number of our experiments would not have been possible without the support by the group of Prof. Gerhard Paulus that is also located at this university. Herzlichen Dank, Gerhard!

Moving further to the west, across the Atlantic, we arrive in the USA, more exactly in Nashville, Tennessee, where people not only love country-music but also sophisticated numerical simulations. This is particularly true for Prof. Kálmán Varga and his team. Köszönöm szépen, Kálmán, for your support!

Quite a bit north from Nashville is Ottawa, the lovely city where I was working during my PhD studies and where the famous National Research Council of Canada is situated. There, André Staudte is leading the REMI research activities. I am very grateful for our collaboration in a likewise stimulating and casual atmosphere. Vielen Dank, André!

Finally, it is my dearest delight to thank my family and friends for their support!

Paper 1

Spatial Control of Recollision Wave Packets with Attosecond Precision

M. Kitzler, M. Lezius

Phys. Rev. Lett. **95**, 253001 (2005)

Paper 2

Optical attosecond mapping by polarization selective detection

M. Kitzler, X. Xie, A. Scrinzi, A. Baltuška

Phys. Rev. A **76**, 11801 (2007)

Paper 3

Angular encoding in attosecond recollision

M. Kitzler, X. Xie, S. Roither, A. Scrinzi, A. Baltuška

New J. Phys. **10**, 25029 (2008)

Paper 4

Laser-sub-cycle two-dimensional electron-momentum mapping using orthogonal two-color fields

L. Zhang, X. Xie, S. Roither, D. Kartashov, Y. Wang, C. Wang, M. Schöffler, D. Shafir, P. B. Corkum, A. Baltuška, I. Ivanov, A. Kheifets, X. Liu, A. Staudte, and M. Kitzler

Phys. Rev. A **90**, 61401 (2014)

Paper 5

Subcycle Control of Electron-Electron Correlation in Double Ionization

L. Zhang, X. Xie, S. Roither, Y. Zhou, P. Lu, D. Kartashov, M. Schöffler, D. Shafir, P. B. Corkum, A. Baltuška, A. Staudte, and M. Kitzler

Phys. Rev. Lett. **112**, 193002 (2014)

Paper 6

Internal Momentum State Mapping Using High Harmonic Radiation

X. Xie, A. Scrinzi, M. Wickenhauser, A. Baltuška, I. Barth, and M. Kitzler

Phys. Rev. Lett. **101**, 33901 (2008)

Paper 7

Laser-subcycle control of sequential double-ionization dynamics of helium

M. Schöffler, X. Xie, P. Wustelt, M. Möller, S. Roither, D. Kartashov, A. M. Sayler, A. Baltuška, G. Paulus, and M. Kitzler

Phys. Rev. A **93**, 63421 (2016)

Paper 8

Attosecond Probe of Valence-Electron Wave Packets by Subcycle Sculpted Laser Fields

X. Xie, S. Roither, D. Kartashov, E. Persson, D. G. Arbó, L. Zhang, S. Gräfe, M. Schöffler, J. Burgdörfer, A. Baltuška, and M. Kitzler

Phys. Rev. Lett. **108**, 193004 (2012)

Paper 9

Disentangling Intracycle Interferences in Photoelectron Momentum Distributions Using Orthogonal Two-Color Laser Fields

X. Xie, T. Wang, S. Yu, X. Lai, S. Roither, D. Kartashov, A. Baltuška, X. Liu, A. Staudte, and M. Kitzler

Phys. Rev. Lett. **119**, 243201 (2017)

Paper 10

Probing the influence of the Coulomb field on atomic ionization by sculpted two-color laser fields

X. Xie, S. Roither, S. Gräfe, D. Kartashov, E. Persson, C. Lemell, L. Zhang, M. Schöffler, A. Baltuška, J. Burgdörfer, and M. Kitzler

New J. Phys. **15**, 43050 (2013)

Paper 11

Attosecond-Recollision-Controlled Selective Fragmentation of Polyatomic Molecules

X. Xie, K. Doblhoff-Dier, S. Roither, M. Schöffler, D. Kartashov, H. Xu, T. Rathje, G. Paulus, A. Baltuška, S. Gräfe, and M. Kitzler

Phys. Rev. Lett. **109**, 243001 (2012)

Paper 12

Selective Control over Fragmentation Reactions in Polyatomic Molecules Using Impulsive Laser Alignment

X. Xie, K. Doblhoff-Dier, H. Xu, S. Roither, M. Schöffler, D. Kartashov, S. Erattupuzha, T. Rathje, G. Paulus, K. Yamanouchi, A. Baltuška, S. Gräfe, and M. Kitzler

Phys. Rev. Lett. **112,** 163003 (2014)

Paper 13

Duration of an intense laser pulse can determine the breakage of multiple chemical bonds

X. Xie, E. Lötstedt, S. Roither, M. Schöffler, D. Kartashov, K. Midorikawa, A. Baltuška, K. Yamanouchi, and M. Kitzler

Sci. Rep. **5**, 12877 (2015)

Paper 14

Electronic Predetermination of Ethylene Fragmentation Dynamics

X. Xie, S. Roither, M. Schöffler, E. Lötstedt, D. Kartashov, L. Zhang, G. Paulus, A. Iwasaki, A. Baltuška, K. Yamanouchi, and M. Kitzler

Phys. Rev. X **4**, 21005 (2014)

Paper 15

Two-Pulse Control over Double Ionization Pathways in CO_2

S. Erattupuzha, S. Larimian, A. Baltuška, X. Xie, M. Kitzler

J. Chem. Phys. **144**, 24306 (2016)

Paper 16

High Energy Proton Ejection from Hydrocarbon Molecules Driven by Highly Efficient Field Ionization

S. Roither, X. Xie, D. Kartashov, L. Zhang, M. Schöffler, H. Xu, A. Iwasaki, T. Okino, K. Yamanouchi, A. Baltuška, and M. Kitzler

Phys. Rev. Lett. **106**, 163001 (2011)

Paper 17

Role of proton dynamics in efficient photoionization of hydrocarbon molecules

X. Xie, S. Roither, M. Schöffler, H. Xu, S. Bubin, E. Lötstedt, S. Erattuphuza, A. Iwasaki, D. Kartashov, K. Varga, G. Paulus, A. Baltuška, K. Yamanouchi, and M. Kitzler

Phys. Rev. A **89**, 23429 (2014)

Paper 18

Enhanced ionisation of polyatomic molecules in intense laser pulses is due to energy upshift and field coupling of multiple orbitals

S. Erattupuzha, C. L. Covington, A. Russakoff, E. Lötstedt, S. Larimian, V. Hanus, S. Bubin, M. Koch, S. Gräfe, A. Baltuška, X. Xie, K. Yamanouchi, K. Varga, and M. Kitzler

J. Phys. B At. Mol. Opt. Phys. **50**, 125601 (2017)

v69/20180719